SPIE PRESS

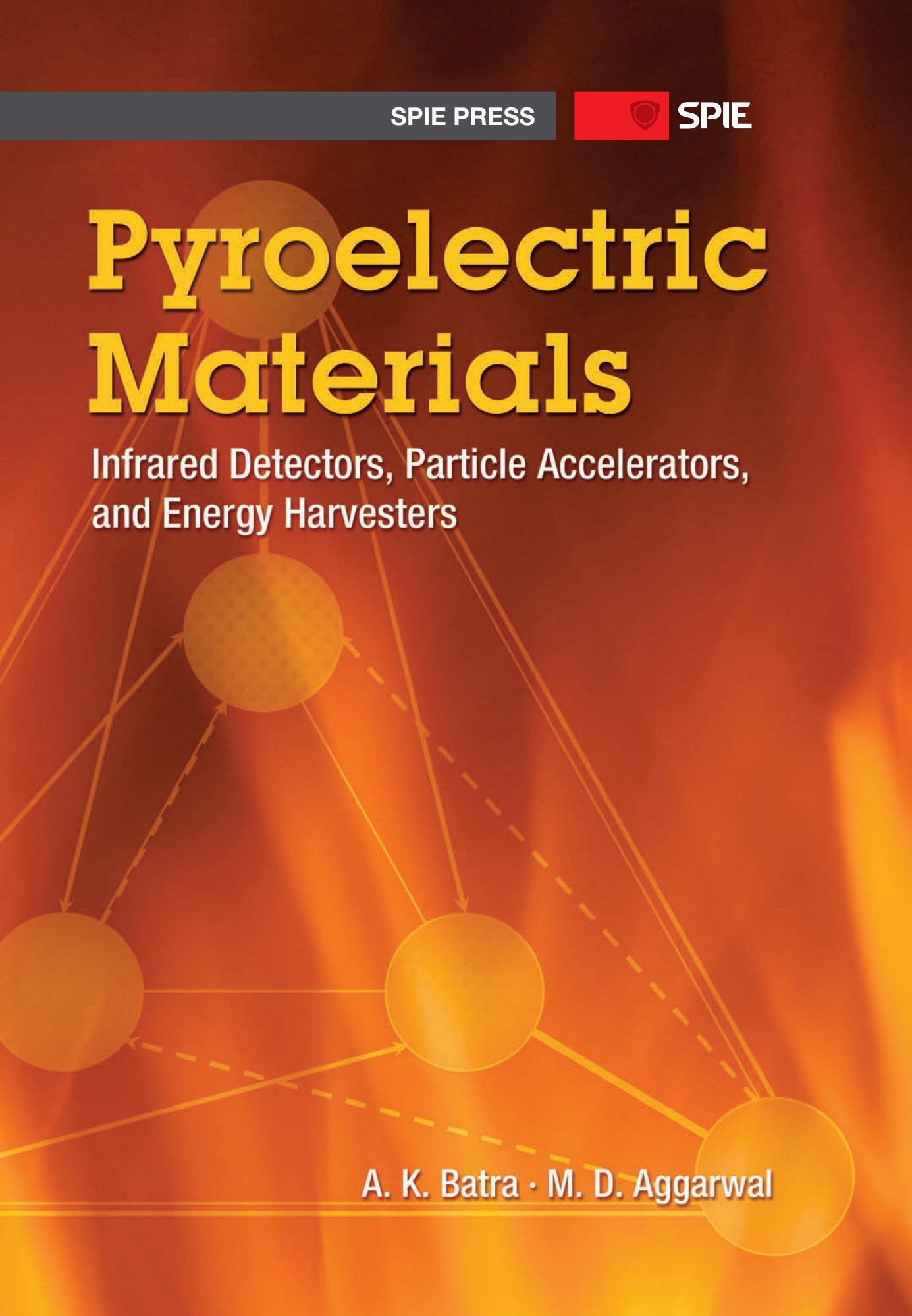

Pyroelectric Materials

Infrared Detectors, Particle Accelerators, and Energy Harvesters

A. K. Batra · M. D. Aggarwal

Pyroelectric Materials

Infrared Detectors, Particle Accelerators, and Energy Harvesters

Pyroelectric Materials

Infrared Detectors, Particle Accelerators, and Energy Harvesters

A. K. Batra
M. D. Aggarwal

SPIE
PRESS
Bellingham, Washington USA

Library of Congress Cataloging-in-Publication Data

Batra, A. K.
Pyroelectric materials : infrared detectors, particle accelerators and energy harvesters / A.K. Batra, M.D. Aggarwal.
pages cm
Includes bibliographical references and index.
ISBN 978-0-8194-9331-6 ISBN 978-0-8194-9332-3 ISBN 978-0-8194-9333-0
1. Pyroelectric detectors Materials. 2. Thermoelectric apparatus and appliances Design and construction. I. Aggarwal, M. D. II. Title.
QC338.5.P95B38 2013
620.1'9 dc23

2013014472

Published by

SPIE
P.O. Box 10
Bellingham, Washington 98227-0010 USA
Phone: +1.360.676.3290
Fax: +1.360.647.1445
Email: Books@spie.org
www.spie.org

Printed in the United States of America
First printing

Table of Contents

Foreword ix

Preface xi

Acknowledgments xiii

Glossary of Symbols and Abbreviations xv

1 Fundamentals of Pyroelectric Materials 1

1.1 Introduction 1
1.2 Classification of Dielectric Materials 1
1.3 Important Dielectric Parameters 5
1.3.1 Electric dipole moment 5
1.3.2 Polar and nonpolar dielectric materials 5
1.3.3 Electric polarization 5
1.3.4 Electric displacement or flux density **D**, dielectric constant ε, and electric susceptibility χ 6
1.3.5 Spontaneous polarization 6
1.4 Electrostrictive Effect 7
1.5 Piezoelectric Phenomena 7
1.6 Pyroelectric Phenomenon 9
1.6.1 Pyroelectric current generation 11
1.7 Ferroelectric Phenomena 14
1.7.1 Ferroelectric domains 14
1.7.2 Ferroelectric hysteresis 14
1.7.3 Poling 15
1.7.4 Paraelectric effect 16
1.8 Conclusions 16
References 16

2 Pyroelectric IR Detectors 19

2.1 Introduction 19
2.2 IR Fundamentals 19
2.3 IR Detectors 21
2.4 Pyroelectric IR Detectors 22
2.4.1 IR-detector operation 22

2.4.2 Pyroelectric-detector responsivity 24
2.4.3 Noise-equivalent power 26
2.4.4 Detectivity 27
2.4.5 Noise 28
2.5 Material Performance Parameters 29
2.5.1 Material figures of merit 30
2.6 Structural Design 30
2.6.1 Characteristics of absorbers 31
2.6.2 Single-element detector design 32
2.6.3 Thin-film-based detectors 34
2.6.4 Hybrid focal-plane arrays 35
2.6.5 Monolith-integrated focal-plane array 35
2.6.6 Advanced lithium-tantalate-detector array 36
2.6.7 Trap detector 37
2.6.8 Resonant detector 38
2.6.9 Srico TFLT™ detector 39
2.7 Pyroelectric-Detector Applications 41
2.8 Conclusions 42
References 42

3 Processing of Key Pyroelectric Materials 47
3.1 Introduction 47
3.2 Bulk Single Crystals 47
3.2.1 Growth of crystals from solution 47
3.2.2 Crystal growth from melt 48
3.3 Preparation of Ceramics 50
3.4 Thin-Film Deposition 51
3.4.1 Nonsolution deposition 51
3.4.1.1 Sputtering technique 51
3.4.1.2 Laser-ablation technique 52
3.4.1.3 Chemical-vapor-deposition technique 52
3.4.2 Solution deposition 54
3.4.2.1 Sol-gel technique 54
3.4.2.2 Metalorganic-deposition technique 55
3.5 Thick-Film Fabrication 59
3.5.1 Thick-film-transfer technology (screen printing) 59
3.6 Fabrication of Polymer–Ceramic Composite Precursors 60
References 62

4 Important Pyroelectrics: Properties and Performance Parameters 65
4.1 Introduction 65
4.2 Important Pyroelectrics 65
4.2.1 Triglycine sulfate crystals and their isomorphs 65
4.2.2 Modified lead titanate 69

4.2.3 Lead zirconate titanate 72
4.2.4 Lithium tantalate and lithium niobate 78
4.2.5 Barium strontium titanate materials system 81
4.2.6 Strontium barium niobate 84
4.2.7 Lead magnesium niobate-lead titanate (PMN-PT) 85
4.3 Organic Pyroelectrics 86
4.4 Pyroelectric–Polymer Composites 87
4.5 Other Pyroelectric Materials 91
4.5.1 Aluminum nitride (AlN) 91
4.5.2 Gallium nitride (GaN) 92
4.5.3 Zinc oxide (ZnO) 92
4.6 Lead-free Pyroelectric Ceramics 93
4.7 Conclusions 93
References 94

5 Innovative Techniques for Pyroelectric IR Detectors 105
5.1 Introduction 105
5.2 Multilayer Structures 105
5.3 Compositionally Graded Structures 107
5.4 Pyroelectric Heterostructures 109
5.5 Use of Nanoporosity 112
5.6 Novel Designs and Techniques 113
5.7 Conclusions 118
References 118

6 Pyroelectric Particle Generators 121
6.1 Introduction 121
6.2 Electrostatistics of a Pyroelectric Accelerator 122
6.2.1 One-crystal system 122
6.2.2 Two-crystal system 123
6.3 D–D Nuclear Fusion and Neutron Generators 125
6.4 Electron and Ion Emitters 129
6.5 X-ray Generators 129
6.6 Applications 131
6.7 Conclusions 131
References 131

7 Pyroelectric Energy Harvesting 135
7.1 Introduction 135
7.2 Energy Transfer 136
7.2.1 Ferroelectric effect 137
7.2.2 Paraelectric effect 138
7.2.3 Phase transitions 138
7.2.4 Pyroelectric performance 139

7.3 Thermodynamic Cycles for Pyroelectric Energy Conversion 139
7.3.1 Heat and work fundamentals 140
7.3.2 Pyroelectric energy harvesting efficiency 143
7.3.3 Carnot cycle for polarization–electric field (PE) cycles 144
7.3.4 Ericsson cycle for the PE cycle 145
7.3.5 Lenoir cycle for the PE cycle 146
7.3.6 Pyroelectric energy conversion based on the Clingman cycle 147
7.3.7 Pyroelectric energy conversion based on the Olsen cycle 148
7.4 Pyroelectric Energy Conversion and Harvesting: Recent Progress 150
7.4.1 Pyroelectric energy harvesting based on the direct pyroelectric effect 150
7.4.2 Pyroelectric energy harvesting based on thermodynamic cycles 163
7.5 Conclusions 168
References 169

Appendix Major Pyroelectric Manufacturing Companies 175

Index 177

Foreword

Materials have played a revolutionary role in the development of the modern technological age, and their various applications have made our lives increasingly comfortable here on our home, the beautiful blue planet Earth. With the application of heat, pyroelectric materials produce electric current, qualifying them for use in uncooled infrared detectors. Infrared detectors are encountered in a vast number of applications in both war and peace. Many of their uses are routine to us in everyday life—for example, the pyroelectric intruder switch-cum-sensor is the key to most domestic burglar alarm systems.

With the advent of new technologies, thermal sensing and imaging have become useful diagnostic tools for medical, industrial, and military applications. In medicine, infrared thermal imaging is applied to detect vascular disorders and arthritic rheumatisms as well as to monitor muscular performances and make preclinical diagnoses of breast cancer. Recently, these materials have been used in nuclear particle generation, and their usefulness in energy harvesting is currently under exploration.

This monograph is the work of Drs. A. K. Batra and M. D. Aggarwal, two of the most prolific scholars and accomplished researchers in the field. Both have significantly contributed to the advancement of knowledge in pyroelectric materials. We are fortunate to have their expertise as part of the faculty of Alabama A&M University (AAMU), and we are grateful that they have been able to devote extra time and effort toward the preparation of this important contribution to pyroelectric literature. I have no doubt that this thought-provoking text will inspire further progress in the fascinating and challenging field of pyroelectrics.

Andrew Hugine Jr., Ph.D.
President
Alabama A&M University
Normal, Alabama
August 2013

Preface

This monograph contains comprehensive cutting-edge information on pyroelectric materials and their preparation, properties, and applications, such as uncooled wideband infrared detectors, particle generators, and ambient energy harvesters. The complete lifecycle of a pyroelectric material is presented here for readers—from the theory of operation, to structure, processing, and applications—providing a cohesive overview of essential concepts, including theoretical background and current developments in the field of pyroelectric devices. It describes the preparation, structure, properties, and figures of merit for practical pyroelectric materials such as triglycine sulfate, lead zirconate titanate, lithium tantalate, lithium niobate, barium strontium titanate, lead magnesium niobate-lead titanate, polyvinylidene fluoride, zinc oxide, and others, including the merits and demerits of their use in devices.

This monograph begins with a brief overview of pyroelectricity, including the nature of a unique class of smart materials and their classification on the basis of crystal classes, namely, ferroelectrics, piezoelectrics, and pyroelectrics. A list of important materials and their applications is also provided. Pyroelectric/ferroelectric phenomena are described in the context of their applications in infrared detectors and energy harvesting.

The book goes on to discuss the mechanisms, operation, and theory of pyroelectric-infrared detectors in detail. Both material figures of merit and material performance are evaluated with a focus on the operational mode of a detector. Design and fabrication techniques for obtaining the highest performance in an infrared detector are presented in detail.

Next, the growth and fabrication of key pyroelectric materials in various forms is covered, including bulk single crystals, polycrystalline ceramics, thin films, thick films, and composites. Based on applicability and requirements, crystal growth techniques are illustrated for nonsolution deposition such as sputtering, laser ablation, and chemical vapor deposition, as well as solution deposition such as sol-gel, metalorganic, spin-coating pyrolysis, and screen printing.

Structures and physical properties of important pyroelectrics are also explored including reviews of current detector performance parameters. The following materials are evaluated: triglycine sulfate, lithium niobate, lithium

tantalate, lead-magnesium niobate/lead titanate, lead zirconate titanate, lead magnesium niobate-lead titanate, strontium barium niobate, zinc oxide, gallium phosphide, organic polymers such as PVDF and P(VDF-TrFE), and composites and other non-lead-based materials. Unique and innovative techniques that have shown the ability to enhance pyroelectric performance are also explored.

The exclusive property of change in electrical polarization resulting from a temperature gradient that causes a charge to build on crystal surfaces gives rise to electrostatic potential and creates an electric field capable of accelerating charged particles to energies approximately hundreds of kilo-electron volts. This phenomenon has recently been applied to nuclear fusion, the generation of neutron, electron, and ion emitters, as well as the generation of x rays. Particle generators are presented diagrammatically with respective principles, theories, and applications.

The fundamentals and principles of energy harvesting via linear and nonlinear properties of pyroelectrics/ferroelectrics are also provided along with an overview of various materials and techniques that are currently being explored for their energy harvesting potential including mathematical modeling.

Additionally, the appendix provides a list of pyroelectric-detector manufacturing companies, imaging devices, and related products and services.

Thoroughly compiled, this monograph will be of benefit to graduate students, engineers, and scientists as a comprehensive guide to modern pyroelectric science and technology, focusing on the analysis and development of infrared detectors, nuclear particle generators, and energy harvesters for commercial, medical, industrial, military, and space applications. We hope that the scope of information will also guide and motivate engineering and science students to initiate new research for the development of innovative pyroelectric devices. For all technical contacts, suggestions, corrections, or exchanges of information, the reader is advised to contact the authors via email.

ashok.batra@aamu.edu
mohan.aggarwal@aamu.edu

Ashok K. Batra
Mohan D. Aggarwal
August 2013

Acknowledgments

Ashok K. Batra

First and foremost, this monograph would not be possible without the inspiration of my dear father who advised me to write this unique scientific resource. I express my gratitude to him and my late mother for instilling important life traits in me such as perseverance, hard work, and humility. I am forever indebted to my wife Nutan, my lifeline, for her constant prayers and her perseverance in staying by my side through thick and thin with total dedication and encouragement. I am eternally grateful to my close-knit family, including my mother in law, who has supported me throughout my career and in authoring this monograph. It is virtually impossible to fully express my gratitude to my admirable uncle and aunt, Dr. S. K. Grover and Manjula Grover, for their unwavering help in all aspects of my life.

I am grateful to Prof. R. B. Lal for sharing his extensive knowledge, valuable insight, and offerings of guidance. A special thanks to Dr. Amar Bhalla for our many stimulating discussions on pyroelectric materials and for his wide knowledge of materials science. I feel privileged to have worked with eminent teachers, including Prof. S. C. Mathur, the late Prof. A. Mansingh, Prof. K. L. Chopra, and Prof. N. K. Bansal. I have benefited from their scientific knowledge and philosophy of life. I would especially like to thank Dr. Chance Glenn, Sr., Dean of the College of Engineering, Technology, and Physical Sciences at AAMU, for his support and, in particular, our fruitful discussions on energy harvesting. I would like to express my appreciation to the university administration, and the faculty and staff of the Physics department for their general support and the friendly atmosphere that they create. Special thanks to Drs. Matthew Edwards, B. R. Reddy, M. Dokhanian, Kamala Bhat, Arjun Tan, and P. Kale for their encouragement. I would also like to give a special thanks to Mrs. Mary Strong for her excellent cooperation.

Additionally, I would like to acknowledge contributions from my research students, especially Dr. Padmaja Guggilla, Dr. James R. Currie, Dr. Jason M. Stephens, Dr. Ryan Moxon, Ashwith Chilvery, and Mychal Thomas. Thanks are also due to Quianna Johnson, Rahul Reddy, and Robert F. Sliz.

The author gratefully acknowledges support for this work through the National Science Foundation grant #EPSCoR R-II-3 (EPS-1158862), HBCU-UP-0928904-HRD grant, and DHS grant # 2010-ST-062-000034.

Mohan D. Aggarwal

I am grateful for the many insightful discussions shared with numerous graduate students, physics faculty, and various mentors during my career as a student of physics. I am thankful to Dr. Chance Glenn, Sr., Dean of the College of Engineering, Technology, and Physical Sciences and other administrators at AAMU for their encouragement during the process of writing this book. Thanks are also due to the various federal agencies that have supported this work, such as the National Science Foundation, National Aeronautics and Space Administration, Department of Defense, and U.S. Army Space and Missile Defense Command. Finally, I thank my wife for making the journey very pleasant by seldom complaining about my long hours of work away from home.

Joint Acknowledgments

We are grateful to Ms. Sheral Roberson, our senior research secretary and graphic designer, for her wholehearted help throughout the manuscript development process. She worked diligently and creatively, often spending late evenings designing and creating diagrams and critically reviewing the manuscript.

In the end, we acknowledge and appreciate well-known researchers and group leaders whose works have been cited and reproduced in the monograph, especially Drs. Scott R. Hunter, Y. Danon, D. Guyomar, R. B. Olsen, L. Pilon, A. Khodayari, and S. K. T. Ravindran.

We are also grateful to the reviewers and editors who gave positive comments and useful suggestions for improvement during the initial stages of the book's production.

Glossary of Symbols and Abbreviations

A	area
ADTGSP	alanine-doped deuterated triglycine sulfate-phosphate
AES	auguer electron spectroscopy
A_R	radiating area
ATGSP	alanine-doped triglycine sulfate-phosphate
ATGSP/As	alanine-doped triglycine sulfate-phosphate/arsenate
A_W	cross-sectional area
BITO	bismuth titanate
BNN	barium sodium niobate
BSN	barium strontium niobate
BST	barium strontium titanate
BTO	barium titanate
c	speed of light
c	elastic stiffness tensor
C	coulomb
CdTGS	cadmium-doped triglycine sulfate
CNT	carbon nanotube
CrLATGS	chromium L-alanine-doped triglycine sulfate
CsLATGS	cesium-L-alanine-doped triglycine sulfate
CuTGS	copper-doped triglycine sulfate
C_v	volume specific heat
CVD	chemical vapor deposition
d	piezoelectric coefficient magnitude
d	piezoelectric coefficient tensor
D	electric displacement magnitude
D	electric displacement or flux density vector
D^*	specific detectivity
D_2O	deuterium oxide
DC	direct current
DLATGS	l-alanine-doped deuterated triglycine sulfate
DRAM	dynamic random access memory

D_{sat}	displacement saturation level
dT	temperature change
DTA	differential thermal analysis
DTGFB	deuterated triglycine fluoberyllate
DTGPS	deuterated triglycine phosphate-sulfate
DTGS	deuterated triglycine sulfate
E	electric field magnitude
E	electric field vector
E_b	electric field breakdown
E_c	coercive field
ECR	electron cyclotron resonance
EO	electro-optical
f	frequency of detector operation
FCE	fully covered electrode
F_D	material figure of merit for high detectivity
FET	field effect transistor
F_I	material figure of merit for high detectivity
FRAM	ferroelectric random access memory
F_V	material figure of merit for high voltage responsivity
g	piezoelectric voltage coefficient tensor
G	thermal conductance
g-c	glass-ceramic
GMO	lead germanium oxide
G_R	thermal radiative radiation
G_W	thermal conductance of wire leads
h	Planck's constant
H	heat capacity
Hrms	rms value of fundamental component of irradiance
Hz	hertz
i_p	pyroelectric current
IR	infrared
ITO	indium tin oxide
JFET	junction-gate FET
k	Boltzmann constant
K	kelvin
KDA	potassium dihydrogen arsenate
KDP	potassium dihydrogen phosphate
KLN	potassium lithium niobate
KN	potassium niobate
KT	potassium titanate
KTN	potassium tantalate niobate
KTP	potassium titanyl phosphate
LATGS	l-alanine-doped triglycine sulfate

LiTGS	lithium-doped triglycine sulfate
LN	lithium niobate
LT	lithium tantalate
MCT	mercury cadmium telluride
MFS-FET	metal-ferroelectric-semiconductor–field effect transistor
MnTGS	manganese-doped triglycine sulfate
MOCVD	metalorganic chemical vapor deposition
MOD	metalorganic deposition
MOSFET	metal-oxide-semiconductor FET
mp	electric dipole moment vector
NDIR	nondispersive IR
NEP	noise equivalent power
NETD	noise-equivalent temperature difference
NiLATGS	nickel l-alanine-doped triglycine sulfate
NLO	nonlinear optical
p	pyroelectric coefficient magnitude
p	pyroelectric coefficient vector
P	polarization magnitude
P	polarization vector
PbO	lead oxide
PCE	partially covered electrode
p_e	enhanced pyroelectric coefficient
PE	polarization-electric field
PECVD	plasma-enhanced chemical vapor deposition
PEG	pyroelectric energy generator
PET	erbium-doped lead titanate
PLAD	pulsed laser ablation deposition
PLT	lead lanthanum titanate
PLZT	lead lanthanum zirconate titanate
PMN-PT	lead magnesium niobate-lead titanate
p_p	primary pyroelectric coefficient
P_r	remnant polarization
P_s	spontaneous polarization magnitude
$\mathbf{P}_s$	spontaneous polarization vector
PST	lead scandium titanate
PT	lead titanate
PTCR	positive temperature coefficient register
PVDF	polyvinylidene fluoride
P(VDF-TrFE)	poly vinylidene fluoride-trifluoroethylene
PZ	lead zirconate
PZT	lead zirconate titanate
q	charge
R	responsivity

RDP	rubidium dihydrogen phosphate
RF	radio frequency
R_G	gate resistance
rms	root mean square
ROIC	readout integrated circuit
RTA	rapid thermal annealing
R_v	voltage responsivity
S	entropy
SBN	strontium barium niobate
SbSI	antimony sulphoiodide
Si	silicon
SSHI	synchronized switch harvesting on inductor interface
T	temperature
TB	tungsten bronze
T_C	Curie temperature
TCD	temperature coefficient of dielectric constant
TGFB	triglycine fluoroberyllate
TGS	triglycine sulfate
TGSe	triglycine selenate
TiO_2	titanium oxide
u_S	multiplexed voltage output signal
V	voltage
VAMWCNTs	vertically aligned multiwall carbon nanotubes
V_n	rms noise value
V_s	detector rms output signal
W	radiant power incident
x	strain magnitude
$\mathbf{x}$	strain tensor
X	stress magnitude
$\mathbf{X}$	stress tensor
XRD	x-ray diffraction
YBCO	yttrium barium copper oxide
ZnTGS	zinc-doped triglycine sulfate
ZrO_2	zirconium oxide

α	thermal expansion magnitude
$\boldsymbol{\alpha}$	thermal expansion coefficient
Δf	noise bandwidth in hertz
ε	permittivity
ε'	real part of dielectric constant
ε''	imaginary part of dielectric constant
ε_0	permittivity of free space
ε_r	dielectric constant (or relative permittivity)

κ	thermal conductivity
λ	wavelength
η	quantum efficiency
Φs	radiation signal
χ	electric susceptibility
ω	angular frequency

Chapter 1
Fundamentals of Pyroelectric Materials

1.1 Introduction

A pyroelectric phenomenon is a manifestation of the temperature dependence of spontaneous polarization on certain solids, which can be either single-crystal or poly-crystalline aggregates. When the temperature of the material is slightly increased, the electrical polarization of the material changes, and voltage can be measured between certain faces of the pyroelectric sample. Conversely, if the temperature of the material is lowered by the same amount, the same magnitudes of polarization and voltage are found with the signs reversed. Thus, pyroelectric materials provide a means of producing infrared (IR) detectors that conveniently operate at room temperature. In this chapter, a number of fundamental aspects of pyroelectricity are described regarding its application in IR detection and energy harvesting. Pyroelectric materials form a subgroup of piezoelectrics, while ferroelectrics form a subgroup of pyroelectrics. Relationships between crystal structure and relevant properties are discussed along with important candidate materials and their applications.

1.2 Classification of Dielectric Materials

All dielectric materials undergo a change in dimension when subjected to an external force, such as a mechanical stress, an electric field, or a change in temperature. This is caused by the displacement of positive and negative charges within a material. When an external electric field is applied to the material, the cations are displaced in the direction of the electric field, and anions are displaced in the positive direction, resulting in net deformation of the material. The change in dimension can be very small or quite large, depending on the crystal class to which it belongs. Depending on the structure of the material, just a small change in dimension can result in a change in electric polarization (dipole moment per unit volume), giving rise to the ferroelectric, piezoelectric, or pyroelectric effect.

Based on symmetry elements of translational position and orientation, there are 230 space groups. Ignoring translational repetition, these groups are broken down into 32 classes (known as the 32 point groups) based on orientation only. Thus, all crystals can be categorized into 32 different classes—i.e., point groups divided by the symmetry elements: (1) center of symmetry, (2) axes of rotation, (3) mirror planes, and (4) several combinations of the elements.[1 3] The 32 point groups are subdivisions of 7 basic crystal systems (in order of ascending symmetry): triclinic, monoclinic, orthorhombic, tetragonal, rhombohedral (trigonal), hexagonal, and cubic. Of these 32 crystal classes, 11 are centrosymmetric and contain an inversion center. Polar properties do not exist for the centrosymmetric point groups because any polar vector can be inverted by an existing symmetry transformation. The remaining 21 noncentrosymmetric groups not containing an inversion center exhibit *piezoelectricity*, with the exception of point group 432. In piezoelectricity, materials produce an electric surface charge in response to applied mechanical stress. Piezoelectricity is the result of coupling mechanical and electric energies within a material. Among the 21 groups not containing an inversion center, 10 polar groups each have a unique polar (permanent electric dipole) axis. Within a given temperature range, the materials of these 10 polar groups are permanently polarized. Rather than the general piezoelectric polarization produced under stress, pyroelectric polarization is developed spontaneously and results in permanent dipoles within the structure. The term *pyroelectricity* is derived from the direct relationship between polarization and temperature. In short, the equilibrium of the electrostatic potential caused by the dipoles can be distorted by mechanical stress (piezoelectricity) or temperature change (pyroelectricity). Following Maxwell's equations, spontaneous polarization is related to surface charges: $\mathbf{P}_s = \sigma_s$. The surface charges are generally compensated by charged defects and/or environment charges. A temperature change affects spontaneous polarization—this is called the *pyroelectric effect*. The pyroelectric effect can be observed only in those materials whose point-group symmetry is consistent with the vector property of the polarization. Pyroelectric materials encompass crystalline materials (whose structures belong to 10 point groups: 1, m, 2, mm2, 3, 3m, 4, 4mm, 6, and 6mm) and ceramics (which are polymeric and composite materials whose structures belong to textural or basic Curie point groups: ∞, ∞m).

Using an external electric field, it is possible to reorient the spontaneous polarization between crystallographically equivalent configurations of certain pyroelectric materials. Analogous to ferromagnetic materials, this is referred to as ferroelectrics. Thus, a ferroelectric material is characterized by its ability to be re-polarized by an external field as well as its ability to be spontaneously polarized. Pyroelectrics can be classified into two main categories: (1) nonferroelectric pyroelectrics, whose polarization cannot be changed with the application of an external electric field and which include some semiconductors and biological materials; and (2) ferroelectric pyroelectrics, whose polarization

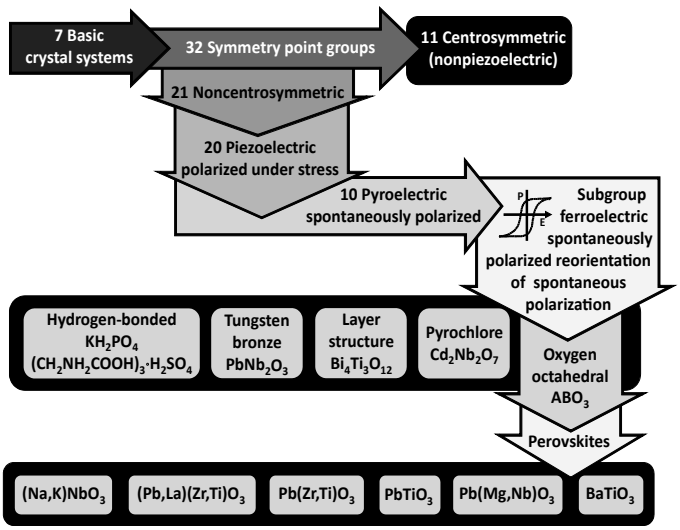

Figure 1.1 Classification of the crystallographic groups by their electrical properties, including a characteristic hysteresis loop.

can be changed with an electrical field and obtained from poling. The pyroelectric effect of ferroelectric pyroelectrics is present below Curie temperature T_C and is more temperature dependent than nonferroelectric pyroelectrics.

Figure 1.1 represents the classification of crystallographic groups by their electrical properties along with some important materials and illustrates a characteristic hysteresis loop that occurs during the reversal of the polarization in a ferroelectric. In ferroelectrics, there exists a Curie temperature T_C above which the ferroelectric material enters a nonpolar, nonferroelectric, or paraelectric crystal phase. Ferroelectric materials tend to behave as linear dielectrics under low electric fields and generally have high electric permittivities. The permittivity of ferroelectric materials depends on the frequency of the applied electric signal, the field, the elastic stress, and the temperature.

A ferroelectric material is therefore pyroelectric, piezoelectric, and noncentrosymmetric. In summation, ferroelectrics represent a subclass of pyroelectrics, which are, in turn, a subclass of piezoelectrics, which generally belong to the main class of dielectrics. Therefore, all ferroelectrics are pyroelectric, and all pyroelectrics are piezoelectric. However, the reverse relationship is not true. The diagram of dielectric classes illustrated in Fig. 1.2 indicates important related applications with shaded demarcation.

A list of key ferroelectric/pyroelectric materials currently being investigated and/or used in various devices is provided in Table 1.1.[3 14] Each of the material groups cited above exhibits certain special characteristics that makes it important for various applications as presented in Fig. 1.2. These materials belong to the *smart materials* class because they exhibit inherent transducer characteristics.

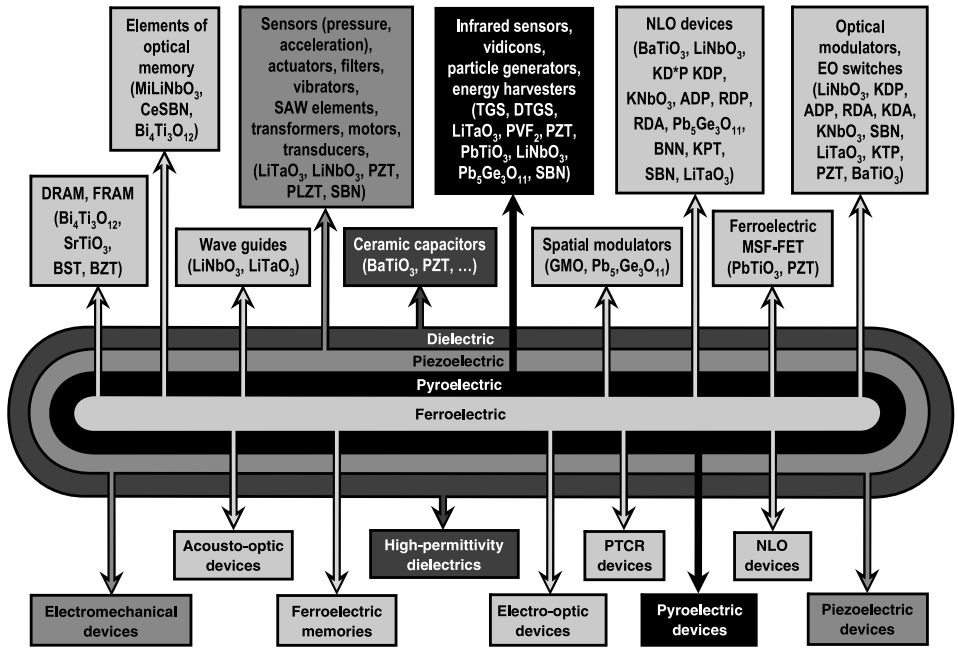

Figure 1.2 Diagram of important materials and selected applications illustrating ferroelectrics as a subclass of pyroelectrics and pyroelectrics as a subclass of piezoelectric materials.[6]

Table 1.1 Important pyroelectric and ferroelectric materials.[3–14]

Ferroelectric family	Ferroelectric material	Chemical formula	T_c (°C)/P_s (μC/cm^2) at T(°C)
Perovskite type	Barium (Ba) titanate	$BaTiO_3$ (BTO)	135 / 26.0(23)
	Potassium (K) niobate	$KNbO_3$ (KN)	435 / 30.0(250.0)
	K tatanate	$KTaO_3$ (KT)	< 271.4
	K tantalate niobate	$KTa_{1-x}Nb_xO_3$ (KTN)	
	Pb zirconate titanate	$PbZr_xTi_{1-x}O_3$ (PZT)	
	Pb scandium titanate	$PbSc_xTi_{1-x}O_3$ (PST)	
	Ba strontium (Sr) titanate	$Ba_xSr_{1-x}TiO_3$ (BST)	
Li Niobate family	Li niobate	$LiNbO_3$ (LN)	1210 / 71(23)
	Li tantalate	LiTaO3 (LT)	665 / 50
Tungsten bronze type	Ba Sr niobate	$Ba_{5x}Sr_{5(1-x)}Nb_{10}O_{30}$ (BSN)	75 / 32
	Ba sodium niobate	$Ba_{5x}Na_{5(1-x)}Nb_{10}O_{30}$ (BNN)	
	K Li niobate	$K_5Li_2Nb_5O_{15}$ (KLN)	430 / 25
KDP family	K dihydrogen phosphate	KH_2PO_4 (KDP)	150 / 4.75 (177)
	K dihydrogen arsenate	KH_2AsO_4 (KDA)	176 / 5.0 (196)
	Rubidium dihydrogen phosphate	RbH_2PO_4 (RDP)	163 /

(*continued on next page*)

Table 1.1 (*continued*)

Ferroelectric family	Ferroelectric material	Chemical formula	T_c (°C)/P_s ($\mu C/cm^2$) at T(°C)
TGS type	Triglycine sulfate	$(NH_2CH_2COOH)_3$ H_2SO_4 (TGS)	49 / 2.8 (30)
	Triglycine selenate	$(NH_2CH_2COOH)_3$ H_2SeO_4 (TGSe)	22 / 3.2 (10)
KTP Family	K titanyl phosphate	$KTiOPO_4$ (KTP)	
Bismuth titanate	Bismuth titanate	$Bi_4Ti_3O_{12}$ (BITO)	673 / > 30
Rare earth molybdate	Gadolinium molybdate	β $Gd_2(MoO)_3$ (GMO)	163 / 0.185 (25)
Pb germanium oxide	Pb germanium oxide	5PbO $3GeO_2$ or $Pb_5Ge_3O_{11}$ (LGO)	
Antimony sulphoiodide	Antimony sulphoiodide	SbSI (SbSI)	20 / 25 (0)
Polymer	Poly (vinylidene fluoride)	(PVDF)	
	Poly (vinylidene fluoride trifluoroethylene)	P(VDF TrFE)	

1.3 Important Dielectric Parameters

1.3.1 Electric dipole moment

When the centers of positive and negative charges are separated by a certain distance in a molecule or atom, the molecule or atom possesses an electric dipole moment given by

$$\mathbf{mp} = qd, \tag{1.1}$$

where q is the charge, d is the separation between the positive and negative charge centers, and **mp** is the vector. The vector direction goes from negative to positive charge, and its unit is coulomb meter (Cm).

1.3.2 Polar and nonpolar dielectric materials

Generally, in nonpolar dielectric materials, the atoms do not possess an electric dipole moment because the centers of positive and negative charges coincide. Upon application of an external electric field, the centers of the positive and negative charges separate, and dipole moments are induced. The induced dipole moments disappear once the electric field is removed.

In polar dielectric materials, each molecule or atom possesses a dipole moment because the centers of the positive and negative charges do not coincide. On application of an external electric field to these materials, the electric dipoles tend to orient themselves in the direction of the field.

1.3.3 Electric polarization

A polar material consists of a large number of atoms or molecules, each possessing an electric dipole moment. The total (or net) dipole moment of the material is a vector sum of all of the individual dipole moments, given by

$$\sum_i \mathbf{mp}. \tag{1.2}$$

The electric polarization **P** is defined as the total dipole moment per unit volume and is given by

$$\mathbf{P} = \frac{\sum_i \mathbf{mp}}{V}, \tag{1.3}$$

where V is the volume of the material. The unit of the polarization **P** is C/m^2 and is sometimes called the surface-charge density. **P** is a vector normal to the surface of the dielectric material.

1.3.4 Electric displacement or flux density D, dielectric constant ε, and electric susceptibility χ

When an electric field **E** is applied to a dielectric material, it develops a finite polarization **P** (induced polarization in nonpolar materials and orientation polarization in polar materials). There are three primary contributions to electric polarization: electronic, ionic, and dipole reorientation-related. The electric displacement or flux density **D** developed inside the material due to the electric external field **E** is given by

$$\mathbf{D} = \varepsilon_0 \mathbf{E} + \mathbf{P}, \tag{1.4}$$

where ε_0 is the permittivity of free space. **D** is also expressed by the relation

$$\mathbf{D} = \varepsilon \mathbf{E} = \varepsilon_0 \varepsilon_r \mathbf{E}, \tag{1.5}$$

where ε_r is the relative permittivity or dielectric constant of the dielectric material. The unit of **D** is C/m^2. The dielectric constant ε_r is also defined by the relation

$$\varepsilon_r = \frac{\mathbf{D}}{\varepsilon_0 \mathbf{E}}, \tag{1.6}$$

where ε_r is a unitless quantity and is always greater than one.

The polarization **P** is directly related to the applied electric field by the relation

$$\mathbf{P} = \varepsilon_0 \chi \mathbf{E}, \tag{1.7}$$

where χ is the electric susceptibility of the materials.

From the above equations, one can obtain the relation between the dielectric constant ε_r and electric susceptibility χ as

$$\varepsilon_r = 1 + \chi. \tag{1.8}$$

1.3.5 Spontaneous polarization

Spontaneous polarization $\mathbf{P}_s$ is the polarization that exists inherently in the material without the application of an external electric field. Pyroelectric and ferroelectric materials exhibit spontaneous polarization. In pyroelectric

materials, external charges mask spontaneous polarization, making it unobservable. In ferroelectric materials, the direction of spontaneous polarization can be changed by applying an external electric field. These concepts are explained in detail in Section 1.7.

1.4 Electrostrictive Effect

All dielectric materials exhibit an electrostrictive effect, in which the application of an external electric field polarizes the material. The process of polarization involves the orientation of the dipoles and results in the deformation of the materials. The strain **x** is related to the polarization **P** by the relation

$$\mathbf{x} = \mathbf{Q}\mathbf{P}^2, \tag{1.9}$$

where **Q** is the electrostrictive coefficient. Using Eq. (1.4), and considering materials with high dielectric constant $\mathbf{P} >> \varepsilon_0 \mathbf{E}$, one can write

$$\mathbf{x} = \mathbf{Q}\mathbf{D}^2 = \mathbf{Q}\varepsilon^2\mathbf{E}^2. \tag{1.10}$$

The tensor form of Eq. (1.10) can be written as

$$x_{ij} = Q_{ijkl}D_{km}D_{ml}. \tag{1.11}$$

It should be noted from Eq. (1.10) that the strain is proportional to the square of the electric field and is therefore independent of the electric field polarity. Electrostriction is a quadratic effect.

1.5 Piezoelectric Phenomena

Dielectric polar materials that belong to the class of noncentrosymmetric crystals are classified as piezoelectric materials. When these materials are subjected to an external electric field, asymmetric displacements of anions and cations cause considerable net deformation of the crystal. The resulting strain is directly proportional to the applied electric field. The strain in a piezoelectric material is expansive or compressive depending on the polarity of the applied field. The effect is called the *piezoelectric effect*, or more precisely, *direct piezoelectric effect*. Piezoelectric materials also develop positive and negative charges on opposite faces when subjected to external mechanical strain by applied pressure or stress. This results in an electric field/voltage across the crystal. This effect is called the *indirect piezoelectric effect.*

The phenomenological approach to piezoelectric effects is explained in Fig. 1.3. The thermodynamically reversible interactions occur among the electrical, mechanical, and thermal properties of a smart material. The lines that join pairs of circles indicate that a small change in one of the variables causes a corresponding change in the others. The lines that join the circles at

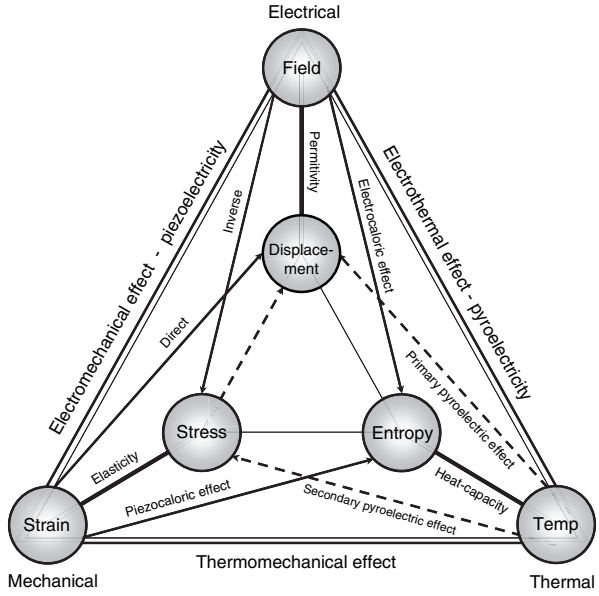

Figure 1.3 Thermodynamic interactions among thermal (temperature), mechanical (strain), and electrical (field) properties of a smart material (in piezoelectrics, pyroelectrics, and ferroelectrics).

different corners of the triangle define the coupling effects. The three direct relations are:

1. The relationship between electric field **E** and displacement **D** defines the permittivity ε as
$$\mathbf{D} = \varepsilon\mathbf{E}. \tag{1.12}$$
2. The relationship between mechanical stress **X** and strain **x** defines the elastic compliance, or elastic constant, **y** as
$$\mathbf{x} = \mathbf{y}\mathbf{X}. \tag{1.13}$$
3. The relationship between temperature T and entropy S defines the heat capacity Q as
$$S = QT^{\ 1}. \tag{1.14}$$

For piezoelectric materials, additional terms are required—a mechanical stress causes not only strain, but also electric polarization, even at constant temperature. Thus, the displacement induced by the stress can be expressed as

$$\mathbf{D} = \mathbf{d}\mathbf{X}, \tag{1.15}$$

where **d** is one of the piezoelectric coefficients with unit C/N.

In the converse piezoelectric effect, one can also express the relationship between electric field and the strain **x** as

$$\mathbf{x} = \mathbf{d}\mathbf{E}. \tag{1.16}$$

In this case, the unit for the piezoelectric coefficient will be m/V. In fact, for the both direct and indirect piezoelectric effects, **d** is identical, so

$$\mathbf{d} = \mathbf{D} \cdot \mathbf{X}^{-1} = \mathbf{x} \cdot \mathbf{E}^{-1}. \tag{1.17}$$

In terms of the electric field produced by a mechanical stress, the relationship becomes

$$\mathbf{E} = \mathbf{gX}. \tag{1.18}$$

In this case, **g** is another piezoelectric voltage coefficient with unit (V/m/N/m^2). It can be expressed as

$$\mathbf{g} = \frac{\mathbf{d}}{\varepsilon} = \frac{\mathbf{d}}{\varepsilon_r \varepsilon_0}. \tag{1.19}$$

In general, piezoelectric properties depend on direction, so they are described in terms of tensors.

1.6 Pyroelectric Phenomenon

The pyroelectric effect (or pyroelectricity) refers to a change in the internal polarization of a material due to small variations in temperature that produce a flow of charges to and from the material's surface. Pyroelectric materials are dielectric materials; they possess a spontaneous electrical polarization that appears in the absence of an applied electrical field or stress. Of 20 noncentrosymmetric crystal classes, 10 contain their own unique polar axis under unstrained conditions. This implies that such crystals are already spontaneously polarized within a particular temperature range. Thus, they exhibit both piezoelectric and pyroelectric effects. Pyroelectricity is a coupled effect where a change in temperature causes a change in electric displacement **D** (C/m^2), as shown in Fig. 1.3. There are two contributions to the pyroelectric effect, represented in Fig. 1.3 by dashed lines. In the first contribution, the primary pyroelectric effect is caused by a change in temperature, which leads to a change in the electric displacement in a crystal under constant strain x, rigidly clamped to prevent expansion or contraction. The primary pyroelectric effect signifies direct coupling between polarization and temperature. In the second contribution, the secondary pyroelectric effect is a result of crystal deformation. This deformation is due to thermal expansion from temperature change that causes strain in the piezoelectric process, which then alters the electric displacement. In short, temperature variation leads to thermal expansion, which leads to electric displacement. It follows that two contributions to spontaneous polarization change caused by temperature variations are thermal expansion and electric displacement. In general experiments, the pyroelectric effect under the constraint of constant stress is the combined effect of both the primary pyroelectric effect and the secondary

pyroelectric effect. Pyroelectric material can be illustrated as a thermal transducer because it converts thermal energy to electrical energy.

Since pyroelectricity is the electrical response of a polar material undergoing temperature change, the pyroelectric effect at constant stress **X** and electric field **E** is stated as[7,8]

$$\left(\frac{\partial \mathbf{D}}{\partial T}\right)_{E,X} = \left(\frac{\partial \mathbf{D}}{\partial T}\right)_{E,x} + \left(\frac{\partial \mathbf{D}}{\partial \mathbf{x}}\right)_{E,T}\left(\frac{\partial \mathbf{x}}{\partial T}\right)_{E,X}, \tag{1.20}$$

where **D**, **x**, and T are the electric displacement, strain, and temperature of the pyroelectric material, respectively. The first term on the right side of the equation is called the primary pyroelectric response or effect. This effect is caused by a charge produced by a change in the polarization due to temperature change when the dimensions of pyroelectric materials are kept constant. If dimensions change with temperature in materials under constant stress, an additional charge is produced due to the secondary pyroelectric effect—the piezoelectric contribution from thermal expansion. The second term, on the right side of Eq. (1.20), represents the secondary pyroelectric effect. For ferroelectrics, the electric displacement is related as

$$\mathbf{D} = \mathbf{P} + \mathbf{dX}, \tag{1.21}$$

where **d** is the piezoelectric coefficient of the ferroelectric materials, and **P** is the polarization, defined as

$$\mathbf{P} = \mathbf{P}_s + \varepsilon\mathbf{E}, \tag{1.22}$$

where **E** is the electric field, $\mathbf{P}_s$ is spontaneous polarization, and ε is permittivity. From Eqs. (1.20) and (1.21), one can derive

$$\mathbf{p} = \left(\frac{\partial \mathbf{D}}{\partial T}\right)_{E,X} = \left(\frac{\partial \mathbf{P}}{\partial T}\right)_{E,X} + \mathbf{E}\left(\frac{\partial \varepsilon}{\partial T}\right)_{E,X}, \tag{1.23}$$

where the first term in the right phrase of Eq. (1.23) is the primary pyroelectric coefficient below the Curie temperature of the material. Curie temperature is the temperature at which a material changes from a ferroelectric (polar) to paraelectric (nonpolar) phase. The second term in the right phrase of Eq. (1.23) is significantly closer to the Curie temperature T_C, where the change of dielectric permittivity due to temperature is a quite substantial. From Eq. (1.23), if $\mathbf{E} = 0$ (there is no applied electric field), or the permittivity of the material is not affected by temperature and the dimensions of the material do not change, then the primary pyroelectric coefficient is the result of a change in spontaneous polarization with temperature. Under these circumstances, we can write the primary pyroelectric coefficient as

$$\mathbf{p}_p = \left(\frac{\partial \mathbf{P}_s}{\partial T}\right)_{E,X}, \tag{1.24}$$

where $\mathbf{p}_p$ designates the pyroelectric coefficient as primary. The secondary pyroelectric coefficient $\mathbf{p}_s$ is described as

$$\mathbf{p}_s = \left(\frac{\partial \mathbf{D}}{\partial \mathbf{x}}\right)_{E,T}\left(\frac{\partial \mathbf{x}}{\partial T}\right)_{E,X} = \left(\frac{\partial \mathbf{D}}{\partial \mathbf{X}}\right)_{E,X}\left(\frac{\partial \mathbf{X}}{\partial \mathbf{x}}\right)_{E,T}\left(\frac{\partial \mathbf{x}}{\partial T}\right)_{E,X} = \mathbf{dc}\boldsymbol{\alpha}, \qquad (1.25)$$

where $\mathbf{c}$ is elastic stiffness, $\mathbf{d}$ is the piezoelectric coefficient, and $\boldsymbol{\alpha}$ is the thermal-expansion coefficient of the material. Thermal deformation and piezoelectricity contribute to $\mathbf{p}_s$. A third contributing factor to $\mathbf{p}$ is the tertiary pyroelectric effect, which derives from inhomogeneous temperature distribution within the sample.[12] The primary pyroelectric effect in ferroelectrics is generally large and negative because the spontaneous polarization decreases or diminishes with increased temperature. Ferroelectrics' secondary pyroelectric effect is considerably smaller and may be positive or negative depending on the values of the constants $\mathbf{c}$, $\mathbf{d}$, and $\boldsymbol{\alpha}$. This explains why in ferroelectrics, experimental observation shows that the larger negative primary pyroelectric effect dominates the pyroelectric coefficients, causing them to be negative. In nonferroelectric pyroelectrics, where this condition is not the standard, there is no simple way to predict the magnitude of the coefficients or whether their sign will be positive or negative. In practice, the total pyroelectric coefficient can be measured and secondary effects are calculated from constants $\mathbf{c}$, $\mathbf{d}$, and $\boldsymbol{\alpha}$, depending on the symmetry of the materials.

It is worth mentioning that the pyroelectric coefficient is in general a vector, but for practical reasons is treated as a scalar. Furthermore, electric displacement **D,** electric field **E**, and polarization **P** vectors are assumed to be collinear and normal to the sample surface, as is the case in all practical applications described in this book. Thus, only their magnitudes are used (shown in italics) in later chapters.

Lee et al. have presented values of primary, secondary, and observed pyroelectric-effect coefficients in various materials, as listed in Table 1.2.[12] It is evident from Table 1.2 that both the primary and secondary effects are important, and, in ferroelectrics, all of the observed coefficients are negative and dominated by the primary effect. In contrast, in pyroelectrics, this dominance may not be the case because the secondary pyroelectric effect could be substantial.

1.6.1 Pyroelectric current generation

This section briefly discusses the physics of current generation utilized in IR detectors. The generation of charges or current during heating and cooling in a pyroelectric sample is illustrated schematically in Fig. 1.4 and explained by the following four conditions:

1. Figure 1.4(a): Spontaneous polarization of the pyroelectric sample without electrodes attracts free charges (represented as positive and negative circles) to the material's surface, thereby masking the charges.

Table 1.2 Primary, secondary, and observed pyroelectric coefficients of various materials at room temperature.[12]

Materials	Point group symmetry	Observed total effect $\mu C/(m^2K)$	Calculated secondary effect $\mu C/(m^2K)$	Primary effect $\mu C/(m^2K)$
Ferroelectrics: Ceramics				
$Pb(Zr_{0.52}\ Ti_{0.05})O_3$:1 wt% Nb_2O_5 (PZT)	∞m	−50.0	+60.0	−110.0
$BaTiO_3$	∞m	−190.0	+80.0	−270.0
$Pb(Zr_{0.92}\ Ti_{0.05})O_3$:1 wt% Nb_2O_5 (PZT)	∞m	−268.0	+37.7	−305.7
Ferroelectrics: Single Crystal				
$Sr_{0.5}Ba_{0.5}Nb_2O_6$(SBN)	4mm	−550.0	−21.0	−529.0
$(NH_2CH_2COOH)_3{\cdot}H_2SO_4$ (TGS)*	2	−270.0	+60.0	−330.0
$LiTaO_3$	3m	−176.0	+2.0	−178.0
$LiNbO_3$	3m	−83.0	+12.9	−95.9
$Pb_5Ge_3O_{11}$	$\bar{3}$	−95.0	+15.5	−110.5
$Ba_2NaNb_5O_{15}$**	2mm	−100.0	+41.8	−141.8
$NaNO_2$	2mm	−140.0	−5.0	−135.0
Nonferroelectrics				
$Li_2SO_4(H_2O)$	2	+86.3	+26.1	+60.2
Tourmaline	3m	+4.0	+3.2	+0.8
Bone	∞	$+25\times10^{-4}$	$+117\times10^{-4}$	-92×10^{-4}
$Ba_2Si_2TiO_8$ (Fresnoite)	4mm	+10.0	+22.0, +16.0	−12.0, −6.0
Li_2GeO_3	2mm	−27.0	−12.8	−14.2
$Ba(NO_2)_2(H_2O)$		−25.3	−3.3	−22.0
Semiconductors (Wurtzite structure)				
CdS	6mm	−4.0	−1.0	−3.0
CdSe	6mm	−3.5	−0.56	−2.94
ZnO	6mm	−9.4	−2.5	−6.9
ZnS***	6mm	0.43	+0.34	—
BeO	6mm	−3.40	−0.008	−339

*Average value of the wide range of reported values between 200 to 350 $\mu C/(m^2K)$

**Maximum value of p measured on the sample

***No reported sign for p^X; no information about the polytypic nature of the sample

2. Figure 1.4(b): Spontaneous polarization of the pyroelectric sample with electrodes (shown connected to an ammeter that is measuring current) at a constant temperature is constant, and no current flows through the external circuit.
3. Figure 1.4(c): If the pyroelectric sample with electrodes is heated, the spontaneous polarization is reduced (shown by $\mathbf{P}_s$ arrow length) through a reduction in dipole movement toward polar alignment, reducing the charge-storage capacity of the material. Any decrease in the quantity of bound charges at the electrodes results in redistribution of the charges,

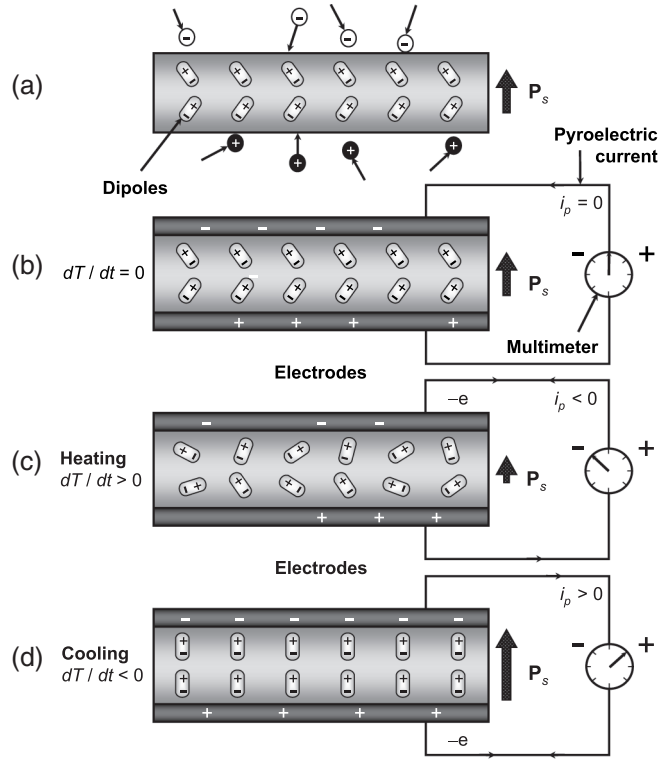

Figure 1.4 Pyroelectric sample with dipoles and polarization vector: (a) without electrodes, (b) with electrodes and connected to an ammeter at constant temperature, (c) while being heated, and (d) while cooling.

thus leading to ejection of bound charges, creating current flow through the external circuit. The ejected bound charges can be stored in a storage device for appropriate applications. The process of collecting charges is performed using the direct pyroelectric effect in energy harvesting.

4. Fig. 1.4(d): Spontaneous polarization is increased if the sample with the electrodes is cooled, attracting ambient charges to the surface of the electrodes, which leads to a current with its sign reversed.

The pyroelectric current i_p, generated upon heating or cooling, is expressed as

$$i_p = Ap\frac{dT}{dt}, \tag{1.26}$$

where i_p is the pyroelectric current, A is the electrode surface area, p is the pyroelectric coefficient, and dT/dt is the rate of temperature change.[8] The current direction depends on the slope of temperature change with respect to time, which depends on the heating and cooling period of the pyroelectric element.

1.7 Ferroelectric Phenomena[1]

Ferroelectric materials are a subclass of pyroelectric materials, which are a subclass of piezoelectric materials. Thus, ferroelectric materials exhibit both piezoelectric and pyroelectric properties. Ferroelectricity is the ability of a material to have a spontaneous polarization $\mathbf{P}_s$ that can be reversed by the application of an electric field. The relationship between an applied electric field and its corresponding polarization or electric displacement is nonlinear and displays hysteresis in certain temperature regions, delimited by a transition point called the Curie temperature T_C. At temperatures above T_C, the crystal is no longer ferroelectric and exhibits normal dielectric behavior. Ferroelectric materials generally exist in a nonpolar phase at temperatures above T_C and have anomalously high dielectric constants, especially near the Curie temperature. At this temperature, the material is said to undergo a transition from ferroelectric phase to paraelectric phase. At $T > T_C$, anomalous behavior closely follows the Curie–Weiss relation:

$$\varepsilon_r = \frac{C}{T \quad T_C}, \tag{1.27}$$

where C is known as the Curie constant. In fact, the anomalous behavior always appears near transition points between two different phases, even at T below T_C. It is worth mentioning that at transition points, there are anomalies because of the change in crystal structure not only in the dielectric constant and polarization, but also in piezoelectric coefficients, elastic constants, and specific heat.

1.7.1 Ferroelectric domains

A ferroelectric domain is defined as a microscopic region in the material within which all of the electric dipoles are oriented in the same direction due to a strong short-range interaction caused by internal electric fields. The size and arrangement of these domains is the result of two competing energies: the domain wall energy and the depolarization energy. Normally, the domains are randomly oriented, so the net polarization is zero in the absence of an external electric field. When an external electric field is applied, the domains tend to become oriented in the direction of the applied field.

1.7.2 Ferroelectric hysteresis

A schematic of a typical hysteresis loop is shown in Fig. 1.5. Note that the lower half of the hysteresis loop occurs when the electric field E increases, and the upper half occurs when E decreases. The electric displacement at zero applied electric field is called the spontaneous polarization $\mathbf{P}_s$. The electric field required to achieve zero polarization is called the coercive field E_c.

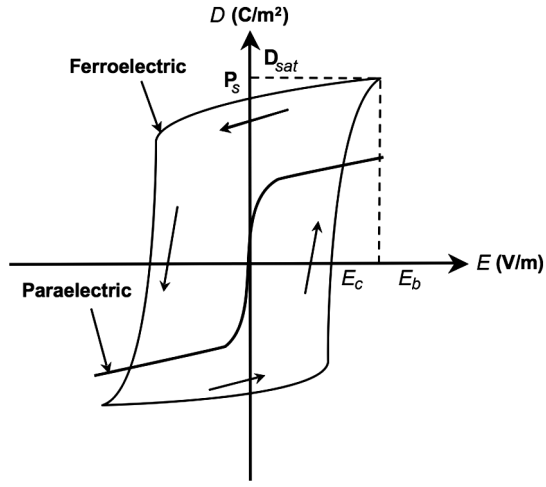

Figure 1.5 Typical electric displacement D versus electric-field E cycle for ferroelectric and paraelectric materials.

Electric displacement also has a saturation level, described as $\mathbf{D}_{sat}$. The strongest electric field that a material can possibly withstand before breakdown is called the electric field breakdown E_b. At applied E_b, a material loses its insulating ability and begins to conduct. When an electric field is applied to a ferroelectric material in an isothermal cycle, Joule heating dissipates the electrical input provided to the system. The energy dissipated per unit volume of the ferroelectric material $\forall$ equals the area enclosed by the D-E diagram of the hysteresis loop:

$$\frac{W}{\forall} = \oint dDE. \tag{1.28}$$

The D_s-E cycle can be used in energy harvesting.

1.7.3 Poling

Poling is the process of using an external electric field to bias the alignment of the polar axes in multidomain materials. As the electric field is increased, more and more domains are oriented, and, at a sufficiently high electric field, almost all of the domains are oriented in the same direction, giving rise to maximum polarization. To pole the material, it is heated to a temperature slightly less than the transition temperature and held there. Then, a sufficiently high electric field is applied for ~2–3 h. The material is then cooled to room temperature with the electric field on. The domains remain frozen. Once room temperature is reached, the electric field is turned off. The material remains in the maximum polarization state.

1.7.4 Paraelectric effect

Paraelectricity describes the ability of a material with no spontaneous polarization to become polarized under an applied electric field. Paraelectric behavior occurs due to: (1) the distortion of individual ions and (2) the polarization of molecules. The domains, or areas of uniform polarization in paraelectric materials, as compared to those of ferroelectric materials, are unordered and have a weak internal electric field. Figure 1.5 demonstrates the relationship between the electric displacement D and electric field E of an ideal paraelectric material. Pyroelectrics having no spontaneous polarization can be observed in Fig. 1.5; however, electric displacement is generated when an electric field is applied. In reality, a paraelectric material often exhibits a small spontaneous polarization and a hysteresis loop. Finally, note that the paraelectric D-E curve is nonlinear because electric permittivity ε is also a function of the electric field **E**.

1.8 Conclusions

Crystals are commonly classified into 7 systems according to their geometric structure. Smart materials belonging to the 20 noncentrosymmetric classes have very interesting and important properties because they exhibit piezoelectricity, pyroelectricity, and ferroelectricity. Based on the requirements of the application, one or more of these properties are exploited. In later chapters, the polarization variation in these materials via temperature and electric field is applied in IR detection, particle generation, and energy harvesters.

References

1. G. Gautschi, *Piezoelectric Sensorics*, Springer Verlag, Berlin Heidelberg (2002).
2. J. Nye, *Physical Properties of Crystals*, Oxford University Press, London, UK, pp. 1–45 (1957).
3. R. B. Lal and A. K. Batra, "Growth and properties of triglycine (TGS) sulfate crystals review," *Ferroelectrics* **142**, 51–82 (1993).
4. S. B. Lang and D. K. Das-Gupta, "Pyroelectricity: fundamentals and applications," *Ferroelectrics Review* **2**(4), 217–354 (2000).
5. A. Rogalski, *IR Detectors*, Gordon and Breach Science Publishers, The Netherlands, pp. 121–147 (2000).
6. R. W. Whatmore and R. Watton, "Pyroelectric materials and devices," in *IR Detectors and Emitters: Materials and Devices*, P. Capper and C. T. Elliott, Eds., Kluwer Academic Publishers, pp. 99–147 (2001).

7. S. B. Lang and A. S. Bhalla, "Special issue on pyroelectricity," *Ferroelectrics* **118**(104), 1–111 (1991).
8. A. J. Moulson and J. M. Herbert, *Electroceramics*, Wiley, Chichester, UK, pp. 411–432 (2003).
9. S. B. Lang and D. K. Das-Gupta, "Pyroelectricity: fundamentals and applications," in *Handbook of Advanced Electronic and Photonic Materials and Devices*, H. S. Nalwa, Ed., Academic Press, New York, pp. 1–55 (2001).
10. Y. Xu, *Ferroelectric Materials and Applications*, North-Holland, Amsterdam (1991).
11. M. E. Lines and A. M. Glass, *Principles and Applications of Ferroelectrics and Related Materials*, Clarendon, Oxford, United Kingdom, pp. 620–632 (1997).
12. M. H. Lee, R. Guo, and A. S. Bhalla, "Pyroelectric sensors," *J. Electroceramics* **2**, 229–242 (1998).
13. J. R. Curie, "Studies on the Functional Ferroelectric Materials for IR Sensors," M.S. Thesis, Alabama A & M University, Normal, Alabama (2004).
14. S. Bauer and B. Ploss, "Interference effects of thermal waves and their applications to bolometers and pyroelectric detectors," *Sensor and Actuator* **25/27**, 417–421 (1991).

Chapter 2
Pyroelectric IR Detectors

2.1 Introduction

Today, IR detectors are widely used for commercial and military applications. The IR region of electromagnetic radiation spans photon wavelengths of 0.7 μm to ~1 mm. The IR region is generally divided into three subregions: near IR (NIR) with a range of 700–1400 nm, mid-wavelength IR (MWIR) with a range of 1400 nm–3 μm, and long-wavelength IR (LWIR) with a range of 3 μm–1 mm. The origins of IR photons are the gases, liquids, and solids that make up the universe. These IR sources can both absorb and emit IR radiation. The dependent relationship of radiation absorption and emission spectra on wavelength helps us identify and evaluate materials in our universe. IR detectors make this valuable information observable to humans through their diverse application in a variety of optical characterization instruments for planetary exploration, space, astrophysics, and atmosphere radiation measurement. IR detection and thermal imaging are currently topics of great interest for both military and commercial applications ranging from night vision, surveillance, driving aids, fire fighting, and various medical applications.

2.2 IR Fundamentals

All objects emit radiation at a rate and wavelength distribution dependent on the temperature T of the object and its spectral emissivity ε. In 1900, Max Planck developed the law of blackbody radiation that predicted the spectral existence of electromagnetic radiation at all wavelengths from a blackbody at a temperature T, given by

$$M_e(\lambda, T) = \frac{2\pi hc^2}{\lambda^5\left(e^{\frac{hc}{\lambda kT}} \quad 1\right)}\left(\frac{\mathrm{W}}{\mathrm{cm}^2\mu\mathrm{m}}\right), \tag{2.1}$$

where $M_e(\lambda, T)$ is the spectral radiant exitance, h is Planck's constant (J · s), c is the speed of light (m/s), λ is wavelength (μm), k is the Boltzmann constant

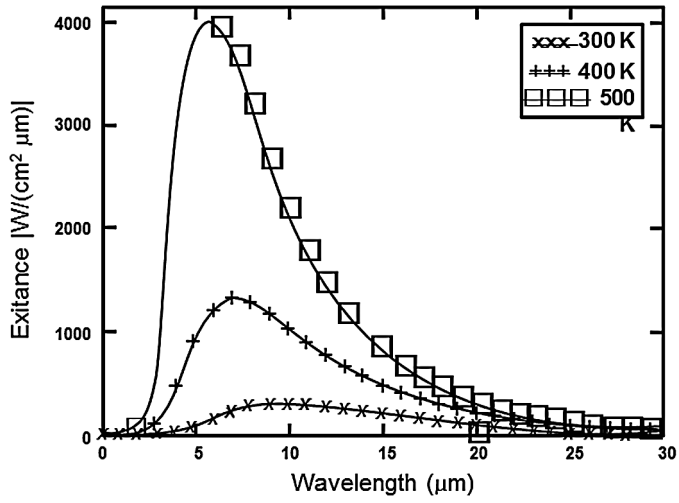

Figure 2.1 Blackbody spectral radiant exitance based on Planck's law.

(J/K), and T is the temperature (K).[1] Figure 2.1 depicts the spectral exitance for temperatures at 300, 400, and 500 K.

The peak wavelength of the radiation for a specific temperature can be quantified using the equation defined by Wien's displacement law:

$$\lambda_{max} = \frac{2898\ \mu\text{mK}}{T}. \tag{2.2}$$

For most of applications, the relevant IR spectra are restricted by minimum and maximum temperatures. The lowest temperature can be represented by the temperature of the human body: approximately 310 K. The highest temperature can be arbitrarily represented by the temperature of jet engine exhaust: 700–1000 K. These temperatures correspond to a wavelength band of 2–15 μm. An additional limitation of terrestrial imaging in the IR region is caused by atmospheric energy absorption. Figure 2.2 illustrates

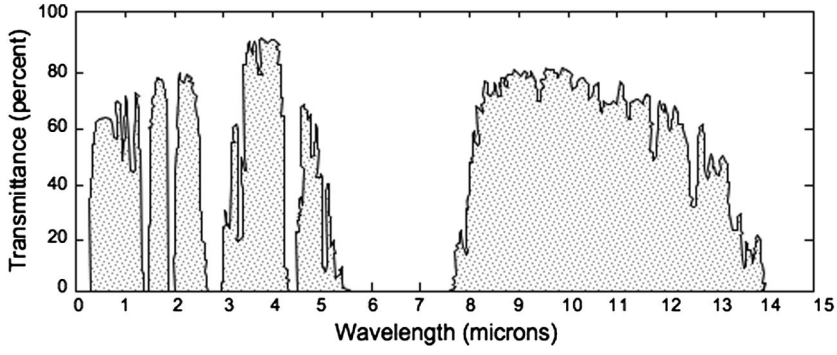

Figure 2.2 Absorption spectra of IR radiation in the atmosphere.

the transmission of IR energy as a function of wavelength for a 1-km path at sea level.[2]

IR transmission in the atmosphere is inevitably restricted to two MWIR bands at 3–5 μm and 8–13 μm. Within these windows, the effects of atmospheric attenuation are minimal, and targets in the IR are easily detected.

2.3 IR Detectors

IR radiation sensors can generally be classified into one of two classes: (1) photon detectors, in which the radiation absorption process directly produces a measurable effect through the generation of photoelectrons or charge-carrier pairs in a photoconductor; or (2) thermal detectors, which are also considered indirect optical detectors because they first convert the absorbed incident radiation into heat, thereby producing a measurable effect via pyro-voltage, thermo-voltage, or resistance. Pyroelectrics, bolometers, Golay cells, and thermopiles belong to the second class.[3]

Thermal detectors rely solely on the total amount of heat energy reaching the detector. Therefore, their response is independent of wavelength. Photon detectors (such as MCT) possess the highest responsiveness within an 8- to 14-μm range, but their spectral range is very narrow—i.e., they are spectrally selective. Figure 2.3 compares the output of photon detectors versus thermal detectors as a function of wavelength, showing not only that the output of thermal detectors is not affected by wavelength, but also that thermal detectors respond at longer wavelengths than photon detectors do.[4]

In addition, the cryogenic cooling often required to achieve optimum operation adds significantly to the cost and complexity of photon detectors. Thermal detectors, on the other hand, are of considerable interest because

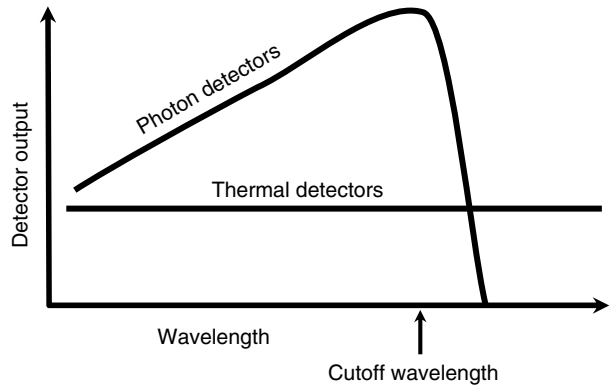

Figure 2.3 The relative output per unit; note the position of the long-wavelength cutoff for photon detectors and the input for photon and thermal detectors as a function of wavelength.

they can deliver relatively high performance at a low cost, while operating at room temperature. Pyroelectric IR detectors are categorized as thermal detectors.

Pyroelectric detectors have the fastest detection response of all of the thermal detectors because molecular-level temperature changes are directly responsible for the detection process. Pyroelectric IR sensing devices have five main advantages over photon IR sensors: (1) sensitivity in a very large spectral bandwidth, limited only by the ability of the sensor to absorb the incident radiation; (2) sensitivity in a very wide temperature range without the need for cooling; (3) low power requirements; (4) relatively fast response time; and (5) generally low-cost construction.[5]

2.4 Pyroelectric IR Detectors[6 14]

2.4.1 IR-detector operation

Pyroelectric detectors have two modes of operation: *pyroelectric* and *dielectric* (bolometer). The two modes for IR detection by ferroelectric materials are illustrated in Fig. 2.4, in which spontaneous polarization $\mathbf{P}_s$ falls to zero at the transition temperature (Curie temperature); relative permittivity rises to a peak during this transition.

The conventional pyroelectric mode for IR detection utilizes falling $\mathbf{P}_s$ with the increase of temperature. The radiation-induced change in the detector temperature results in a change of polarization that is equivalent to a flow of charges. However, the second mode, described as dielectric bolometer, utilizes the change of dielectric permittivity with temperature in the region of the ferroelectric phase transition. In this mode, the detector operates with an applied bias that charges the ferroelectric element. Heat from the absorption of incident radiation causes an increase in permittivity, resulting in a signal voltage.

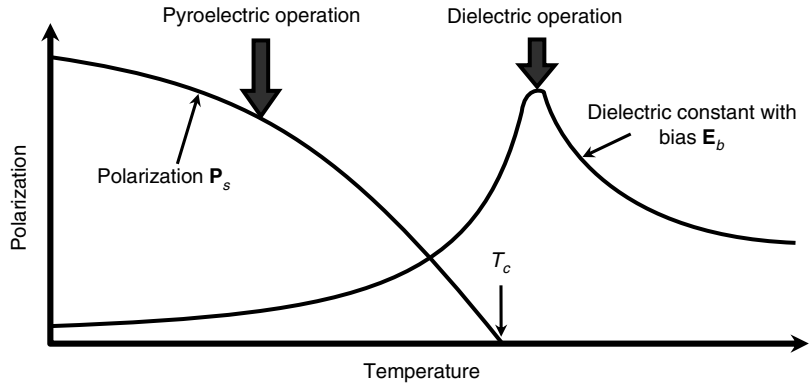

Figure 2.4 Operating modes for ferroelectric materials as IR detectors.

Pyroelectric detectors are thermal detectors that use temperature-dependent spontaneous polarization, or the pyroelectric effect, to detect incident radiation. Pyroelectric materials are dielectric materials that possess a spontaneous electrical polarization that occurs in the absence of an applied electrical field or stress. The pyroelectric coefficient p is due to the contribution of the dielectric permittivity and spontaneous polarization, as can be observed in the following:

$$p = \frac{dP}{\partial T} = \left(\frac{d\varepsilon}{dT}\right)\varepsilon_0 E + \left(\frac{dP_s}{dT}\right), \tag{2.3}$$

where dT is the rate of temperature change.

In the absence of a direct current (DC) bias, or when dielectric permittivity is temperature independent, the first term in Eq. (2.3) is zero, and the value of the pyroelectric coefficient depends only on the spontaneous polarization $\mathbf{P}_s$. Of the two modes of operation for a pyroelectric detector, the "true" pyroelectric mode can operate only in the pyroelectric or ferroelectric state of the material, while the dielectric mode becomes active through the application of a biasing field. Therefore, the dielectric mode can also be operated in the paraelectric phase of the material. In the pyroelectric mode, large spontaneous polarization changes caused by temperature change near the ferroelectric phase transitions lead to large pyroelectric coefficients. However, there are two advantages to working in the dielectric (bolometer) mode: (1) larger pyroelectric coefficients can be achieved using an electric field for operation, a fact that can be explained by the presence of remnant polarization or by a rounded hysteresis loop produced by defects and domains in the ferroelectric; and (2) losses are lower due to an applied electric field impeding the domain boundary motion. Therefore, both the applied electric field and temperature are utilized to achieve optimum detector response.

A pyroelectric detector is basically a capacitor whose spontaneous polarization vector is oriented normal to the plane of the electrodes. Incident radiation absorbed by the pyroelectric material is converted into heat, resulting in a temperature variation dT and, thus, changing the magnitude of the spontaneous polarization. Changes in polarization alter the surface charge of the electrodes. To maintain neutrality, charges are expelled from the surface, resulting in a *pyroelectric current* in the external circuit. The pyroelectric current is given by

$$i_p = Ap\frac{dT}{dt}, \tag{2.4}$$

where A is the electrode surface area, p is the pyroelectric element, and dT/dt is the pyroelectric coefficient and rate of temperature change.

The pyroelectric current depends on the temperature change with time. Therefore, a pyroelectric device that is coupled to any temperature changing effect is considered to be an alternating current (AC) capacitance device.

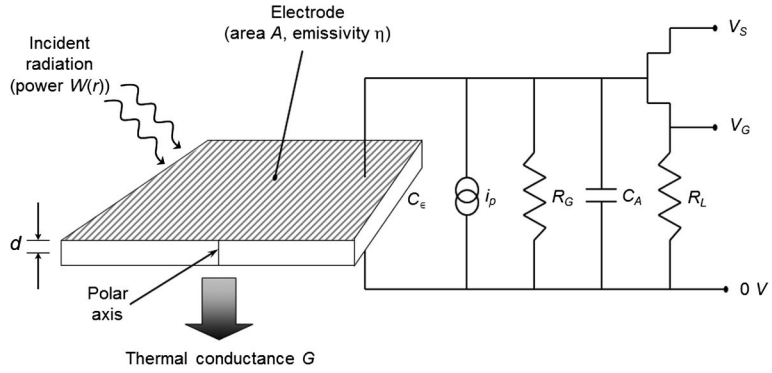

Figure 2.5 Schematic diagram of a pyroelectric detector.

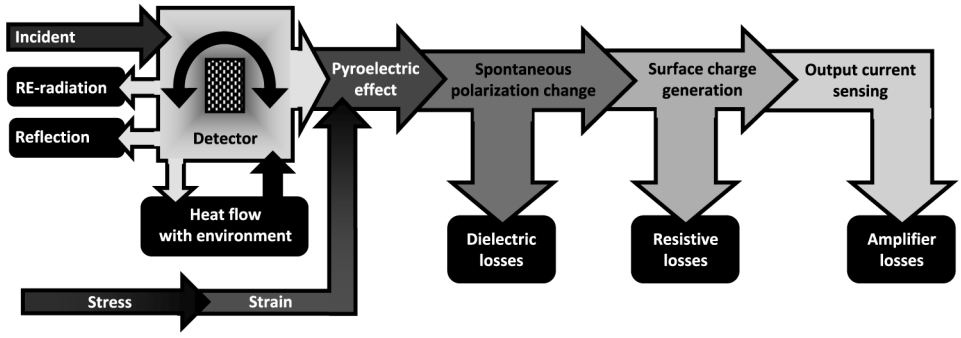

Figure 2.6 Flowchart of the conversion from thermal to electrical pyroelectric IR detector via optical, thermal, and electrical processes with losses.

Determining the electrical response of a pyroelectric detector requires analysis of both the thermal and electrical circuits. Measurement of the electrical response is usually made using the detector arrangement shown in Fig. 2.5.

In the simplest arrangement, the detector element is suspended in a vacuum by its wire leads. The wire leads carry charge to and from the electrodes and are also used to control the thermal conductance G between the element and its heat sink. The charge displaced from the electrodes is very small and thus requires an amplifier. The total spontaneous polarization of a ferroelectric capacitor is on the order of hundreds of nanocoulombs for a 1-mm^2 device. Figure 2.6 illustrates the individual stages of the transformation from IR radiation to an electrical signal with the associated losses.

2.4.2 Pyroelectric-detector responsivity

Three main components play an important role in the performance of a pyroelectric thermal detector: (1) the pyroelectric element, (2) the thermal link, and (3) the heat sink. A pyroelectric detector is typically exposed to a

sinusoidally modulated beam with frequency ω and amplitude W_o of radiation-carrying power W equated as[3 13]

$$W = W_o(1 + e^{i\omega t}). \tag{2.5}$$

At an angular frequency ω, thermal sources usually produce continuous radiation. The incoming radiation must be modulated to obtain a thermal gradient, which produces the pyroelectric current expressed in Eq. (2.4). Typically, modulation of the radiation is achieved by mechanically chopping using a rotating slotted disk. Absorption of the incident radiation results in a temperature rise $d\theta$ in the sensor. The sensor thermal response to this temperature change depends on the heat capacity H of the detector, the η fraction of absorbed photons, and the thermal conductance G coupling the detector to its surroundings. The combined effect of these factors is described by the equation for a thermal circuit:

$$\eta W = H\frac{d\theta}{dt} + G\theta. \tag{2.6}$$

Solving Eq. (2.6) for the sinusoidal power fluctuations given in Eq. (2.5) results in a temperature-fluctuation amplitude θ_ω of the detector, shown as

$$\theta_\omega = \eta W(G^2 + \omega^2 H^2)^{-1/2}. \tag{2.7}$$

The phase difference between the incident radiation and the temperature oscillations is given as

$$\phi = \tan^{-1}\left(\frac{\omega H}{G}\right), \tag{2.8}$$

and the thermal time constant is given as

$$\tau_T = \frac{H}{G} = \frac{cAd}{G}, \tag{2.9}$$

where c' is the specific heat of the detector material, A is the area of the detector, and d is the thickness of the detector.

The thermal conductance between the detector element and its surroundings is the sum of its radiative conductance G_R, and the thermal conductance of the wire links G_W is expressed as

$$G = G_R + G_W. \tag{2.10}$$

The Stefan–Boltzmann law of thermal radiation gives the radiative conductance as

$$G_R = 4\eta\sigma T^3 A_R, \tag{2.11}$$

where σ is the Stefan–Boltzmann constant, and A_R is the radiating area with emissivity η.

The thermal conductance through a wire is given as

$$G_W = \frac{\kappa A_W}{l}, \tag{2.12}$$

where κ is the thermal conductivity, A_W is the cross-sectional area, and l is the length of the wire.

The current responsivity is the pyroelectric current per watt of incident power, defined as

$$R_i = \frac{i_p}{W_o} = \frac{\eta p A \omega}{G(1 + \omega^2 \tau_T^2)^{1/2}}. \tag{2.13}$$

To determine the voltage response of the device, the electrical circuit of Fig. 2.5 must be taken into consideration. The voltage responsivity of the detector measured at the gate of the amplifier is

$$R_v = \frac{V}{W_o} = \frac{i_p |Z|}{W_o} \tag{2.14}$$

and depends on the electrical impedance of the circuit, defined as

$$Z = \frac{R}{(1 + \omega^2 \tau_E^2)^{1/2}}, \tag{2.15}$$

where $\tau_E = RC$ is the electrical time constant τ_E for the circuit shown in Fig. 2.5.

The total circuit capacitance is $C = C_E + C_A$, and resistance is $R = (1/R_E + 1/R_G + 1/R_L)^{-1}$. Combining Eqs. (2.14) and (2.15) results in the following voltage responsivity (pyroelectric voltage per watt of incident power):

$$R_v = \frac{\eta p A \omega R}{G(1 + \omega^2 \tau_T^2)^{1/2}(1 + \omega^2 \tau_E^2)^{1/2}}. \tag{2.16}$$

To achieve the greatest voltage response, both the detector-load circuit impedance and the current response must be maximized. The impedance is maximized with large R, small ω, and small c. The current response given in Eq. (2.13) is maximized with large η, large p, small c, and small d.

The chopping frequency can have a significant effect on the magnitude of the detector voltage response. Figure 2.7 shows how the chopping frequency ($f = \omega/2\pi$) affects the voltage response for $\tau_E > \tau_T$. In the case shown, the left slope refers to electrical roll-off, and the right slope refers to thermal roll-off. This curve is dependent on the properties of the different materials and the choice of τ_E, as illustrated in Table 2.1.

2.4.3 Noise-equivalent power

In determining detector performance, merely evaluating responsivity is insufficient. Various noise sources in the detector element, load, and measuring circuit lead to limitations for small signal detection. The sensitivity

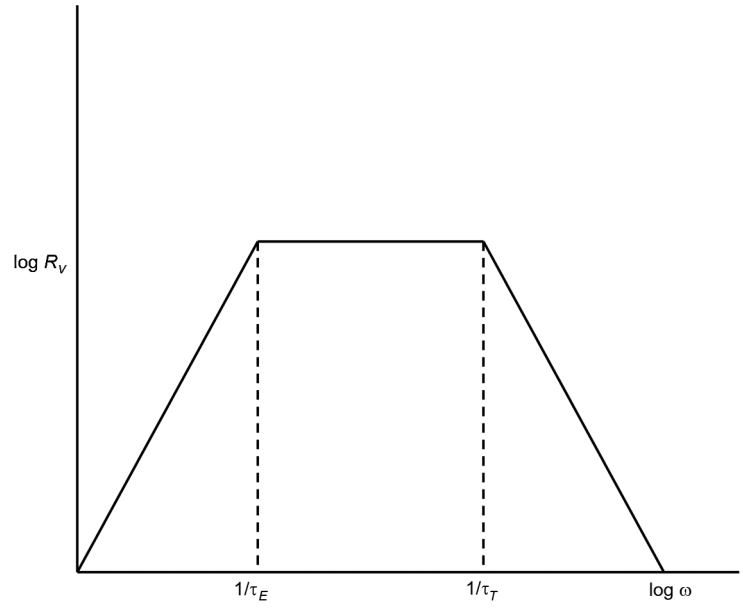

Figure 2.7 Log-log plot of voltage responsivity versus a sinusoidally modulated frequency.

Table 2.1 Voltage responsivity versus time constants and chopping frequency (where p is the pyroelectric coefficient).

	Low frequency	Medium frequency	High frequency	
$\tau_T > \tau_E$	$\frac{\eta p A \omega R}{G}$	$\frac{\eta p R}{cd}$	$(C_E > C_A)$	$(C_A > C_E)$
$\tau_T < \tau_E$		$\frac{\eta p}{GC}$	$\frac{\eta p}{c\omega\varepsilon\varepsilon_0 A}$	$\frac{\eta p}{cd\omega C_A}$

of a detector is often expressed as noise-equivalent power (NEP), which is the signal power incident on the bolometer that produces a signal-to-noise ratio of unity per 1 Hz of electronic bandwidth, expressed as

$$NEP = \frac{\Delta V_n 1}{R_v}. \tag{2.17}$$

2.4.4 Detectivity

Detectivity is the inverse of NEP and is defined as

$$D = \frac{1}{NEP}, \tag{2.18}$$

and the specific detectivity is $D^* = A^{\frac{1}{2}}D$. The use of D^* can be misleading in the discussion of the performance of pyroelectric detectors because some of the noise sources depend on the area A of the detector. D^* is useful for comparing devices of different electrode areas.

2.4.5 Noise

The noise sources of the pyroelectric element limit the detectable radiation flux (or the signal-to-noise ratio). The noise sources are temperature noise, Johnson noise, input-noise voltage of the preamplifier, and input-noise current of the preamplifier:

$$\Delta V_N^2 = \Delta V_T^2 + \Delta V_J^2 + \Delta V_i^2 + \Delta V_v^2. \tag{2.19}$$

Each term in Eq. (2.19) depends on frequency and refers to unit bandwidth. Thermal noise is the change in output voltage that arises from random changes in the temperature of the pyroelectric detector. These thermal fluctuations are produced by the random exchange of heat and photons between the detector and its surroundings. For a detector linked to its surroundings by wire leads and situated in an evacuated chamber, the thermal noise arises from the thermal radiation G_r, impinging on the detector and the thermal conductance G_w of the wire leads. The thermal noise voltage is given as

$$\Delta V_T = \frac{R_v}{\eta}(4kT^2G)^{\frac{1}{2}}, \tag{2.20}$$

where $G = G_r + G_w$. To minimize thermal noise, it is necessary to minimize thermal conductance and operation temperature. The smallest value of thermal noise for a given temperature is obtained when radiative conductance dominates thermal conductance. Ultimate detector sensitivity is limited by background radiation fluctuations. The thermal noise of a radiation-limited detector depends on the temperature of $T^{5/2}$.

Johnson noise arises from the random motion of charge carriers in the crystal and the electrical circuit. In practice, the pyroelectric crystal is not a perfect capacitor. The crystal's dielectric loss contributes to the detector Johnson noise. The Johnson noise voltage per unit bandwidth is given by

$$\Delta V_J = \left(\frac{4kT}{R}\right)^{\frac{1}{2}}\left(\frac{1}{R^2} + \omega^2 C^2\right)^{\frac{1}{2}}. \tag{2.21}$$

The total resistance R is the value of the gate resistance R_G and loss equivalent resistance $R_E = (\omega C_E \tan\delta)^{-1}$ configured electrically in parallel. Likewise, C is the total capacitance of the detector C_E and circuit C_A configured in parallel. At low frequencies $\omega \ll (R_G C_E \tan\delta)^{-1}$, and Eq. (2.21) simplifies to

$$\Delta V_J = \left(\frac{4kTR_G}{1 + \frac{1}{\tan^2\delta}}\right)^{\frac{1}{2}} C_E \gg C_A. \tag{2.22}$$

In Eq. (2.22), Johnson noise is minimized by low-temperature operation, small R_G, and small dielectric loss tanδ. An approximation of high frequency $\omega = (R_G C_E \tan\delta)^{-1}$ simplifies Johnson noise voltage to

$$\Delta V_J = \left(4kT \frac{\tan\delta}{\omega C_E}\right)^{\frac{1}{2}} C_E \gg C_A. \tag{2.23}$$

Minimizing Johnson noise in high-frequency operation is accomplished by operating at a low temperature and high frequency with large detector capacitance.

Other noise sources may reside in the electrical equipment, such as in the first stage of the signal amplifier and microphonic effects. The signal-amplifier noise depends on the gate-leakage current of the field effect transistor (FET) and Johnson noise of the channel resistance. Preamplifier-voltage noise typically becomes a relevant factor only at high frequencies and below ~ 0.5 Hz, where $1/f$ noise begins to dominate. Preamplifier-voltage noise is represented as a current generator in series or voltage source in parallel with the input circuit. Vibrations in the electrical components cause microphonic noise. Vibration in the wire leads may result in charge fluctuations $\partial Q = V\partial C + C\partial V$ and/or changes in capacitance. In addition, since pyroelectric materials are also piezoelectric, stress from vibrations can cause fluctuations in the spontaneous polarization. These changes in electrical behavior can add to the noise. Thermally induced transients can also add to noise pulses from fast changes in ambient temperature by superimposing on normal pyroelectric response.

2.5 Material Performance Parameters

At the low frequencies intended for pyroelectric detector operation, thermal or Johnson noise dominates. Assuming that the detector element capacitance is greater than that of the signal amplifier, and operation is in the high frequency roll-off regime, detectivity can be expressed as

$$D = \frac{\eta p}{C_v} \left(\frac{1}{\omega k T d A \varepsilon\varepsilon_0 \tan\delta}\right)^{\frac{1}{2}}. \tag{2.24}$$

The material figure-of-merit expression F_D, derived from Johnson-noise-limited detectivity, is

$$F_D = \frac{p}{C_v} \left(\frac{1}{\varepsilon\varepsilon_0 \tan\delta}\right)^{\frac{1}{2}}. \tag{2.25}$$

Detectivity of a thermal-noise-limited detector response, assuming that thermal radiance dominates thermal conductance, can be derived from the preceding equations to become

$$D = \left(\frac{\eta}{16 A k \sigma T^5}\right)^{\frac{1}{2}}. \tag{2.26}$$

Thermal-noise-limited detectivity is independent of material parameters. Assuming that the emissivity is unity, room temperature (300 K) thermal-noise-limited specific detectivity is 1.8×10^{10}cm $Hz^{1/2}W^{-1}$, as compared with 3.7×10^{10} cm $Hz^{1/2}$ W^{-1} at 90 K. Operating the detector at the passive cooling limit (90 K) increases the performance of the detector by more than one order of magnitude. Lowering the detector operating temperature affects the specific detectivity to a lesser extent in the Johnson-noise-limited case, T^5 versus $T^{1.5}$.

2.5.1 Material figures of merit

When assessing the performance of materials for IR sensors, look for low dielectric constant and loss, a high pyroelectric coefficient, and low volume-specific heat. Additionally, important figures of merit for materials under optimum detector-operation conditions, which can be derived from the preceding analysis, are

$$F_I = p/C_v \qquad \text{for high current detectivity,} \tag{2.27}$$

$$F_V = p/C_v\varepsilon' \qquad \text{for high voltage responsivity,} \tag{2.28}$$

$$\text{and} \quad F_D = p/C_v(\varepsilon'')^{\frac{1}{2}} \qquad \text{for high detectivity,} \tag{2.29}$$

where p is the pyroelectric coefficient, C_v is the volume-specific heat of the element, ε' is the real part of the dielectric constant, and ε'' is the imaginary part of the dielectric constant (dielectric loss). It is important to note that in the following chapters, C_v is not considered for comparison.

Bauer and Ploss developed the following figures of merit for when the pyroelectric element is placed on a substrate that acts as a heat sink, leading to infinite thermal conductivity:[14]

$$F_I = p/\kappa \qquad \text{for high current detectivity,} \tag{2.30}$$

$$F_V = p/\kappa\,\varepsilon' \qquad \text{for high voltage responsivity,} \tag{2.31}$$

$$\text{and} \quad F_D = p/\kappa_v(\varepsilon'')^{\frac{1}{2}} \qquad \text{for high detectivity,} \tag{2.32}$$

where κ is the thermal conductivity of the pyroelectric element.

2.6 Structural Design

In this section, a brief description of the design of single-element pyroelectric detectors and array devices is presented. Single-element pyroelectric detectors consist of a single thin slice of crystal, ceramic, or polymer foil and an amplifier circuit. A pyroelectric sensor is composed of several layers, as shown in Fig. 2.8. The top layer, which absorbs and stores the incident energy, is followed by a thin metallic layer that acts as an electrode for the pyroelectric capacitor. The next layer is the pyroelectric crystal, and the bottom layer is the second metallic

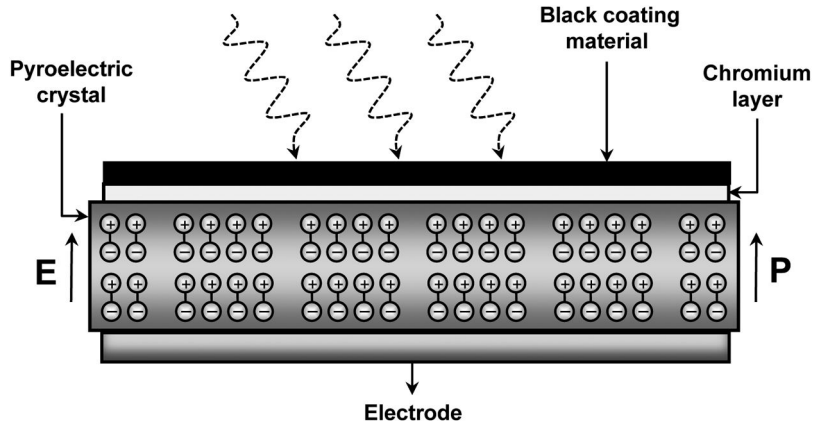

Figure 2.8 Structure of a pyroelectric sensor.

electrode. Incident radiation heats the top layer and/or the pyroelectric crystal. The absorbed energy causes a temperature change, which produces the polarization change due to the pyroelectric effect. The resultant electric field can be detected by means of a suitable preamplifier. The material and design of the absorber affect the performance of the thermal sensor because the incident light must be efficiently absorbed in order for the thermal sensor to achieve maximum sensitivity—absorber characteristics are described in the following section.

2.6.1 Characteristics of absorbers

Pyroelectric detectors exhibit a broad and uniform spectral response that is limited almost solely by the characteristics of the absorbing materials that cover the detector's radiation receiving area. Traditionally, various absorbers have been used. The maximum absorption of heat can be obtained by depositing an absorbing layer on the detector. A suitable IR absorbing layer can be applied to provide the detector with a *flat* spectral response over a considerable wavelength range. To achieve high efficiency, the absorber must: (1) work at a wide range of wavelengths, (2) possess high damage resistance, and (3) have low thermal mass to allow for a rapid transfer of the absorbed power to the sensing element. Four main designs have traditionally been used:[15 29]

1. Metal-black coatings show significant absorption in the visible and near-IR region. They have high thermal capacity but represent a fragile absorber system.[15] The metal blacks are from metals such as gold, platinum, aluminum, and nickel. The major advantage of the metal blacks over black paint is their low thermal mass.
2. Thin metal shows a very constant value over the whole IR, explaining the wide use of such films as IR absorbers.[16]
3. Quarter-wavelength absorbers yield up to 95% absorption of the incoming radiation.[27] However, they still have high thermal capacity. Their structure is shown below in Fig. 2.9.

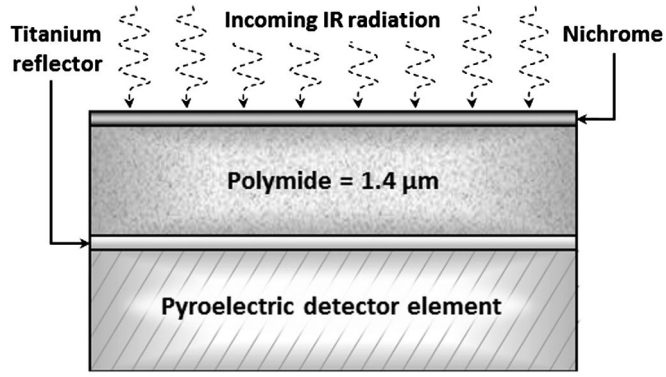

Figure 2.9 Quarter-wavelength-absorber structure for 8- to 14-μm IR radiation.

4. A mesh of lossy wires was created when Bock et al. proposed a spider-web-type absorber for the terahertz regime to decrease thermal capacity, yielding an experimental absorptivity of 70%.[29]

In the recent past, Lehman et al. have grown carbon multiwall nanotubes (MWNTs) by hot-wire chemical vapor deposition using lithium niobate as an absorber.[17] The authors found the absolute spectral responsivity of 600–1800 nm to be spectrally uniform, with variations within only a few percent. Yang et al. described vertically aligned multiwall carbon nanotubes (VAMWCNTs) as the world's *darkest material*.[18] Recently, Lehman and Sanders have grown VAMWCNTs through water-assisted chemical vapor deposition on a large-area lithium-tantalate-pyroelectric detector. They found that it is possible to achieve nearly ideal values of detector reflectance uniformly—less than 0.1% from 400 nm to 4 μm and less than 1% from 4 to 14 μm. Their findings along with other important data on reflectivity using silicon and a detector are presented in Table 2.2.[19 26]

The metal films are deposited at the top and bottom of the quarter-wavelength structure. The top metal film exposed to the IR radiation is impedance matched to the free space so that 50% of the incident radiation is absorbed and 50% is transmitted. The transmitted radiation goes through a quarter-wavelength dielectric layer and is reflected by the lower metal film, which has a very high reflectivity and then destructively interferes, giving rise to zero reflection and 100% absorption, ideally.[28]

2.6.2 Single-element detector design

The typical design for a single-element pyroelectric detector is shown in Fig. 2.10. Most commercial detectors consist of about 2 × 2 mm of lithium tantalate and wafers of a few microns in thickness mounted on a shallow cylindrical substrate. The sensing element can be raised above the base by

Table 2.2 Comparisons of reflectance values of absorber metal-black coatings.[19–26]

Absorber Material	Wavelength (μm)	Reflectance (Approx.)	Reference
Carbon paint	10	0.05	19
Platinum black	10	0.03	19
Gold black (on $LiTaO_3$)	10	0.05	20
Nickel phosphorus (on Cu)	0.6	0.2	22
Gold black (on Cu)	10	0.01	23
MWCNTs (mat on $LiTaO_3$)	0.6	0.15	21
SWCNTs (mat on $LiTaO_3$)	10	0.75	24
VAMWCNTs (on Si)	10	0.01	25
VAMWCNTs (on Si)	0.6	0.0005	25
VAMWCNTs (on Si)	10	0.001	25
VAMWCNTs (on Si)	0.6	0.001	25
VAMWCNTs (on Si)	10	0.01	25
VAMWCNTs (on $LiTaO_3$)	0.6	0.001	26
VAMWCNTs (on $LiTaO_3$)	10	0.01	26

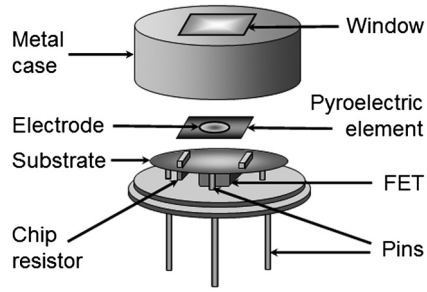

Figure 2.10 Typical design of a single-element pyroelectric detector.

means of springs and wires, and mounted using adhesive posts, bars, a hollow base, and mica plates of low thermal conductivity. The radiation absorption of the electroded pyroelectric element can affect the output of the detector. In order to increase absorption, a metallic thin film, metal-black paste, and evaporated or electroplated metal black are commonly used as absorbers. The sensor has very high impedances. To resolve this issue, a simple FET [junction-gate FET (JFET) or metal-oxide-semiconductor (MOSFET)] with an appropriate load resistance, or an operational amplifier (OPAMP) with feedback resistance in the detector package, is utilized to convert impedance to low output and to detect small charges. Thus, output from the sensor element is received via a wire bond to a discrete JFET amplifier. A disadvantage of the single element is its sensitivity to a drift in ambient temperature and piezoelectric microphonic noise. To reduce this type of interference, two oppositely polarized detector elements are connected either in series or in parallel. The two elements must be of equal area if connected in parallel, with only one element exposed to radiant flux.

The other detector element is optically inactive (blind element). Since changes in the surrounding environment affect both elements equally, the signals from the two oppositely polarized elements cancel each other out, and no output is observed from them.

2.6.3 Thin-film-based detectors

Rapid advances in thin-film technology have produced detectors directly coupled to integrated circuits.[30 32] In achieving high sensitivity, an effective thermal-isolation structure is as important as large pyroelectric coefficients.

Recently, Tan et al. described a new Au/Pt-PZT-Pt IR-detecting structure that minimizes the thermal conductance of a device using a silicon substrate with a microbridge (illustrated in Fig. 2.11).[33] In order to decrease heat loss through the substrate, the authors selected Si_3N_4/SiO_2 film as a transition layer. To minimize common-mode interferences, such as mechanical vibrations and change in ambient temperature, they fabricated a dual-element configuration.[33]

Willing et al. fabricated a Si_3N_4/SiO_2-membrane structure with a voltage response showing a plateau in the frequency regime below 4 Hz with a value of 460 V/W by bulk micromachining 1D arrays with a lead zirconate titanate (PZT) thin-film element (Fig. 2.12).[34]

In order to define the noise limit of the sensor element of the point detector and linear arrays, the hybrid method is more efficient and inexpensive because: (1) the pyroelectric structure is obtained by surface micromachining on top of the readout wafer; and (2) the detector array is fabricated on a

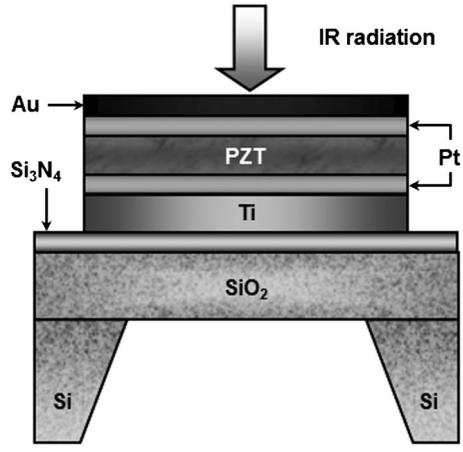

Figure 2.11 Dual-element PZT pyroelectric detector. Adapted from Ref. 33 with permission from Elsevier.

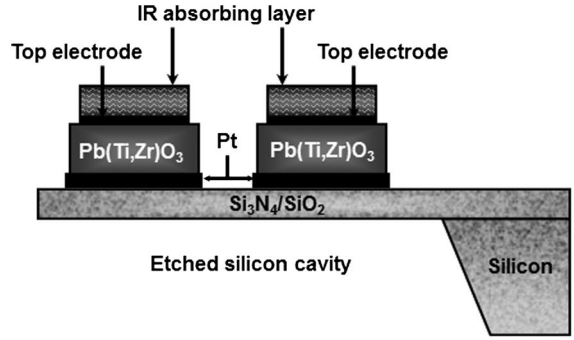

Figure 2.12 Typical structure of pyroelectric elements with a linear array on a thin membrane fabricated via micromachining. Adapted from Ref. 34 with permission from Elsevier.

different wafer and added later to the readout wafer using a suitable bonding technique that assures vertical alignment of the electrical contacts.

2.6.4 Hybrid focal-plane arrays

In the past, hybrid focal-plane arrays have been fabricated with sufficient sensitivity.[34,35] Owen et al. fabricated a FPA with a noise-equivalent temperature difference (NETD) of 0.1 K or less by reticulating a ceramic barium strontium titanate (BST) wafer, ground down and bonded to the readout chip in a mesa structure (see Fig. 2.13).[36] The absorbing layer is a transparent organic λ/4 layer sandwiched between a semitransparent metal layer and a common electrode.

2.6.5 Monolith-integrated focal-plane array

Hanson et al. have successfully developed a monolithically integrated FPA of a pyroelectric lead lanthanum zirconate titanate (PLZT) thin film of 320 × 240 pixels in the size of 50 × 50 μm (see Fig. 2.14).[37] The sensor structure consists of suspended pyroelectric thin-film plates created using a sacrificial-layer

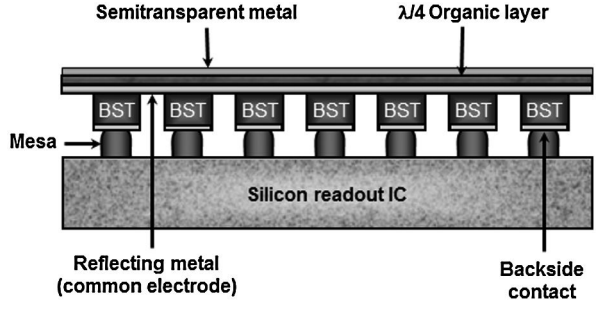

Figure 2.13 BST focal-plane-array structure (adapted from Ref. 36 with permission).

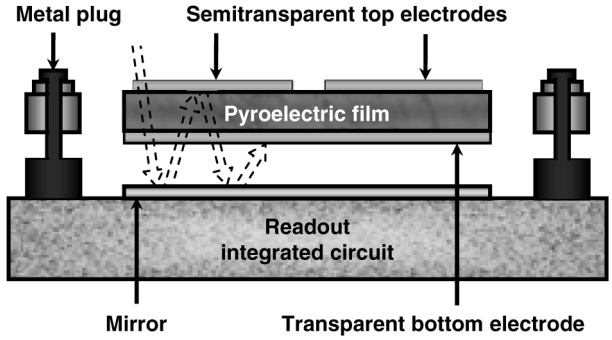

Figure 2.14 Monolithically integrated FPA through a pyroelectric detector pixel cross section (adapted from Ref. 37 with permission).

technique with a gap to trap IR radiation. The authors have demonstrated thermal imaging with NETD at around 200 mK in the laboratory stage of fabrication. Major problems, such as film stresses, cracking, warping, metal oxidation, and interdiffusion reactions have prevented the process from being transferred from the laboratory to complex device fabrication.

2.6.6 Advanced lithium-tantalate-detector array

Figure 2.15 shows the fundamental structure of an IR camera manufactured by DIAS IR GmbH.[38] The detector array consists of 128 or 256 pixels, each with an active area of $A_S = a \cdot b$ aligned in the y direction with center-to-center pitch c. The chopped radiation signal Φs passes through an IR-transmissive window before striking the active surface of the pyroelectric chip where it is absorbed, causing a temperature change, and thus, generating an electrical charge via the pyroelectric effect. A readout-integrated circuit (ROIC) produces a multiplexed voltage output signal u_S.

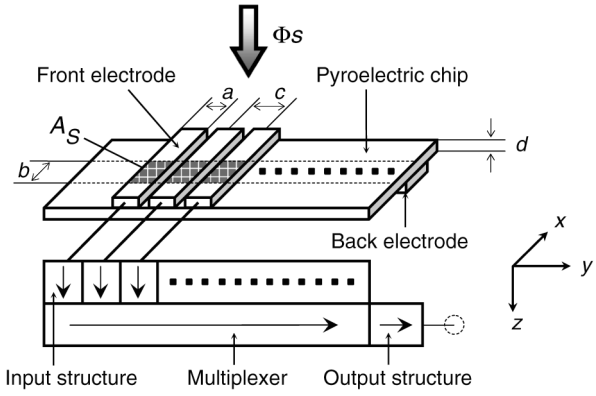

Figure 2.15 Fundamental structure of a linear pyroelectric array (adapted from Ref. 38).

The linear array includes a lithium tantalate chip with 128 sensitive elements and a thickness of 20 μm. The pixel size is $a \cdot b = 90 \cdot 100\ \mu m^2$ with a pitch c of 100 μm. The signals generated in the sensitive elements are processed in a CMOS circuit that contains both analog and digital sections. The analog section handles sensor-signal processing by means of a multiplexer, low-noise preamplifier (with individual gain control for each pixel), output amplifier, resistor–capacitator (RC) low-pass filter, and a sample-and-hold circuit. The digital section delivers the clock-pulse output used by the analog section. The pyroelectric chip and CMOS readout circuit are positioned on a thick-film wiring carrier mounted in hermetically sealed metal housing. Incident light is received by the detector elements via an IR filter. Filters with specific pass-band characteristics are used to optimize the performance of the detector arrays for operation within the 8- to 14-μm, 3- to 5-μm, 4.8- to 5.2-μm, and 1.4- to 1.8-μm spectral bands. Sensitivity of the detector array is maximized by reducing the thickness (5 μm) of the pyroelectric chips, fabricated using ion-beam etching techniques.

2.6.7 Trap detector

For the absolute determination of radiant powers and energies, Mellouli et al. fabricated and investigated a pyroelectric *trap* detector using the radiant electrical substitution method. This consists of comparing an electrical heating power (used as a reference) to the incident optical radiant.[39]

The trap detector is shown in a schematic cross section in Fig. 2.16. The basic structure and shape are simple, consisting of both a copper rectangular tail plane and an inclined tail plane with an angle opening to 30 deg. This V copper form acts as a heat sink, maintained at thermodynamic temperature. The entrance diameter of the trap is 19 mm. A PVF_2 pyroelectric film, 9 μm in thickness, is glued to the interior surfaces.

Two thin-film aluminum electrodes are placed on the surface of the pyrofilm. The pyroelectric front surface is separated from the heater by a thin

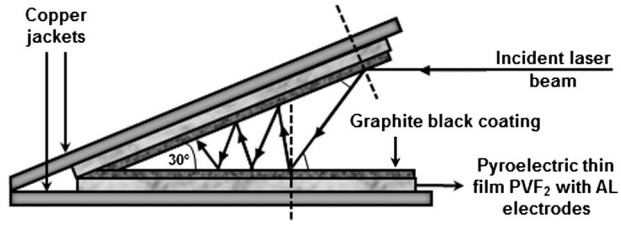

Figure 2.16 Simplified cross section of the pyroelectric trap detector. Adapted from I. Mellouki, O. Touayar, T. Ktari, F. Saadallah, J. Bastie, and N. Yacoubi, "Study and realization of trap pyroelectric detector for absolute high radiant power and energies," *Meas. Sci. Technol.* **15**, 384–388 (2004) [doi: 10.1088/0957-0233/15/2/011], with permission from IOP Publishing.

Mylar® layer. On the front surface of the Mylar, a thick layer of graphite is deposited over an area 12 mm long and 10 mm wide, with a thickness of 20 μm. On one hand, this layer serves as a black coating to convert the radiant energy into heat, and on the other hand, it acts as an electrical heating element with a resistance of about 1000 ohms, which converts the electrical energy supplied by the pulse generator into heat. The authors found that the device presents linear behavior in the power range from about 20 mW to about 1 W and a spectral-responsivity scale of 250–2500 nm. The calculated device sensitivity was found to be 6.361 V/W with an uncertainty of 0.001 V/W and a total-reflection-loss factor of 3×10^{4}.

2.6.8 Resonant detector

Gokhale et al. have developed a novel uncooled IR detector using a combination of piezoelectric (electrostrictive), pyroelectric, and resonant effects with a sensitivity that is orders of magnitude higher than that of quartz-based resonators.[40] The architecture consists of a parallel array of a high-Q gallium nitride (GaN) micromechanical resonator coated with an IR-absorbing layer of SiNx and carbon nanotube (CNT) nanocomposite. GaN is used because it possesses high piezoelectric and pyroelectric coefficients and can be grown on silicon substrate via low-cost batch fabrication. The nanocomposite absorber demonstrates high efficiency when converting the IR energy into heat. The generated heat causes a shift in frequency characteristics of the GaN resonator because of pyroelectric and piezoelectric effects. IR detection is achieved by sensing the shift in the resonance frequency and amplitude of an exposed GaN resonator as compared to the reference resonator included in the array. A reference resonator is used to reduce noise and cancel the frequency shift caused by other changes such as increases in the ambient temperature fluctuations, mechanical shock, and acceleration. A schematic view of GaN-IR-detector architecture is illustrated in Fig. 2.17. It may be recalled that in

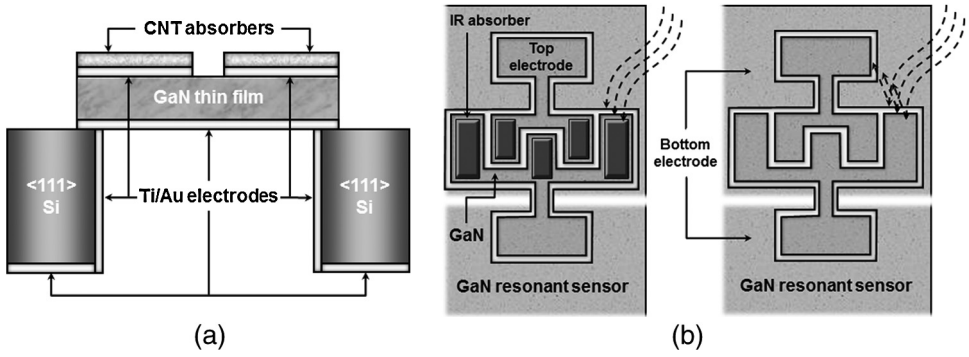

Figure 2.17 Schematic view of GaN-IR-detector architecture (adapted from Ref. 41).

Table 2.3 The contributions of different effects in shifting the resonant frequency of GaN resonator IR detector.[43]

Mechanism	Sensitivity (ppm/K)	Frequency change SiN*x* absorber (ppm)	Predicted frequency change CNT nanocomposite-absorber (ppm)
TCF induced	17.7	3.3984	15.2928
Piezoelectric (linear) strain	0.5	0.096	0.432
Pyroelectric electrostrictive (quadratic)	1505	288.96	1300.32
Measured frequency change (sensor)		183	
Measured frequency change (reference)		13	

resonant IR sensors, the change in physical dimensions (due to thermal expansion) and the change in elasticity of the material are the main factors in the change in resonant frequency of the device.[40 42]

Thus, the temperature-induced change in frequency (TCF) of these resonators is due to the material's elasticity. It is worth mentioning that incident IR radiation on a GaN surface results in the spontaneous generation of charge, and hence, generates a voltage across the GaN film. This voltage causes an additional change in the resonant frequency that exceeds the TCF-induced change by orders of magnitude. The sensitivity of the detector is further enhanced by using additional thin-film absorbers that efficiently absorb IR power. The different effects of shifting the resonant frequency of a GaN resonator IR detector are tabulated in Table 2.3. For details, refer to the publications of Rais-Zadesh et al.[42,43]

2.6.9 Srico TFLT™ detector[44]

Srico, Inc. has combined the emerging technologies of wafer bonding and ion-slice-layer transfer to achieve both uniform and thin monocrystalline lithium tantalate films on device-carrier substrates. The thin-film lithium tantalate (TFLT™) layers have ranged in size from 3 to 25 mm. In addition to thin-film formation, Srico has developed periodic domain-engineered patterns in thin films to suppress noise sources outside of the detector aperture. Domain-engineered periodic patterns effectively and reliably depole the film. Judicious use of domain engineering can also be applied within the device aperture to suppress standing wave acoustic noise. Using TFLT™ technology, Srico, Inc. has demonstrated a record-breaking 20 times the detector-performance improvement relative to state-of-the-art commercial products. Further reductions in thickness are expected to enable room-temperature pyroelectric detector sensitivity approaching 100 times that of current commercially available devices. The fabrication process developed is illustrated in Fig. 2.18. The TFLT™ process begins with a 3-in. bulk wafer of lithium tantalate.

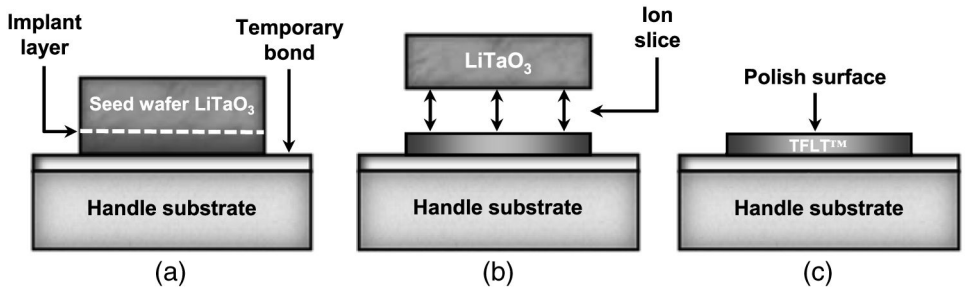

Figure 2.18 Sirco, Inc. TFLT™ fabrication process (adapted from Ref. 44).

Depending on the application, a domain pattern can be formed in the wafer prior to the TFLT™ process. A full wafer-ion implant is performed to create a highly stressed implant layer at a depth determined by the implant energy. This depth defines the film thickness and is typically 5–10 μm. The implanted wafer is then temporarily bonded face down to a handle substrate for further processing. Either selective wet etching or a high-temperature step is used to separate or "slice" the seed wafer along the ion-implant plane, leaving a thin portion of the seed wafer still attached to the handle wafer. Polishing is used to smooth the sliced surface, and annealing is performed to remove any residual implant stress. The bulk-quality TFLT™ film can be further processed for the specific application or transferred directly to a device carrier. Device carriers are typically composed of 0.5-mm thick ceramic or quartz discs with center aperture openings of 2–5 mm in diameter. In other cases, the carrier is a silicon wafer, either with or without an open window. After transferring the TFLT™ film, metal coatings and wire leads are applied to the top and bottom. If the TFLT™ layer is domain-patterned over the entire film, an additional poling step may be performed to activate the aperture region. The thin nature of the ion-sliced films enables *in situ* poling of devices to activate a pyroelectric response only within the desired aperture. Noise contributions normally present outside of the aperture are nullified by the periodic domain pattern. An illustration of the domain-engineered TFLT™ pyroelectric detector is shown in Fig. 2.19. The layer ensures efficient detection at wavelengths from the visible into the terahertz regime. The entire assembly is packaged in a standard TO can for testing.

The voltage responses for both a 25-μm film-reference device and a TFLT™ device were 800 V/J and 6.12 kV/J, respectively. Correcting for detector areas, the results indicated about a 300% improvement for the ion-sliced device relative to the state-of-the-art 25-μm film device. This result proved that the silicon-mounted films have a performance advantage, even without backside-window formation in the silicon substrate. Furthermore, the authors investigated ceramic-mounted TFLT™ films with an open-window aperture of 2 mm. Multiple devices exhibited consistent performance with

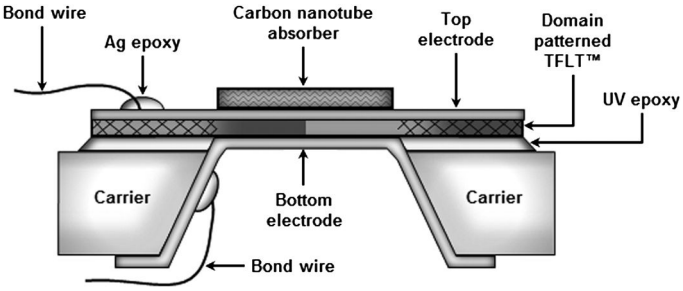

Figure 2.19 TFLT™ domain-engineered detector (adapted from Ref. 44).

current responsivity of 4.26–4.5 μA/W. Some devices were hybrid packaged with an integrated TIA circuit to determine noise-limited performance. Hybrid-packaged devices exhibited NEP of less than 200 pW/$\sqrt{}$Hz at a voltage responsivity greater than 0.8 MV/W. Typical D^* values were greater than 2.10^9 cm$\sqrt{}$Hz/W for these 2-mm aperture devices. TFLT™ films were also transferred to sapphire in a manner similar to that used for ceramic carriers. Room-temperature performance for sapphire-mounted devices was comparable to that found for ceramic carriers.

2.7 Pyroelectric-Detector Applications[11,44,45]

Recent applications for IR detectors are found in thermal-energy harvesting for micro-electric generators. Uncooled pyroelectric-IR detectors are used in many applications, including, but not limited to: air quality monitoring, alcohol detection, anesthesiology testing, atmospheric temperature measurement, automatic door switch mechanisms, biomedical imaging, border patrol systems, ear thermometers, earth position sensors, earth resource detection, engine analysis, facial recognition, fire alarm systems, forest fire detection, gas analyzers, glass processing, horizon sensors, human sensors, IR detection, IR spectrometers, interferometers, interplanetary probes, intrusion detectors, IR-flame detection, laser detection, laser power control mechanisms, law enforcement systems, liquid-fuel analysis, meteorology, microwave detectors, nondispersive IR (NDIR) gas analysis, optical waveguide studies, petroleum exploration, plasma analysis, plastic processing, pollution detection, position sensors, pyroelectric vidicons, pyrometers, radiometers, rail safety systems, reflectance measurements, remote sensing, satellite-based IR detection at 90 K, sky radiance, solar cell studies, traffic control systems, UV to FIR (THz) detection, vision testing, and x-ray detectors. Potential commercial applications for high-performance pyroelectric devices are listed in Table 2.4.[44]

Table 2.4 Potential commercial applications for high-performance pyroelectric devices.[44]

Research applications	Medical & industrial applications	Government applications
• Optical calibration transfer standards • High precision broadband radiometers • High sensitivity, room temperature, broadband, THz power sensors	• IR detectors for blood gas analyzers • Rugged, nonhygroscopic IR detectors for FTIR systems • THz image sensors for noninvasive medical diagnostics • Nondestructive IR or THz material testing • Improved pulsed laser sensors • IR flame detectors • Cancer research and diagnostics	• Low noise horizon sensor for satellite applications • Calibration system for IR target designators • Quad detectors for laser targeting and alignment • Broadband detectors for THz measurement, control, or calibration • THz field communications systems

2.8 Conclusions

Through this review of the fundamentals of pyroelectric detectors, design, and various structures and applications, we find that materials engineering combined with thin-film processing techniques can help improve requisite and desired performance. Integration technology is principally important in obtaining the optimum combination of required thermal properties as well as the requirements for electrical readout. However, the candidate material of choice for commercial applications is still lithium tantalite, which offers higher detector detectivity D^* along with novel fabrication techniques.

References

1. R. W. Boyd, *Radiometry and the Detection of Optical Radiation,* Wiley, New York (1983).
2. Wikipedia, "IR window," accessed April 2013, http://www.wikipedia.org/wiki/IR window.
3. G. Reike, *Detection of Light,* Cambridge University Press, Cambridge (2003).
4. R. W. Whatmore, "Pyroelectric devices and materials," *Rep. Prog. Phys.* **49**, 1335–1386 (1986).
5. A. K. Batra, M. D. Aggarwal, M. Edwards, and A. S. Bhalla, "Present status of polymer: ceramic composites for pyroelectric IR detectors," *Ferroelectrics* **366**, 84–121 (2008).
6. R. B. Lal and A. K. Batra, "Growth and properties of triglycine (TGS) sulfate crystals: review," *Ferroelectrics* **142**, 51–82 (1993).
7. S. B. Lang and D. K. Das-Gupta, "Pyroelectricity: fundamentals and applications," *Ferroelectrics Review* **2**(4), 217–354 (2000).

8. A. Rogalski, *IR Detectors*, Gordon and Breach Science Publishers, The Netherlands (2000).
9. R. W. Whitmore and R. Watton, "Pyroelectric materials and devices," in *Infrared Detectors and Emitters: Materials and Devices*, P. Capper and C. T. Elliott, Eds., Kluwer Academic Publishers (2000).
10. A. J. Moulson and J. M. Herbert, *Electroceramics*, Wiley, Chichester, UK (2003).
11. S. B. Lang and D. K. Das-Gupta, "Pyroelectricity: fundamentals and applications," in *Handbook of Advanced Electronic and Photonic Materials and Devices* (Vol. 4), H. S. Nalwa, Ed., Academic Press, New York (2001).
12. Y. Xu, *Ferroelectric Materials and Applications*, North-Holland, Amsterdam (1991).
13. J. R. Curie, "Studies on the Functional Ferroelectric Materials for IR Sensors," M.S. Thesis, Alabama A & M University, Normal, Alabama (2004).
14. S. Bauer and B. Ploss, "Interference effects of thermal waves and their applications to bolometers and pyroelectric detectors," *Sensors and Actuators A* **25**, 714–422 (1991).
15. W. R. Blevin and J. Geist, "Influence of black coatings on pyroelectric detectors," *Applied Optics* **5**, 1171–1178 (1974).
16. F. Jutzi, D. H. B. Wicaksono, G. Pandraud, N. de Rooij, and P. J. French, "Far-IR sensors with LPCVD-deposited low-stress Si-rich nitride absorber membrane (Part 1 optical absorptivity)," *Sensors and Actuators* **152**, 119–125 (2009).
17. J. H. Lehman, R. Deshpande, P. Rice, B. To, and A. C. Dilon, "Carbon multi-walled nanotubes grown by HWCVD on a pyroelectric detector," *IR Physics and Technology* **47**, 246–250 (2006).
18. Z. P. Yang, L. Ci, A. J. Bur, S. Y. Lin, and P. M. Ajayan, "Experimental observation of an extremely dark material made by a low density nanotube array," *Nano Lett.* **8**, 446–451 (2008).
19. D. Betts, F. Clark, J. J. Cox, and J. A. Larkin, "IR reflection properties of five types of black coating for radiometric detectors," *J. Physics E: Scientific Instruments* **18**, 689–696 (1985).
20. J. H. Leyman, E. Theocharous, G. Eppeldauer, and C. Pannell, "Gold-black coatings for freestanding pyroelectric detectors," *Measurement Science and Technology* **14**, 916–922 (2003).
21. J. H. Leyman, K. E. Hurst, A. M. Radojevic, A. Dilon, and R. M. Osgood, "Multiwall carbon nanotube absorber on a thin-film lithium niobate pyroelectric detector," *Opt. Lett.* **32**, 772–774 (2007).

22. S. Kodama, M. Horiuch, T. Kunii and K. Kuroda, "Ultra-black nickel-phosphorous alloy optical absorber," *IEEE Trans. Instrum. Meas.* **39**, 230–232 (1990).

23. D. J. Advena, V. T. Bly, and J. T. Cox, "Deposition and characterization of far-IR absorbing gold black film," *Appl. Opt.* **32**, 1136–1144 (1993).

24. E. Theocharous, C. Engtrakul, A. C. Dilon, and J. Lehman, "IR responsivity of pyroelectric detector with a single-wall carbon nanotube coating," *Appl. Opt.* **47**, 3999–4003 (2008).

25. K. Mizuno, J. Ishii, H. Kishida, and K. Hata et al., "A black body absorber from vertically aligned single-walled carbon nanotubes," *Proc. Natl. Acad. Sci., USA*, **106**, 16044–16047 (2009).

26. J. Lehman, A. Sanders, L. Hanssen, B. Wilthan, J. Zeng, and C. Jensen, "Very black IR detector from vertically aligned carbon nanotubes and electric-field poling of lithium tantalate," *Nano Lett.* **10**(9), 3261–3266 (2010).

27. L. N. Hadley and D. M. Dennison, "Reflection and transmission interference filters," *J. Optical Society of America* **37**, 451–453 (1947).

28. J. J. Monzon and L. L. Sanchez-Soto, "Optical performance of absorber structures for thermal detectors," *Applied Optics* **33**, 5137–5141 (1994).

29. J. J. Bock, D. Chen, P. D. Mauskopf, and A. E. Lange, "A novel bolometer for IR millimeter-wave astrophysics," *Space Science Reviews* **74**, 229–235 (1995).

30. B. Willing, M. Kohli, P. Muralt, and O. Oehler, "Thin film pyroelectric array as a detector for an IR gas spectrometer," *IR Physcis Technology* **39**, 443–449 (1998).

31. N. M. Shorrocks, A. Patel, M. J. Walker, and A. D. Parson, "Integrated thin film PZT pyroelectric detector arrays," *Microelectron. Eng.* **29**, 56–66 (1998).

32. P. Muralt, "Micromachined IR detectors based on pyroelectric thin films," *Reports on Progress in Physics* **64**, 1339–1388 (2001).

33. Q. Tan, W. Zhang, C. Xue, J. Xiong, J. Lui, J. Li, and T. Liang, "Design, fabrication, and characterization of pyroelectric thin film and its application for IR gas sensors," *Microelectronics Journal* **40**, 58–62 (2009).

34. B. Willing, M. Kohli, P. Muralt, N. Setter, and O. Oehler, "Gas spectrometry based on pyroelectric thin film arrays integrated on silicon," *Sensors and Actuators A* **66**, 109–113 (1998).

35. R. Watton, P. A. Perkins, and J. P. Gillham, "Uncooled IR imaging: hybrid and integrated bolometer arrays IR technology and applications," *Proc. SPIE* **2744**, 486–499 (1996) [doi: 10.1117/12.243488].

36. C. M. Hanson, H. R. Beratan, R. A. Owen, M. Corbin, and S. McKenney, "Uncooled thermal imaging at Texas Instruments," *Proc. SPIE* **1735**, 17–26 (1992) [doi:10.1117/12.138624].
37. C. M. Hanson, H. R. Beratan, and J. F. Belcher, "Uncooled IR imaging using thin film ferroelectrics," *Proc. SPIE* **4288**, 298–303 (2001) [doi: 10.1117/12.429417].
38. G. Hofmann and R. Köhler, personal communication (2012).
39. I. Mellouki, O. Touayar, T. Ktari, F. Saadallah, J. Bastie, and N. Yacoubi, "Study and realization of trap pyroelectric detector for absolute high radiant power and energies," *Meas. Sci. Technol.* **15**, 384–388 (2004) [doi: 10.1088/0957-0233/15/2/011].
40. V. J. Gokhale, Y. Sui, and M. Rais-Zadeh, "Novel uncooled detector based on gallium nitride micromechanical resonators," *Proc. SPIE* **8353** 835319 (2012) [doi: 10.1117/12.920450].
41. M. Rais–Zadch, "Gallium nitride micromechanical resonators for IR detection," *Proc. SPIE* **8373** (2012) [doi: 10.1117/12.919941].
42. V. J. Gokhale, J. Roberts, and M. Rais-Zadeh, "Sensitive uncooled IR detectors using gallium nitride resonators and silicon nitride absorbers," Department of Electrical Engineering and Computer Science, University of Michigan, Ann Arbor, Michigan, and Nitronex Corporation, Durham, North Carolina, http://web.eecs.umich.edu/~minar/pdf/0129 Gokhale full paper.pdf.
43. Y. Sui, V. Gokhale, O. A. Shenderova1, G. E. McGuire, and M. Rais-Zadeh, "A thin film IR absorber using CNT/nanodiamond nanocomposite," *MRS Spring Meeting & Exhibit,* San Francisco (2012).
44. V. Stenger, M. Shnider, S. Sriram, D. Dooley, and M. Stout, "Thin film lithium tantalate (TFLT™) pyroelectric detectors," *Proc. SPIE* **8261**, 82610Q (2012) [doi: 10.1117/12.908523].
45. H. Akram, "Pyroelectric detectors and their applications," *IEEE Trans. Industry Applications* **27**(5), 2301–2307 (1989).

Chapter 3
Processing of Key Pyroelectric Materials

3.1 Introduction

Pyroelectric materials have been fabricated in bulk single crystals, ceramic (polycrystalline), films, and composite forms. This chapter briefly reviews and describes all of the major and relevant techniques for processing key materials.

3.2 Bulk Single Crystals

The growth of bulk single crystals, although simple in principle, requires meticulous attention to detail. Knowledge of the phase diagram for both the constituents of the crystals and any solvent involved is essential. The mechanical and electrical equipment involved must be able to ensure uniform conditions over the extended growth period required to cultivate a single crystal of any size. Furthermore, apparati must mitigate excessive vibrations and thermal disturbances.

3.2.1 Growth of crystals from solution

Highly homogeneous crystals can be grown by slow cooling saturated solutions of chosen materials or, sometimes, by the slow evaporation of a solution at a constant temperature. The growth of crystals from solution at low temperatures occupies an important place in the area of crystal growth techniques, especially because materials are not stable at elevated temperatures.

A number of concepts for solution-crystal growth systems are found in the literature.[1] One of the best methods for growth of both inorganic and organic crystals from solution is to slowly lower the temperature of a solution, provided the material has a positive temperature coefficient of solubility. In this method, a saturated solution of the material is prepared in an appropriate solvent at a chosen temperature and kept at this temperature for 24 h. The seed-holding rod is then inserted into the growth chamber, after which it is rotated. The growth process is enacted by lowering the temperature slowly at

a preprogrammed rate, typically 0.05–2.0 °C per day, depending on the solubility of the chosen material. The complete crystallization process may take from one to several weeks. To terminate the growth process, the grown crystals are taken out of the solution without incurring thermal shock. Conditions for this solution-growth method must include the proper solvent of the pyroelectric material with a positive temperature coefficient of solubility. Large pyroelectric crystals, made with such materials as triglycine sulfate (TGS) and potassium dihydrogen phosphate (KDP), have been successfully grown using the solution-growth method. Single crystals of TGS are usually grown from an aqueous solution through either the temperature-lowering or solvent-evaporation method. The authors have successfully grown large TGS crystals using the crystallizer illustrated and described in Ref. 1. The major components of a typical crystallizer designed by the authors are shown in Fig. 3.1.

Several advancements in crystallizer designs and techniques have made growing TGS crystals more efficient.[2–5] Brezina et al. designed a crystallizer for growing L-alanine-doped deuterated triglycine sulfate (DLATGS) crystals by isothermal evaporation of D_2O.[2] Satapathy et al. have described a novel technique for mounting the TGS seeds and a crystallizer.[3] Banan has also described seed holders and a crystallizer for growing pure and doped TGS crystals.[4] TGS crystals weighing more than 100 grams have been grown from solution with ethyl alcohol additions.[5] When alcohol is mixed in an aqueous solution of TGS, a portion of the water in the solution associates with the alcohol, concentrating the solution. Thus, the supersaturation can be controlled to a certain degree, making it easier to grow TGS crystals. To achieve success when growing crystals from aqueous solutions, it is important to prepare a solution with a carefully determined saturation temperature and solubility profile, and to ensure the absence of any foreign particles.

3.2.2 Crystal growth from melt

The Czochralski crystal-growth technique is illustrated in Fig. 3.2 with the various components labeled.[6] To qualify for crystal growth using the Czochralski technique, the material should have a relatively low vapor pressure. The crucible material should be nonreactive with the crystal-growth material above its melting point. The Czochralski system is based on the following procedure: (1) the material is melted in a crucible and kept for few hours at a temperature above the melting point, (2) the temperature is then reduced to a value slightly above the freezing point, which is determined by cooling the melt until crystals begin appearing on the surface, (3) the temperature is slightly lowered, and a seed (cut in the appropriate orientation) is inserted into the melt and kept in that position for a half an hour or so, (4) the pulling mechanism of the seed is initiated, (5) if the temperatures have been chosen correctly (based on the material used), the seed should form the

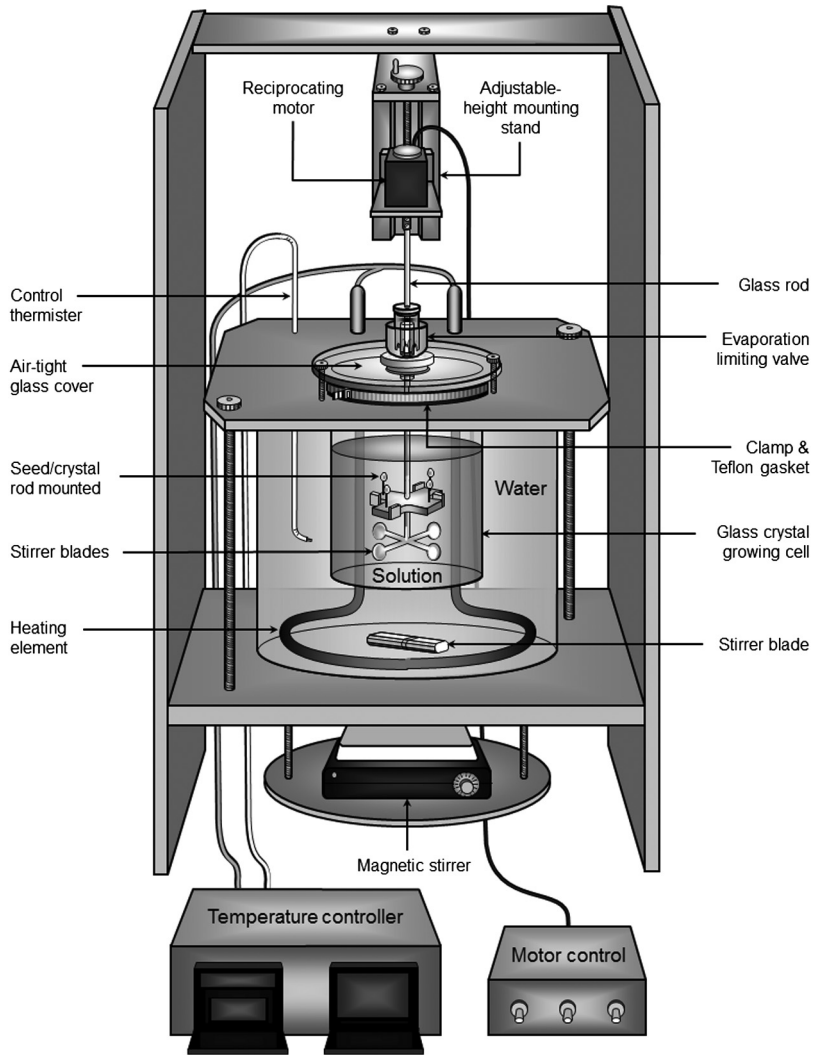

Figure 3.1 A solution-growth crystallizer designed and fabricated at AAMU.[1]

crystallization center. If the crystal grows very fast and becomes visible to the naked eye, increase the temperature of the melt by a degree or so. This must be done carefully because if the melt is overheated, the crystal will dissolve and separate from the melt. The diameter of the pulled crystal is controlled by manipulating both the melt temperature and the pulling rate. Suitable thermal engineering of both axial and radial temperature gradients is needed to reliably grow single crystals of desired dimensions. Pyroelectric single crystals of lithium tantalate, lithium niobate, potassium tantalate niobate, and others have been successfully grown using the Czochralski method.[7]

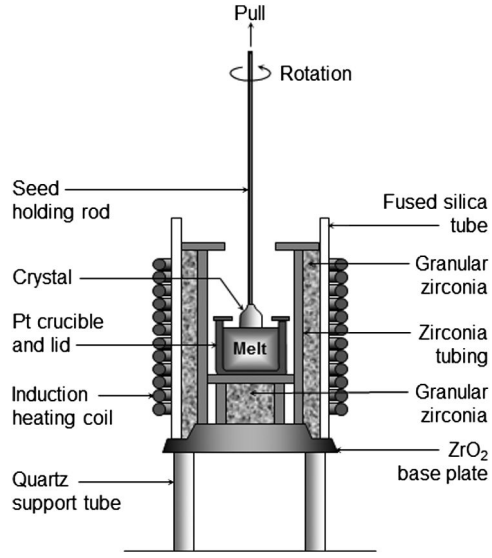

Figure 3.2 Schematic diagram of Czochralski crystal growth technique.

3.3 Preparation of Ceramics

Ceramic oxide compositions can generally be produced by thoroughly mixing the constituents as oxides or compounds (such as carbonates and nitrates), which readily decompose into oxides and calcines at the correct (material-specific) temperature, giving substantial interdiffusion of the cations. The calcine is then ground and compressed into the desired shape and sintered at a temperature a few hundred degrees above the calcination temperature.[8] For example, for the calcination of lead zirconate titanate [PZT: $Pb(Zr, Ti)O_3$], the raw materials PbO, TiO_2, and ZrO_2 are mixed in the molar ratio of 2:1:1, pressed into lumps, and then calcined in ambient air at 800°C to obtain the perovskite phase. The calcination temperature is of great value as it influences the density and, hence, the electromechanical properties of the final product. However, calcining PZT at $T > 800\,°C$ could cause lead (Pb) loss, resulting in detrimental effects on the electrical properties. Calcination at the appropriate temperature is, therefore, necessary to obtain the best electrical and mechanical properties. After calcining, the lumps are ground by milling. The green bodies should have a material-specific minimum density before they can be sintered. The desired shape and minimum green density can be acheived through various techniques including powder compaction, slip casting, and extrusion.

The choice of method depends on several factors, including the type of powder used, the particle size distribution, the state of agglomeration, the desired shape, and the thickness of the part. After shaping, the green bodies are

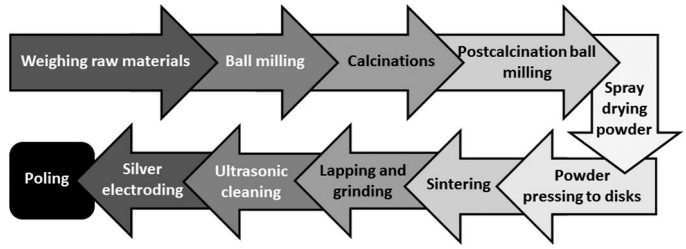

Figure 3.3 Flowchart of fabrication and processing of ferroelectric ceramics.

heated slowly to between 500 and 600 °C to remove any binder present. The binder burnout rate should be $\leq$ 1–2 °C/min in order to allow the gasses to exit slowly without forming cracks and blisters in the ceramic pieces. After the binder burnout is complete, the samples are raised to a higher temperature for sintering. The sintering temperature and time must be optimum to allow for proper densification without abnormal grain growth. The sintering of oxide ceramics must be carried out in an oxidizing atmosphere or in air. For ceramics containing lead (such as PZT, PT, PLZT, etc.), lead loss occurs at temperatures above 800 °C. In order to reduce lead loss during sintering, samples must be kept on a sealed crucible containing saturated vapor. Figure 3.3 is a flowchart showing the fabrication of ceramics and sample preparation for characterization.

3.4 Thin-Film Deposition

The fabrication of ferroelectrics began with simple thermal evaporation of $BaTiO_3$ by Feldman in 1955.[9] Since then, a number of deposition techniques have been developed. The various techniques can be classified into two categories: solution deposition and nonsolution deposition. This section provides a brief review of techniques for the fabrication of PZT films.

3.4.1 Nonsolution deposition

3.4.1.1 Sputtering technique

The convenience and high melting point of PZT materials used in sputtering methods [DC, RF magnetron, electron cyclotron resonance (ECR) magnetron, and ion beam], make it the most widely used technique for fabricating ferroelectric thin films.[10] During the sputtering process, the material is set as a sputtering target, serving as the cathode in the electric circuit. The substrates are placed on a grounded anode and positioned at a predetermined distance from the target. The target might consist of a series of individual elements aligned on a rotatable stage or a ceramic target that contains the required compositions.

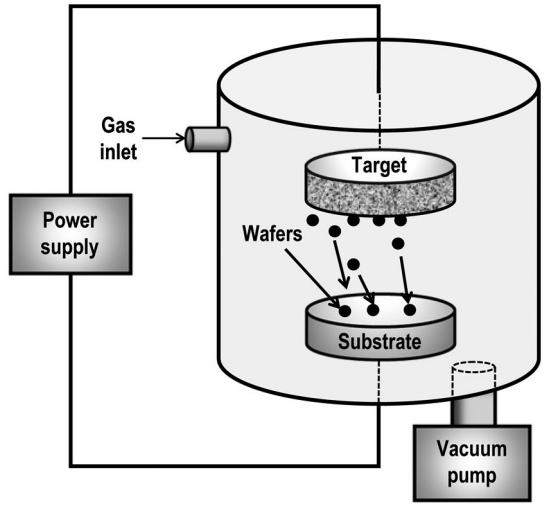

Figure 3.4 Schematic diagram of a simple sputtering system.

During the sputtering process, compositional ions are separated from the surface of the target and deposited on the substrates. Both cold and hot stages are used in the PZT film preparation. The major problem associated with the sputtering process is stoichiometric control because the sputter rate of each element is different. The basic concept of a sputtering principle is illustrated in Fig. 3.4.

3.4.1.2 Laser-ablation technique

Pulsed laser ablation deposition (PLAD) is a promising method for producing ferroelectric films because of its high deposition rate and stoichiometric control. This technique can be used to produce stoichiometric films even from a target material composed of five elements. Studies of PZT thin films have shown that the compositional–fluence uniformity and the target–substrate distance are the two major factors that affect PZT thin-film quality. The higher the fluence, the higher the deposition rate, but larger particles emitted from the target impair the quality of the films. To date, particulate-free PZT films have not been achieved through the PLAD technique.[11] A basic system setup used for fabricating thin films by PLAD is illustrated in Fig. 3.5.

3.4.1.3 Chemical-vapor-deposition technique

Chemical vapor deposition (CVD) involves the transportation of volatile compounds to the reaction chamber by carrier gas, where they are exposed to the substrates. Chemical reactions take place at or near the substrate surface, resulting in a solid phase that condenses on the substrates. The CVD process can be significantly improved by making use of energy sources such as a laser beam, electron beam, or ion beam. Formed by a focused energy source, the

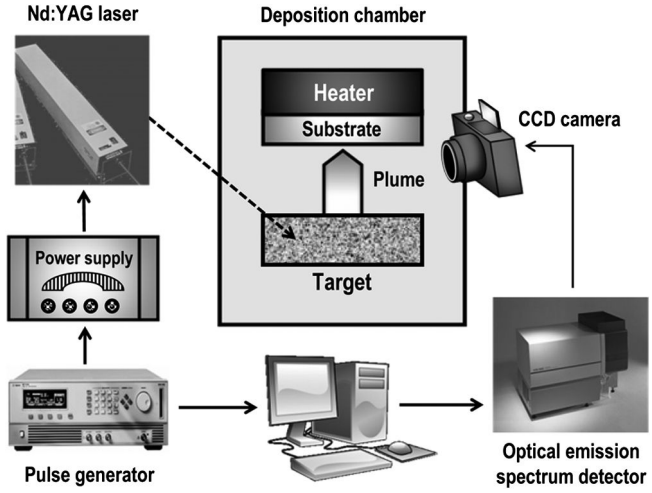

Figure 3.5 Experimental setup for the pulsed laser ablation deposition (PLAD) technique.

plasma accelerates the decomposition of gases and improves the quality of the films. Termed plasma-enhanced CVD (PECVD), this technique provides good-quality PZT films at low processing temperatures.[12] A schematic of a CVD apparatus is shown in Fig. 3.6.

The metalorganic CVD (MOCVD) technique uses metalorganic compounds as volatile reactants. Recently, interest in using this technique to fabricate PZT films has increased because of its usefulness and high potentiality, as well as the recent development of new source materials. The advantages of MOCVD include composition and crystalline structural control, a high growth rate, and significantly good step coverage.[13] By using the MOCVD technique, uniform PZT and PLZT thin films can be produced with less than a $\pm 1.5\%$ variation in film thickness on a 6- to 8-inch silicon wafer, and variations below 5% in both $Pb/(Zr + Ti)$ and $Zr/(Zr + Ti)$.[14]

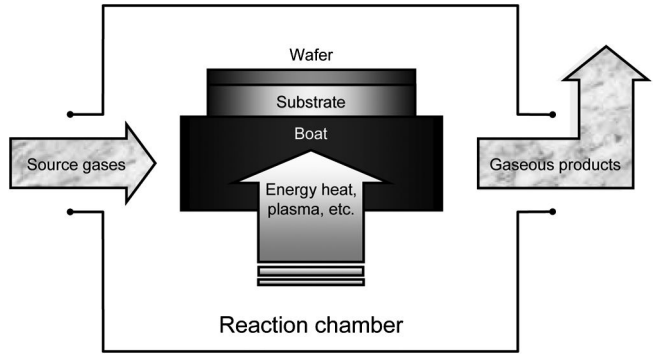

Figure 3.6 Chemical vapor deposition (CVD) process.

Auguer electron spectroscopy (AES) depth profiling indicates a uniform composition throughout the thickness of the PZT films.[15]

3.4.2 Solution deposition

A solution deposition technique enables excellent stoichiometric control of complex mixed oxide systems and is a fast, cost-efficient method for preparation of oxide thin films. The most commonly used solution techniques are sol gel and metalorganic deposition (MOD). In solution deposition for PZT films, metal-organic starting reagents are widely used as precursor compounds, including alkoxide $M(OR)_n$, where M is a metal element, and R is an alkyl group; carboxylate $[M(OOCR)_n]$; and β-biketonate $[MO_x(CH_3COCHCOCH_3)_n]$ with compounds of lead, zirconium, and titanium.[16–18]

3.4.2.1 Sol-gel technique

Sol-gel technology is one of the most popular methods for PZT thin-film deposition because of the advantages it offers, including high chemical purity, stoichiometric control, low-temperature processing, simple techniques, and microstructure control via chemical reactions. The basic steps in sol-gel processing involve the synthesis of a gel-precursor solution, or sol gel, and its application to a substrate using a spin- or dip-coating technique. The resulting gel layer is pyrolyzed to form an oxide ceramic film. In 1984, Fukushima and his colleagues were the first to report using sol-gel techniques to prepare PZT films.[19] They used butanol as the solvent for lead ethylhexanate, titanium tetrabutoxide, and zirconium acetalacetonate. Since then, great effort has been made to use the sol-gel technique to prepare PZT films. Thus far, sol-gel processes can be classified into two categories based on the following characteristics: (1) the use of 2-methoxyethanol as a reactant and solvent, and (2) hybrid processes using chelating ligands such as acetic acid or ethanolamine to reduce alkoxide reactivity.

In 2-methoxyethnol processing, metal–oxygen–metal bonds are formed as follows:

$$M(OR)_n + H_2O \rightarrow M(RO)_{n-1}(OH) + ROH,$$
$$2M(RO)_{n-1}(OH) \rightarrow M_2O(OR)_{2n-2} + H_2O,$$
$$M(OR)_n + M(OR)_{n-1}OH \rightarrow M_2O(OR)_{2n-2}(OH) + ROH.$$

A key step in 2-methoxyethanol processing is the substitution of methoxyethoxy with Ti- and Zr-propoxide starting reagents. This substitution produces a less-sensitive precursor solution. The substitution is performed as follows:

$$M(OR)_n + nR'OH \rightarrow M(OR')_n + nROH.$$

A hybrid process also utilizes alkoxide compounds as starting reagents but modifies the reaction with other reagents, such as acetic acid and

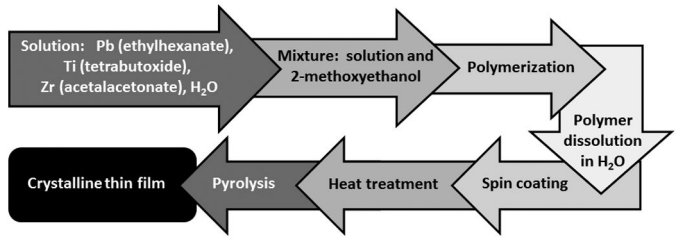

Figure 3.7 Flowchart of sol-gel processing of thin films.

acetylacetone diethanolamine. The key reaction is chelation for acetic acid as shown below:

$$M(OR)_n + xCH_3COOH \rightarrow M(OR)_{n\ x}(OOCCH_3)_x + xROH.$$

Acetic acid reduces the susceptibility of the starting reagent to hydrolysis and condensation. A flowchart representing the various processing steps for producing films (such as PZT films) is demonstrated in Fig. 3.7. A typical sol-gel process yields a single-layer PZT film of about 0.1-μm in thickness. In order to obtain thicker films (0.5 μm), multicoating is generally used. Tu and Milne modified the sol-gel technique/process using a diol-based sol-gel process for PZT-film deposition, obtaining 0.5-μm and thicker films in single coatings.[20,21] The resultant thicker films create a great advantage in film utilization in such applications as microactuators, pyroelectric sensors, and multilayer capacitors.

3.4.2.2 Metalorganic-deposition technique

The MOD method for thin-film fabrication has been recognized for more than one hundred years.[22] The process begins with the dissolving of precursor compounds in a proper solvent to obtain a true solution. The precursor solution is then coated onto a substrate though spin coating or spraying. The wet films are heated to remove any remaining solvent that did not evaporate during the deposition step, and then the organic films are pyrolyzed into inorganic films. If thicker film is required, the coating and pyrolysis processes are usually repeated several times until the required thickness is achieved. Finally, the films are postannealed to the desired crystalline phase, grain size, orientation, and oxygen content of the films.

The advantages of MOD are: (1) the desired cations are mixed at the molecular level; (2) it requires a low processing temperature; (3) the precursor solution is very stable in air; (4) in almost all cases, the deposition process can be conducted in air; and (5) the process is easily applicable to substrates of any size and shape. Recently, the MOD method has become a promising technique for oxide film preparation.

Precursor synthesis. In the molecular structure of precursor compounds using MOD, the ligands are bonded to the center metal ion through a heteroatom bridge. The bridge atom can be O, S, P, or N. A metalorganic compound diagram is:

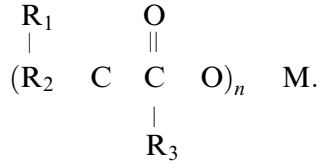

Because most of the metalorganic compounds suitable for oxide-film fabrication are not commercially available, the success of oxide-film fabrication from MOD processes strongly depends on the availability or synthesis of metalorganic compounds. So far, a number of methods have been developed to synthesize various metal precursors for producing oxide films through the MOD process, including: (1) double decomposition from ammonium soap, (2) neutralization, (3) metathesis reaction from metal acetate, and (4) metathesis reaction from metal alkoxide.

Metal carboxylates are the most commonly used beginning materials in the MOD process for oxide films. As with double decomposition reactions, metal carboxylate salts are synthesized through the reaction between the metal salt (typically hydrated nitrates or chlorides) and a preparation of the ammonium soap of carboxylic acid. The process is:

$$NH_4OH + RCOOH \rightarrow RCOONH_4 + H_2O$$

$$MX_n + nRCOONH_4 \rightarrow M(RCOO)_n + n(NH_4)x.$$

When the resultant metal carboxylate becomes solid particles, the powder is filtered and washed to separate the metal carboxylate from the solution. If the result is a liquid, the metal carboxylate can be extracted from the aqueous solution using a nonpolar solvent such as xylene or benzene.

Solvent process. In MOD, a liquid solution of organic compounds is prepared by the dissolution of metal precursors in a suitable solvent. The solvent should fulfill the following requirements: (1) high solvency for the precursors, (2) no interaction with the precursors, (3) adjustable viscosity, (4) adequate vapor pressure, (5) affordable, (6) nontoxic and noncorrosive.

Xylene and propionic acid are common solvents for an MOD process. In cases where a single solvent does not meet all of the requirements, mixed solvents are utilized. The combination of two or three solvents can greatly improve a mixed solvent's overall solvency. During the precursor solution preparation process, the order in which the precursor solvents are added to the mixture is very important because of the micelle nature of the soap solutions. In a thermodynamically stable state, micelles are aggregates of three or more

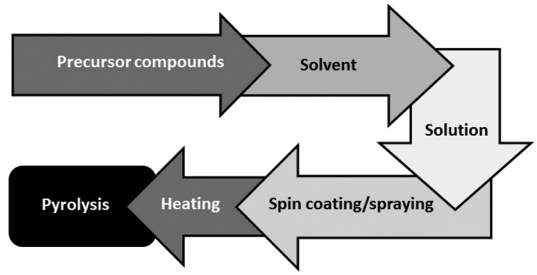

Figure 3.8 Flowchart of the metalorganic deposition method.

soap molecules existing in liquid.[23] The aggregation of polar carboxylate molecules can form a compact closed configuration rather than a linear chain configuration, thus producing a nonpolar structure. This results in the low viscosity of carboxylate soaps in low polarity solvents.

The advantage of a soap solution in organic solvents is its ability to dissolve certain compounds by enclosing the molecules in the core of the micelles. The polar carboxylate molecules are not dissolved in the solvent. For example, lanthanum acetate is difficult to dissolve in xylene but is easily dissolved in a xylene solution of titanium di-methoxy-neodecanoate. To achieve this, the order of precursor additions is important because it determines the types of micelles that exist in the solution and their solubility, thereby determining the solubility of the precursors in the solvent. In PZT film studies carried out by Sayer et al., it was found that in solution preparation, zirconium propoxide must be added before titanium isopropoxide to avoid the formation of mono or diacetylated products, which cause hydrolyzation to occur too quickly.[18] A typical process for fabricating films by MOD is represented in Fig. 3.8.

Pyrolysis processes. The pyrolysis process is the most important step in the metalorganic deposition process because it produces the microstructure of the film. The volume change of the film during this stage is typically very large, with ratios of 6/30 for deposited thickness to fired thickness. An inadequate heating rate during this phase can lead to various defects, such as cracks and voids in the fired film. Unfortunately, there is no standard for selecting an optimized heating rate. Spinning is the most commonly used technique for depositing a uniform coating on a substrate in the MOD process. After spin coating, the green organic films are usually heat treated in air or oxygen at 300–500 °C to remove any remaining solvent that did not evaporate during the deposition step and to convert the organic film into an inorganic film. Homogeneous thermal decomposition is critical in order to avoid elemental

separation and to form uniform phases and properties in a multicomponent system. The thermal decomposition of carboxylates is suggested to be a free-radical mechanism. According to this mechanism, decomposition reactions go through the following three steps: (1) generation of the free radicals by thermal fission, (2) fragmentation and/or rearrangement of organic ligand, and (3) oxidation of fission fragments of organic ligands by an oxidative chain reaction. In a mixture of metalorganic compounds, the free radicals generated by the decomposition of the least-stable metalorganic compound triggers the decomposition of the other precursors if their decomposition temperatures are not too different. This effect lowers the overall decomposition temperature, as compared to that of the individual components in the system.

PZT films by MOD. So far, the PZT films prepared by the MOD technique are comparable to those fabricated by other techniques. Among the precursors used for MOD, metal neopentanoate, neoctanoate, and neodecanoate salts are the most commonly used precursor compounds. Xylene, propionic acid, and butanol are the most widely used solvents. Vest and Zu used lead 2-ethylhexanoate [$Pb(C_7H_{15}COO)_2$], titanium di-methoxy dineodecanoate [$Ti(OCH_3)_2(C_9H_{19}COO)_2$], and zirconium octanoate [$Zr(C_7H_{15}COO)_4$] as precursor compounds for preparing PZT films. Xylene was used as the solvent for each, and the remnant polarization of the PZT films was $P_r = 25\ \mu C/cm^2$ with a dielectric constant of 600.[17]

Klee et al. used lead 2-ethylhexanoate, Ti-tetra-*n*-butylate, and Zr-acetylacetonate as starting compounds and butanol as the solvent to prepare PZT films.[24] They found that due to the high carbon content of MOD films, a high weight loss occurred during annealing. High weight loss is usually accompanied by a large volume change, which causes cracking problems. Their results suggest that MOD-derived films crystallize into a single-phase perovskite phase at a lower temperature than in the sol-gel processes. In order to minimize the cracking problem, Haertling used short-chain carboxylate and β-diketonate as precursors.[25] The precursor solution not only showed an improved aging rate, but also less film cracking due to the small shrinkage associated with lower-organic-content precursors.

In most of the thin-film deposition techniques, the as-deposited PZT films have an amorphous structure. Postannealing is, therefore, necessary to convert this amorphous phase into the desired ferroelectric perovskite phase. A typical microstructure for PZT films is a rosette-type structure, where the rosette-like or spherulitic grains (perovskite phase) coexist with a nanocrystalline matrix (pyrochlore phase).[26,27] The existence of the pyrochlore phase in the PZT films is attributed to the loss of PbO during the phase evolution, a loss that inhibits the pyrochlore-to-perovskite phase transformation. It is

widely accepted that pyrochlore has a cubic structure with a formulation of $A_2B_2O_{7-x}$, richer in Zr and more deficient in Pb than the perovskite structure.

Two explanations have been suggested to explain the mixed-phase structure of PZT films. One suggestion is that as deposited amorphous films first crystallize in a fine-grained intermediate nonferroelectric pyrochlore phase, the pyrochlore phase is converted into the perovskite phase during high-temperature treatment. Because of the high surface-to-volume ratio, the evaporation of Pb from PZT films is favored during the postannealling process. The consequence is the presence of the Pb-deficient pyrochlore phase in the films. The composition deviation of the pyrochlore phase from the ABO_3 stoichiometry increases with temperature and the time span of annealing, and depends on the substrate. Another explanation is that the amorphous films become a two-phase structure due to simultaneous crystallization of both pyrochlore and perovskite phases at high temperatures.

Studies have shown that, depending on the film's composition, the amorphous-to-pyrochlore phase transformation takes place in the temperature range of 400–550 °C, whereas the transformation between the pyrochlore perovskite phases occurs at 450 °C. The transformation between pyrochlore perovskite phases is a nucleation-controlled process. The activation energies of the 53/47-type PZT are 441 KJ/mol for nucleation and 112 KJ/mol for growth.[28,29] The volume change accompanying the pyrochlore-to-perovskite formation is ~13%.[30] Microstructure studies also demonstrate that the Zr-rich films not only have a larger grain size but are also more pyrochlore-phase attributing, due to a higher nucleation barrier and the high tendency of Zr to form the pyrochlore phase.[29]

3.5 Thick-Film Fabrication

3.5.1 Thick-film-transfer technology (screen printing)

In this method, screen-printing ink and organic ingredients containing solvent, dispersing agent, and plasticizer are first incorporated with the binder and then blended. The active pyroelectric powder is subsequently added and mixed. In order to screen print, a desired mask (screen) is placed over all but the printing substrate. A squeegee held at a 45-deg angle is placed on the screen behind the ink dollop and smoothly moved in an orthogonal direction across the entire substrate with minimal downward force. The screen is then gently lifted away from the substrate. Next, the sample is removed from the fixture and allowed to rest for 10 min, after which, it is dried on a hot plate at 100 °C for 15 min. The process is repeated to add additional layers onto the

substrate. After the final coating, the film is sintered at an appropriate temperature and for a proper amount of time. A detailed description of a laboratory screen-printing apparatus and the process for fabricating PZT films on various substrates is described by A. K. Batra et al.[31] Besides the techniques cited above, ferroelectric films have also been fabricated using various other methods (e.g., spray coating, rapid quenching, jet printing, aerosol deposition, and gas deposition).[32–36]

3.6 Fabrication of Polymer–Ceramic Composite Precursors

Fabrication of 0-3 connectivity composites is simple, allowing for commercial production of these composites in a cost-effective manner.[37] As a result, most composites are fabricated as active pyroelectric and polymer-based diphasic samples. Composites involving simple fabrication methods that have shown promising results are described in this section. Polymer components can be either polar or nonpolar. A popular alternative approach is to use the sol-gel synthesis method. Preparation of a 0-3-connectivity composite consists of mixing the ceramic particles in a hot rolling mill with softened thermoplastic polymer, followed by producing thin-film composites by high-pressure casting at the softening temperature of the polymer. With a thermoset polymer such as epoxy, the mixing can be done at room temperature with the correct proportion of resin, hardener, and ceramic powder.[37,38]

In solvent casting, a polymer is first dissolved in a suitable solvent, then an electroactive ceramic powder is added and mixed/dispersed. That mixture is then stored in a suitable container for evaporatation. After evaporation, the resultant film is hot pressed at the crystallization temperature of the polymer. Problems linked to poor distribution of the ceramic inclusions (poor adhesion of component phases, or air bubbles in the composites) are remedied during the mixing operation. An agglomeration of ceramic particles present in the solution may be overcome by lowering the polymer viscosity via heating during the ultrasonic mixing process. A typical procedure for preparing a P(VDF-TrFE):PZT composite involving the use of spin coating in the fabrication of 0-3 connectivity composites is: (1) dissolve a suitable amount of the polymer P(VDF-TrFE) in methyl-ethyl-ketone (MEK) to form a solution (P mix), (2) add a requisite amount of nanoceramic (PZT) powder, (3) ultrasonically agitate the mixture for several hours to break-up the agglomerates and disperse the ceramic powder uniformly in the copolymer solution; (4) deposit a thin film of this composite solution (nP mix) on a conducting electrode substrate using a spin-coating technique; (5) anneal the film for 2–3 h in air at 130 °C; and (6) deposit the top electrode on the film for testing.[39–41] The steps involved in fabricating films with nP mix by spin coating are illustrated in Fig. 3.9. A flowchart representing the various steps involved in fabricating composite films is shown in Fig. 3.10.

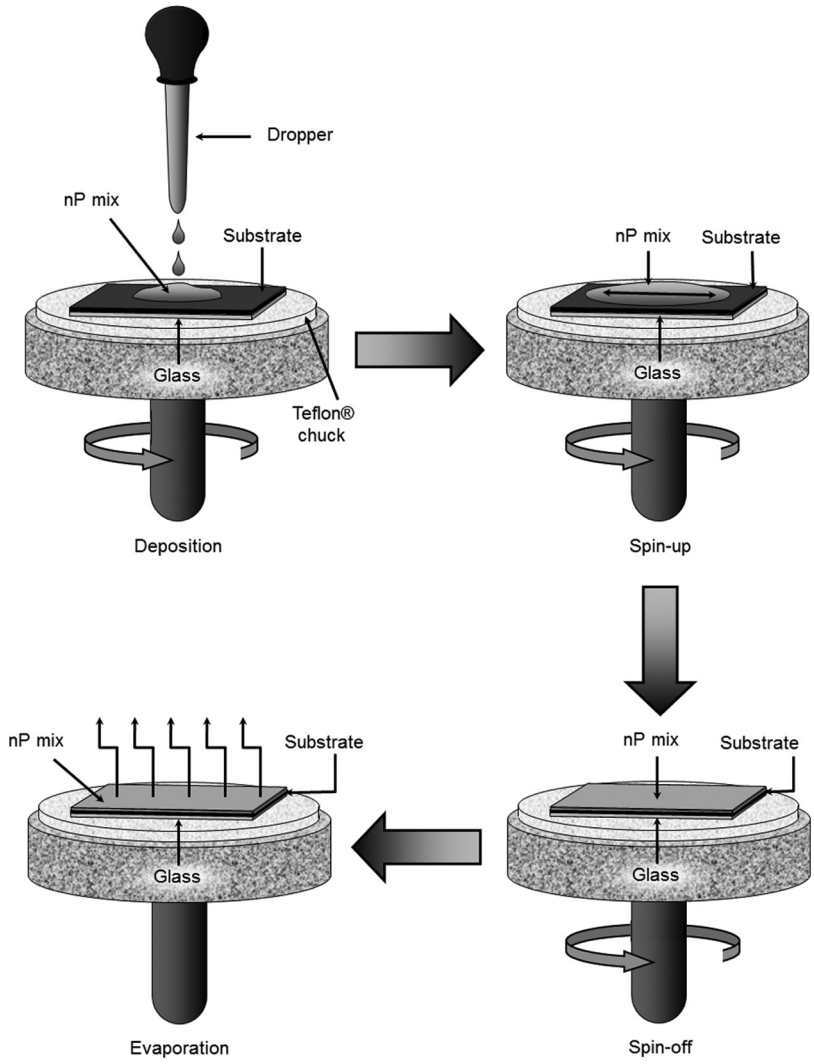

Figure 3.9 Spin-coating technique processing steps.

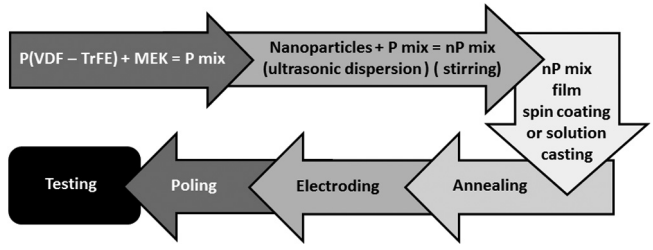

Figure 3.10 Flowchart of the fabrication of polymer-ceramic composite films.

References

1. M. D. Aggarwal, J. R. Currie, B. G. Penn, A. K. Batra, and R. B. Lal, "Solution growth and characterization of single crystals on Earth and in microgravity," NASA **NASA/TM-2007-215187** (2007).
2. B. Brezina, M. Havrankova, and M. Vasa, "Enhanced growth of non-polar {001} growth sectors of deuterated triglycine sulfate doped with L-alanine (LADTGS)," *Crystal Research Technology* **27**(1), 13–20 (1992).
3. S. Satapathy, S. K. Sharma, A. K. Karnal, and V. K. Wadhawan, "Effects of seed orientation on the growth of TGS crystals with large (010) facets needed for detector applications," *J. Crystal Growth* **240**, 196–202 (2002).
4. M. Banan, "Growth of Pure and Doped Triglycine Sulfate Crystals for Pyroelectric IR Detector Applications," M.S. Thesis, Alabama A & M University, Normal, Alabama (1986).
5. Z. D. Deng, "A new method of growth ferroelectrics crystal," *Ferroelectrics* **39**, 1237–1379 (1981).
6. E. Diéguez, J. L. Plaza, M. D. Aggarwal, and A. K. Batra, "Czochralski growth of oxide photorefractive crystals," in *Handbook of Crystal Growth*, Springer, New York, pp. 245–280 (2010).
7. Y. Xu, *Ferroelectric Materials and Their Applications*, North-Holland, London, pp. 217–231 (1991).
8. A. J. Moulson and J. M. Herbert, *Electroceramics*, Wiley, England, pp. 361–381 (2003).
9. C. Y. Feldman, "Formation of the thin films by $BaTi0_3$ by evaporation," *Rev. Sci. Inst.* **26**(5), 463–465 (1955).
10. L. O. Auciello, A. I. Kingon, and S. B. Krupanidhi, "Sputtering synthesis of ferroelectric films and heterostructures," *MRS Bulletin* **21**(6), 25–30 (1996).
11. L. O. Auciello and R. Ramesh, "Laser-ablation deposition and characterization of ferroelectric capacitors for nonvolatile memories," *MRS Bulletin* **21**(6), 31–36 (1996).
12. M. de Keijser, "Chemical vapor deposition of electroceramic thin films," *MRS Bulletin* **21**(6), 37–43 (1996).
13. M. Shimizu and T. Shiosak, "MOCVD of ferroelectric PZT and PLZT thin films for memory device applications in ferroelectric thin films," *Proc. Materials Research Society* **361**, 295–361 (1994).
14. M. de Keijser, P. J. van Veldhoven, and G. J. M. Dormans, "Organometallic chemical vapor deposition of lead zirconate titanate," in *Science and Technology of Electroceramic Thin Films*, L. O. Auciello

and R. Waser, Eds., NATO Kluwer Academic Publishers, *Science Series E* **284**, 75 (1995).

15. Y. Gao and B. A. Tuttle, "Growth and characterization $PbTiO_3$ and PZT thin films by MOCVD in ferroelectric thin films," *Proc. Materials Research Society* **310**, 361–337 (1994).
16. K. D. Budd, S. K. Dey, and D. A. Payne, "Sol-gel processing of PT, PZ, PZT, and PLZT thin films," *Proc. British Ceramic Society* **36**, 107–121 (1985).
17. R. W. Vest and W. Zhu, "Films of 64/40 PZT by the MOD process for memory applications," *Ferroelectrics* **119**, 61–75 (1991).
18. G. Yi, Z. Wu, and M. Sayer, "Preparation of $Pb(Zr,Ti)O_3$ thin films by sol gel processing: electrical, optical, and electro-optic properties," *J. Applied Physics* **64**(5), 271–274 (1988).
19. J. Fukushima, K. Kodaira, and T. Matsushita, "PZT films by sol-gel," *J. Materials Science* **19**, 596–601 (1984).
20. Y. L. Tu and S. J. Milne, "Characterization of single layer PZT (53/47) films prepared from an air-stable sol-gel route," *J. Materials Research* **10**(12), 3222–3231 (1995).
21. Y. L. Tu and S. T. Milne, "A study of the effect of process variables on the properties of PZT films produced by a single layer sol-gel technique route," *J. Materials Science* **30**, pp. 2507–2516 (1995).
22. J. Huang, "Microstructure and Properties of Zr-rich $Pb(Z_xTi_{1-x})O_3$ Thin Films Prepared by Metallo-organic Deposition Technique," Ph.D. Thesis, University of Cincinnati, Ohio (1997).
23. N. Pilpel, "Properties of organic solution heavy metal soaps," *Chem. Review* **63**, 221–225 (1963).
24. M. Klee, R. Eusemann, W. Wiser, and W. Brand, "Processing and electrical properties of Pb $(Zr_xTi_{1-x})O_3$ ($x = 0.2$–0.75) films: comparison of metallo-organic decomposition and sol-gel processes," *J. Applied Physics* **72**(4), 1566–1576 (1992).
25. G. H. Haertling, "PLZT thin films prepared from acetate precursors," *Ferroelectrics* **119**, 51–56 (1991).
26. B. A. Tuttle, T. J. Headley, R. W. Bunker, R. W. Schwartz, T. J. Zender, C. L. Hernandez, D. C. Goodnow, R. J. Tissot, and J. Michael, "Microstructure evolution of PZT thin films prepared by hybrid metalorganic deposition," *J. Materials Research* **7**(7), 5007–5013 (1992).
27. A. H. Carim, B. A. Tuttle, D. H. Doughty, and S. L. Martinez, "Microstructure of solution-process PZT thin film," *J. Am.Ceram. Soc.* **74**(6), 1455–1458 (1991).
28. C. K. Kwok and S. B. Desu, "Seeding layer for PZT films," *J. Materials Research* **8**, 339–344 (1993).

29. C. K. Kwok and S. B. Desu, "Transmission electron microscopy study of PZT thin films," in *Ceramic Transactions, Ferroelectric Films*, A. Bhalla and K. M. Nair, Eds., *J. Am. Ceram. Soc.* **23**, 73–84 (1992).
30. J. A. Voigt, B. A. Tuttle, T. J. Headley, and D. L. Lamppa, "The pyrochlore-to-perovskite transformation in solution-derived lead zirconate titanate thin films," *Materials Research Society Proc.* **361**, 361–395 (1994).
31. A. K. Batra, M. A. Alim, J. R. Currie, and M. D. Aggarwal, "The electrical response of the modified lead titanate based thick-films," *Physica B* **404**, 1905–1911 (2009).
32. M. Ichiki, L. Zhang, Z. Yang, T. Ikehara, and R. Maeda, "Lead zirconate titanate film formation with spray coating method," *Jpn. J. Appl. Phys.* **42**, 5927–5930 (2003).
33. S. Kang, H. Kim, K. Takahashi, K. Yukino, M. Tsukioka, and F. Okamura, "Preparation of modified lead zinc niobate compound thick films by rapid quenching," *Jpn. J. Appl. Phys.* **32**, 4254–4257 (1993).
34. H. Adachi, Y. Kuroda, T. Imahashi, and K. Yanagisawa, "Preparation of piezoelectric thick film using a jet print system," *Jpn. J. Appl. Phys.* **36**, 1159–1163 (1997).
35. J. Akedo and M. Lebedev, "Effect of annealing poling conditions on piezoelectric properties of PZT thick films by aerosol deposition method," *J. Crystal Growth* **235**, 415–420 (2002).
36. M. Ichiki, J. Akedo, A. Schroth, R. Maeda, and Y. Ishikawa, "X-ray diffraction and scanning electron microscopy observation of PZT thick film formed gas deposition method," *Jpn. J. Appl. Phys.* **36**, 5815–5819 (1997).
37. C. J. Dias and D. K. Das-Gupta, "Inorganic ceramic/polymer ferroelectric composite electrets," *IEEE Trans. Diel. Elect. Ins.* **3**(5), 706–734 (1996).
38. S. B. Lang and D. K. Das-Gupta, "Pyroelectricity: fundamentals and applications," *Ferroelectrics Review* **2**(4), 217–354 (2000).
39. P. Guggilla, "Studies on Pyroelectric Materials for IR Sensor Application," Ph.D. Thesis, Alabama A & M University, Normal, Alabama (2007).
40. P. Guggilla, A. K. Batra, M. D. Aggarwal, and R. B. Lal, "Investigation on nanocomposites for pyroelectric IR sensors," *Proc. SPIE* **5724**, 295–297 (2005) [doi: 10.1117/12.592233].
41. P. Guggilla and A. K. Batra, "0-3 composite film preparation" Alabama A & M University, Normal, Alabama, unpublished.

Chapter 4
Important Pyroelectrics: Properties and Performance Parameters

4.1 Introduction

Important pyroelectric materials described in this chapter include: triglycine sulfate (TGS); lead (Pb) zirconate titanate, $PbZrTiO_3$ (PZT); Pb titanate, $PbTiO_3$ (PT); lead magnesium niobate-lead titanate (PMN-PT); polyvinylidene fluoride (PVDF); lithium (Li) tantalate, $LiTaO_3$ (LT); composites; lead-free ceramics; and others.

4.2 Important Pyroelectrics

4.2.1 Triglycine sulfate crystals and their isomorphs

The TGS family, chemical formula $(NH_2CH_2COOH)_3{\cdot}H_2SO_4$, is a well-known ferroelectric material used in room-temperature IR detector applications.[1] Pyroelectric detectors based on TGS are uniformly sensitive to radiation in the wavelengths ranging from UV to far IR and do not require cooling, unlike quantum detectors. The structure of TGS crystals is monoclinic below Curie temperature (49 °C). There are two chemical formulas in the elementary cell of the lattice. The crystal is monoclinic with a space group of $P2_1$ in the ferroelectric phase. Above the Curie temperature, in the paraelectric phase, there are two mirror planes m at $y = ¼$ and ¾ and a space group of $P2_{1/m}$. The ferroelectric effect is associated with an asymmetrical arrangement of the glycine group G I in which the mirror plane m and the proton exchange between glycine groups G II and G III. The proton exchange is associated with the exchange role of zwitterions between two groups.[1] b-cut/(010) (also a cleavage plane) crystals are used for detector fabrication.

Single crystals of TGS are usually grown from aqueous solution by method of temperature lowering or solution evaporation.[2 7] TGS crystals containing additions of ethyl alcohol and weighing more than 100 grams have also been grown from solution.[8] When mixing alcohol in an aqueous solution of TGS, part of the solution's water associates with the alcohol, thereby concentrating the solution. In this manner, supersaturation can be controlled to a certain degree, making it easier to grow a TGS crystal such as that shown in Fig. 4.1.

TGS-family-based IR detectors provide the highest voltage responsivity. However, handling difficulties associated with their water solubility, hygroscopic nature, and fragility have confined their use to single-element detectors and vidicons where sensitivity is the primary concern. Furthermore, these crystals depole, and their operational temperature range is limited. Many modifications have been proposed and evaluated for their effectiveness at increasing the limited usage of TGS crystals while maintaining the same

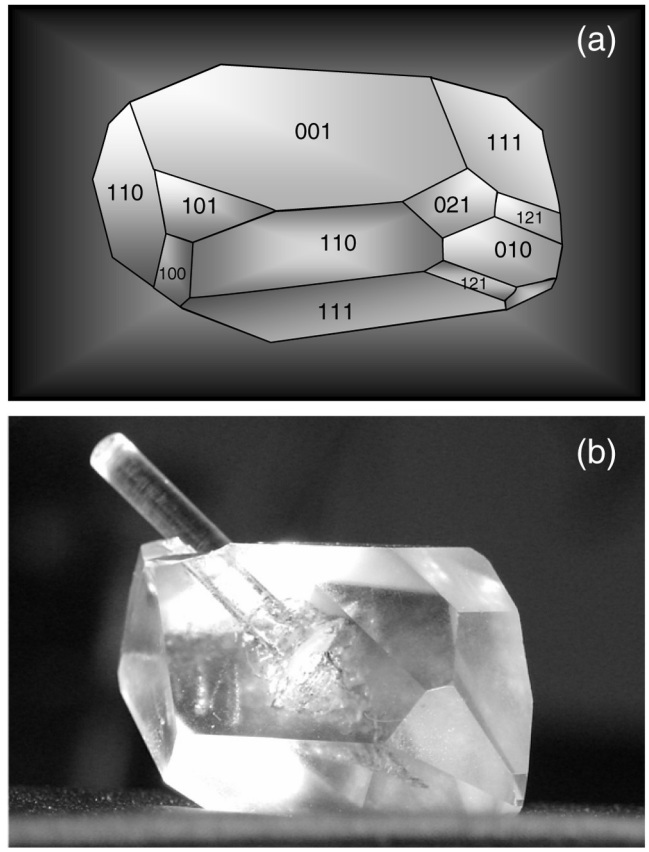

Figure 4.1 (a) A diagram of normal crystal growth, and (b) a photograph of a TGS crystal grown at AAMU.

basic structure in pyroelectric IR detection applications. Modifications include: (1) deuteration of TGS (DTGS); (2) substitution of fluoroberyllic acid for sulfuric acid to obtain triglycine fluoroberyllate (TGFB) and its deuteration, DTGFB; (3) substitution of selenic acid for sulfuric acid to obtain triglycine selenate (TGSe); (4) doping with cations such as Li, Mn, Cd, Zn, or Cu to obtain LiTGS, MnTGS, CdTGS, ZnTGS, or CuTGS, respectively; (5) substitution of L-alanine (LATGS) for glycine and simultaneous doping with cations such as Ni, Cr, or Cs and L-alanine to obtain NiLATGS, CrLATGS, or CsLATGS, respectively.[1]

The alanine molecules within L-alanine create an internal electric field because they contain an extra methyl group that prevents them from rotating within the lattice. The internal electric field produces poled TGS crystals, thereby leading to stabilization of spontaneous polarization. As a result, the dipoles are fixed with respect to the crystal structure and do not disappear at Curie temperature. LATGS crystals can be thermally cycled through the Curie temperature and retain their spontaneous polarization, thereby avoiding the poling process. There is an associated increase in the performance figures of merit, depending on the L-alanine content in the TGS lattice. However, growth yield is not 100%, and crystals usually crack during polishing. Also, uniform doping of L-alanine in the TGS lattice is difficult to acheive. Table 3.1 compares the performance figures of merit for modified TGS crystals at their optimum/room temperature to pure TGS crystals. From the information contained in this table, it can be inferred that deuteration of TGS provides a marked improvement to the voltage responsivity and, depending on the deuteration level, increases the Curie temperature to 60 °C, thereby increasing the temperature range of detector operation.

Bye and Keve studied the pyroelectric properties of x-ray-irradiated/field-treated TGS detectors and compared these with LATGS detectors.[9] Improvements in the figures of merit for x-ray irradiated/field-treated TGS detectors were comparable with those of L-alanine-doped TGS detectors. In this case, uniformity in properties and yield for large-area crystals was 100%. Therefore, the authors proposed that a small-area, single-element detector be manufactured from LATGS, whereas an x-ray irradiated/field-treated TGS would be required for thermal imaging applications requiring large areas of uniform properties.

A marginal improvement in the performance figures of merit has also been achieved by doping with cations. Loiacono and Dougherty suggested that higher concentrations of Zn, Cd, or Cu would give promising results.[10] Encouraging results have been reported regarding crystals grown from solutions doped with L-alanine and cations such as Cs, Ni, or Cr, where a marked increase can be seen in the performance figures of merit. Furthermore, Cs and alanine doping (CsLATGS) produce more uniformly doped crystals as is evident from the shape of the hysteresis loop compared with that of

LATGS. However, the growth yield of these crystals is lower than that of pure TGS crystals. Recently, TGS crystals doped with organic molecules, such as L-lysine, urea, urea + L-alanine, thiourea, guanidine, and others, have had encouraging results.[11 16] Both a higher performance and an increase in range of operational temperature have been shown with TGFB and DTGFB, but the growth and processing of these crystals is dangerous due to the presence of toxic beryllium.

It has been reported that large anisotropy in the principal dielectric constant tensor coefficients can be used to obtain an improved F_V in the TGS crystal family by making oblique crystal cuts, resulting in the normal electroded faces of the detector no longer being parallel to the polar axis.[17 19] This is because an effective pyroelectric coefficient exhibits a cosine dependence on the angle of rotation, while a dielectric constant depends on a cosine-squared relationship. A factor of two improvements can be obtained in F_V by cutting the crystal at an optimum angle.

Various alternative techniques to the long crystal growth processes have been explored for thin film preparation, including lapping and polishing to thin slices of crystals. Whipps and Bye have prepared thin polycrystalline films by using sedimentation from a fluid suspension of freeze-dried crystallites of TGS on glass slices and compressing to remove porosity.[20] However, the pyroelectric performance of films prepared in this manner was lower than that from single-crystal devices of similar dimensions.[21] Hadni et al. developed a technique by which oriented thin films of TGS can be grown by nucleation of crystals in an array of submicroscopic holes etched in a substrate.[22] Hadni and Thomas have shown that it is possible to make a pyroelectric detector by growing an epitaxial layer of TGS on a gold electrode with a thickness smaller than one μm.[23] The pyroelectric detectivity, in this case, was found to be better than that of a bulk TGS detector at 40 °C. The authors have also shown that the detectivity of triglycine selenate (TGSe) epitaxial detector grown on bulk TGS crystal is six times better than the best detector made under similar conditions by Mullard in the UK. Recently, an alternative fabrication technique for nano-composite crystallographically oriented thin films of TGS with functional properties has been demonstrated.[24] The films were fabricated by controlled growth of TGS nano crystals inside an array of aluminium oxide cylindrical nanopores.

A seen in Table 4.1, crystal selection depends on the required application. For high-current-responsivity applications, TGSe-based devices are advantageous. For high-voltage and detectivity applications at room temperature, various doped crystals, such as LATGS, NiLATGS, CsLATGS, and ATGSP/As are more useful. For a wide range of high-temperature operational applications, DTGFB seems more promising than TGS. However, actual use of these experimental crystals in an IR detector or vidicon tube will determine if the predicted improvement in the signal-to-noise ratio is realized.

Table 4.1 Material characteristics and figures of merit for modified TGS crystals.[1–19]

Crystals	Temperature measured (°C)	F_I p ($10^{-5} \times Cm^{-2} °C^{-1}$)	ε'	F_V p/ε' ($10^{-5} \times Cm^{-2} °C^{-1}$)	F_D $p/\sqrt{\varepsilon''}$ ($10^{-5} \times Cm^{-2} °C^{-1}$)
TGS	Room temp.	16 45	20 100	0.5 1.14	0.4 121.0
DTGS	25.0	25 70	18 22.5	~1.4	
LATGS	25.0	22 70	26 35	~0.88 2.0	31.8 92.5
Field x ray treated TGS	21.0	38	26	1.4	41.3
DLATGS	25.0	25	22	1.13	
LiTGS	Room temp.	40	40	1.0	
MnTGS	Room temp.	56	40	1.4	
CdTGS	40.0			1.28	
CuTGS	40.0			1.28	
ZnTGS	40.0			1.41	
CrLATGS	35.0	50	40	1.25	179.7
NiLATGS	35.0	82	51	1.8	213.0
CaLATGS	35.0	134	41	3.26	189.5
ATGSP	25.0	65	30 32	2.0	155.5
ATGSAs	25.0	70	32	2.1 2.3	
ADTGSP	25.0	27.5	23	1.19	
TGFB	60.0	70	50	1.4	
ATGAs	25.0	70	32	2.18	
TGPS	Optimum temp.	21 25	14 15	1.5	
DTGPS	Optimum temp.	19 25	11 14	2.0	
TGSe	21.0	420	420	1.0	40.0
Oblique cut TGS	35.0			~1.7	
Oblique cut ADTGSP	35.0			~1.9	

4.2.2 Modified lead titanate

Before discussing the properties of lead titanate, it is important to describe the perovskite family of crystals. This family consists of oxygen octahedral ferroelectrics with the general formula of ABO_3, where O is oxygen and A is a cation with larger ionic radius than cation B. This structure can be described as a 3D network of corner-sharing BO_6 octahedra containing a twelve-fold coordinated site occupied by A cations. The A and B cations can contain a wide range of ions in order to provide ferroelectric structure. Most ferroelectrics with a perovskite-type structure are compounds of either $A^{2+}B^{4+}O_3^{2-}$ or $A^{1+}B^{5+}O_3^{2-}$-type formula. Most of the useful ceramics have perovskite structure, such as: barium titanate ($BaTiO_3$), lead titanate ($PbTiO_3$), lead zirconate titanate ($PbZr_{1-x}Ti_xO_3$, abbreviated as PZT), lead lanthanum zirconate titanate (PLZT), potassium niobate ($KNbO_3$, abbreviated as KN),

potassium sodium niobate ($K_xNa_{1-x}NbO_3$, abbreviated as KNN), and potassium tantalate niobate ($KTa_xNb_{1-x}O_3$, abbreviated as KTN).[25]

Two groups of perovskites have been extensively studied for their pyroelectric properties: (1) rhombohedral structures based on modified lead zirconate (PZ), and (2) tetragonal structures based on modified lead titanate (PT). A small single crystal can be grown from a variety of fluxes in both cases. Most studies have been conducted on ceramics because ceramics offer a number of advantages over other candidate crystalline materials. These advantages include: (1) they have a low manufacturing cost in large areas using standard mixed-oxide processes; (2) they are both mechanically and chemically robust; (3) they can be processed into thin wafers; (4) they possess a high Curie temperature, allowing for high-temperature operation; and (5) they can be modified to control important parameters—such as the pyroelectric coefficient, dielectric constant and loss, Curie temperature, electrical impedance, and mechanical properties—through the introduction of selected dopants into the lattice.[26] A unit cell of a PZT ABO_3 structure is shown in Fig. 4.2.

$PbTiO_3$ is a ferroelectric that possesses a tetragonal structure at room temperature, a high Curie point (490 °C), and a high spontaneous polarization (up to 75 μCcm^{-2}).[27] Although growth from single crystals by flux and top-seeded solution is possible, growth of crystals more than 1 cm in size is very difficult, thereby restricting the material to ceramic form for practical use. High spontaneous lattice strain associated with the phase transition makes the fabrication of pure $PbTiO_3$ ceramics impractical because they are mechanically unstable at room temperature. A wide range of dopants has been

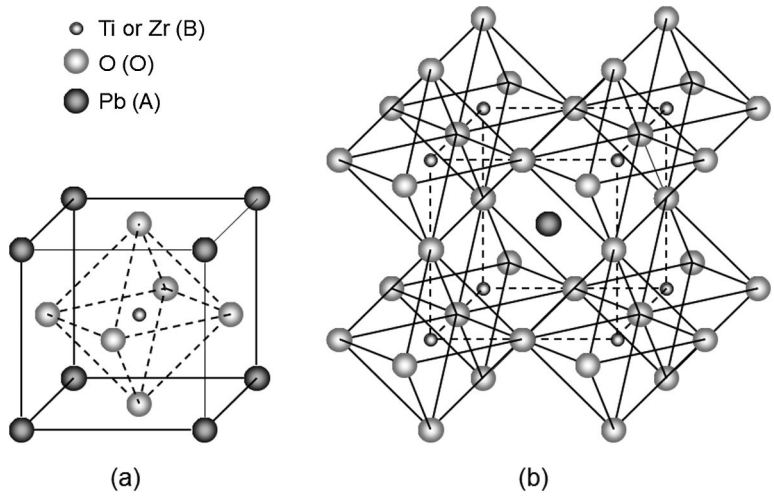

Figure 4.2 Unit cell of a PZT ABO_3 structure: (a) a cubic model and (b) a polyhedral model.

explored in an effort to stabilize properties of pure $PbTiO_3$ ceramics including manganese and rare earths.

$Pb_{1.05\ x}\ La_x\ Ti_{1\ \ x/4}O_3$ ($x = 0 - 0.2$) thin films were obtained by a screen-printing method on Au bottom electrodes using Si (l00) substrates at the annealing temperature of 600 °C. The maximum pyroelectric coefficient of 1.07×10^{-8} C/cm^{2}K was obtained at $x = 0.1$ after poling.[28] Diffusion levels of (Pb, La) TiO_3 to the Au and Pt electrodes were equal. Therefore, Au electrodes for these films can be prepared at a low cost for practical use by screen printing.

Lanthanum-modified lead titanate thin films with different La contents were fabricated on a Pt/Ti/SiO_2/Si substrate using the sol-gel method. The pyroelectric coefficients were 1.3 to 2.5×10^{-5} C/m^{2}K and increased as La content increased.[29] Pyroelectric lead titanate ($PbTiO_3$) thin films deposited by sol-gel processing have been characterized for possible use in microsensor applications. Based on a comparison with other IC-compatible pyroelectric materials' relevant properties, $PbTiO_3$ possesses a very high pyroelectric coefficient over a wide operating temperature range. The measured pyroelectric coefficient for $PbTiO_3$ films at 297 K, with thicknesses ranging from 0.2 to 0.6 μm, is 75 to 96×10^{-5} C/m^{2}K. Research efforts have attempted to integrate pyroelectric material into a micromachined membrane structure.[30] A key advantage of this type of composite structure is its low thermal mass, which is useful in high-sensitivity pyroelectric detection. The measured blackbody voltage responsivity of $PbTiO_3$ is 2.2×10^4 V/W for a pyroelectric element with an active area of 4×10^{-4} m^2 at 297 K with a chopping frequency of 100 Hz. Normalized detectivity D^* at 100 Hz is 1.0×10^9 cmHz$^{1/2}$/W. Response time (measured by the pulsed laser-beam method) for a device with an area ranging from 2×10^{-6} to 7×10^{-4} cm^2 is 2–20 μs.

Investigations have been conducted in the deposition of single-phase perovskite lead titanate thin films by planar multitarget sputtering on silicon substrates covered with a thin Pt bottom electrode.[31] These films exhibited almost random crystallographic orientation. The films are self-polarized, meaning that they exhibited pyroelectric currents without poling treatment. Their pyroelectric coefficient was 1.7×10^{-4} C/m^{2}K after additional furnace annealing and poling. Annealing also reduced dielectric loss tanδ from 0.05 to 0.01.

Thin films in the PCT (Pb, Ca:TiO_3) system have been successfully prepared by sol-gel processing on indium tinoxide (ITO)-coated 6059 glass substrates.[32] The perovskite phase of PCT is formed with a polycrystalline tetragonal structure at 650 °C. The electrical properties of these films have been characterized and ferroelectric hysteresis loops observed. The pyroelectric coefficient and figures of merit have been calculated, with the observation that the PCT films exhibit very good pyroelectric properties. PCT 76/24

is expected to provide high IR-detector performance due to its high voltage-responsivity value, high detectivity, and comparatively smaller value of dielectric constant and loss tangent than lead titanate.

Chang and Lai utilized RF sputtering methods to deposit lead titanate thin films with different Ca contents on a $Pt/Ti/SiO_2/Si$ substrate.[33] The authors found that at 50 °C the pyroelectric coefficient increased from 0.8×10^{-4} to 1.89×10^{-4} C/m^2K. Details on pyroelectric thin films for pyroelectric sensors can be found in an excellent review article by Muralt.[34]

4.2.3 Lead zirconate titanate

PZT-based ferroelectric-oxide ceramics offer a number of advantages over single-crystalline materials such as TGS, LT, PVDF, etc., in regards to their use in pyroelectric IR detection. PZT is a solid solution phase of the $xPbZrO_3(1 - x)$ $PbTiO_3$ $(0 < x < 100)$ binary system. For use in pyroelectric-IR detectors, ferroelectric-oxide ceramics have a relatively low manufacturing cost according to the standard processing steps and are also both mechanically and chemically robust. Their mechanical strength enables the creation of large-area wafers that can be easily machined into thin sections. In comparison to pyroelectric-performance TGS single crystals, ferroelectric-oxide ceramics are not hygroscopic, do not possess a fragile nature that can lead to technical difficulties in the processing, and do not have a problem with the environmental temperature for operation and storage. Ferroelectric materials used in pyroelectric-IR detectors operate only below the Curie temperature T_C because above T_C they become depoled. Ferroelectric-oxide ceramics have a high Curie temperature, and, thereby, present no danger of depoling during normal usage within a wide range of ambient temperatures (i.e., –50 to 100 °C). The pyroelectric performance of PZT-type ceramics can be readily modified by the inclusion of selected dopants (elements) into the lattice to control desired parameters.

The pyroelectric properties of a hot-pressed PLZT 8/40/60 were investigated in depth to evaluate its potential as a material for pyroelectric IR detectors.[35] The results of the measurements show that 8/40/60 has a relatively high dielectric constant, high pyroelectric coefficient, and favorable thermal and mechanical characteristics comparable with those of 8/65/35. The calculated figures of merit for 8/40/60 based on the measured properties were compared with other PLZTs of 8/65/35, 12/40/60, and 14/40/60 compositions, as well as with an $LiTaO_3$ single crystal. The results indicate that PLZT 8/40/60 is a promising material for small-area voltage-mode IR detectors. PLZT 8/40/60 material has a permanent bias to its polarization, making repoling after a temperature excursion above the Curie temperature unnecessary.

Suaste-Gomez et al. reported the pyroelectric properties of a $Pb_{0.88}Ln_{0.08}Ti_{0.98}$ $Mn_{0.02}O_3$(Ln = La, Sm and Eu) ferroelectric system, represented in Table 4.2 as PLTM for La, PSTM for Sm, and PETM for

Eu.[36] Pyroelectric properties of the multicomponent ferroelectric-ceramic materials prepared using the hot pressing technique have been investigated at room temperature by Czekaj et al. for both tetragonal *T* and rhombohedral *R* phase areas, and a morphotropic *M* phase boundary on the basis of solid solutions of[37]

$PbTiO_3$-$bZrO_3$-$PbNb_{2/3}Zn_{1/3}O_3$-$PbSb_{2/3}Mn_{1/3}O_3$-$PbW_{1/2}Mg_{1/2}O_3$ (system I),

$PbTiO_3$-$PbZrO_3$-$PbNb_{2/3}Zn_{1/3}O_3$-$PbSb_{2/3}Mn_{1/3}O_3$-$PbNb_{2/3}Mn_{1/3}O_3$ (system II).

From these investigations, the average value of the pyroelectric coefficient obtained in the *M* region was 500 $\mu Cm^{-2}K^{-1}$ for system II and 400 $\mu Cm^{-2}K^{-1}$ for system I. The maximum value of dielectric permittivity obtained in the *M* region was 1380 for system II and 1440 for system I. The pyroelectric coefficient values obtained for system I and system II make these systems candidate materials for practical applications in pyroelectric detectors with high current responsivity.

Guggilla et al. extensively studied the pyroelectric and dielectric properties of various ceramics such as STPZT-1 (PLZT), STPZT-2 (PLZT + MnO_2), and BM740 (modified PZT obtained from Sensor Technology Ltd., Canada) for their applications in IR sensors. The authors compared the results to other candidate materials including a multiple PZT-type ceramic studied by other researchers.[38,39] The material figures of merit at 50 °C were calculated from measured parameters (dielectric constants and a pyroelectric coefficient) for their use in pyroelectric IR detectors. Ceramics, namely STPZT-2 and BM740, are remarkably desirable for pyrosensor applications due to their large pyroelectric coefficient and low dielectric loss. Also important is that the materials investigated can withstand a high operating temperature (up to 100 °C). The results of those investigations are presented in Table 4.2

Perovskite ceramics of a modified lead zirconate-titanate PZT-type have been extensively studied because of their excellent dielectric, electro-optical, piezoelectric, and pyroelectric properties. Oxygen ions with 200-keV energy

Table 4.2 Physical properties and figures of merit for various pyroelectric PZT-type bulk materials.[35–39]

Ceramic	$F_I \quad p$ ($\mu Cm^{-2}C^{-1}$)	ε'	$F_V \quad p/\varepsilon'$ ($\mu Cm^{-2}C^{-1}$)	$F_D \quad p/\sqrt{\varepsilon''}$ ($\mu Cm^{-2}C^{-1}$)
Modified PZT	380	290	1.3	408.6
PLZT	450	700	0.64	170.4
PLZT	350	1129	0.31	62.2
PLTM	13.2 @ T_C	13236 @ T_C	0.0001 @ T_C	
PSTM	6.14 @ T_C	6141 @ T_C	0.0001 @ T_C	
PETM	5.51 @ T_C	5510 @ T_C	0.001 @ T_C	
STPZT1	379.5	1156.6	0.33	79.6
STPZT2	408.5	768.6	0.53	287.6
BM740	300	631.3	0.47	98.0

and doses of 1.0×10^{16} ions/cm^2 were irradiated onto a commercially available modified PZT sample used in IR detectors with good pyroelectric properties, and the response of dielectric and pyroelectric properties before and after irradiation showed a decrease in dielectric constants ε' and ε'' and also confirmed a pyroelectric coefficient.[39]

Very thin films of lead zirconate titanate (PZT 40/60)—0.26 μm or less—have been prepared on Pt-coated oxidized Si substrates (Pt/Ti/SiO_2/Si) using the sol-gel process.[40] These films were of high density, with fine grains of about 0.2 μm, annealed in the range of 600–700 °C in an oxygen atmosphere. X-ray diffraction patterns showed a single-phase perovskite-type structure. Deb et al. investigated the influence of a poling treatment on the dielectric and pyroelectric properties as well as the dielectric constants and pyroelectric properties.[40] Dielectric constants and pyroelectric coefficients for room temperature were 1300 and 840×10^{-5} C/m^2 °C for poled PZT films, and 68.0 and 10.3×10^{-5} C/m^2 °C, respectively, for unpoled. The remanent polarization was 37.8 μC/cm^2, and a coercive field was 146 kV/cm at a switching voltage of 16 V, respectively, peak-to-peak at a frequency of 200 kHz. The remanent polarization and coercive field were found to vary slowly with temperature. The material was also difficult to depole. It was suggested by the authors that these films would be suitable for IR detector applications.

PLZT films around 3-μm thick with compositions of $[(Pb_{0.925}La_{0.075})(Zr_y/Ti_{1-y})_{0.981} + 0.5$ mass % $MnO_2]$ (where $y = 0-0.1$), which have an appropriately small relative-dielectric constant (~200), were deposited on Pt(l00)/MgO (l00) by RF-magnetron sputtering.[41] The pyroelectric properties of PLZT films were investigated in detail as potential element materials for pyroelectric IR sensors.[41] Assuming that the volume-specific heat C_v of the present films is 3.2 J/cm^{3}K, the PLZT films exhibited the highest figure of merit of 1.4×10^{-10} Ccm/J and F.M.D* (figure of merit for high D^*) of 1.6×10^{-8} Ccm/J, which were around 1.8 and 1.5 times larger than those of PLT films, respectively. Consequently, the figures of merit for the pyroelectric IR sensors could be improved by adding a small amount of Zr to PLT.

PLZT 12/40/60 thick films (prepared by screen-printing techniques) have been characterized electrically.[42] It has been found that the sintering time and poling manner influenced the dielectric and pyroelectric properties. The best results were obtained at sintering parameters of 1100 °C for 5 h. Room-temperature poling results in slightly reduced values of the pyroelectric coefficient but enables higher poling fields of up to 5×10^6 Vm^{-1}. The room-temperature relative permittivity is about 200, and the dielectric loss is less than 0.014. The room-temperature pyroelectric coefficient is about 1.5×10^{-4} Cm^{-2} K^{-1}. All of these properties (except the pyroelectric coefficient) are better than those measured on bulk ceramics and are comparable to commonly used single-crystal pyroelectrics. The thick-film technology introduced and discussed by the authors offers significant

advantages in pyroelectric sensor production. The possibility of varying the process parameters allows for some flexibility in choosing the characteristics of the resulting pyroelectric layers.

The pyroelectric and dielectric properties of Pb $(Zr_{0.3},Ti_{0.7})$ O_3 PZT thin film are systematically investigated as functions of film thickness ranging from 0.3 to 1 μm.[43] For better detectivity of the film, a high pyroelectric coefficient, low dielectric coefficient, and loss tangent are needed. These can be achieved by highly textured (111)-preferred orientation and dense microstructure. To obtain the preferred orientation with increasing film thickness, a step-by-step annealing process is applied using highly (111)-textured Pt-bottom electrodes. With increasing film thickness, polarization-hysteresis-loop squareness and remanent-polarization values are maximized. Although there is a slight variation in the preferred orientation with film thickness, dielectric properties are markedly changed due to microstructural variation. Because of the large improvement in loss tangent, the figure of merit is improved with thickness. It is maximized at a thickness of 1 μm. The maximum pyroelectric coefficient measured by the Byer–Roundy method is 38×10^{-5} C/m^2K.

Epitaxially grown and polycrystalline PT, PLT, and PZT thin films with thicknesses of 1–2 μm have been prepared on $Pt/Ti/SiO_2/Si$ substrates by means of a sol-gel spin-coating technique.[44,45] Ferroelectric thin films have good crystallization behavior and excellent dielectric and pyroelectric properties. The pyroelectric coefficients for thin films of PT are 2.9×10^{-8} C/cm^2K, for PLT are 3.37 to 5.25×10^{-8} C/m^2K, and for PZT are 6.10×10^{-4} C/m^2K. The figures of merit for the voltage responsivity of thin films of PT at 0.60×10^{-10} Ccm/J for PLT are 0.59 to 0.78×10^{-10} Ccm/J, and for PZT they are 0.63×10^{-10} Ccm/J. The figures of merit for current responsivities of these films are 9.0×10^{-9} Ccm/J, 10.5 to 16.0×10^{-9} Ccm/J, and 19.1×10^{-9} Ccm/J, respectively; and the figures of merit for detectivities are 0.74×10^{-8} Ccm/J, 0.79 to 1.13×10^{-8} Ccm/J, and 0.83×10^{-8} Ccm/J, respectively.

The effects of Mn doping on the ferroelectric and pyroelectric properties of $Pb(Zr_{0.3}\ Ti_{0.7})O_3$ PZT thin films on $Pt/Ti/SiO_2/Si$ substrates has been investigated.[46] Mn-doped (1 mol%) PZT (PMZT) showed almost no hysteretic fatigue up to 10^{10} switching bipolar pulse cycles, coupled with excellent retention properties. A low-permittivity interfacial layer that generally forms between the Pt electrode and PZT films does not occur in PMZT. It was proposed that Mn dopants are able to reduce oxygen vacancy mobility in PZT films, and that Mn^{2+} ions consume the oxygen vacancies generated during repeated switching, forming Mn^{4+} ions. These mechanisms are probably responsible for their low-observed-fatigue characteristics. Mn doping brings additional benefits to the electrical properties of PZT films. The relevant pyroelectric coefficients p of a 700-μm thick film are 3.52×10^{-4} $Cm^{-2}K^{-1}$, and the detectivity figures of merit are $F_D = 3.85 \times 10^{-5}$ $Pa^{-0.5}$ at 33 Hz for Mn-doped PZT, compared with $p = 2.11 \times 10^{-4}$ $Cm^{-2}K^{-1}$ and $F_D = 1.07 \times 10^{-5}$ $Pa^{-0.5}$ for the undoped PZT

films. This means that Mn-doped PZT thin films are excellent candidates for device materials in both memory and pyroelectric applications.

Highly *c*-axis oriented PLZT films with compositions of $(Pb_{0.925}La_{0.075})(Zr_yTi_{1-y})_{0.981}O_3$, where $y = 0.2$–0.4, were deposited on Pt(100)/MgO(100) by RF-magnetron sputtering, which applied an intermittent deposition composed of the repetition of deposition and nondeposition.[47] It was confirmed that the highest figures of merit F_V and F_D for the pyroelectric IR sensors were obtained using powders with excess PbO of 20 mol% added to PLZT as sputtering targets in the preliminary experiment. Among the three samples studied, the PLZT film with $y = 0.2$ exhibited the highest figures of merit for voltage responsivity Rv of approximately 5.3×10^{13} Cm/J—around 1.8 times larger than that of PLZT ceramic with $y = 0.2$.

Thin films of PZT and 1% tantalum-oxide-doped PTZT $[Pb_{0.9950}(Zr_{0.525}Ti_{0.465}Ta_{0.010})O_3]$ deposited on Pt(200)/SiO_2/Si(100) using the DC unbalanced magnetron sputtering method have been investigated.[48] The films were grown at deposition temperatures in the range of 300–750 °C for 3 h, followed by annealing at 700*b* °C for one hour for each deposited film. The films showed tetragonal structure with preferred orientation to the 100- and 200-crystal planes. The calculated lattice constants for PZT thin film are $a = b = 4.056$ Å, $c = 4.105$ Å. The calculated lattice constants for PTZT thin film are $a = b = 4.056b$ Å, $c = 4.068b$ Å. The conductivity of PZT films is between 2.24×10^{13} Ωm^{-1} and 5.00×10^{12} Ωm^{-1}, whereas the conductivity of PTZT films is between 1.02×10^{9} Ωm^{-1} and 1.90×10^{8} Ωm^{-1} (for films deposited at the temperature ranges mentioned above). The voltage responsivity measured at a chopper frequency of 2000 Hz and wavelength of 947 nm is 62.1 to 80*b* μV/W and 61 to 76.4 μV/W for PZT and PTZT thin films, respectively. Meanwhile, the pyroelectric coefficient p is in the range of 9.54 to 12.3×10^{-4} C/m^2K for PZT thin films and 9.35 to 11.7×10^{-4} C/m^2K for PTZT thin films. These results show that PZT and PTZT thin films are suitable for use in pyroelectric IR sensors.

Epitaxially grown and polycrystalline PT, PLT, and PZT thin films with thickness of 1–2 μm have been prepared on Pt/Ti/SiO_2/Si substrates by means of the *modified* sol-gel spin-coating technique.[49] Ferroelectric thin films have good crystallization behavior and excellent dielectric and pyroelectric properties. The pyroelectric coefficients of PT and PLT thin films are 2.9×10^{-4} C/m^2K and 3.37 to 5.25×10^{-4} C/m^2K, respectively. The figures of merit for voltage responsivity of PT and PLT thin films (F_I) are 0.60×10^{-10} Ccm/J and 0.79 to 1.13×10^{-8} Ccm/J, respectively. The figures of merit for current responsivity of these films are 9.0×10^{-9} Ccm/J and 10.5 to 16.0×10^{-9} Ccm/J, and the figures of merit for detectivity of these films are 0.74×10^{-8} Ccm/J and 0.79 to 1.13×10^{-8} Ccm/J, respectively.

Various PLZT films were prepared on platinized Si wafers. The dielectric constant and dissipation factors decreased and increased, respectively, with

higher firing temperature due to PbO loss. The pyroelectric activity in the PLZT films was dependent on composition. PZT 53/47 exhibited the highest pyroelectric coefficient at 7.7×10^{-4} C/m^{2}K (at a heating rate of 1 K/min). $PbTiO_3$ film exhibited a low pyroelectric coefficient ($<2 \times 10^{-5}$ C/m^{2}K) due to its (100)-preferred orientation. It was observed that the pyroelectric coefficient decreased as the rate increased—at high heating rates, the films were unable to conduct heat uniformly, causing a decrease in the calculated pyroelectric coefficient.[50]

PZT films with various Nb-doping levels (PNZT) were deposited on $Pt(111)/TiO_2/SiO_2/Si(100)$ substrate via the CVD technique, followed by rapid thermal annealing (RTA).[51] The introduction of the first seeding layer significantly improved the crystallization quality after RTA annealing. The dielectric constant of PNZT films increased with the increase of Nb doping concentration. PZT films with 1% Nb doping exhibited higher remnant polarization (49.33 μC/cm^2), pyroelectric coefficient (4.6×10^{-4} C/m^{2}K), and figures of merit (1.89×10^{-5} Jm^{3}K^{-1}), which indicate that $Pb(Zr_{0.2}Ti_{0.8})_{0.99}Nb_{0.01}O_3$ would be a good candidate for pyroelectric IR sensor applications.

PZT [$Pb(Zr_{0.52}Ti_{0.48})O_3$, PZT] thin films are fabricated by a magnetron sputtering technique on a $Pt/Ti/SiO_2/Si$ substrate at room temperature and annealed by means of a CO_2 laser with a resulting temperature below 500 °C.[52] It was found that the annealed film with a laser-energy density of 490 W/cm^2 for 25 s has a typical perovskite phase, uniform crystalline particles of about 90 nm, and a high pyroelectric coefficient of 1.15×10^{-4} Cm^{-2}K^{-1}. Thus, laser-annealed PZT thin films are very promising for uncooled detectors and other pyroelectric applications.

Bruchhaus et al. systematically investigated the stresses in highly (111)-oriented $Pb(Zr_xTi_{1-x})O_3$ (PZT) thin films deposited by a planar multitarget sputtering technology with x ranging from 0 to 0.6.[53] It is worth mentioning that the domain orientations in PZT films are largely controlled by stress during each step of deposition and have greater effects on the resulting properties of films. The major advantages of multitarget sputtering technology are: thin films with precise composition control; prevention of stoichiometric variations on the target surface during repeated use; a higher deposition rate due to sputtering from metals in the metallic mode; and compatibility with silicon technology. The authors found that the films on the tetragonal side of the phase diagram with a Zr content of up to 25% exhibited strong self-polarization and a strong shift in the C-V curves due to compressive stress. Thus, films exhibited promising properties for their use in pyroelectric detector arrays with pyroelectric coefficients of $>2 \times 10^{-4}$ C/m^{2}K without poling, and dielectric loss as low as 0.6%.

Dorey and Whatmore investigated uranium-doped lead magnesium niobate with lead zirconate titanate (PMNZTU) composite thick film fabricated on silicon substrate using a new composite sol-gel technique and processed at 710 °C.[54] The maximum figures of merit ($F_V = 3.45 \times 10^{-2}$ Cm^{-2}C^{-1},

Table 4.3 Material and figure-of-merit characteristics of Perovskite films grown using different methods.[40–54]

Material	Substrate	$F_I \quad p$ ($10^{5} \times$ $Cm^{2}\,°C^{1}$)	ε'	$F_V \quad p/\varepsilon'$ ($10^{5} \times Cm^{2}\,°C^{1}$)	$F_D \quad p/\sqrt{\varepsilon''}$ ($10^{-5} \times$ $Cm^{-2}\,°C^{-1}$)
$PbTiO_3$ (screen print)		60	200	0.3	
$PbTiO_3$ (sol gel)		25	190	0.13	23.4
La modified $PbTiO_3$ (screen print)	Au coated SiO_2/Si(100)	10.7			
La modified $PbTiO_3$ (sol gel)	Pt/Ti/SiO_2/Si	1.3 2.5			
$PbTiO_3$ film (sol gel)	Polycrystalline Si	85 115	150 400	0.56 0.28	56.6
$PbTiO_3$ film (multitarget sputter)	Pt coated Si	17	180	0.09	12.6
Ca modified $PbTiO_3$ (sol gel)	ITO coated glass	46	99	0.46	12.8
$PbTiO_3$ film (sputter)	(001)Pt/MgO	25	97	0.25	32.8
PLZT (ceramic) (8/40/60)		120	4285	0.02	10
PLZT (ceramic)		45	700	0.06	17.0
PZT (40/60) (sol gel)	Pt coated oxidized Si	85	1004	0.08	10.1
Mn PZT (sol gel)	Pt/Ti/SiO_2/Si	35.3	255	0.13	28.6
PLZT (12/40/60) (screen print)	Pt/alumina	15	190	0.07	9.2
PLZT (12/40/60) (ceramic)		35	1129	0.03	6.2
PLZT (RF magnetron sputter)	Pt/MgO(110)	81	205	0.39	51.9
PZT (30/70) (spin coat)	Pt/Ti/SiO_2/Si	24	600	0.04	10.9
PZT (sol gel)	Pt(111)/Ti/SiO_2/Si	61.0	300	0.20	28.7

$F_D = 1.01 \times 10^{5}\,Pa^{1/2}$) calculated were comparable with screen-printed thick films. Dorey and Whatmore concluded that the ability of this technique to directly integrate thick film onto silicon substrate at temperatures as low as 710 °C, while maintaining competitive figures of merit, is of considerable interest for future device applications. Table 4.3 illustrates the properties of various PZT films grown using different methods.

4.2.4 Lithium tantalate and lithium niobate

Lithium tantalate ($LiTaO_3$, abbreviated as LT) and lithium niobate ($LiNbO_3$, abbreviated as LN) have similar structures. They are one of a large number of oxygen octahedral ferroelectrics (ABO_3). The neighboring oxygen octahedrals are connected through an oxygen ion that serves as a common "tie-end." The symmetry of both crystals belongs to the point group 3m in the trigonal ferroelectric phase at room temperature. The symmetry changes to the point group 3m in the paraelectric phase above Curie temperature. At room

temperature, the lattice parameters of the trigonal unit cell are $a = 5.4944$ Å, $\alpha = 55$ deg $52'$ in $LiNbO_3$, and $a = 5.4740$ Å, $\alpha = 56$ deg $10'$ in $LiTaO_3$. Sometimes, it is more convenient to choose a hexagonal cell for description, with Li and Ta ions occupying two-thirds of the octahedral interstices between the layers.

LT also possesses a high melting point (1650 °C) and is insoluble in water.[25] These factors make the material one of the most stable pyroelectrics, with a very wide temperature range of operation. It is generally used in single-crystal form, with crystals grown using the Czochralski method, and wafers of more than 50 mm in diameter, which are commercially available. LT possesses a moderate pyroelectric effect and dielectric constant, which combine to give a response figure that is about one-quarter that of triglycine sulfate. $LiTaO_3$ is widely applied in pyroelectric point detectors in single-crystal form, due to its high pyroelectric coefficient of about 230 $\mu C/m^2K$ and low relative permittivity of 47. This results in an excellent figure of merit F_V of 4.9, combined with low dielectric losses of 0.1%. However, very low values of dielectric loss (about 10^{-4}) have been reported for this material, giving it a potential F_D about four times greater than DTGS, although the loss of commercially available material is higher. However, with the lowest-loss materials, high D^* figures can be achieved with low-noise amplifiers. By using ion-beam milling to fabricate very thin ($\sim$ 2–5 μm) elements in structures and packages in which thermal conductance had been minimized, Stokowski et al. demonstrated D^* figures as high as $8.5 \times 10^8 cmHz^{1/2}W^{-1}$ at 30 Hz.[55] In addition, the ion milling technique provides the advantage of clean, relatively damage-free surfaces that enable the fabrication of detector wafers with various geometrical structures.

$LiTaO_3$ has also been used by Roundy for 1D detector arrays interfaced to a CCD multiplexing chip.[56] The one disadvantage for $LiTaO_3$ in this application is that the high thermal diffusivity reduces the arrays' minimum resolvable temperature difference at high spatial frequencies. The robustness, high performance, and wide availability of this material—including its ability to withstand high-energy IR radiation with a fast response time of 0.5 ns—make it a popular choice for commercial detectors. Norkus gives a short review on pyroelectric IR detectors based on lithium tantalate.[57] Lithium tantalate ($LiTaO_3$) thin films ($\sim$ 0.5 μm) have been successfully deposited on Pt(111)/SiO_2/Si(100) substrates by means of sol-gel spin-coating technology. Figures of merit for IR detectors were studied for $LiTaO_3$ thin films. High figures of merit F_V of 2.1×10^{-10} Ccm/J and F_D of 2.4×10^{-8} Ccm/J exist because of the relatively low dielectric constant ε_r of 35 and high pyroelectric coefficient 4.0×10^{-4} C/m^2K of the films. The pyroelectric IR detector abricated using $LiTaO_3$ thin film exhibits a voltage responsivity R_v of 4584 V/W at 20 Hz and a high specific detectivity D^* of 4.23×10^7 $cmHz^{1/2}/W$ at 100 Hz.[58]

For integration with readout electronics and simplified processing, deposition of thin films from solution precursors is desirable. In order to optimally use the spontaneous polarization of $LiTaO_3$ along the *c* axis of its hexagonal unit cell, the thin films need to be grown with a (001) orientation of platinized silicon. Investigation of different parameters like pyrolysis temperature, heating rate, final heat treatment temperature, and cooling rate, revealed that the heating rate determines the development of the desired (001) orientation. Slow heating of 1 °C/s results in (001)-oriented $LiTaO_3$ thin films, while faster ramps lead to random or (110)-textured films. After precursor deposition by spin coating and pyrolysis at 350 °C, a gel-like solid amorphous film remains. During RTA, this layer crystallizes. Preferred heterogeneous nucleation at the $LiTaO_3$/Pt interface can be expected with slow heating, resulting in a (001)-oriented layer due to local epitaxy with the (111)-textured platinum. For fast heating rates of 63 °C/s, bulk or surface nucleation may dominate, leading to random- or (110)-textured films. Electrical measurements after poling the films in an external electric field of 50 kV/cm at 200 °C showed a pyroelectric coefficient of 171 $\mu C/m^2K$ and a dielectric constant of 40, resulting in a figure of merit of $F = 4.2$, comparable to the single-crystal values of 4.9.[59]

$LiTaO_3$ thin film has been deposited by RF-magnetron sputtering, with an Li-enriched target comprising Li_2O_2/Ta_2O_5 (55%/45 wt%) on membranes of SiN_x with the aim of thermal microsensor performance. The best pyroelectric coefficient of LT films (400 nm) obtained for a growth temperature of 620 °C and a pressure of 0.67 Pa is 40 $\mu C/m^2K$.[60]

Thin films of LT have been deposited by RF sputtering on RuO_2- or SiO_2-coated silicon substrates. Two electrical contact configurations have been used. The first is a thin capacitor with an RuO_2 buried electrode and a gold, nickel, or RuO_2 upper electrode. The second configuration includes a recourse to RuO_2 interdigitated electrodes fabricated using a photolithographic process. Ferroelectric hysteresis measured with a Sawyer–Tower circuit shows a spontaneous polarization of about 20 $\mu C/cm^2$ and an electric coercive field of 3 kV/cm. The dynamic pyroelectric response has been measured as a function of frequency at various temperatures. From 100 Hz to 1 kHz at room temperature, the pyroelectric current and voltage responses are 12 $\mu A/W$ and 18 V/W, respectively. The effects of the poling process have also been investigated by the authors, and significant improvements in the pyroelectric response have been obtained.[61]

$LiNbO_3$ crystals display larger secondary pyroelectricity than the LT does due to a change in the polarization from thermal expansion. The secondary pyroelectric coefficient 2.3×10^{-5} C/m^2K (which is found to be 25% of first pyroelectric coefficients—8.3×10^{-5} C/m^2K) has been found.[62] Due to this property, LN has limited commercial application. Recently, Gebre et al. extensively investigated the general pyroelectric coefficient of pure and doped

Table 4.4 Material characteristics and figures of merit for modified LN crystals.[63]

Crystals*	$F_I \quad p$	ε'	$F_V \quad p/\varepsilon'$	$F_D \quad p/\sqrt{\varepsilon''}$
	$(10^{-5} \times \text{Cm}^{-2}\,^{\circ}\text{C}^{-1})$		$(10^{-5} \times \text{Cm}^{-2}\,^{\circ}\text{C}^{-1})$	$(10^{-5} \times \text{Cm}^{-2}\,^{\circ}\text{C}^{-1})$
$LiNbO_3$ (LN) single crystal (at T 50 °C)	7.2	31.4	0.23	21.1
LN: Fe single crystal (at T 50 °C)	33.8	50.1	0.68	65.0
LN: Fe/Mn single crystal (at T 50 °C)	9.0	47.3	0.16	20.9
LN: Eu single crystal (at T 50 °C)	15.3	39.3	0.39	39.2
$LiNbO_3$ single crystal (at T 25 °C)	4.0	30	0.13	

* LN:Fe is Fe-doped LN; LN:Fe/Mn is LN doubly doped with Fe and Mn; LN:Eu is LN doped with Eu.

Figure 4.3 Pure and doped lithium niobate crystals grown at AAMU.

LN crystals, as shown in Table 4.4, and found that Fe-doped LN crystals are attractive for use in detectors because of their higher figures of merit compared to LN.[63] A photograph of pure and doped lithium niobate crystals grown at AAMU is shown in Fig. 4.3.

4.2.5 Barium strontium titanate materials system

Barium strontium titanate, $BaSrTiO_3$ (BST), a perovskite ferroelectric material, has electronic and microwave applications that include use in pyroelectric devices. When the BaSr ratio equals 0.7/0.3, the tetragonal-to-cubic phase is near room temperature. Ceramic and single BST crystals have

the highest pyroelectric coefficient ever obtained from pyroelectric materials at 23×10^{-2} C/m^2 °C. However, ceramic and single BST crystals are difficult, expensive, and time-consuming to fabricate.[64] Many efforts have been made to integrate BST thin films with silicon processing for a higher pyroelectric coefficient. Related efforts and important findings are covered in this section.

BST ($Ba_{0.64}Sr_{0.36}TiO_3$) thin films have been prepared using the sol-gel method on a platinum-coated silicon substrate. The resulting thin films show strong dielectric and pyroelectric properties. The dielectric constant is 592, and the dissipation factor is 0.028 for a $Ba_{0.64}Sr_{0.36}TiO_3$ thin film at a frequency of 200 Hz. The peak pyroelectric coefficient is 1080 μC/m^{2}K at 30 °C. The pyroelectric coefficient is 1860 μC/m^{2}K at room temperature (25 °C), with a figure of merit ($p/d\varepsilon'':d$ thickness in μm) of 37.4 μC/m^{3}K. The high pyroelectric coefficients and greater figures of merit of $Ba_{0.64}Sr_{0.36}TiO_3$ thin films make it a candidate for thermal IR detection and imaging.[65] Lee et al. obtained BST films with a considerably high pyroelectric coefficient of 240×10^{-5} Cm^{-2}K^{-1}.[66]

Barium strontium titanate ($Ba_{1-x}Sr_xTiO_3$) ferroelectric thin films have been prepared by MOD on Pt/Ti/SiO_2/Si substrates on a micromachined wafer in order to fabricate a dielectric bolometer-type IR sensor.[67] The x-ray diffraction (XRD) pattern and *D-V* hysteresis curve were measured to investigate the effects of the final annealing temperature and time on the properties of the film. The results show that the films annealed at 700 °C or 800 °C, and they all had good perovskite structure, with the 800 °C-annealed film having better ferroelectric loops. Films annealed at 800 °C, but with varying annealing times of 5–60 min, showed similar perovskite structures to one another. The films annealed for 30–60 min had the best ferroelectric loops. The temperature coefficient of the dielectric constant (TCD) of the MOD-made BST thin film on micromachined substrate is about 1%/K. The uniformity of the BST film on a micromachined Si wafer has also been proven useful for the operation of a sensor array. Chopperless operation has been attained and the IR response of the fabricated sensor evaluated with R_v of 0.4 kV/W and D^* of 1.0×10^8cm Hz$^{1/2}$/W.

Sengupta et al. investigated films of $Ba_{0.64}Sr_{0.36}TiO_3$, $Ba_{0.94}Sr_{0.36}$-$Ti_{0.06}Zr_{0.18}O_3$, and $Ba_{0.64}Sr_{0.36}TiO_3$/0.50 wt% MgO compositions by ceramic tape casting and a pulsed laser deposition method, as these compositions are well represented in the literature.[68] The data obtained for their patented $Ba_{0.64}Sr_{0.36}TiO_3$/0.50 wt% MgO composition shows a reduction in the dielectric constant and lower dielectric loss, thereby contributing to a higher pyroelectric figure of merit. Their detailed results are presented in Tables 4.5 and 4.6.

Tetragonal $Ba_{0.8}Sr_{0.2}TiO_3$ thin films with large columnar grains, 100–200 nm in diameter, have been prepared on Pt/Ti/SiO_2/Si substrates using a 0.05-M solution precursor by sol-gel processing. The ferroelectric phase transition in the prepared $Ba_{0.8}Sr_{0.2}TiO_3$ thin films is broadened and

Table 4.5 Physical properties and figures of merit for BST samples.[68]

Tape-cast material	$F_I \quad p$ (μCm ^{2}°C ^{1})	ε'	$F_V \quad p/\varepsilon'$ (μCm ^{2}°C ^{1})	$F_D \quad p/\sqrt{\varepsilon''}$ (μCm^{-2}°C^{-1})
$Ba_{0.64}Sr_{0.36}TiO_3$	759	4478	0.09	103.5
$Ba_{0.94}Sr_{0.06}Zr_{0.18}Ti_{0.82}O_3$	96.5	1818	0.05	25.39
$Ba_{0.94}Sr_{0.06}TiO_3$/0.25 wt% MgO	593	2370	0.25	197.6
$Ba_{0.94}Sr_{0.06}TiO_3$/0.25 wt% MgO	550	1370	0.4	183.3

Table 4.6 Physical properties and figures of merit for BST thin-film samples.[69]

Thin film	$F_I \quad p$ (μCm ^{2}°C ^{1})	ε'	$F_V \quad p/\varepsilon'$ (μCm ^{2}°C ^{1})	$F_D \quad p/\sqrt{\varepsilon''}$ (μCm^{-2}°C^{-1})
$Ba_{0.64}Sr_{0.36}TiO_3$	1940	594	3.2	520.1
$Ba_{0.94}Sr_{0.06}Zr_{0.18}Ti_{0.82}O_3$	1260	1119	1.2	100.8
$Ba_{0.94}Sr_{0.06}TiO_3$/0.25 wt% MgO	187	505	0.37	93.5
$Ba_{0.94}Sr_{0.06}TiO_3$/0.25 wt% MgO	129	297	0.43	62.3

suppressed to 40 °C with a maximum dielectric constant of ε_r (100 kHz) = 680. The observed low-dissipation factor $\tan\delta = 2.6\%$ and high pyroelectric coefficient $p = 4.586 \times 10^{-4}$ C/m^{2}K at 33 °C render the prepared $Ba_{0.8}Sr_{0.2}TiO_3$ thin films promising for uncooled IR-detector and thermal-imaging applications.[69]

$(Ba_{0.6}Sr_{0.3}Ca_{0.1})TiO_3$ powders were prepared by the sol-gel method using a solution of Ba, Sr, and Ca acetate with Ti isopropoxide. The specimens were doped with $MnCO_3$ (0.1 mol%) and Y_2O_3 (0.5 mol%) and fabricated by the cold isostatic-press method. A urethane pot and zirconia ball were used in the mixing and grinding process, and the green pellets were sintered at 1450 °C for 2 h in an alumina crucible. The specimen exhibited a dense, void-free grain structure with a grain size of about 3 μm. At Curie temperature, the dielectric constant was 16,600, and the dielectric loss was 1.2%. The specimen under a 4-kVcm ^{1} DC-bias field showed a maximum pyroelectric coefficient of 550×10^{-5} Cm ^{2}K ^{1} at Curie temperature. The figures of merit for specific detectivity D^* of the specimen, with an applied DC 8 kVcm ^{1} bias field, was the highest value achieved, with 17.6×10^{-9} CcmJ ^{1} at Curie temperature.[70]

SiO_2-doped $Ba_{0.85}Sr_{0.15}TiO_3$ (SBST) glass-ceramic (g-c) films with a perovskite structure have been prepared on Pt/Ti/SiO_2/Si substrates using the sol-gel technique. Differential thermal analysis (DTA), XRD, and atomic force microscopy (AFM) are employed to analyze both the synthesizing process and the microstructure of SBST g-c films.[71] The ferroelectricity and crystallization

behavior of SBST films are discussed by Liu et al.[71] They found that the synthesis temperature of SBST15 film is greater than that of pure BST film by about 60 °C. The grain size decreases, and the ferroelectricity of SBST g-c films is degenerated, but their loss tangent and leakage-current density decrease with increasing SiO_2 contents. Both the TCD and pyroelectric coefficients of SBST5 film at 20–25 °C were measured at 4.6% °C ^{1} and 8.1 × 10 ^{4} Cm ^{2}K ^{1}, respectively. Those values are about two-thirds that of the pure BST films. The BST g-c film with 5 mol% SiO_2 dopant is a promising advanced candidate material for uncooled IR focal plane arrays applied at near room temperature.[71]

Liu et al. prepared BST $(Ba_{1-x}Sr_x)TiO_3$ thin films with $x = 0$, 0.05, 0.10, and 0.15 (BST, BST5, BST10, BST15, respectively) on $Pt/Ti/SiO_2/Si$ substrate by the improved sol-gel method. The resulting thin films showed very good dielectric and pyroelectric properties. At 25 °C and 10 kHz, the dielectric constants of the thin films were: BST at 320, BST5 at 375, BST10 at 400, and BST15 at 425. Their loss tangents were found to be 0.035, 0.041, 0.024, and 0.01, respectively. The maximum pyroelectric coefficient for BST10 film was found to be 12 × 10 ^{4} C/m^2K at 35 °C.[72]

4.2.6 Strontium barium niobate

Strontium barium niobate (SBN) solid-solution series $(Sr_{1-x}Ba_xNb_2O_6)$, where $0.2 < x < 0.8$, has a tetragonal tungsten-bronze (TB)-type structure and belongs to a point group with 4-mm symmetry. It possesses excellent pyroelectric and EO properties. Due to good mechanical and nondeliquescent properties, SBN is an ideal pyroelectric material. By changing the ratio Sr/Ba, the Curie temperature of SBN can be altered in the range from 60 °C to 250 °C. The tetragonal TB-type ferroelectric SBN possesses a spontaneous polarization of 32 $\mu C/cm^3$ (Sr/Ba = 75/25) and a polar axis along the c axis of the tetragonal lattice.[73] The pyroelectric coefficients of crystals of different composition of Sr/Ba are listed in Table 4.7. Detectors fabricated through this process have high stability in air without a protective window, as in the case of TGS. Furthermore, a thin plate of SBN has a high absorption capacity in the IR region above 10 μm without blackening. The advantage is that it has no apparent piezoelectric response below a frequency of 50 MHz. It is widely

Table 4.7 Physical properties and figures of merit for SBN crystals.[73]

Crystal $Sr_{1-x}Ba_xNb_2O_6$	F_I p (10 ^{2} C/m^2K)	ε'
x 0.27	0.28	8200
x 0.33	0.11	1800
x 0.40	0.085	610
x 0.52	0.065	380
x 0.75	0.030	180

Table 4.8 Figures of merit for SBN samples at 40 °C.[74]

Sample	$F_I \quad p$ ($10^{-2} \times C/m^2K$)	ε'	$F_V \quad p/\varepsilon'$ ($10^{-2} \times C/m^2K$)	$F_D \quad p/\sqrt{\varepsilon''}$ ($10^{-2} \times C/m^2K$)
LSBN 1% La	1×10^{-4}	850	11.8	
LSBN 3% La	1.5×10^{-4}	1100	13.6	
LSBN 5% La	6×10^{-5}	530	11.3	

Table 4.9 Physical properties and figures of merit for textured SBN ($Sr_xBa_{1-x}Nb_2O_6$) ferroelectric ceramics—SBN53/47 HF (⊥): parallel to pressing axis SBN53/47; HF (‖): perpendicular to pressing axis.[76]

Ceramic	$F_I \quad p$ ($10^{-4} \times C/m^2K$)	ε'	$F_V \quad p/\varepsilon'$ ($10^{-4} \times C/m^2K$)	$F_D \quad p/\sqrt{\varepsilon''}$ ($10^{-4} \times C/m^2K$)
SBN53/47 HF (⊥)	5.1	980	0.0052	1.2
SBN53/47 HF (‖)	4.0	468	0.0085	2.63
SBN63/37 HF (⊥)	2.3	4579	0.0005	0.18
SBN63/37 HF (‖)	0.67	1412	0.00047	0.12

used for fast detectors. The main shortcoming of SBN is that its dielectric constant is not low enough for application at high frequencies. Its high-frequency figure of merit (p/ε) is an order of magnitude less than that of TGS. So, SBN thin-film detectors are mainly used for small-area, low-frequency applications. Amorin et al. investigated the effect of lanthanum (La) cation as a dopant in the polarization of the $Sr_{0.3\ 3y/2}La_yBa_{0.7}Nb_2O_6$ (LSBN) system, where $y = 0.01, 0.03, 0.05$.[74] The pyroelectric coefficient and the spontaneous polarization of these materials were found to increase with La-cation doping up to a maximum value of 3% in concentration. The pyroelectric properties diminish with a 5% doping of La. Results are provided in Table 4.8.

Chen et al. investigated SBN films fabricated on silicon and fused-silica substrates prepared using the sol-gel method. The pyroelectric coefficient at room temperature was 2×10^{-4} C/m^2K at 27 °C—the same order of magnitude as that of the SBN single crystals.[75] Venet et al. fabricated textured SBN ferroelectric ceramics with $x = 0.53$ and 0.63 using a hot forging (HF) method.[76] Table 4.9 summarizes the F_I, F_V, and F_D values for SBN-textured ceramics. In the perpendicular direction with respect to the forging axis, the SBN53/47 ceramic has the third-highest F_I value, indicating its potential in the fabrication of fast-pulse pyroelectric devices.

4.2.7 Lead magnesium niobate-lead titanate (PMN-PT)

PMN-PT [$(1-x)Pb(Mg_{1/3}Nb_{2/3})O_{3\ x}PbTiO_3$] relaxor-based single crystals have rhombohedral symmetry at $x \leq 0.30$, tetragonal symmetry at $x \geq 0.35$, and

Table 4.10 Physical properties and figures of merit for PMN-PT samples.[77–86]

Crystals	$F_I \quad p$ (10^{-4} C/m^{2}K)	ε'	$F_V \quad p/\varepsilon'$ (10^{-4} C/m^{2}K)	$F_D \quad p/\sqrt{\varepsilon''}$ ($10^{-4} \times$ C/m^{2}K)
PMN 0.13PT <111> direction poled	32.6	3107	0.01	10.18
PMN 0.21PT <111> direction poled	17.9	961	0.018	10.59
Fe doped PMN 0.38PT	584×10^{-6}	310		
PMN.29PT	12.8	515	0.024	7.1
Mn PMN 0.29PT	16.2	688	0.023	27.9

morphotropic symmetry at $0.30 < x < 0.35$. PMN-PT is a new generation of single crystals that has been widely investigated due to its excellent dielectric, piezoelectric, and optical properties. However, few investigations have reported on its pyroelectric performance.[77 86] Table 4.10 demonstrates some of the noteworthy pyroelectric properties and calculated figures of merit for these materials.

4.3 Organic Pyroelectrics

In this section we will briefly discuss the properties of polymers used in pyroelectric IR detectors. With the discovery of pyroelectric response in polyvinylidene fluoride (PVF_2 or PVDF) and polyvinyl fluoride (PVF) comes a new area of organic materials research for their use in pyroelectric IR detection devices. PVDF is inherently polar. With respect to the carbon atom in the unit, the hydrogen atoms are positively charged, and the fluorine atoms are negatively charged. The repeat unit of ($-CH_2-CF_2-$) or $(CH_2CF_2)n$, in which the carbon-hydrogen bonds with the electrically polar carbon-fluorine, can take up a number of stable configurations determined by the treatment of the polymer. PVDF can be crystallized into at least four different polymorphous phases, depending on the film preparation conditions. Two forms—β (or I) and α (or II)—are of particular importance. In form α, PVDF (formed from slow-cooled melts or an acetone solution) is nonpiezoelectric, the bonds are in a trans-gauche-trans-gauche configuration, and the molecules are stacked, giving a nonpolar unit cell. Form α can be converted into form β by stretching and electrically poling with a suitable field. In form β, the molecular groups are in an all-trans configuration, and the molecules are assembled to give a polar unit cell. Form β is orthorhombic with point group A mm2, $z = 2$, $a = 8.47$, $b = 4.9$, $c = 2.56$ Å. Density is 1.76 Kgm^{-3}.[87] This form of PVDF is pyroelectric, and its basic physical properties are presented in Table 4.11. Recently, in parallel with PVDF, the polymers of VDF-TrFE have been found to be ferroelectric.[88] Like PVDF, the vinylidene fluoride/trifluoroethylene (VDF/TrFE) copolymer consists of a crystalline and an amorphous fraction.

Table 4.11 Material characteristics and figures of merit for P(VDF/TrFE).[88]

Material	F_I p ($10^{-5} \times Cm^{-2} °C^{-1}$)	ε'	F_V p/ε' ($10^{-5} \times Cm^{-2} °C^{-1}$)	F_D $p/\sqrt{\varepsilon''}$ ($10^{-5} \times Cm^{-2} °C^{-1}$)
P(VDF/TrFE) 50/50	4.0	18.0	0.2	5.06
P(VDF/TrFE) 56/44	3.8	12.0	0.3	7.0
P(VDF/TrFE) 70/30	5.5	8.0	0.68	20.0
P(VDF/TrFE) 75/25	3.3	7.4	0.4	9.4
P(VDF/TrFE) 80/20	3.1	7.0	0.44	9.1
PVF_2	3.0	10.0	0.3	6.8

Unlike PVDF, the introduction of a small amount of TrFE causes the copolymer to crystallize directly into form β from melt. The VDF/TrFE copolymer can, therefore, become pyroelectric without stretching, as is the case with PVDF. The similarity between the electrical and physical properties of PVDF and 65/35 VDF/TrFE copolymers are shown in Table 4.11.

A comparison of frequently used thin-film ferroelectrics shows that the application of P(VDF/TrFE) in low-cost sensors can be advantageous, although the figures of merit are lower. Copolymer film can be easily deposited onto a silicon wafer in post-processing after readout circuit fabrication—for example, by spin coating of a copolymer solution. Furthermore, the very low thermal conductivity provides good thermal insulation between the pyroelectric film and readout circuitry. The chosen P(VDF/TrFE) with a molar content of 70% VDF shows a spontaneous polarization of 8 μCcm^{-2} and a pyroelectric coefficient of 3.5×10^{-5} $Cm^{-2}K^{-1}$, as well as a dielectric constant of 8 and a dielectric loss of about 0.018 at 25 °C. The investigation proves the suitability of the copolymer P(VDF/TrFE) for use in pyroelectric sensors and arrays.[89] Production of thin-poled films is inexpensive and simple. Their properties are comparable to those of the frequently used lithium tantalate sensors.

In the recent past, several other polymers that exhibit pyroelectric response have been molecularly engineered.[90,91] The important organic compounds with amphiphilic molecules (which have a hydrophobic tail and a hydrophilic head group) have been fabricated via the Langmuir–Blodgett (LB) technique and investigated for their applications in IR-sensing devices. Table 4.12 lists some important organic materials along with their characteristics. Advantages of organic films are low dielectric loss and the ease of fabricating high-quality films with precise thickness and desired symmetry.[91]

4.4 Pyroelectric–Polymer Composites

Pyroelectric–polymer composites can be considered an established substitute to conventional electro-ceramics and to ferroelectric polymers. These composites have a unique blend of polymeric properties such as mechanical

Table 4.12 Material characteristics and figures of merit for important organic pyroelectrics.[90]

Material	F_I p (μCm ^{2}K ^{1})	ε'	tan δ	F_V (μCm ^{2}K ^{1})	F_D (μCm ^{2}K ^{1})
[Ru(PPh$_2$biP)$_2$]PhOC$_{16}$/ behenic acid	1.07	3.4	0.004	0.31	9.18
Z type liquid crystal LB film	1.0	5.8		0.17	
WTA/docosylamine superlattice	1.9	2.7		0.70	
Hexadec l ene maleic anydride alternating polymer/ l docosylamine	0.8	2.9 3.8	0.02 0.114	0.21 0.27	1.22 3.32
Linear polysiloxane/ eicosylamine	9.6	2.6	0.011	3.69	56.77
Linear polysiloxane/ eicosylamine with CdCl$_2$	12.2	2.4	0.012	5.08	71.89
Copolymer of fluorinated alkylmethacrylate & methacrylic acid/p (p octadecylaminophenyl azo) benezensulfamide	0.0025	2.2 3.0		0.0008 0.001	
lH,lH$_1$,2H$_1$ 2H per flourode conoylmonoit aconate monomer/eicosylamine	4.9	2.8	0.011	1.75	27.92
lH,lH$_1$,2H$_1$ 2H per fluorode conoylmonoit aconate polymer/eicosylamine	3.9	2.8	0.012	1.39	21.28
A mixed polysiloxane/ eicosylamine	5.6	4.8	0.008	1.17	28.57
Ploysiloxane/eicosylamine	12.0		0.016	3.61	52.06
T butyl calix[4]arene acid/ amine	1.5				6.8
T octyl calix[8]arene acid/ amine	6.9				26.1
T butyl calix[8]arene acid/ amine	14.33				75.2
Z type azobenzene derivative LB film	22.0				

flexibility, high strength, formability, and low cost with high electro-active properties of ceramic materials. The composites contain two or more chemically different materials or phases. In these materials, it is possible to tailor electrical and mechanical properties catering to a wide variety of applications. Recent studies on ceramic-polymer-based pyroelectric composites show potential usefulness via large-area, lightweight, enhanced-strength, flexible, IR-sensing elements. Thus, composites based on pyroelectric ceramic

particles embedded in polymer possess hybrid properties derived from individual components. These hybrid properties include large pyroelectric coefficients of ceramic material and excellent mechanical strength, formability, and robustness of the polymer, eventually useful for IR detectors without the need for a substrate. An overview of the theory uses models to predict dielectric behavior and the pyroelectric coefficient. Fabrication techniques for biphasic composites as well as a review of the latest work can be found in Ref. 92.

The dielectric constant and pyroelectric coefficient have been investigated on TGS–PVDF composites with different proportions of TGS.[93] The variation of dielectric and pyroelectric coefficients with temperature for composites were found to be the same as those reported for TGS single crystals. Furthermore, it was reported that with 50 wt% of TGS particles in the composite, the figure of merit is the largest among all of the other compositions investigated. It was also shown that the D^* value of detectors made of a TGS composite reaches up to 5 to 7×10^7 $cmHz^{1/2}W^{-1}$. Wang et al. investigated TGS particles of 45–75 μm of different volume fractions (up to an 80 vol. fraction) dispersed in organic solvent for the preparation of films using the solution-casting technique.[94] It was observed that the pyroelectric coefficient increased to 90 $\mu C/m^2K$, and the figure of merit p/ε increased to 3.3 with an 80% volume of TGS particles. A novel technique used in the fabrication of a ATGS-PVD-oriented film is the application of a high electric field during the preparation of the film.[95] It was also reported that the PVDF: ATGS (L-alanine-doped TGS) with the highest field grains became oriented to the *b* axis when the field was increased to be perpendicular with the *b* axis. With a field of 10 kV/cm, better results have been reported for a dielectric constant of ~10 and a pyroelectric coefficient of ~30 $\mu C/m^2K$ at about 30 °C. Recently, Yang et al. performed an extensive and noteworthy study on TGS:P (VDF-TrFE) composites with various volume fractions (0.05–0.43) of TGS embedded in P(VDF-TrFE).[96] The pyroelectric coefficient varied from 32 to 102 $\mu C/m^2K$. The dielectric constant increased from 9.66 to 12.27, while the dielectric loss decreased from 0.021 to 0.008. The two phases of samples were poled in same direction, and the pyroelectric coefficient was reinforced, while the piezoelectric contribution partially cancelled out. The low piezoelectric activity in the pyroelectric composite is an asset, as it reduces vibration-induced noise. TGS/P(VDF-TrFE) is a good candidate as a sensing element in pyroelectric IR-detecting devices.

A detailed study on the pyroelectric and piezoelectric properties of PT-P (VDF-TrFE) composites gives the maximum value of pyroelectric coefficient with a 54% volume fraction of the particles.[97] The pyroelectric coefficient and dielectric constant were 40.7 $\mu C/m^2K$ and 57.3, respectively, giving a value of 0.71 for the figure of merit. However, the maximum value for the figure of merit (0.92) for a composite with 49% volume fractions was obtained only when the ceramic phase was poled. However, when both of the phases were

poled, the pyroelectric coefficient and dielectric constant were 69.2 $\mu C/m^2K$ and 55, respectively, giving the figure of merit value of 1.24. The pyroelectric properties of $PbTiO_3$-P(VDF-TrFE) 0-3 nanocomposite films fabricated using various volume fractions of ceramic particles of about 70 nm in size have been investigated by Chen et al.[98] The authors were able to fabricate films up to a volume fraction of only 12% due to the problem of agglomeration. The films were prepared using the spin-coating method on aluminum-coated glass. All of the figures of merit reported (F_I, F_V, and F_D) showed an increase of volume fraction in lead-titanate ceramic particles. Results obtained for pyroelectric properties are shown in Fig. 4.4. It was concluded that the pyroelectric coefficient of the composite with a 12% volume fraction of PT was 40% higher than that of the polymer. A value of $D^* = 1.2 \times 10^7$ cmHz $^{1/2}$W ^{1} has been achieved in composite films of $(Pb_{0.8}Ca_{0.2})$ TiO_3:P(VDF-TrFE), prepared using an appropriate number of ceramic particles smaller than 100 nm in size.[99] Nanocrystalline calcium-modified lead titanate (PCLT) exhibited a nanoparticle-volume-fraction maximum of around 0.11 for F_V and F_D.[100] The figures of merit were 35% higher than they were with the poled copolymer. A noteworthy study performed on thin films deposited on a silicon substrate [consisting of 12 vol.% of nano-sized lanthanum- and calcium-modified lead titanate embedded in P(VDF-TrFE) 70/30 matrix] formed pyroelectric sensors with three different configurations. The maximum specific detectivity D^* was reported as 1.3×10^7 cm $Hz^{1/2}$/W (at 1 kHz), 2.11×10^7 cm$Hz^{/2}$/W (at about 300 Hz), and 2.8×10^7 cm$Hz^{1/2}$/W (between 5 and 100 Hz), respectively. The authors suggested that sensors fabricated with PCLT/P(VDF-TrFE) nanocomposites have potential use in silicon-based pyroelectric sensors.[101]

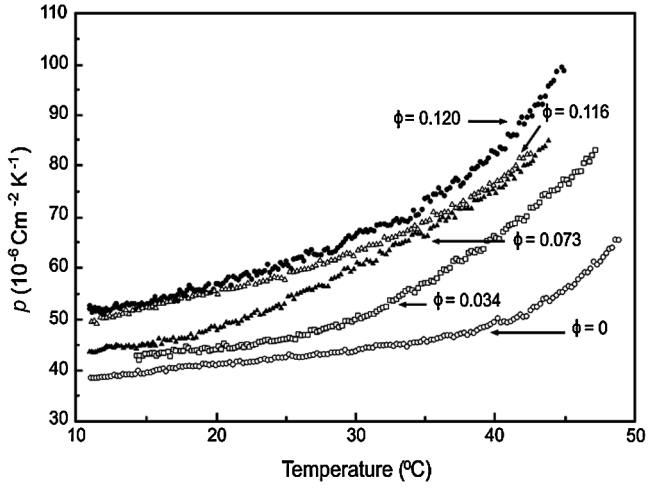

Figure 4.4 Pyroelectric coefficients of composite films with various volume fractions for ceramic lead titanate as a function of temperature. Adapted from Ref. 98 with permission from Elsevier.

Specific detectivities of 4.2×10^6 and 3.4×10^7 $cmHz^{1/2}W^{-1}$ of PCLT/P (VDF-TrFE) film have been obtained on a porous silicon and plastic [polyethylene terephthatate (PET)] substrate, respectively.[102] These specific detectivities were found to be 1–2 orders of magnitude higher than that of the sensor on a bulk-silicon substrate fabricated under similar conditions. The values for F_V, pyroelectric coefficient, and dielectric constant were 3.74 $\mu C/m^2K$, 56.5 $\mu C/m^2K$, and 11, respectively. Lam et al. used thermoplastic elastomer and polyurethane (PU) to fabricate a 0-3 composite with PZT. With a 30% volume fraction of PZT, the value of the pyroelectric coefficient at room temperature was found to be 90 $\mu C/m^2K$—more than tenfold higher than a PZT:PVDF composite with the same volume fraction of ceramic.[103] It was concluded that large electrical conductivity may enhance the pyroelectricity in composites.

Recently, thick films of 0-3 composites of lead zirconate titanate ceramic and polyvinylidene-trifluorethylene copolymers have been produced by spin coating on a gold-coated silicon wafer.[104] A pyroelectric coefficient of 92 $\mu C/m^2K$ has been measured for composites with 20% volume of ceramic. For composites with 10 and 20 vol.% of ceramic, voltage and current figures of merit are higher than they are in PZT thick films.

Lithium tantalate (LT: $LiTaO_3$) ceramic particles have been incorporated into a P(VDF-TrFE) 70/30 mol% copolymer matrix to form composite films. The films were prepared using the solvent-casting method with the LT powder homogeneously dispersed in the P(VDF-TrFE) copolymer matrix in various volume fractions. Electrical properties such as the dielectric constant, dielectric loss, and pyroelectric coefficient have been measured as a function of temperature as well as frequency. In addition, the materials' figures of merit have been calculated to assess the material's use in IR detectors. Results show that LT-P (VDF-TrFE) fabricated composite films have potential for uncooled IR-sensor applications operating at moderate temperatures.[105] The figures of merit for important 0-3 composites are listed in Table 4.13 for reference.

4.5 Other Pyroelectric Materials

A strong pyroelectric effect is one of the most important features in some semiconducting materials, such as group-III nitride oxides AlN, GaN, and ZnO. Studies on the pyroelectric properties of GaN and AlN are still in preliminary stages. Further theoretical and experimental studies are required to fully understand the characteristics of the pyroelectric effect of III nitrides. New pyroelectronic-device concepts will certainly emerge to take full advantage of the unique properties of III-nitride-based materials.[106]

4.5.1 Aluminum nitride (AlN)

Pyroelectric properties of high-quality (0001) AlN films grown on (111) Si substrates were studied by Fuflyigin et al.[107] In these films, the polar axis

Table 4.13 Material characteristics and figures of merit for selected important composites.[92]

Sample	$F_I \quad p$ (μCm ^{2}K ^{1})	ε'	$F_V \quad p/\varepsilon'$ (μCm ^{2}K ^{1})
P(VDF TrFE) (commercial sample)	34.0	16.1	2.1
PVDF (commercial sample)	38.0	5.3	5.7
P(VDF TrFE)70/30 (commercial sample)	412.0	11.0	3.7
PT(vol 62%):PVDF fabricated with dispersoid ceramic grains pressed into thin films of 30 70 μm	130.0	54.0	2.4
PLZT(26.27wt%):P(VDF TrFE) fabricated with dispersoid ceramic grains using the solution casting method for thick films of $\sim$ 20 μm	16.7	25.0	0.66
PLZT (12.33wt%):nano P(VDF TrFE) fabricated with dispersoid ceramic grains using the solution casting method for thick films of $\sim$ 20 μm	9.0	14.12	0.64
PZT (vol. 50%):PVDF	90.0	10.0	0.11
PZT (vol. 50%):P(VDF TrFE)	39.0	118.0	0.33
TGS:PVDF	30.0	10.0	3.0
BT:PVC	0.08	3.7	0.02
PLZT (10.57wt%):P(VDF TrFE) fabricated with dispersoid ceramic grains using the solution casting method for thick films of $\sim$ 30 μm	11.07	33.15	0.33

<0001> is oriented perpendicular to the film's plane. The value of the pyroelectric coefficient was in the range of 6 to 8 $\mu C/m^2K$, yielding a p/ε figure of merit of 0.8–0.95. The pyroelectric coefficient was independent of both temperature and applied bias. Leakage current as low as 1 to 2 $\times$ 10 ^{9} A/cm^2 was measured at 5 V on large-area devices. Results indicate that AlN films might be a good candidate for pyroelectric thin-film devices.

4.5.2 Gallium nitride (GaN)

Wurtzite GaN is a natural pyroelectric with polarization in the direction of the *c* axis. Bykhovski et al. reported the pyroelectric properties of type-*n* gallium-nitride film deposited over basal-plane sapphire substrate.[108] The resulting pyroelectric voltage was on the order of 10^4 V/mK—comparable to that of pyroelectric ceramics, such as PZT and BT.

4.5.3 Zinc oxide (ZnO)

Zinc oxide (ZnO) is a unique material that exhibits multiple semiconducting, piezoelectric, and pyroelectric properties.[109] The production of primary pyroelectricity in ZnO is due entirely to the thermal displacement of oxygen relative to the location of zinc in the unit cell, whereas the secondary pyroelectric coefficient is due to polarization produced by thermal expansion. The total pyroelectric coefficient of ZnO has been measured at room temperature as –9.4 $\mu C/m^2 \cdot K$, with a magnitude that varies between

–0.28 $\mu C/m^2 \cdot K$ at 20 K and about –11 $\mu C/m^2 \cdot K$ at 500 K.[110] The secondary pyroelectric coefficient can be calculated from the piezoelectric stress and thermal expansion coefficients for ZnO as –5.2 $\mu C/m^2 \cdot K$ at 300 K, and the total coefficient, by difference, as –4.2 $\mu C/m^2 \cdot K$ at room temperature.[111] Hsiao et al. utilized a two-step sputtering process to deposit the ZnO film on Si/SiN/Au/Cr to improve the responsivity of a ZnO pyroelectric sensor. The top electrodes that partially cover the ZnO film (an additional nickel film is deposited over the uncovered part) obtain a voltage responsivity around 8 V/W at 500 Hz.[112] Chong et al. fabricated an array consisting of 4×4 pyroelectric ZnO sensing elements by magnetron sputtering on a self-suspended silicon nitride/silicon oxide membrane.[113] The performance of the sensor in terms of specific detectivity D^*, as measured by the authors, had a maximum D^* of 1.3×10^5 $cmHz^{1/2}/W$ at a frequency of 140 Hz for a laser wavelength of 690 nm.[113]

4.6 Lead-free Pyroelectric Ceramics

Ferroelectric ceramics, such as lead titanate and lead zirconate, are widely used in sensors and other devices due to their superior piezoelectric and pyroelectric properties. However, the use of lead-based ceramics has caused serious environmental pollution. The toxicity of these materials both during the manufacturing process (caused by evaporation of lead) and after fabrication is of serious concern. Therefore, there is a great need to develop lead-free ceramics to replace the lead-containing ceramics in various applications including pyroelectric IR sensors. In the recent past, efforts have been made to investigate lead-free bismuth sodium titanate (BNT) and its variations.[114–116] Lau et al. investigated ($K_{0.5}Na_{0.5}NbO_3$)-based (KNN) and ($Bi_{0.5}Na_{0.5}TiO_3$–$Bi_{0.5}K_{0.5}TiO_3$)-based (BNKT) ceramics and their thermal, dielectric, and pyroelectric properties for their potential in pyroelectric sensor applications.[116] The authors fabricated the following compositions:

$[(K_{0.5}Na_{0.5})_{0.96}Li_{0.04}](Nb_{0.8}Ta_{0.2})O_3$-KNLNT,

$[(K_{0.5}Na_{0.5})_{0.96}Li_{0.4}](Nb_{0.84}Ta_{0.1}Sb_{0.06})O_3$-KNLNTS,

$[(Bi_{0.5}(Na_{0.95}K_{0.05})0.5]_{0.95}Ba_{0.05}TiO_3$-BNKBT,

$[(Bi_{0.5}(Na_{0.94}K_{0.05}Li_{0.016})0.5]_{0.95}Ba_{0.05}TiO_3$-(BNKLBT).

Table 4.14 lists the pyroelectric coeffecients and figures of merit for some lead-free ceramic samples. The BNKLBT ceramic shows excellent pyroelectric properties as compared with KNN-based and PZT ceramics.

4.7 Conclusions

This chapter has explored various important pyroelectric materials in single crystalline, and polycrystalline thin-film forms, listing important pyroelectric performance parameters. From a commercial/performance viewpoint, TGS,

Table 4.14 Pyroelectric coefficients and figures of merit for lead-free ceramic samples.

Sample	ε_r	tanδ	ρ (kg/m^3)	c_v ($\times 10^6$J/m^{3}K)	p (μC/m^{2}K)	F_I ($\times 10^{12}$ p/c_v m/V)	F_V $p/c_v\varepsilon_r\varepsilon_0$ (m^2/C)	F_D $p/c_v\sqrt{\varepsilon_r\varepsilon_0}$ tanδ (μPa$^{1/2}$)
KNLNT	1230	0.0182	5081	0.263	165	123.5	.011	8.82
KNLNTS	1520	0.0181	4556	0.448	190	93.1	0.007	5.98
BNMBT	853	0.0278	5800	0.288	325	194.6	0.026	13.43
BNKLBT	858	0.0294	5770	0.283	360	220.5	0.029	14.75
PZT	1990	0.0140	7700	0.380	414	141.5	0.008	9.01

lithium tantalite, and PVDF are the most suitable materials, whereas thin-film-based detectors are the most appropriate where compatibility with silicon technologies is required. Lithium-tantalate-based detectors give inferior performance as compared to TGS, due to their lower pyroelectric coefficient and slightly higher relative permittivity. However, they have the following advantages: high chemical stability, low loss, a high Curie temperature, and insolubility in water. SBN single crystals have favorable figures of merit F_D. Pyroelectric ceramics offer a number of advantages: they are inexpensive to manufacture in a large area, mechanically and chemically robust, possess a high Curie temperature, and do not suffer from thermally induced spikes. Pyroelectric polymers are attractive for use in vidicon applications because of their superior mechanical properties, ease of fabrication, low permittivities, and low thermal conductivity. However, to obtain a direct comparison among them and suggest one over the other is not possible, as their uses are specific to the application for which they are needed. Thus, the detector area, operating frequency, operating temperature range, maximum incident power, environmental stability, availability, cost, and applications are all important parameters to consider.

References

1. R. B. Lal and A. K. Batra, "Growth and properties of triglycine (TGS) sulfate crystals review," *Ferroelectrics* **142**, 51–82 (1993).
2. H. V. Alexandru, C. Berbecaru, F. Stanculescu, L. Pintilie, I. Matei, and M. Lisca, "Doped TGS crystals for IR detection and sensors," *Sensors and Actuators A* **113**, 387–392 (2004).
3. M. Banan, A. K. Batra, and R. B. Lal, "Growth and morphology of TGS crystals," *J. Mat. Sci. Lett.* **8**, 1348–1349 (1989).
4. M. Banan, R. B. Lal, A. K. Batra, and M. D. Aggarwal, "Effect of poling on the morphology and growth rate of TGS crystals," *Cryst. Res. Technol.* **24**(3), K33 (1989).
5. N. Nakatan, "Ferroelectric domain structure and internal bias field in TGS crystals," *Jpn. J. Appl. Phys.* **30**(12A), 3445–3449 (1991).

6. L. Yang, A. K. Batra, and R. B. Lal, "Growth and characterization of triglycine sulfate (TGS) crystals grown by cooled sting technique," *Ferroelectrics* **118**(1), 85–91 (1991).
7. M. Banan, R. B. Lal, and A. K. Batra, "Modified triglycine sulfate (TGS) single crystals for pyroelectric IR detector applications," *J. Mat. Sci.* **27**, 2291–2297 (1992).
8. Z. D. Deng, "A new method of growth ferroelectrics crystal," *Ferroelectrics* **39**, 1237–1239 (1981).
9. K. L. Bye and E. T. Keve, "Structural inhibition of ferroelectric switching in triglycine sulfate x-ray treatment," *Ferroelectrics* **4**, 87–95 (1972).
10. G. M. Loiacono and J. P. Dougherty, "Final technical report (contract no DAAK70-77-C-0098)" Night Vision and Electro-optics Laboratories, Fort Belvoir, VA (1978).
11. M. H. Lee, R. Guo, and A. S. Bhalla, "Pyroelectric sensors," *J. Electroceramics* **2**, 229–242 (1998).
12. J. Chang, A. K. Batra, and R. B. Lal, "Growth and properties of urea-doped triglycine sulfate (UrTGS) crystals," *J. Crystal Growth* **158**, 284–288 (1996).
13. J. Novotny, J. Zelinka, and F. Moracev, "Broadband IR detectors on the basis of PATGS/Pt(IV) single crystals," *Sensors and Actuators A* **119**, 300–304 (2005).
14. A. K. Batra, M. D. Aggarwal, and R. B. Lal, "Growth and characterization of doped DTGS crystals for IR sensing devices," *Mat. Lett.* **57**, 3943–3948 (2003).
15. G. Su, Y. He, H. Yao, Z. Shi, and Q. Wu, "A new pyroelectric crystal L-lycine-doped TGS (LLTGS)," *J. Crystal Growth* **209**, 220–222 (2000).
16. K. Meera, R. Muralidharan, A. K. Tripathi, R. Dhanasekaran, and P. Ramasamy, "Growth of thiourea-doped TGS crystals and their characterization," *J. Crystal Growth* **260**, 414–421 (2004).
17. A. Shaulov, W. A. Smith, and N. Y. Rao, "Advantages of obliquely cut TGS crystals in pyroelectric applications," *Ferroelectrics* **38**, 967–970 (1981).
18. A. Shaulov and W. A. Smith, "Optimum cuts of monoclinic m crystals for pyroelectric detectors," *Ferroelectrics* **49**, 223–228 (1984).
19. A. Shaulov, "Improved figure of merit in obliquely cut pyroelectric crystals," *Appl. Phys. Lett.* **39**(2), 180–183 (1981).
20. P. W. Whipps and K. L. Bye, "Polycrystalline tri-glycine sulphate-selenate materials for pyroelectric applications," *Ferroelectrics* **7**, 183–185 (1974).

21. K. L. Bye, P. W. Whipps, and E. T. Keve, "High internal bias fields in TGS (L-alanine)," *Ferroelectrics* **4**, 253–256 (1972).
22. A. Hadni, R. Thomas, and C. Erhard, "An unusual type of epitaxial growth," *Physica Status Solidi (a)* **39**, 419–424 (2006).
23. A. Hadni and R. Thomas, "The use of a regular distribution of minute pinholes for the epitaxial growth of an oriented thin film," *Thin Solid Films* **81**, 247–256 (1981).
24. M. Nitzani, R. Yasinov, and S. Berger, "Pyroelectric Nano-composite crystallographically oriented thin films of triglycine (TGS)," *Ferroelectrics* **390**, 115–121 (2009).
25. Y. Xu, *Ferroelectric Materials and Their Applications*, North-Holland, London, pp. 225–231 (1991).
26. J. R. Curie, "Studies on the Functional Ferroelectric Materials for IR Sensors," M.S. Thesis, Alabama A&M University, Normal, Alabama (2004).
27. E. Yamaka, T. Hayashi, and M. Matsumoto, "$PbTiO_3$ pyroelectric IR detector," *IR Physics* **11**, 247–248 (1971).
28. T. Futakuchi and K. Tanino, "Pyroelectric properties of La-modified $PbTiO_3$ thin films prepared by screen printing," *Jpn. J. Appl. Phys.* **33**, 5294–5296 (1994).
29. K. No, C. G. Choi, D. S. Yoon, T. H. Sung, Y. C. Kim, I. S. Jeong, and W. J. Lee, "Pyroelectric properties of sol-gel derived lanthanum modified lead titanate thin films," *Jpn. J. Appl. Phys.* **35**, 2731–2733 (1996).
30. C. Ye, T. Tamagawa, P. Schiller, and D. L. Polla, "Pyroelectric $PbTiO_3$ thin film for micro-sensor applications," *Sensors and Actuators A* **35**, 77–83 (1992).
31. B. Pachaly, R. Bruchhuas, D. Pitzer, H. Huber, W. Wersing, and F. Koch, "Pyroelectric properties of lead titanate thin films deposited on Pt-coated Si wafers by multi-target sputtering," *Integrated Ferroelectrics* **5**, 333–338 (1994).
32. S. Chopra, S. Sharma, T. C. Goel, and R. G. Mendiratta, "Structural, dielectric, and pyroelectric studies of $Pb_{1-x}Ca_xTiO_3$ thin films," *Solid State Communications* **127**, 299–304 (2003).
33. C. C. Chang and Y. C. Lai, "The fabrication and characterization of $(Pb,Ca)TiO_3$ pyroelectric thin films with different Ca contents," *J. Appl. Phys.* **101**, 104106-1–104106-6 (2007).
34. P. Muralt, "Micromachined IR detectors based on pyroelectric thin films," *Rep. Prog. Phys.* **64**, 1339–1388 (2001).
35. K. K. Deb, "Pyroelectric characteristics of a hot-pressed lanthanum-doped PZT [PLZT (8/40/60)]," *Mat. Lett.* **5**, 222–226 (1987).

36. E. Suaste-Gomez, R. Gonzalez-Ballesteros, and V. Castillo-Rivas, "Pyroelectric properties of $Pb_{0.88}Ln_{0.08}Ti_{0.98}Mn_{0.02}O_3$ (Ln = La, Sm, Eu) ferroelectric ceramic system," *Mat. Character.* **50**, 349–352 (2003).
37. D. Czekaj, A. Lisinska, M. F. Kuprianov, and Y. N. Zakharov, "Pyroelectric properties of the multi-component ferroelectric ceramic materials," *J. Europ. Ceram. Soc.* **19**, 1149–1152 (1999).
38. P. Guggilla, A. K. Batra, J. R. Currie, M. D. Aggarwal, and R. B. Lal, "Pyroelectric ceramics for IR detection applications," *Mat. Lett.* **60**, 1937–1942 (2006).
39. A. K. Batra, P. Guggilla, M. D. Aggarwal, and R. B. Lal, "Effects of O^+ irradiation on IR sensing characteristics of modified PZT ceramic," *Nuclear Instruments and Methods in Physics Research B* **246**, 369–373 (2006).
40. K. K. Deb, K. W. Bennett, P. S. Brody, and B. M. Melnick, "Pyroelectric characteristics of thin PZT (40/60) film on platinum film for IR sensors," *Integrated Ferroelectrics* **6**, 253–264 (1996).
41. M. Kobune, S. Fujii, R. Takayama, and A. Tomozawa, "Preparation and pyroelectric properties of PLZT thin films," *Jpn. J. Appl. Phys.* **35**, 4980–4983 (1996).
42. A. Loziński, F. Wang, A. Uusimäki, and S. Leppävuori, "PLZT thick film for pyroelectric sensors," *Meas. Sci.Technol.* **8**, 33–37 (1997).
43. J. S. Yang, S. H. Kim, D. Y. Park, E. Yoon, J. S. Park, T. S. Kim, S. G. Kang, and J. Ha, "Thickness effects on the pyroelectric properties of chemical-solution-derived $Pb(Zr_{0.3}Ti0_{.7})O_3$ thin films for IR devices," *Jpn. J. Appl. Phys.* **42**, 5956–5959 (2003).
44. J. S. Yang, S. H. Kim, J. H. Yeom, C. Y. Koo, C. S. Hwang, E. Yoon, D. J. Kim, and J. Ha, "Piezoelectric and pyroelectric properties of Pb(Zr, Ti)O_3 films for micro-sensors and actuators," *Integrated Ferroelectrics* **54**, 515–525 (2003).
45. C. Shi, L. Meidong, L. Churong, Z. Yike, and J. D. Costa, "Investigation of crystallographic and pyroelectric properties of lead-based perovskite-type structure ferroelectric thin films," *Thin Solid Films* **375**, 288–291 (2000).
46. Q. Zhang and R. W. Whatmore, "Improved ferroelectric and pyroelectric properties in Mn-doped lead zirconate titanate thin films," *J. Appl. Phys.* **94**, 5228–5233 (2003).
47. M. Kobune, H. Ishito, A. Mineshige, S. Fujii, R. Takayama, and A. Tomozawa, "Relationship between pyroelectric properties and electrode sizes in (Pb, La)(Zr, Ti)O_3 (PLZT) thin films," *Jpn. J. Appl. Phys.* **37**, 5154–5157 (1998).

48. Y. Darvina Irzaman, A. Faud, P. Arifin, M. Budiman, and M. Barmawi, "Physical and pyroelectric properties of tantalum-oxide-doped PZT thin films and their application for IR sensors," *Phys. Stat. Sol. (a)* **199**, 416–424 (2003).
49. L. Shaobo and L. Yanqiu, "The crystalization and electrical properties of lead-based ferroelectric thin films for uncooled pyroelectric IR detector," *J. Mat. Sci.: Materials in Electronics* **15**, 545–548 (2004).
50. K. C. McCarthy, F. S. McCarthy, G. Teowee, T. J. Bukowski, T. P. Alexander, and D. R. Uhlmann, "Pyroelectric properties of various sol-gel derived thin films," *Integrated Ferroelectrics* **17**, 377–385 (1997).
51. H. Han, S. Kotru, J. Zhong, and R. K. Pandey, "Effect of Nb doping on pyroelectric property of lead zirconate titanate films prepared by chemical solution deposition," *IR Physics and Technology* **51**, 216–220 (2008).
52. X. Tian, Y. Li, and Z. Xu, "Laser annealing of $Pb(Zr0_{.52}Ti_{0.48})O_3$ thin films for pyroelectric detectors," *Thin Solid Films* **517**, 5855–5857 (2009).
53. R. Bruchhaus, D. Pitzer, M. Schreiter, and W. Wersing, "Optimized PZT thin films for pyroelectric IR detector arrays," *J. Electroceramics* **3** (2), 151–162 (1999).
54. R. A. Dorey and R. W. Whatmore, "Pyroelectric PZT/PMNZTU composite thick films," *J. Europ. Ceram. Soc.* **25**, 2379–2382 (2005).
55. S. E. Stokowski, J. D. Venables, N. E. Byer, and T. C. Ensign, "Ion-beam milled, high-detectivity pyroelectric detectors," *IR Physics* **16**, 331–334 (1976).
56. C. B. Roundy, "Pyroelectric self-scanning IR detector arrays," *Appl. Opt.* **18**, 843–945 (1979).
57. V. Norkus, "Pyroelectric IR detectors based on lithium tantalate: state of the art and properties," *Proc. SPIE* **5251**, 121–128 (2003) [doi: 10.1117/12.513884].
58. M. C. Kao, H. Z. Chen, C. N. Wang, and Y. C. Chen, "Pyroelectric properties of sol-gel derived lithium tantalite thin films," *Physica B* **329**, 1527–1528 (2003).
59. A. Seifert and P. Muralt, "$LiTaO_3$ thin films for pyroelectric devices," unpublished.
60. L. Nougaret, P. Combette, and F. Pascal-Dalannoy, "Growth of lithium tantalate thin films by radio-frequency magnetron sputtering with lithium enriched target," *Thin Solid Films* **517**, 1784–1789 (2009).
61. P. F. Schmid and F. Levy, "Ferro- and Pyro-electric properties of lithium tantalate ($LiTaO_3$) thin films," *J. Korean Phys. Soc*. **32**, pp. S1454–S1456 (1998).

62. K. Wong, *Properties of Lithium Niobate*, Michael Faraday House, Herts, UK pp. 91–108 (2002).
63. T. Gebre, A. K. Batra, P. Guggilla, M. D. Aggarwal, and R. B. Lal, "Pyroelectric properties of pure and doped lithium niobate crystals for IR sensors," *Ferroelectric Lett.* **31**, 131–139 (2004).
64. M. E. Lines and A. M. Glass, *Principles and Applications of Ferroelectrics and Related Materials*, Clarendon Press, Oxford, pp. 491–495 (1979).
65. T. Zhang and H. Ni, "Pyroelectric and dielectric properties of sol-gel derived barium-strontium-titanate ($Ba_{0.64}Sr_{0.36}TiO_3$) thin films," *Sensors and Actuators A* **100**, 252–256 (2002).
66. J. S. Lee, J. Park, J. Kim, J. Lee, Y. H. Lee, and S. R. Hahn, "Preparation of (Ba,Sr)TiO_3 thin films with high pyroelectric coefficients," *Jpn. J. Appl. Phys.* **38**, L574–L576 (1999).
67. H. Zhu, J. Miao, M. Noda, and M. Okuyama, "Preparation of BST ferroelectric thin films by metal organic decomposition for IR sensors," *Sensors and Actuators A* **110**, 371–377 (2004).
68. S. Sengupta, L. C. Sengupta, J. Synowczynski, and D. A. Rees, "Novel pyroelectric sensor materials," *IEEE Trans. Ultra. Ferro. and Freq. Cont.* **45**(6), 1444–1452 (1998).
69. J. Cheng, X. Meng, J. Tang, S. Guo, and J. Chu, "Pyroelectric $Ba_{0.8}Sr_{0.2}TiO_3$ thin films derived from 0.5 M solution precursor by sol-gel processing," *Appl. Phys. Lett.* **75**, 3402–3404 (1999).
70. D. Kang, M. Han, S. Lee, and S. Song, "Dielectric and pyroelectric properties of barium strontium calcium titanate ceramics," *J. Europ. Ceram. Soc.* **23**, 515–518 (2003).
71. S. Liu, M. Liu, S. Jiang, C. Li, Y. Zeng, Y. Huang, and D. Zhou, "Fabrication of SiO_2-doped $Ba_{0.85}Sr_{0.15}TiO_3$ glass-ceramic films and the measurement of their pyroelectric coefficient," *Mat. Sci. and Eng.* **B99**, 511–515 (2003).
72. S. Liu, M. Liu, S. Jiang, Y. Zeng, C. Li, S. Chen, Y. Huang, and D. Xia, "Preparation and characterization of $Ba_{1-x}Sr_xTiO_3$ thin films for uncooled IR focal plane arrays," *Mat. Sci. and Eng. C* **22**, 73–77 (2002).
73. A. M. Glass, "Investigation of the electrical properties of $Sr_{1-x}Ba_xNb_2O_6$ with special reference to pyroelectric detection," *J. Appl. Phys.* **40**, 4699–4313 (1969).
74. H. Amorin, F. Guerreo, J. Portelles, I. Gonzalez, A. Fundora, J. Siqueiros, and J. Valenzuela, "Effect of La^{3+} doping on the polarization of the LSBN ceramic system," *Solid State Comm.* **106**, 555–558 (1998).
75. C. J. Chen, Y. Xu, R. Xu, and J. D. Mackenzie, "Ferroelectric and pyroelectric properties of strontium barium niobate films prepared by the sol-gel method," *J. Appl. Phys.* **69**, 1763–1765 (1991).

76. M. Venet, I. A. Santos, J. A Eiras, and D. Garcia, "Potentiality of SBN textured ceramics for pyroelectric applications," *Solid State Ionics* **177**, 589–593 (2006).

77. X. Wan, X. Tang, J. Wang, H. L. W. Chang, and C. L. Choy, "Growth and pyroelectric properties of 0.2 mol% Fe-doped $Pb(Mg_{1/3}Nb_{2/3})O_3$-$0.38PbTiO_3$ single crystals by a dynamic technique," *App. Phys. Lett.* **84**, 4711–4713 (2004).

78. Y. Tang, X. Zhao, X. Wan, X. Feng, W. Jin, and H. Luo, "Comparison, dc bias and temperature dependence of pyroelectric properties of <111>-oriented $(1–x)$ $Pb(Mg_{1/3}Nb_{2/3})O_3$ $_xPbTiO_3$ crystals," *Mat. Sci. and Eng. B* **119**, 71–74 (2005).

79. Y. Tang, X. Wan, X. Zhao, X. Pan, D. Lin, and H. Luo, "Large pyroelectric response in relaxor-based ferroelectric $(1–x)Pb(Mg_{1/3}Nb_{2/3})$ O_3 $_xPbTiO_3$ single crystals," *J. App. Phys.* **98**, 084104-1–084104-4 (2005).

80. J. T. Wang and C. Zhang, "Pyroelectric properties of $0.7Pb(Mg_{1/3}Nb_{2/3})$ O_3 $_{0.3}PbTiO_3$ ceramics," *J. App. Phys.* **98**, 054103 (2005).

81. G. Sebald, L. Seveyrat, D. Guyomar, L. Lebrun, B. Guiffard, and S. Pruvost, "Electrocaloric and pyroelectric properties of $0.75Pb(Mg_{1/3}Nb_{2/3})$ O_3-$0.25PbTiO_3$," *J. App. Phys.* **100**, 1241121 (2006).

82. S. E. Aleksandrov, G. A. Gavrilov, A. A. Kapralov, E. P. Smirnova, G. Y. Sotnikova, and A. V. Sotnikov, "Relaxer ferroelectrics as promising materials for IR detectors," *Solid-State Electronics* **74**, 72–76 (2004).

83. P. Kumar, S. Sharma, O. P. Thakur, C. Prakash, and T. C. Goel, "Dielectric, piezoelectric, and pyroelectric properties of PMN-PT (68:32) system," *Ceramics International* **30**, 585–589 (2004).

84. Y. Tang, L. Luo, Y. Jia, H. Luo, X. Zhao, H. Xu, D. Lon, and M. Es-Souni, "Mn-doped $0.71Pb(Mg_{1/3}Nb_{2/3})O_3$-$0.29PbTiO_3$ pyroelectric crystals for uncooled IR focal plane arrays applications," *Appl. Phys. Lett.* **89**, 162906-1–162906-3 (2006).

85. F. Kochary, M. D. Aggarwal, A. K. Batra, R. Hawrami, D. Lianos, and A. Burger, "Growth and electrical characterization of the lead magnesium niobate-lead titanate (PMN-PT) single crystals for piezoelectric devices," *J. Mater Sci: Mat. Electron*. **19**, 1058–1063 (2008).

86. M. Davis, D. Damjanovic, and N. Setter, "Pyroelectric properties of $(1–x)$ $Pb(Mn_{1/3}Nb_{2/3}O_3$ $_xPbTiO_3$ and $(1–x)Pb(Zn_{1/3}Nb_{2/3}O_3$ $_xPbTiO_3)$ single crystals using a dynamic method," *J. Appl. Phys.* **96**, 2811–2815 (2004).

87. *Ferroelectric Polymers*, H. Singh Nalwa, Ed., Marcel Dekker, New York, pp. 183–232 (1995).

88. B. Ploss and S. Bauer, "Charaterization of materials for integrated pyroelectric sensors," *Sensors and Actuators A* **25–27**, 407–411 (1991).
89. N. Neumann, R. Kohler, and G. Hofmann, "Pyroelectric thin film sensors and arrays based on P(VDF-TrEF)," *Integrated Ferroelectrics* **6**, 212–230 (1995).
90. R. Capan, "Organic pyroelectric materials for device applications," *BAU FBE Dergisi* **12**, 75–90 (2010).
91. B. Tesnel, A. Topacli, C. Topacli, M. Durmus, and V. Ahsen, "Characterization of Langmuir–Blodgett films of arachidic acid and 1,2-bis(dodecyloxy)04,5-diaminobenzene in pyroelectric devices," *Colloids and Surfaces A: Eng. Aspects* **299**, 244–251 (2007).
92. M. D. Aggarwal, J. R. Currie, B. G. Penn, A. K. Batra, and R. B. Lal, "Polymer-ceramic composite materials for pyroelectric-IR detectors: an overview," NASA **NASA/TM-2007-215190** (2007).
93. M. Wang, C. S. Fang, and H. S. Zhuo, "Study on the pyroelectric properties of TGS-PVDF composites," *Ferroelectrics* **118**, 191–197 (1991).
94. Y. Wang, W. Zhong, and P. Zang, "Pyroelectric properties of ferroelectric-polymer composite," *J. App. Phys*. **74**(1), 512–524 (1993).
95. C. S. Fang, Q. W. Wang, and H. S. Zhuo, "Preparation and pyroelectric properties of oriented composite ATGS-PVDF film," *J. Korean Phys. Soc*. **32**, S1843–S1845 (1998).
96. Y. Yang, H. L. W. Chan, and C. L. Choy, "Properties of triglycine sulfate/poly(vinylidene fluoride-trifluoroethylene) 0-3 composites," *J. Mat. Sci.* **41**, 251–258 (2006).
97. H. L. W. Chan, W. K. Chan, Y. Zhang, and C. L. Choy, "Pyroelectric and piezoelectric properties of lead titanate/polyvinylidene fluoride-trifluoroethylene 0-3 composites," *IEEE Trans. Dielec. and Elec. Ins*. **5**(4), 505–512 (1998).
98. Y. Chen, H. L. W. Chan, and C. L. Choy, "Pyroelectric properties of $PbTiO_3$/P(VDF–TrFE) 0-3 nanocomposite films," *Thin Solid Films* **323**, 270–274 (1998).
99. Q. Q. Zhang, B. Ploss, H. L. W. Chan, and C. L. Choy, "Integrated pyroelectric arrays based on PCLT/P(VDF-TrFE) composite," *Sensors and Actuators A* **86**, 216–219 (2000) .
100. Q. Q. Zhang, H. L. W. Chan, B. Ploss, and C. L. Choy, "PCLT/P(VDF-TrFE) nanocomposite pyroelectric sensors," *IEEE Trans. Ultra. Ferro. and Freq. Cont*. **48**(1), 154–160 (2001).
101. Q. Q Zhang, H. L. W. Chan, and C. L. Choy, "Dielectric and pyroelectric properties of P(VDF-TrFE) and PCLT–P(VDF-TrFE) 0-3

nanocomposite films," *Composites Part A: Applied Science and Manufacturing* **30**, 163–167 (1999).

102. J. H. Li, N. Y. Yuan, and H. L. W. Chan, "Preparation of PCLT/P (VDF-TrFE) based on plastic film substrate," *Sensors and Actuators A* **100**, 231–235 (2002).
103. K. S. Lam, Y. W. Wong, L. S. Tai, Y. M. Poon, and F. G. Shin, "Dielectric and pyroelectric properties of lead zirconate titanate/ polyurethane composites," *J. Appl. Phys.* **96**(7), 3896–3899 (2004).
104. M. Dietze, J. Krause, C. H. Solterbeck, and M. Es-Souni, "Thick film polymer-ceramic composites for pyroelectric applications," *J. Appl. Phys.* **101**, 054113-1–054113-7 (2007).
105. A. K. Batra, J. Corda, P. Guggilla, M. D. Aggarwal, and M. E. Edwards, "Dielectric and pyroelectric properties of $LiTaO_3$:P(VDF-TrFE) composite film," *Proc. SPIE* **7213**, 721313 (2009) [doi: 10.1117/ 12.807948].
106. W. S. Yan, R. Zhang, X. Q. Xie, P. Han, R. L. Jiang, and S. L. Gu, "Temperature dependence of the pyroelectric coefficient and spontaneous polarization of AlN," *Appl. Phys. Lett.* **90**, 212102-1–212102-3 (2007).
107. V. Fuflyigin, E. Salley, A. Osinsky, and P. Norris, "Pyroelectric properties of AlN," *Appl. Phys. Lett.* **77**(19), 3075–3077 (2007).
108. A. D. Bykhovski, V. V. Kaminski, M. S. Sur, Q. C. Chen, and M. A. Khan, "Pyroelectricity in gallium nitride thin films," *Appl. Phys. Lett.* **69**(21), 3254–3256 (1996).
109. Z. L. Wang, "Nanostructures of ZnO," *Appl. Phys. Lett.* **84**(15), 26–33 (2004).
110. K. H. Hellwege and A. M. Hellwege, Eds., "Subvolume B: piezoelectric, pyroelectric, and related constants," in *Low Frequency Properties of Dielectric Crystals of Landolt-Börnstein: Group III Condensed Matter*, Springer–Verlag, Berlin, pp. 903–936 (1984).
111. S. C. Abrahams, "Structure relationship to dielectric, elastic and chiral properties," *Acta Cryst.* **A50**(6), 658–685 (1994).
112. C.-C. Hsiao, K.-Y. Huang, and Y.-C. Hu, "Fabrication of a ZnO pyroelectric sensor," *Sensors* **8**, 185–192 (2008).
113. N. Chong, H. L. W. Chan, and C. L. Choy, "Pyroelectric sensor array for in-line monitoring of IR laser," *Sensors and Actuators A* **96**, 231–238 (2002).
114. T. Takenaka and H. Nagata, "Current status of lead-free piezoelectric ceramics," *J. Europ. Ceramic Society* **25**, 2693–2700 (2005).

115. E. V. Tamana, V. V. Kiran, and T. B. Sankaram, "Dielectric and pyroelectric properties of Sr-modified $(Na_{0.5}B_{i0.5})Bi_4TiO_4$ ceramics," *J. Alloys and Compounds* **456**, 271–276 (2008).

116. S. T. Lau, C. H. Cheng, S. H. Choy, D. M. Lin, K. W. Kwok, and H. L. W. Chen, "Lead-free ceramics for pyroelectric applications," *J. Appl. Phys.* **103**, 104105-1 (2008).

Chapter 5
Innovative Techniques for Pyroelectric IR Detectors

5.1 Introduction

In addition to developing new ferroelectric thin films and advanced architecture designs, efforts to enhance detectivity and thermal resolution of pyroelectric detectors are still in progress. Some unique techniques for enhancing the performance of pyroelectric IR detectors are discussed in this chapter. The ability to increase pyroelectric responsivity manifold has been demonstrated by the use of these techniques.

5.2 Multilayer Structures

When Alexe and Pintilie performed the thermal analysis of a pyroelectric bimorph structure for a sinusoidally modulated heat flow, they revealed the possibility of obtaining a larger signal than that of a homogeneous pyroelectric structure.[1] The ratio between the signal generated from a bimorph structure and the signal generated from a homogeneous structure under the same conditions depends on the material properties and on the modulation frequency. This ratio, computed for a particular bimorph, is up to 4 at 1 kHz. The main conclusion from the above discussion is that in certain conditions, the signal generated by a pyroelectric bimorph structure could be greater than the signal generated by a homogeneous pyroelectric detector that is made from only one of the two materials of the bimorph.

Lang and Alexe conducted theoretical and experimental studies of pyroelectric bimorph radiation detectors.[2] The bimorphs consisted of two thin layers on a substrate, the upper one having a large pyroelectric coefficient and a large permittivity, the lower one having a smaller pyroelectric coefficient and a smaller permittivity. The upper layer of the electrode absorbs the incident radiation. If the radiation is modulated at a sufficiently high frequency, the thermal waves produced will partially penetrate the lower layer, so that the effective pyroelectric coefficient is dominated by that of the

upper layer. However, the capacitance of the bimorph is the series combination of the two layers, and is lower than that of either of them on their own. This gives a larger voltage responsivity than that achieved when using either of the two layers alone. The analysis was verified experimentally using a PLZT 12/30/70/PZT 30/70 bimorph. The design of a PLZT 8/35/65/$LiTaO_3$ bimorph was simulated. The calculated voltage responsivity was more than 100 times that of a PLZT 8/35/65 monomorph with the same thickness. A pyroelectric bimorph IR detector can be constructed to have voltage responsivity much higher than that of a monomorph. The theory was experimentally verified by tests of a PLZT 12/30/70/ PZT 30/70 bimorph. A much improved design of PLZT 8/35/65/LT was studied in simulation calculations. The calculations showed that it is possible to make a bimorph with a voltage responsivity of more than a hundredfold that of a monomorph of the same thickness.

High-quality multilayer ferroelectric thin films based on erbium-doped lead titanate $Pb_{(1\ x)1.1}Er_xTi_{1\ x/4}O_3$ (PET), where $x = 0.05$ and $Pb_{1.1}(Zr_{0.58}Fe_{0.2}Nb_{0.2}Ti_{0.02})O_3$ (PZFNT) have been processed via chemical solution deposition on textured (111) $Pt/Ti/SiO_2/Si$ substrates.[3] The dielectric, ferroelectric, and pyroelectric properties were characterized. It was shown that the multilayer film exhibits the relaxor-type behavior found for pure PZFNT, and that its transition temperature of 310 °C at 1 kHz lies between those of PET and PZFNT. The dielectric constant of 520 also lies between those of PET and PZFNT. The ferroelectric properties are considerably improved over those of the monomorph films. An unusually high pyroelectric coefficient of about 620 $\mu Cm^{-2}K^{-1}$ was obtained from measurements of the temperature dependence of the remnant polarization between 30–80 °C. The voltage and current responses, measured using a modulated near-IR laser, could be improved by two to three orders of magnitude over those of PZFNT. The thermal time constant τ_T is found to be three orders of magnitude lower than the electrical time constant τ_E, indicating that the high thermal conduction rate in the substrate determines the detector responsivity. In conclusion, this work shows that it is possible to tune the dielectric properties of ferroelectric thin films through the proper choice of heterostructures. The figure of merit for pyroelectric applications can be considerably improved via the use of multilayer thin films. A poling of the film is not necessary due to self-polarization, and high output voltages and currents can be achieved despite the transparency of the films and the use of thick platinized Si substrates. In this respect, the response of the film is expected to improve via the use of micromachined detector elements.

Ferroelectric $Pb(Zr_{0.3}Ti_{0.7})O_3/PbTiO_3$ multilayer thin films are fabricated by the sol-gel method.[4] The properties of PZT/PT multilayer thin films with different PZT-and PT-layered stacking structures have been systematically studied. The structures of the films are shown in Fig. 5.1.

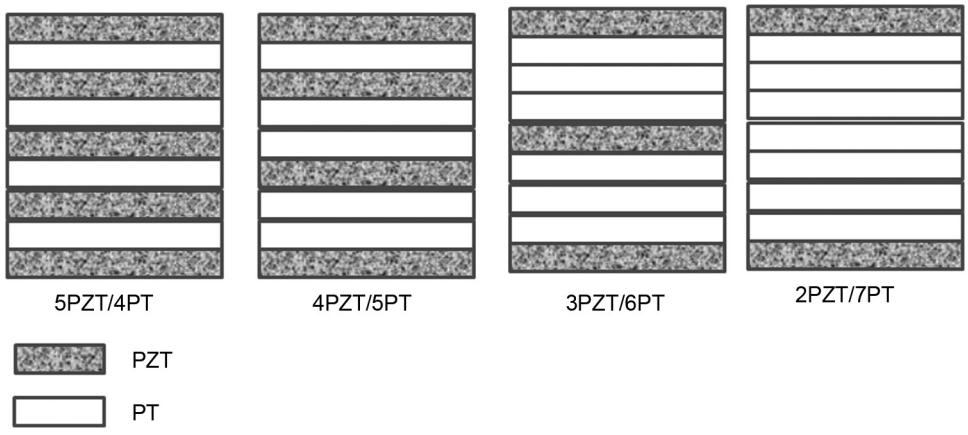

Figure 5.1 The stacked structures of PZT and PT films.

All of the films were dense and smooth with a single perovskite phase. "Pinched" ferroelectric hysteresis loops are found for multilayer thin films. The dielectric constant of multilayer thin film decreases when the PT volume fraction increases. The dielectric loss of 5PZT/4PT multilayer thin film is comparable to that of pure PZT; however, all of the other multilayer thin films show much higher dielectric loss. When compared to the pure PZT thin film, the 5PZT/4PT multilayer film has comparable pyroelectric coefficient, reduced dielectric constant, and comparable dielectric loss. Therefore, the 5PZT/4PT thin film shows a higher pyroelectric detectivity figure of merit (2.1×10^{-5} Pa$^{1/2}$) and is found to be better than pure PZT thin film and a promising material structure for pyroelectric application.

Sun et al. performed a comparison study on sol-gel-prepared $Pb(Zr_{0.3}Ti_{0.7})O_3$ and $Pb(Zr_{0.3}Ti_{0.7})O_3/PbTiO_3$ multilayer thin films for pyroelectric IR detectors and found PZT/PT to be a promising candidate for IR detectors due to the reduced dielectric constant of the multilayer structure.[5]

5.3 Compositionally Graded Structures

Compositionally graded ferroelectric devices, such as ones formed from potassium tantalum niobate and barium strontium titanate, have recently been shown to demonstrate a whole new pyroelectric phenomenon.[6,7] Upon interrogating capacitor-like structures with a strong electric field (active rather than passive mode operation), free charge was found to preferentially accumulate on one electrode of the devices, a result of the inherent asymmetries provided by the internal self-biases created by the compositional gradients.[6 8] The *pumping action* of the graded ferroelectric devices leads to offsets, or shifts, along the displacement axis in otherwise conventional displacement-versus-electric-field ferroelectric hysteresis loops. It has been

demonstrated that such effects are not a result of nonlinear or asymmetric contact effects, leakage currents, or field breakdown within the material. The position and direction of the offsets were found to be determined by the polarization gradients, temperature, and magnitude of the periodic excitation fields—the *pumping force*. Effective pyroelectric coefficients as large as 5×10^{-2} C/m^2 °C, with peak responsivity at approximately 50 °C, have also been reported for compositionally graded BST ferroelectric thin-film devices formed on silicon.[8] Linearly graded (by composition) BST devices were formed by the authors in a customized magnetron sputter system consisting of a bottom Pt/Ti electrode deposited on an oxide silicon wafer, with the BST thin films having continuous composition change from $BaTiO_3$ to $Ba_{0.7}Sr_{0.3}TiO_3$ and a top Au/Cr electrode.[8] The structure in shown in Fig. 5.2 with a $BaTiO_3$ composition at the film/substrate surface and a $Ba_{0.7}Sr_{0.3}TiO_3$ composition at the free surface of the film.[8] These effective pyroelectric coefficients are nearly two orders of magnitude larger than those observed from conventional pyroelectric BST thin-film ferroelectric detectors.[8–10]

Tang et al. prepared a compositionally graded structure of PZT [$Pb(Zr_xTi_{1-x})O_3$] thin films with Zr/Ti ratio from 10/90 to 40/60 grown on $PbZrO_3$-buffered $Pt/Ti/SiO_2/Si$ substrates using a simple sol-gel process.[11] The structure, surface morphology, and dielectric properties of the graded PZT films were measured by XRD, field-emission scanning electron microscopy and Auger electron spectroscopy, and an impedance analyzer, respectively. The results showed that the graded PZT films on $PbZrO_3$-buffered $Pt/Ti/SiO_2/Si$ substrates have a preferred (111) orientation. At 100 Hz, the dielectric

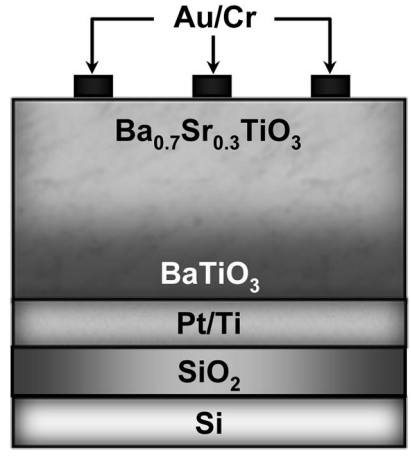

Figure 5.2 A graded-down BST thin-film structure. Adapted with permission from J. V. Mantese, N. W. Schubring, A. L. Micheli, A. B. Catalan, M. S. Mohammed, R. Naik, and G. Auner, "Slater model applied to polarization graded ferroelectrics," *Appl. Phys. Lett.* **71**, 2047–2049 (1997). Copyright 1997, AIP Publishing LLC.

constant and dissipation factor of the graded PZT film are 255 and 0.032, respectively. The pyroelectric coefficient p of compositionally graded PZT film was measured by a dynamic technique. The p value of the graded PZT film is 349 $\mu C/m^2K$ at 25 °C, and the figure of merit of specific detectivity F_D is $16.4 \times 10^{6} Pa^{0.5}$ at 100 Hz. The typical small-signal dielectric constant and dissipation factor of the graded film at a frequency of 100 Hz were 255 and 0.032, respectively. At room temperature, the pyroelectric coefficient and figure of merit of specific detectivity F_D of the graded PZT film were 349 $\mu C/m^2K$ and 16.4×10^{6} Pa $^{0.5}$, respectively. These results qualify these materials for use in pyroelectric sensors.

Tang et al. also reported that the compositionally graded PCT $[(Pb_{1-x}Ca_x)TiO_3]$ thin films of $x = 0$ and 24 mol% were fabricated on Pt/Ti/SiO_2/Si substrates using a modified sol-gel process.[12] The final structure consists of two layers; upgraded films start from $PbTiO_3$ on the Pt electrode and go to the top PCT layer, whereas films with the opposite gradient are called downgraded films. Highly (100)-oriented graded PCT thin films have been obtained with an annealing temperature of 600 °C. At 100 kHz, the dielectric constants were 79 and 128, respectively, for the upgraded and downgraded PCT films. The pyroelectric coefficient p of the graded films was measured using a dynamic technique. At room temperature, the values of p and figures of merit F_D of the upgraded and downgraded PCT films are 95 $\mu C/m^2K$ and 9.1×10^{6} Pa $^{0.5}$, 112 $\mu C/m^2K$ and 8.6×10^{6} Pa $^{0.5}$, respectively.

In conclusion, compositionally graded PCT thin films were grown on Pt/Ti/SiO_2/Si substrates using a modified sol-gel technique with a high degree of preferred (100) orientation in the *a*-axis direction. At 100 kHz, the relative permittivity and dissipation factors were 79 and 0.025, and 129 and 0.024 for the upgraded and downgraded PCT films, respectively. At room temperature, the pyroelectric coefficients p of the upgraded and downgraded PCT films were 95 and 112 $\mu C/m^2K$, respectively. The figures of merit F_D for high detectivity of the upgraded and downgraded PCT films were 9.1×10^{6} and 8.6×10^{6} Pa $^{0.5}$, respectively. The results make these materials useful for pyroelectric sensors.

5.4 Pyroelectric Heterostructures

The primary role of electrodes in the pyroelectric detector is to define the active- or charge-collection area. Tipton investigated the mechanism by which electrodes can also influence IR energy absorption, modify the growth kinetics of pyroelectric material, and influence the polarization of ferroelectric domains.[13] By carefully engineering the electrode system, one can optimize the IR responsivity. In the various applications of pyroelectric sensors and array design, metal electrodes are used, providing a high-conductance path

between the pyroelectric capacitor and the readout circuit. It is worth mentioning that for optimum performance, the highest possible crystalline and dipole orientation are required in pyroelectric materials. Thus, growing the pyroelectric materials on a polycrystalline surface will not produce the maximum degree of orientation. To achieve maximum orientation, one should require that the electrode system prompt the formation of an oriented pyroelectric layer when designing the sensor. Platinum, with a face-centered cubic lattice spacing of 3.92 Å, is well matched to the lead titanate *a*-axis lattice spacing of 3.899 Å. However, the bottom Pt electrode is typically deposited over an amorphous insulator such as SiO_2 or Si_3N_4 in IR imaging devices and is usually polycrystalline. As an electrode to conventional metals, perovskite-type conductive oxides can be used as the electrode materials. It has been proposed by the authors that $La_{1-x}Sr_xCoO_3$ (LSCO) can be used with proper composition and is an ideal material to replace conventional metal electrode systems in many applications. A La-Sr-Co/Pb-La-Zr-Ti-O/La-Sr-Co-O (LPL) system heterostructure was fabricated on a (001)-oriented $LaAlO_3$ (LAO) substrate using a pulsed excimer laser deposition system as shown in Fig. 5.3.

Using the structure, authors could obtain *c*-axis-oriented growth of poled pyroelectric film.[13] With the above cited concept of producing poled film, Tipton et al. have observed enhanced pyroelectric response in sub-100-nm, epitaxial heterostructure films $PbZr_{0.4}Ti_{0.6}O_3$ (PZT) contacted with conducting perovskite oxide top and bottom electrodes of $La_{0.5}Sr_{0.5}CoO_3$ (LSCO).[14] The enhancements are obtained in capacitors where the bottom electrode is processed under reducing conditions. This leads to an asymmetric, temperature-dependent internal field that is produced within the ferroelectric capacitance and manifests itself as a strongly shifted ferroelectric hysteresis loop. Because the shifted coercive voltage lies near the unbiased operating point, the pyroelectric film has a large value of dP/dE. The product $(dP/dE)(dE/dT)$ gives

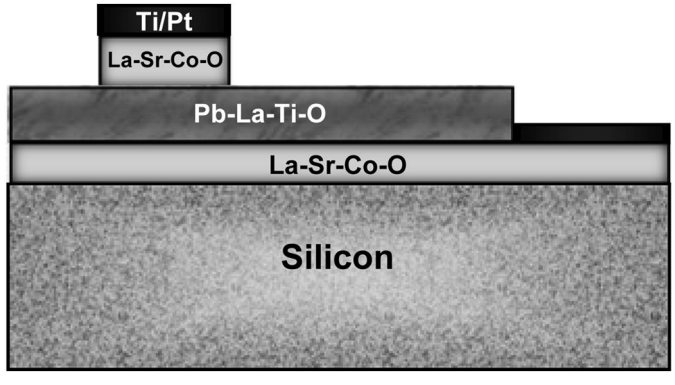

Figure 5.3 A pyroelectric heterostructure cross section (adapted from Ref. 13).

rise to enhanced pyroelectric response. This effect is due to introducing oxygen vacancies into the bottom electrode. Based on the above behavior, the authors derived the "enhanced" pyroelectric coefficient p_e equation:

$$p_e = \left(\frac{\partial D}{\partial T}\right) = \left[\frac{dP_1}{dT} + \frac{\partial E}{\partial E}\left(\varepsilon_o + \frac{\partial P_2}{\partial E}\right)\right], \tag{5.1}$$

where E, P_1, P_2 are the electric field, polarization (temperature dependent), and second polarization (internal electric field dependent), respectively. The first term in Eq. (5.1) is the intrinsic pyroelectric coefficient, while the second term on the right side is the enhancement due to the temperature-dependent internal field. The large pyroelectric response arose from the fact that the polarization function has been modified by the internal electric field. It was speculated that the increase in dP/dE is due to fixed-defect dipoles in the PZT film caused by oxygen vacancies. An enhanced pyroelectric coefficient of 200 to 300×10^{-5} Cm^{-2}K^{-1} was observed by them as compared to the calculated value of approximately 300×10^{-5} Cm^{-2}K^{-1} based on the model of Eq. (5.1). The large pyroelectric response and its stability were very promising from a device point of view. The material figure of merit for detector detectivity F_D for the fabricated asymmetric device structure was approximately 6.7, which was three times larger than the symmetric device structure without an internal field. Thus, the authors proposed that introducing oxygen vacancies into the bottom electrode produces a large temperature-dependent electric field across the PZT layer and, thus, increases the pyroelectric coefficient. Their data shows a 10–30 times increase in performance by the above cited novel structure.

Recently, Wang et al. investigated $Bi_{1.5}Zn_{1.0}Nb_{1.5}O_7$-buffered (BZN) Ba$(Ti_{0.85}Sn_{0.15})O_3$ (BTS) heterostructures deposited on $LaNiO_3/SiO_2/Si$ substrates by pulsed laser deposition.[15] Authors observed that the film and interface microstructures, as well as the dielectric and pyroelectric properties of BTS thin film, can be controlled by the thickness of the BZN buffer layer. It was further observed that the BZN layer suppresses interdiffusion between BTS and the bottom electrode, resulting in a reduction in dielectric loss and leakage current. The pyroelectric properties of different thicknesses of BZN-buffered BTS thin films at 293 K and 100 Hz under different applied electric fields are tabulated in Table 5.1. Although p decreases as the buffer layer thickness increases, F_D attains a maximum (16.3×10^{-5} Pa$^{1/2}$) with a 10-nm BZN buffer layer due to a large reduction in the dielectric loss from ~0.035 to 0.009. F_D for BZN-buffered BTS thin films is therefore higher than those reported for more conventional pyroelectric films such as $Pb(Sr_{0.5}Ta_{0.5})O_3$ (9×10^{-5} Pa$^{1/2}$ at 100 Hz, 325 K, and 12 Hz) and bulk $(Ba_{0.65}Sa_{0.35})TiO_3$ (10.7×10^{-5} Pa$^{1/2}$ at 40 kV/cm, 291 K, and at 21 Hz). The authors concluded that improvements in the tunable and pyroelectric properties of BTS films can be achieved in future device fabrication by controlling the thickness of the BZN layer.[15]

Table 5.1 Pyroelectric properties of different thicknesses of BZN-buffered BTS thin films (at 293 K and 100 Hz).[15]

BZN (thickness) (nm)	p ($\times 10^{-4}$ C/m^{2}K)/ [applied field] (kV/cm)	p ($\times 10^{-4}$ C/m^{2}K)/ [applied field] (kV/cm)	F_D ($\times 10^{-5}$ Pa$^{-1/2}$)/ [applied field] (kV/cm)	F_D ($\times 10^{-5}$Pa$^{-1/2}$)/ [applied field] (kV/cm)
0	36.7 / [25]	44.5 / [50]	8.55 / [25]	12.6 / [50]
10	20.9 / [25]	24.7 / [50]	12.5 / [25]	16.3 / [50]
20	11.8 / [25]	14.3 / [50]	8.26 / [25]	10.6 / [50]
40	5.71 / [25]	7.48 / [50]	5.15 / [25]	6.98 / [50]

IR detectors consisting of thin-film $PbZrTiO_3/YBa_2Cu_3O_{7-x}$-oxide heterostructures have been fabricated.[16] The yttrium barium copper oxide (YBCO) thin film used as the bottom conductive electrode significantly increases the performance of a pyroelectric IR detector. A detectivity value of $\sim 10^8$ cmHz$^{1/2}$/W has been obtained at room temperature for simple heterostructure device configurations in the IR-wavelength range of 1–20 μm. Reactive ion etching has been used to etch the YBCO and the other oxide layers for the development of an air bridge structure, which further reduces thermal mass and increases the operation frequency of the IR detector. MSPZT/YBCO heterostructures were epitaxially grown on YSZ/Si and LAO substrates for IR pyroelectric detectors. The pyroelectric coefficient of MSPZT thin films in the heterostructures was $\sim 80 \times 10^{-5}$ C/m^{2}K, and a detectivity of $\sim 10^8$ cmHz$^{1/2}$/W was achieved for the simple MSPZT/YBCO flat detectors. The heterostructure detector with an airbridge showed three times higher IR photoresponse at a chopper frequency of 30 Hz.

Xu et al. explored a new Mn- and Sb-doped Pb(Zr, Ti) $O_3/YBa_2Cu_3O_{7-y}$ (PMSZT/YBCO) heterostructure fabricated on Si substrate with a YSZ buffer layer by pulsed laser deposition for high performance, uncooled IR detectors.[17] This structure resulted in high figures of merit.[17]

5.5 Use of Nanoporosity

In the recent past, an introduction of nanoporosity in a pyroelectric film has been shown to cause a decrease in the dielectric constant and has been exploited in enhancing the pyroelectric performance of IR sensors.[18,19] Suyal, Seifert, and Setter successfully deposited PZT thin porous film using the sol-gel process with the addition of a polymer as a volatile phase. Pore size can be controlled by the molecular weight and the concentration of polymer.[18] The authors found the dielectric constant to be strongly dependent on porosity, while pyroelectric coefficients changed moderately. In PZT film, the relative permittivity can be decreased from 150 to 95 with Zr/Ti ratios of 45/55 and 15/85,

respectively. For PZT (Zr/Ti = 45/55), the F_V and F_D values increased from 0.28 to 1.0 $\mu C/m^2K$ and from 38 to 80 $\mu C/m^2K$, whereas for PZT (Zr/Ti = 15/85) these values increased from 0.88 to 1.95 $\mu C/m^2K$ and from 79 to 139 $\mu C/m^2K$, respectively, by porous microstructure. This enhancement in values is due to a reduction in the relative permittivity by forming a composite with voids. Similarly, in $PbCa_{1-x}TiO_3$ (PCT) the figures of merit F_V and F_D were shown to be 4.8 and 250 $\mu C/m^2K$, respectively.[18]

5.6 Novel Designs and Techniques

Querner et al. proposed and studied a novel procedure for increasing the sensitivity of pyroelectric detectors and documented a mathematical and physical analysis of the procedure.[20] It is well known that a reduction of the detector element thickness has two effects. On one hand, it raises the voltage responsivity and leads to a reduced heat capacity of the element and, therefore, to a higher temperature change due to the absorbed heat flow. On the other hand, the electrical capacity of the element increases, causing a decrease in responsivity. The authors of this work showed that the first effect can be achieved by inserting a 3D pattern of recessed holes in the sensitive element; this effect is much larger than the other one, and, therefore, one can increase the responsivity. Due to a 3D pattern etched into the sensitive element, lateral heat flux spreading is used to improve the responsivity. The layout of the lithium tantalate chip used is shown in Fig. 5.4. The chip was produced by ion beam etching.

Based on the use of detectors in the 1- to 15-μm range, thermal analysis shows that all of the radiation for passive electric components is absorbed at the crystal, whereas radiation for active components is absorbed by the front electrode. Both have the same absorption coefficients. The holes do not act as light traps, which would modify the absorption of the detectors because the dimensions of the holes are much bigger than the wavelengths of the incident radiation. The preliminary results obtained by the authors concluded that the 3D-patterned structure in sensor design has an important influence on the sensor parameters of the pyroelectric detector elements. Depending on the structure width and other geometrical parameters, the achievable responsivity can be increased by more than 150% for a structure width s of about 232 μm and a thickness of $d_p = 1$ μm in comparison to a common detector structure.

Recently, Hsiao and Yu investigated a novel design via fabricating a 3D ZnO film by the aerosol-deposition rapid process, which induces lateral temperature gradients on the sidewalls of the responsive element, thereby increasing the temperature variation rate and improving the performance of the pyroelectric sensor.[21] A schematic diagram of the multilayer ZnO

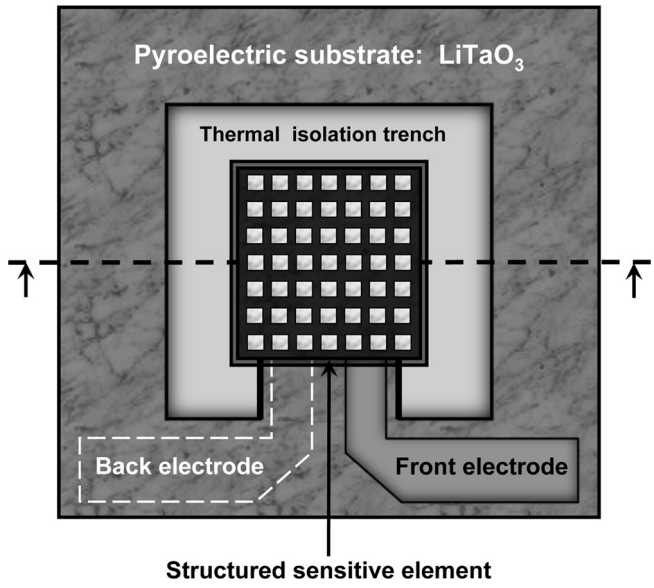

Figure 5.4 A chip layout and cross section of the sensitive element (adapted from Ref. 20 with permission from Elsevier).

pyroelectric device with a comb-like electrode and a 3D ZnO film is provided in Fig. 5.5.

Figure 5.6 shows the voltage response *Rv* of the comb-like electrode-3D-ZnO-IR-device samples for each electrode layout ameliorated by laser annealing.

Figure 5.6 shows that the ZnO pyroelectric device with the comb-like electrode design possessed a voltage response about nine times greater than that with a fully covered electrode at a low frequency. At a high frequency of about 3000 Hz (33 μs), the investigated device has a voltage response about four times that of the fully covered electrode structure. The authors concluded that the 3D ZnO film did indeed induce lateral temperature gradients on the sidewalls of the ZnO layer, thereby increasing the temperature variation rate of the responsive element, enhancing its voltage response and reducing the response time.

Ivry et al. reported that the pyroelectric coefficient of self-supported films of $BaTiO_3$ ($\sim 1 \times 10^{-2}$ C/m^{-2} K^{-1}) with polycrystalline macrodomains might be up to two orders of magnitude larger than that of a single $BaTiO_3$ crystal (0.02×10^{-2} C/m^{-2} K^{-1} at 25 °C) under similar conditions.[22] The authors observed that this enhancement strongly depends on the film geometry and appears only in bucked films where ferroelectric grains undergo self-organization into polycrystalline macrodomains. The authors posited that the enhancement of the pyroelectric effect is related to a 90-deg polarization switch.

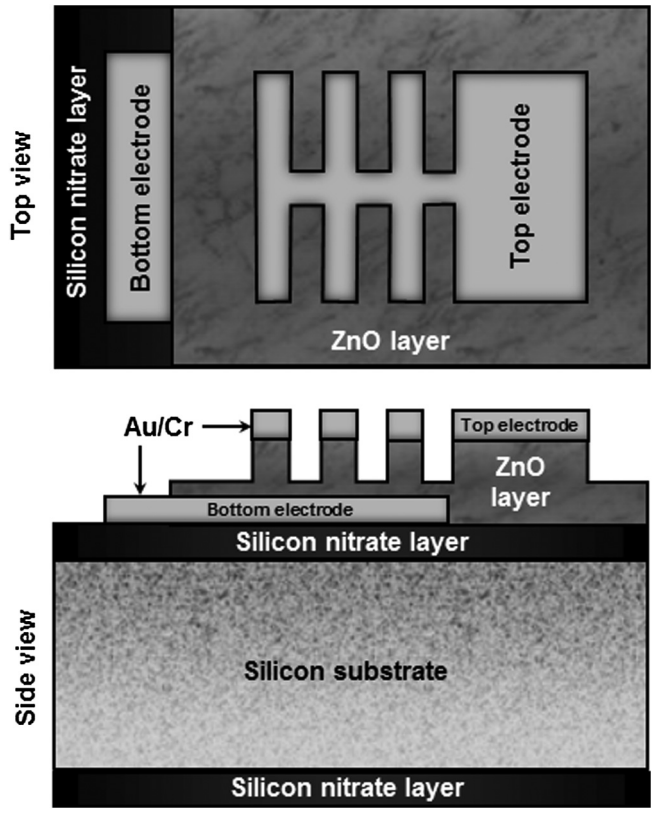

Figure 5.5 Multilayer ZnO pyroelectric device with comb-like electrodes with 3D ZnO f lm (adapted from Ref. 21).

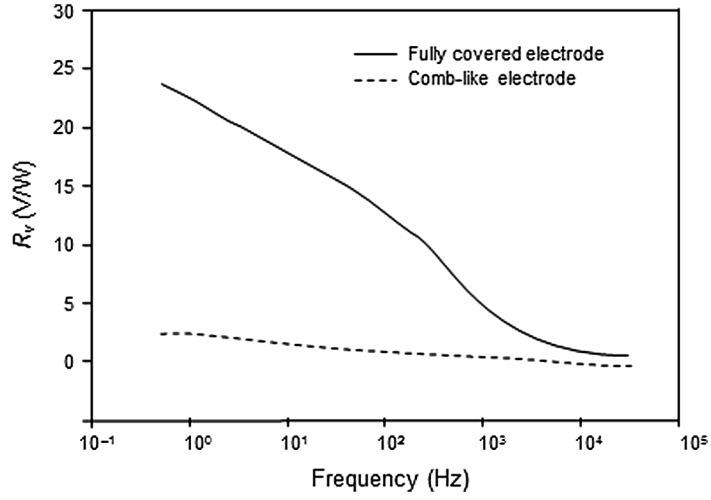

Figure 5.6 Voltage responsivity versus frequency of the fabricated ZnO sensor with a fully covered and comb-like electrode (adapted from Ref. 21).

Lehman et al. proposed a large-area domain-engineered pyroelectric radiometer with high spatial- and spectral-response uniformity that is an excellent primary transfer standard for measurements in the near- and mid-IR wavelength regions.[23] The domain engineering consisted of inverting the spontaneous polarization over a 10-mm-diameter area in the center of a uniformly poled, 15.5 × 15.5-mm square, with a 0.25-mm-thick $LiNbO_3$ plate.[22] Gold black was used as the optical absorber on the detector surface, and an aperture was added to define the optically sensitive detector area. Their results indicate significantly reduced acoustic sensitivity without a loss of optical sensitivity. The detector noise-equivalent power was not exceptionally low but was nearly constant for different acoustic backgrounds. In addition, the detector's spatial response uniformity variation was less than 0.1% across the 7.5-mm-diameter aperture, and reflectance measurements indicated that the gold-black coating was spectrally uniform within 2%—from 800 to 1800 nm. The domain-engineered pyroelectric radiometer is the only alternative compared with HgCdTe, InSb photoconductors, or commercially available pyroelectric detectors, which are capable of measurement uncertainty on the order of 0.1%. The primary role of the radiometer was to extend and improve the National Institute of Standards and Technology spectral responsivity scale from the visible to the near-IR wavelength range.

Nakamura and Itagaki proposed a new structure, which consists of interdigital electrodes, deposited on periodically inverted domains of a ferroelectric crystal.[24] Because only a shallow region close to the crystal surface is pyroelectrically active in this structure, the surface charges are quickly induced in response to IR irradiation, providing high responsivity. A pyroelectric detector fabricated using periodically antipolar domains, formed by selective proton exchange and subsequent heat treatment of $LiTaO_3$ crystal, has experimentally demonstrated a high current responsivity in a high-frequency range of IR-power modulation. It was also suggested that because of the shallow region of pyroelectric material in this detector, a higher responsivity could be obtained by decreasing the periods of the domains and interdigital electrodes.

Recently, enhanced ferroelectric and pyroelectric properties have been demonstrated in trilayered BLT/NBT/BLT and PZT/NBT/PZT thin films fabricated on Pt/Ti/SiO_2/Si substrates by chemical solution deposition.[25]

Wu et al. found that the pyroelectric properties of BST films could be greatly enhanced by depositing (100)-$Ba_{0.65}Sr_{0.35}TiO_3$ (BST) films on Pt/Ti/SiO_2/Si substrates using a low-temperature self-buffered layer.[26] In common practice, BST film is deposited on Pt substrate, and films are generally polycrystalline due to a lattice mismatch between Pt and BST. This mismatch is harmful to the pyroelectric properties of BST films. To mitigate this problem, the authors first deposited a BST buffer layer at 200 °C and then raised the temperature to 550 °C; subsequently, the BST bulk films grew. The

authors demonstrated that the microstructure of BST films strongly depends on the surface morphology of the annealed self-buffered layer.[25] The pyroelectric coefficient and material figures of merit obtained for (100)-BST with a BST buffer layer 20 nm in thicknesses were 1.16×10^4 $\mu Cm^{-2} K^{-1}$ and 2.18×10^{-4} $Pa^{-1/2}$, respectively. The pyroelectric coefficient and material figures of merit obtained for (100)-BST without a BST buffer layer were 0.074×10^4 $\mu Cm^{-2} K^{-1}$ and 0.218×10^{-4} $Pa^{-1/2}$, respectively. The IR detectivity obtained at 25 °C and 21 Hz for the (100)-BST film capacitor thermally isolated by a 500-nm SiO_2 layer was 9.4×10^7 $cmHz^{1/2}/W$. The authors posited that improvement in the thermal isolation of the pyroelectric film element would produce an improved IR response.

Wei et al. aimed to design a partially covered electrode (PCE) instead of a traditional fully covered electrode (FCE) in order to improve the absorption of incident energy in a pyroelectric element under the high-transmission-coefficient condition (90%) of ZnO in the 400- to 800-nm wavelength range.[27] The design of a MEMS-based sensor structure is shown in Fig. 5.7.

The authors fabricated and investigated three groups of sensors with various layer thicknesses and effective areas, and both partially and fully covered electrodes. The PCE covers 50–65% of the exposed surface for incident energy absorption. The uncovered ZnO will directly receive the incident laser energy and improve the absorption efficiency of the sensor. The voltage responsivity of the PCE sensors was 4–50 times higher than that of FCE sensors, depending on the thickness of the pyroelectric and thermal barrier layers, and the current responsivity was found to be 2–40 times higher. The authors also coined the term *thermal efficiency*, defined as η/G_T (η and G_T are the absorption coefficient of the absorption layer and thermal

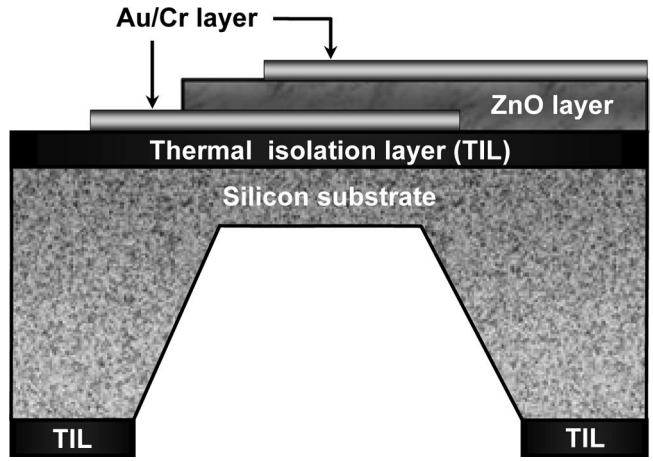

Figure 5.7 Design of a MEMS-based ZnO sensor with a partially covered electrode. Adapted from Ref. 27 with permission from Elsevier.

conductance, respectively) to provide insight into how thermal efficiency affects the responsivity. The trend of the thermal efficiency was similar to that of the voltage responsivity: it is larger for PCEs than FCEs, thus, larger responsivity is obtained with a PCE sensor.

Shaulov proposed a broadband thermal detector based on pyroelectric materials with temperature-dependent electrical conductivity.[28] This detector combines the properties (notably the frequency response) of a thermistor bolometer and a pyroelectric detector (PTB). Shaulov demonstrated that with suitable choices in detector parameters, there is a uniform frequency response above and below the thermal relaxation frequency. Acting simultaneously as a thermistor and a pyroelectric detector, the PTB combines the advantages of both detectors. Specifically, in the PTB, the thermistor component provides a low-frequency response, while the pyroelectric component provides a high-frequency response. As a result, a flat frequency response can be obtained over a broad band. The above-cited characteristic was demonstrated with a PTB made of a $Cu_3B_7O_{13}Cl$ crystal.

5.7 Conclusions

Though various designs and structures have been proposed and demonstrated to enhance the performance of pyroelectric detectors, their use in the actual fabrication of detector systems will prove whether their predicted performance can be realized in practice.

References

1. M. Alexe and L. Pintilie, "Thermal analysis of the pyroelectric bimorph as radiation detector," *IR Physics & Technology* **1**, 949–954 (1995).
2. S. B. Lang and M. Alexe, "Optimization and experimental verification of a pyroelectric bimorph radiation detector," *Applied Ferroelectric* 07803-4959-8/98, 195–198 (1998).
3. M. Es-Souni, S. Iakovlev, and C. H. Solterbeck, "Multilayer ferroelectric thin film for pyroelectric applications," *Sensors and Actuators A* **109**, 114–119 (2003).
4. L. Sun, O. K. Tang, W. Liu, W. Zhu, and X. Chen, "Characterization of sol-gel derived $Pb(Zr_{0.3}Ti_{0.7})O_3/PbTiO_3$ multilayer thin films," *Ceramics International* **30**, 1835–1841 (2004).
5. L. L. Sun, O. K. Tan, W. G. Liu, X. F. Chen, and W. Zhu, "Comparison study on sol-gel $Pb(Zr_{0.3}Ti_{0.7})O_3$ and $Pb(Zr_{0.3}Ti_{0.7})O_3/PbTiO_3$ multilayer thin films for pyroelectric IR detectors," *Microelectronic Engineering* **66**, 738–744 (2003).

6. N. W. Schubring, J. V. Mantese, A. L. Micheli, A. B. Catalan, and R. J. Lopez, "Dynamic pyroelectric enhancement of homogeneous ferroelectric materials," *Phys. Rev. Lett*. **68**, 1778 (1992).
7. J. V. Mantese, N. W. Schubring, A. L. Micheli, and A. B. Catalan, "Ferroelectric thin films with polarization gradients normal to the growth surface," *Appl. Phys. Lett*. **67**, 721–723 (1995).
8. J. V. Mantese, N. W. Schubring, A. L. Micheli, A. B. Catalan, M. S. Mohammed, R. Naik, and G. Auner, "Slater model applied to polarization graded ferroelectrics," *Appl. Phys. Lett*. **71**, 2047–2049 (1997).
9. S. Zhong, S. P. Alpay, Z.-G. Ban, and J. V. Mantese, "Effective pyroelectric response of compositionally graded ferroelectric materials," *Appl. Phys. Lett*. **86**, 092903-1–092903-2, (2005).
10. F. Jin, G. W. Auner, R. Naik, N. W. Schubring, J. V. Mantese, A. L. Micheli, A. B. Catalan, and A. L. Micheli, "Giant effective pyroelectric coefficient from graded ferroelectric devices," *Appl. Phys. Lett*. **73**(19), 2838–2840 (1998).
11. X. G. Tang, J. Wang, H. L. W. Chan, and A. L. Ding, "Growth and electrical properties of compositionally graded $Pb(Zr_xTi_{1-x})O_3$ thin film on $PbZrO_3$ buffered Pt/Ti/SiO2/Si substrates," *J. Crystal Growth* **267**, 117–122 (2004).
12. X. G. Tang, H. L. W. Chan, and A. L. Ding, "Electrical properties of compositionally graded lead calcium titanate thin films," *Solid State Comm*. **127**, 625–628 (2003).
13. C. W. Tipton, "Pyroelectric properties of La-Sr-Co-O/Pb-La-Ti-O/La-Sr-Co-O heterostructures," U.S. Army Research Laboratory Report, Adelphi, Maryland (1999).
14. C. W. Tipton, K. Kirchner, R. Godfrey, M. Cardenas, S. Aggarwal, H. Li, and R. Ramesh, "Enhanced-response pyroelectric hetero-structures," *Appl. Phys. Lett*. **77**(15), 2388–2390 (2000).
15. S. J. Wang, S. Miao, I. M. Reaney, M. Q. Lai, and L. Lu, "Enhanced tunable and pyroelectric properties of $Ba(Ti_{0.85}Sn_{0.15})O_3$ (BTS) thin films with $Bi_{1.5}Zn_{1.0}Nb_{1.5}O_7$ (BZT) buffer layers," *Appl. Phys. Lett*. **98**, 082901-1–08290-3 (2010).
16. N. J. Wu, Y. Q. Xu, Y. S. Chen, and A. Ignatiev, "Pyroelectric/superconducting oxide heterostructures for uncooled wide-band IR detection," *Physica C* **341–348**, 2743–2744 (2000).
17. Y. Q. Xu, N. J. Wu, and A. Ignatiev, "(Mn,Sb) doped-$Pb(Zr,Ti)O_3$ IR detector arrays," *J. Appl. Phys*. **88**(2), 1004–1007 (2000).
18. G. Suyal, A. Seifert, and N. Setter, "Pyroelectric nanoporous films: synthesis and properties," *App. Phys. Lett*. **81**(2), 1059–1061 (2002).

19. G. Suyal and N. Setter, "Enhanced performance of pyroelectric microsensors through the introduction of nanoporosity," *J. Europ. Ceramic Society* **24**, 247–251 (2004).
20. Y. Querner, V. Norkus, and G. Gerlach, "High-sensitive pyroelectric detectors with internal thermal amplification," *Sensors and Actuators A: Physical*. **172**(1), 169–174 (2011).
21. C.-C. Hsio and S.-Y. Yu, "Improved response of ZnO films for pyroelectric devices," *Sensors* **12**, 17007–17022 (2012).
22. Y. Ivry, V. Lyahouitskaya, I. Zon, and I. Lubomirsky, "Enhanced pyroelectric effect in self-supported films of $BaTiO_3$ with polycrystalline macrodomains," *Applied Physics* **99**, 172905-1–172905-5 (2007).
23. J. Lehman, G. Eppeldauer, J. A. Aust, and M. Racz, "Domain-engineered pyroelectric radiometer," *Applied Optics* **38**(34), 7074–7055 (1999).
24. K. Nakamura and M. Itagaki, "Pyroelectric IR detectors using periodic inverted domains of $LiTiO_3$," *Jpn. J. Appl. Phys*. **33**, 5404–5406 (1994).
25. Y. Guo, M. Li, W. Zhao, D. Akai, K. Sawada, M. Ishida, and M. Gu, "Ferroelectric and pyroelectric properties of $(Na_{0.5}Bi_{0.5})TiO_3$-$BaTiO_3$ based trilayered thin films," *Thin Solid Films* **517**, 2974–2978 (2009).
26. C. G. Wu, Y. R. Li, J. Zhu, X. Z. Liu, and W. L. Zhang, "Great enhancement of pyroelectric properties for $Ba_{0.65}Sr_{0.35}TiO_3$ films on Pt-Si substrates by inserting a self-buffered layer," *J. Appl. Phys*. **105**, 044107-1–044107-4 (2009).
27. C. S. Wei, Y. Y. Lin, Y. C. Hu, C. W. Wu, and C. K. Shin, "Partial-electroded ZnO pyroelectric sensors responsivity improvement," *Sensors and Actuators A*, **128**, 18–24 (2006).
28. A. Shaulov, "Broad band IR thermal detector," *Sensors and Actuators* **5**, 207–215 (1984).

Chapter 6
Pyroelectric Particle Generators

6.1 Introduction

Pyroelectric crystals are anisotropic/noncentrosymmetric crystals that are polarized at equilibrium conditions. The net dipole moment per unit volume of the crystal is not zero. The magnitude of polarization without the application of an applied field or temperature gradient is known as the spontaneous polarization P_s. Spontaneous polarization creates charges on the surface of the crystal.[1] However, these surface charges are compensated by extrinsic effects, such as surface flashover and the attraction of stray charges to the surface of the crystal in ambient air, so the surface is electrically neutral.

Pyroelectric crystals are cut such that the two faces are normal to the dipole moments (polarization) of the unit cells, effectively creating $-Z$ and $+Z$ faces. During thermal equilibrium, the $-Z$ face has negative spontaneous polarization, and the $+Z$ face has positive spontaneous polarization. The change in polarization due to a temperature gradient causes a charge to build on the crystal surface in vacuum that gives rise to an electrostatic potential. This charge creates an electric field capable of accelerating charged particles to energies approximately hundreds of keV. Fields of around 100 kV/cm can be achieved with temperature changes in tens of degrees if a lithium tantalate crystal with spontaneous polarization of 50 μC and a dielectric constant of 45 is heated or cooled in vacuum, thereby suppressing the ambient screening of the bound polarization charges. Furthermore, barrier tunneling can take place as the electric field strengthens, causing electron emission from the $-Z$ surface during cooling. Upon striking the surrounding environment, these ions and electrons create Bremsstrahlung x rays. Research by various investigators has shown that the above effect is strong enough to create compact sources of x rays, electrons, ions, and neutrons via deuterium–deuterium (D–D) fusion.[2–12]

Recently, Kukhtarev et al. demonstrated the production of electron and x-ray beams via pyroelectric and photogalvanic effects.[7] The electric field of the crystal also creates a beam of accelerated ions in a direction opposite to the electron beam, due to emitted electrons creating ion pairs in the fill gas. An opportunity to create ultraportable x ray and electron sources is offered by

the pyroelectric crystals' ability to be heated using only a few watts of power. The production of radiation must be controlled for intensity, energy, and production period in order to develop a compact radiation source.[13]

6.2 Electrostatistics of a Pyroelectric Accelerator

Fullem and Danon have derived detailed equations for calculating the potential and field strength of both single-crystal and two-crystal pyroelectric accelerators.[14] Their work in this regard greatly expanded on physical concepts to create a more in-depth understanding of the physics of pyroelectric accelerators. There are two systems of pyroelectric accelerators: single- or one-crystal and two-crystal. In the single-crystal system, one face of the crystal is grounded, and the other electrically floats facing a grounded target. The ungrounded surface and target are separated by a vacuum gap or low-pressure gas. In the two-crystal system, the grounded target is replaced by a second, oppositely faced, Z^- and Z^+ crystal. Schematics for the one-crystal system and two-crystal system utilized for mathematical analysis via cylindrical crystals with a polarization axis normal to planes A, B and C are illustrated in the following sections. Fullem and Danon also verified expressions from finite-element modeling with comparisons to experiential results.[14] The expressions had a factor of approximately four discrepancies between the potential predicted by the idealized model and the actual experiment measurements from both one- and two-crystal systems. A brief description of the proposed modeling is given in the following paragraphs.

6.2.1 One-crystal system

When the crystal illustrated in Fig. 6.1 experiences a temperature change, the charges develop on surface B ($Q_B = \mathrm{A}p\Delta T$). As a result, a potential exists across the crystal and the gap, thus, accelerating electrons or ions present in the gap. The sign of the charge on surface B and the direction of the electric field in the gap are dependent on whether the orientation of the axis of polarization is facing toward or away from B and whether or not the crystal has been heated or cooled. The one-crystal-system model shows the crystal and gap as two capacitors because they both act electrically as capacitors. Surface B is common to both capacitors, which are electrically parallel to each other. Fig. 6.1 represents the equivalent circuit.

The equivalent capacitance (ignoring fringing fields) of this system is calculated as follows:

$$C_{eq} = C_{cr} + C_{gap} = \frac{\varepsilon_0 \varepsilon_{cr} A}{L_1} + \frac{\varepsilon_0 \varepsilon_{gap} A}{L_g}, \tag{6.1}$$

where ε_0 is free-space permittivity, ε_{cr} is the pyroelectric crystal, and ε_{gap} is the gap.

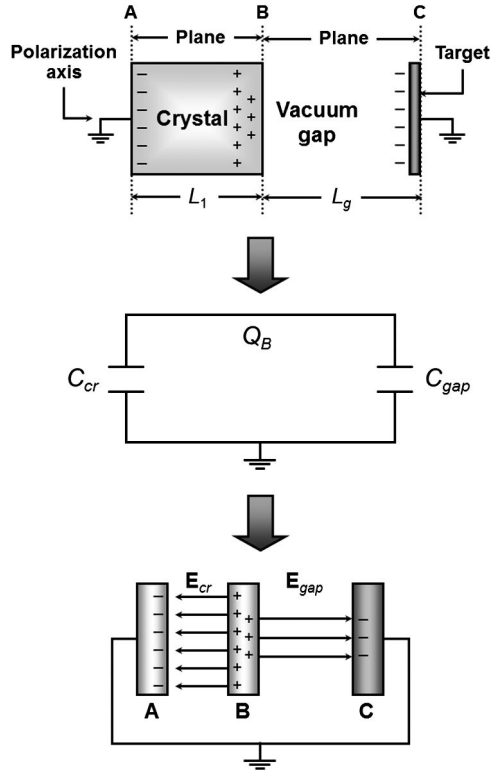

Figure 6.1 Mechanism of a one-crystal pyroelectric accelerator system. Adapted from Ref. 14 with permission from AIP Publishing LLC.

In many cases where $C_{cr} > C_{gap}$, the potential across the gap can be simplified as

$$V = Q_B/C_{cr} = p\Delta T L_1/\varepsilon_{0cr}. \tag{6.2}$$

The electric field strength in the gap is calculated as

$$E_G = V/L_g = p\Delta T/\varepsilon_0\left(\frac{L_g\varepsilon_{cr}}{L_1} + \varepsilon_{gap}\right). \tag{6.3}$$

6.2.2 Two-crystal system

As illustrated in Fig. 6.2, it is possible to employ two oppositely faced crystals to achieve a larger potential across the gap. With oppositely facing crystals, the polarization axes of the two crystals are antiparallel. It is also possible to face the crystals in the same direction of polarization, for which the mathematical analysis of Eq. (6.4) is valid. Note that the potential and field in the gap will be zero for crystals facing the same direction if the crystals are

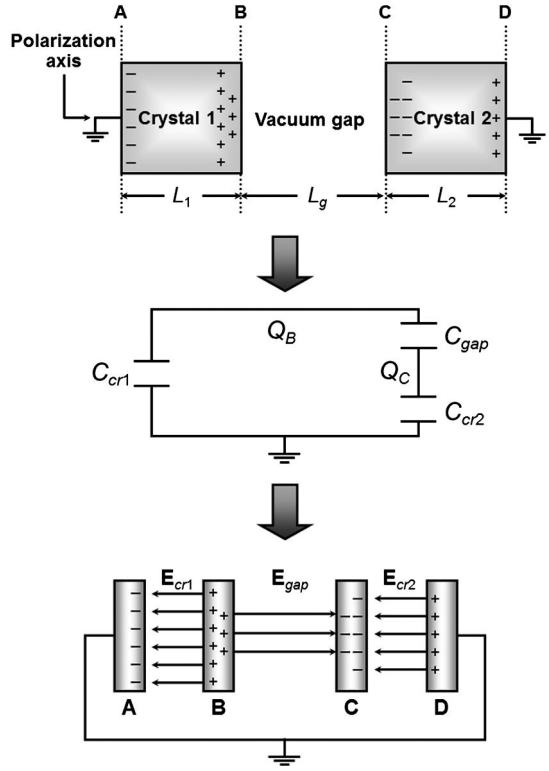

Figure 6.2 The mechanism of a two-crystal pyroelectric accelerator system. Adapted from Ref. 14 with permission from AIP Publishing LLC.

identical, experiencing identical temperature changes. The two-crystal system possesses three capacitors: C_{cr1}, C_{gap}, and C_{cr2}. When the two crystals experience temperature changes, charges develop on surfaces B and C, and their magnitudes are given by

$$Q_B = Ap_1\Delta T_1, \quad Q_c = Ap_2\Delta T_2, \tag{6.4}$$

where 1 represents the parameters of crystal 1, and 2 represents the parameters of crystal 2. The values of Q_B and Q_C are determined by the respective crystals and their temperature profile according to Eq. (6.4).

The potential across the gap can be obtained from $Q_B = Q_1 + Q_{gap}$ and $Q_C = Q_2 + Q_{gap}$, as follows:

$$V_{gap} = \frac{Q_{gap}}{C_{gap}} = \frac{(Q_c C_{cr1} \quad Q_B C_{cr2}) C_{gap}}{(C_{cr2} C_{cr1} + C_{cr2} C_{gap} \quad C_{cr1} C_{gap})} \tag{6.5}$$

Fullem and Danon also verified expressions for V_{gap} from finite element modeling with comparisons to experimental results for lithium tantalate

crystals.[14] Finite element analysis agrees with a calculation of within 3%, allowing for a better understanding of pyroelectric accelerators.

6.3 D–D Nuclear Fusion and Neutron Generators

Pyroelectric fusion (pyrofusion) offers several advantages over other energy sources: low cost, power consumption of only a few watts, and a smaller size. These advantages have not yet extended to the neutron yield of electrostatic confinement sources or portable neutron generators. However, the two share the advantages of the ability to be turned off to eliminate shielding concerns and can be very compact and inexpensive.[5] The current generation of pyroelectric neutron sources does not produce neutrons at a high enough intensity to be commercially useful, but that is slowly changing. The basic arrangement for a thermal neutron generator is illustrated in Fig. 6.3, where MCA is a multichannel analyzer.

The deuterium ions are created at the tungsten tip and attracted to the grounded copper mesh behind the deuterated target. Nuclear fusion occurs when they collide with the target, thereby creating neutron and ^{3}He according to the following fusion reaction:

$$ {}^{2}_{1}\mathrm{H} + {}^{2}_{1}\mathrm{H} \rightarrow {}^{3}_{2}\mathrm{He} + {}^{1}_{0}\mathrm{n}. \tag{6.6} $$

The neutrons are thermalized in the moderator and detected in the neutron detector.

The researchers exploiting neutron generation via D–D fusion were able to increase the yield of the neutron production using paired crystals to allow superimposition of the field from two crystals.[8–12] Commercial neutron generators generally require a high-voltage power supply to achieve the electrostatic fields necessary for ionizing and accelerating deuterium (or

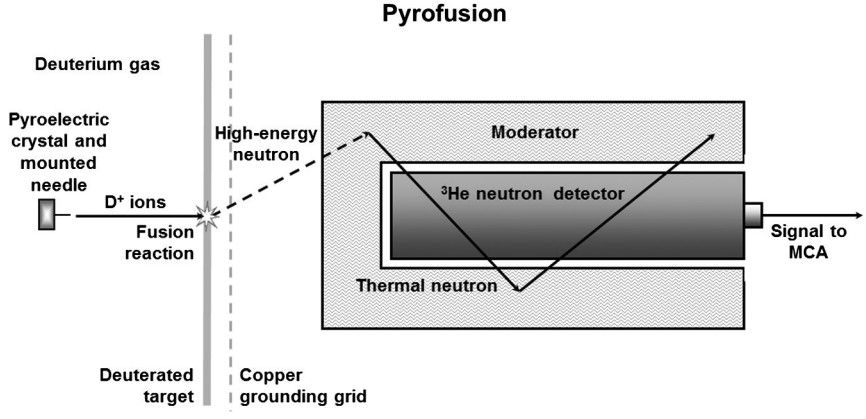

Figure 6.3 Thermal neutron generator.

tritium) gas into a deuterated target. By heating or cooling a pyroelectric crystal using 10–20 W of power (considering thermal losses), a single crystal can generate an electrostatic potential of about 100 kV, which is sufficient to achieve D–D fusion. The two-crystal system typically doubles, accelerating potential and enabling deuterium ions to be accelerated with a maximum measured energy of approximately 220 keV. Higher energy increases the likelihood of fusion because the D–D fusion cross section is energy-dependent. Since pyroelectric crystals can generate hundreds of kiloelectron volts, a neutron generator can be engineered to be small, battery operated, and portable.

Several challenges must be solved before such a system can come to fruition. One of the main challenges is the reproducibility of results. One reason for the lack of reproducibility is that the temperature profile is not precise across the crystal from one experiment to another because of the lack of a controlled thermal management system. Other reasons include high voltage discharges and erosion of the field-emitting tip used locally to enhance the electric field. By introducing tritium into the system, the neutron yield increases to 10^6 n/s, which makes the system suitable for some applications, such as a calibration source, research, and homeland security. In working toward this goal, researchers have constructed a portable prototype vacuum system capable of being sealed after it has been evacuated and filled with deuterium gas.[12] Preliminary experiments using this portable system have been conducted.

The portable prototype vacuum chamber consists of a 9.3-cm long, 7.62-cm diameter chamber, with 3.3-cm reducer flanges to minimize the overall vacuum volume. Two isolation valves that can be closed after the system is pumped down and filled with deuterium gas are attached. Two 1-cm thick, 2-cm diameter lithium-tantalate ($LiTaO_3$) crystals were used in these experiments. Figure 6.4 illustrates the two-crystal-flange system. Heating and cooling of the crystals was achieved using a pair of thermoelectric module-temperature controllers (TECs).

Gillich et al. performed several experiments to determine a thermal cycle for each of the two crystals in which both crystals would be thermally in-phase during cooling.[12] The tip crystal was heated from 27 to 130 °C over a period of 5 min, then allowed to soak at 130 °C for a period of 3 min. It was then cooled to 15 °C over a period of 5 min. The target crystal was heated from 27 to 145 °C over a period of 5 min, then allowed to soak at 145 °C for a period of 3 min. The target crystal was then allowed to cool naturally. Neutron emission occurred during the crystal-cooling phase. The portable prototype vacuum system establishes a more stable environment for pyrofusion experiments and improves the reproducibility of experimental results. An average of 507 net counts (with a standard deviation of 72) equating to 9200

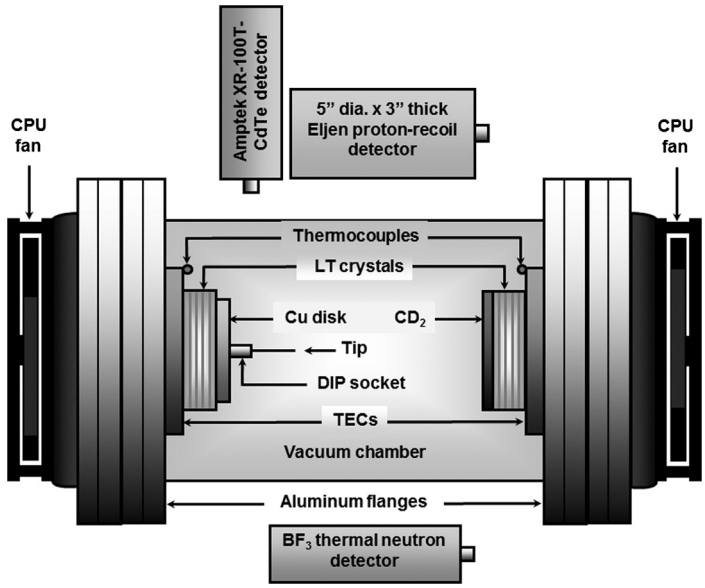

Figure 6.4 Prototype two-crystal, lithium-tantalate system in vacuum, where DIP is for a dual in-line package. Adapted from Ref. 12 with permission from Elsevier.

(with a standard deviation of 1300) was achieved over 5 consecutive thermal cycles.

Tornow et al. proposed and demonstrated neutron production with a pyroelectric double-crystal assembly without a nanotip, as illustrated in Figs. 6.5 and 6.6.[15] Two cylindrical $LiTaO_3$ crystals, facing each other's deuterated circular face, were exposed to deuterium gas at an ambient pressure of a few millitorr. Neutrons were produced by the $^2H(d,n)^3He$ fusion reaction upon the heating and cooling of the crystals, with a distance of about 4 cm between the Z^+

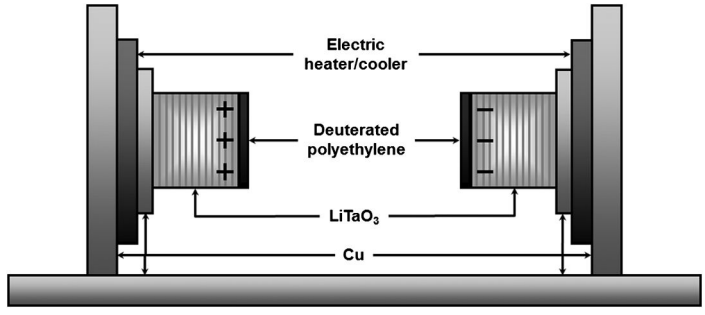

Figure 6.5 Double-crystal arrangement for a neutron generator. Adapted from Ref. 15 with permission from Elsevier.

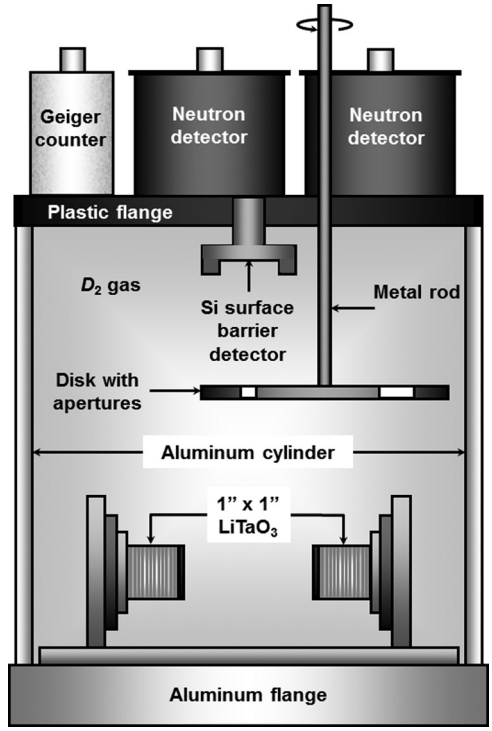

Figure 6.6 Side view of a double-crystal neutron generator. Adapted from Ref. 15 with permission from Elsevier.

and Z cut crystal faces. 2.5-MeV neutrons were detected by organic liquid scintillation detectors equipped with neutron-gamma pulse-shaped discrimination electronics to reject pulses generated by the intense x-ray flux. During the cooling phase of naked crystals, deuterium ion-beam D^{2+} energies of up to 400 keV were obtained, as deduced from the associated electron Bremsstrahlung endpoint energy. The highest electron-beam energy observed during the heating phase was 360 keV. The maximal energies were about 10% lower, with a layer of deuterated polyethylene evaporated on the front face of the crystals. The observed neutron yields of up to 500 per thermal cycle result in a total neutron production yield of about 1.6×10^4 neutrons per thermal cycle.

Naranjo et al. demonstrated a compact 14.1-MeV neutron source through which deuterons were accelerated into a tritiated target by the action of a pyroelectric crystal.[16] The expected flux was about 3×10^5 n/s at the ion currents measured. Although the measured flux was much less than expected, spectral analysis of the neutron signal unambiguously verified a 14.1-MeV neutron signal far above the background. The experimental fusion rate was

limited by surface flashover and time development of a surface barrier on the target due to chemical contamination.

Gillich et al. used thin films of vertically aligned tungsten nanorods to enhance field ionization in pyroelectric-crystal D–D-fusion experiments resulting in increased neutron production.[17] The tungsten nanorods were deposited on a single $LiTaO_3$ crystal using sputter deposition at glancing angles. The combination of a single tungsten tip with a thin film of nanorods on the face of the crystal yielded about four times the number of neutrons than did either a single tip or a thin film of nanorods alone.

6.4 Electron and Ion Emitters

Pyroelectric crystals exhibit a change in polarization when heated or cooled, resulting in the potential to eject electrons from the crystal surface and accelerate them to energies above 100 keV within a beam that changes in energy, yet is monoenergetic at a given point in time. Pyroelectric crystals can be heated with power of only a few watts, offering an opportunity to create ultraportable x-ray and electron sources. The electric field of the crystal also creates a beam that accelerates ions in a direction opposite to the electron beam due to emitted electrons, creating ion pairs in the fill gas. The phenomenon of pyroelectric electron emission has been employed to develop miniature x-ray sources, such as the Cool-X by Amptek (www.amptek.com/coolx.html).[5] The electrons emitted by the crystal can interact with the atoms of the fill gas to create electron–ion pairs. The positive ions are then accelerated in an opposite direction to that of the electrons and can reach energy on the order of 100 keV in a single-crystal source. What energy the positive ions in a two-crystal source are accelerated to is unknown. However, it can be assumed that the energy would be greater than 100 keV, due to the success of greatly increasing electron energy when using two-crystal electron sources.

6.5 X-ray Generators

Cool-X is a novel, miniature x-ray generator (see Fig. 6.7) developed by Amptek Inc. that uses a pyroelectric crystal to generate energetic electrons to produce x rays in target material (Cu).[5] The hermetically sealed package has a thin beryllium window that allows the x rays to be transmitted. Cool-X does not use radioisotopes or high-power x-ray tubes. It is a self-contained, solid-state system that generates x rays when the crystal is thermally cycled. When heated, a pyroelectric crystal exhibits a spontaneous decrease of polarization. Hence, as the temperature increases, an electric field develops across the crystal. For the specific crystal orientation with the $-Z$ face pointing to the target, the top surface of the crystal becomes positively charged and attracts

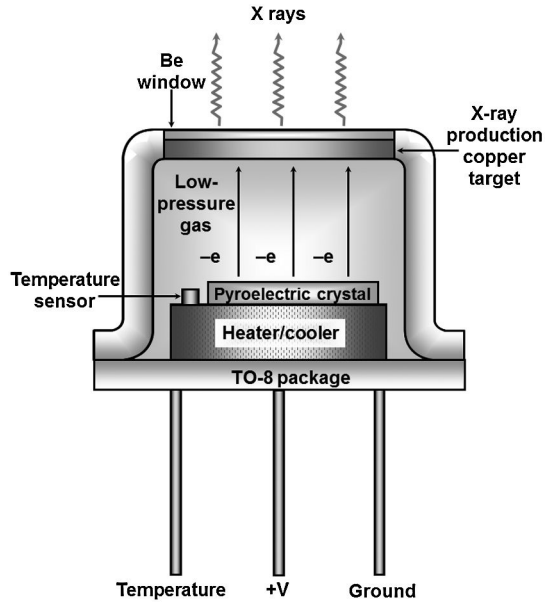

Figure 6.7 Amptek Cool-X miniature x-ray generator (adapted from Ref. 5 with permission from Amptek, COOL-X).

electrons from the low-pressure gas in the environment. As the electrons impinge on the surface of the crystal, they produce characteristic x rays (tantalum) as well as Bremsstrahlung x rays. When the cooling phase starts, the spontaneous polarization increases, and the electrons from the top surface of the crystal accelerate toward the Cu target, which is at ground potential. At this part of the cycle, Cu-characteristic x rays are produced, as well as Bremsstrahlung x rays. When the crystal temperature reaches its low point, the heating phase begins again. The cycle length of Cool-X can be varied between 2 and 5 min.

Recently, Hanamoto et al. presented an energy spectra of x rays measured at pressures of 5–50 Pa produced by an $LiTaO_3$ single crystal.[13] The energy spectra showed that the number of x rays increased exponentially, and the endpoint energy of the spectra increased linearly, with the decrease of pressure at pressures of 10–25 Pa. Maximum endpoint energy of about 22 keV was obtained using a $LiTaO_3$ single crystal with 0.5-mm thickness at a pressure of 10 Pa. The maximum energy produced by the experimental setup was estimated with the assumption that the $LiTaO_3$ single crystal forms a parallel-plate capacitor. The estimated energy reasonably agreed with the measured energy.[13] Recently, a target-changeable palm-top-size x-ray tube was realized using a pyroelectric LT crystal as the electron source and detachable vacuum flanges.[19] It was demonstrated that when silver and titanium plates (area $= 10\,mm^2$) were used as targets, silver $L\alpha$ and titanium K lines were clearly observed by bombarding

electrons on the targets for 90 s. In addition to its ease of exchanging the targets, the pyroelectric x-ray tube conveniently works with 3-V batteries.

6.6 Applications

A portable x-ray generator powered by a dry battery can be used for x-ray fluorescence analysis in addition to other applications.[18 21] The discovery of the pyroelectric x-ray generator in 1992 by Brownridge[18] led to a recent interest in the application of the pyroelectric effect as a means of producing useful radiation.[20] X rays with energies greater than 200 keV can be used to fluoresce the K shell of thorium. Ida and Kawai demonstrated an x-ray fluorescence setup with a pyroelectric x-ray generator and a secondary target for the determination of Cr in steel and measured an absolute amount of 1.3 μg Cr.[21] Neidholdt and Beauchamp have demonstrated the design and implementation of a novel ambient-pressure pyroelectric ion source (APPIS) for mass spectrometry.[22] Recently, Neidholdt and Beauchamp also presented studies of the ionization mechanism operative in the ambient pyroelectric ionization source and its applications in the detection of simulants for chemical nerve agents.[23]

6.7 Conclusions

This chapter reviewed the status of research in pyroelectric-based particle generators and their applications. Simple heating or cooling of pyroelectric crystals in vacuum, namely lithium tantalite, has been used as the basis for compact sources of x rays, electrons, ions, and neutrons. Various designs and configurations of crystals have been theoretically and experimentally investigated to optimize the performance of generators. It has been proposed that a high enough therapeutic dose of electrons for medical applications can be generated with current technology. A few applications of x-ray and ion production have been demonstrated for elemental analysis and mass spectrometry, respectively. Pyroelectric x-ray sources can be further improved for flux and energy via modeling and target design. It is expected that continued development of pyroelectric x-ray sources will lead to wide-scale implementation for industrial x-ray fluorescence and therapeutic medical applications.

References

1. S. B. Lang, *Sourcebook of Pyroelectricity*, Gordon and Breach, New York, pp. 10–21 (1974).
2. J. A. Geuther, Y. Danon, F. Saglime, and B. Sones, "Electron acceleration for x-ray production using paired pyroelectric crystals,"

Proc. Sixth International Meeting on Nuclear Applications of Accelerator Technology **261**(1), 124 (2003).

3. J. A. Geuther and Y. Danon, "High-energy X-ray production with pyroelectric crystals," *J. App. Phys.* **97**, 104916-1–104916-5 (2005).
4. J. D. Brownridge and S. Raboy, "Investigations of pyroelectric generation of x-rays," *J. Appl. Phys.* **86**, 1 (1999).
5. Amptek, "Miniature X-ray generator with pyroelectric crystal," accessed May 15, 2013, www.amptek.com/coolx.html.
6. A. Jeffrey, A. Geuther, and Y. Danon, "Electron and positive ions acceleration with pyroelectric crystals," *J. Appl. Phys.* **97**, 074109, 1–5 (2005).
7. N. V. Kukhtarev, T. V. Kukhtareva, G. Stargell, and J. C. Wang, "Pyroelectric and photogalvanic crystal accelerators," *J. Appl. Phys*. **106**, 014111-1–014111-7 (2009).
8. J. Geuther, Y. Danon, and F. Saglime, "Nuclear reactions induced by a pyroelectric accelerator," *Phys. Rev. Lett*. **96**, 054803-1–0544803-4 (2006).
9. B. Naranjo, J. Gimzewski, and P. Seth, "Observation of nuclear fusion driven by a pyroelectric crystal," *Nature* **434**, 1115–1117 (2005).
10. A. Jeffrey, A. Geither, and Y. Danon, "Enhanced neutron production from pyroelectric fusion," *Appl. Phys. Lett*. **90**, 174103-1–174103-3 (2007).
11. Y. Danon, "A novel compact pyroelectric x-ray and neutron course," *Final Report, DOE NEER Grant DE-FG07-041596*, submitted by RPI (2007).
12. D. Gillich, A. Kovanen, B. Herman, T. Fullem, and Y. Danon, "Pyroelectric crystal neutron production in portable prototype vacuum system," *Nuc. Inst. Meth. Phys. Res. A* **602**, 306–510 (2009).
13. K. Hanamato, A. Kawabe, A. Sakoda, T. Kataoka, and M. Okada, "Pressure dependence of x-rays produced by an $LiTaO_3$ single crystal at low pressures," *Nuc. Inst. Meth. Phys. Res. A* **669**, 66–69 (2012).
14. T. Z. Fullem and Y. Danon, "Electrostatics of pyroelectric accelerators," *J. App. Phys.* **106**, 074101-1–074101-6 (2009).
15. W. Tornow, W. Corse, S. Crimi, and J. Fox, "Neutron production with a pyroelectric double-crystal assembly without nano-tip," *Nuc. Inst. Meth. Phys. Res. A* **624**, 699–707 (2010).
16. B. Naranjo, S. Putterman, and T. Venhaus, "Pyroelectric fusion using a tritiated target," *Nuc. Inst. Meth. Phys. Res. A* **632**, 43–46 (2011).
17. D. J. Gillich, R. Teki, T. Z. Fullem, A. Kovanen, E. Blain, D. B. Chrisey, T. M. Lu, and Y. Danon, "Enhanced pyroelectric crystal D–D nuclear fusion using tungsten nanorods," *Nano Today* **4**, 227–234 (2009).

18. J. D. Brownridge, "Pyroelectric x-ray generator," *Nature* **358**, pp. 287–288 (1992).
19. S. Imashuku and J. Kawai, "Development of target changeable palm-top pyroelectric x-ray tube," *Rev. Sci. Inst.* **83**, 016106-1–016106-3 (2012).
20. J. A. Geuther and Y. Danon, "Applications of pyroelectric accelerators," *Nuc. Inst. Meth. Phys. Res. B* **261**, 110–113 (2007).
21. H. Ida and J. Kawai, "An x-ray fluorescence spectrometer with a pyroelectric x-ray generator and a secondary target for the determination of Cr in steel," *Spectrochimica* **60**, 89–93 (2005).
22. E. L. Neidholdt and J. L. Beauchamp, "Ambient pressure pyroelectric ion source for mass spectrometry," *Anal. Chem*. **79**, 3945–3948 (2007).
23. E. L. Neidholdt and J. L. Beauchamp, "Ionization mechanism of the ambient pressure pyroelectric ion source (APPIS) and its applications to chemical nerve agent detection," *J. Am. Soc. Mass Spectrom*. **20**, 2093–2099 (2009).

Chapter 7
Pyroelectric Energy Harvesting

7.1 Introduction

Energy harvesting (or energy scavenging) technology captures unused ambient energy, such as vibration, strain, light, temperature gradients, temperature variations, gas flow energy, and liquid flow energy, and converts it into usable electrical energy. Even though advances have been made, the batteries that power portable microelectronics and wireless devices provide only a finite amount of power. Energy harvesting is a perfect solution for the problem of finite battery power for various low-power applications, providing sustained, cost-effective, and environmentally friendlier sources of power. Unconventional methods for waste-energy harvesting and scavenging are being explored to provide sustained power to these micro- and nanodevices.[1–3] Efforts are being made to garner electric power from mechanical vibrations, light, spatial variations, and temporal temperature variations.[1–3] Another potential source for low-power electronics is the thermal- and mechanical-waste energy of asphalt pavement, especially via pyroelectricity. However, this potential has not yet been extensively explored. An exception is Israel's current large-scale effort to pave kilometers of roads with a specially designed series of piezoelectric modules in the pavement.[4]

Pyroelectric materials are able to convert most of the electromagnetic radiation's spectrum (ultraviolet, IR, microwave, x rays, and terahertz) energy into electrical energy; that is, they transform *photons to phonons and then to electrons*.[5] Since it follows that these materials can be exploited for conversion of thermal energy to electricity, they have been investigated recently for energy harvesting via pyroelectric linear and nonlinear properties. One key advantage of pyroelectrics over thermoelectrics is the stability of many pyroelectric materials at up to 1200 °C or more, which enables energy harvesting from high-temperature sources, thereby increasing thermodynamic efficiency.

It is noteworthy that annually more than 100 TJ of low-grade waste heat (10 °C to 250 °C) is discharged by industries worldwide, such as electric power stations, glass manufacturers, petrochemical plants, pulp and paper mills,

steel and other foundries, and the automobile industry. In the United States in 2009, around 55% of the energy generated from all of the sources was lost as waste heat.[6] Technology to recover this low-grade waste heat or convert into usable electricity could save industrial sectors billions of dollars annually and reduce greenhouse gases. Pyroelectric electric generators (PEGs) can play a significant role in such technology. This chapter presents a review of PEGs with discussions on linear and nonlinear energy harvesting processes, thermodynamics of pyroelectrics, and an investigation of important pyroelectric materials with modeling of numerically simulated results for energy conversion.

7.2 Energy Transfer

This section briefly discusses the pyroelectric effect, the physics of pyrocurrent generation, ferroelectricity, related phase transitions, and the application of these elements in energy harvesting. The reader can refer to Chapter 1 for more details on the concepts of pyroelectric and ferroelectric effects. Smart materials such as piezoelectrics, pyroelectrics, and ferroelectrics, are different from ordinary materials because of their ability to sense their environment and respond in a controlled fashion to external stimuli, such as stress, temperature, and electric and magnetic fields. Pyroelectric material is a type of smart material with the ability to become electrically polarized by temperature variation. Pyroelectricity is a coupled effect that is characterized by a change in temperature corresponding to a change in electric displacement $\mathbf{D}$ (C/m^2):

$$d\mathbf{D}=\mathbf{p}d\theta, \tag{7.1}$$

where $\mathbf{p}$ is the pyroelectric coefficient (C/m^2K), and θ is the temperature. Both electric displacement and the pyroelectric coefficient $\mathbf{p}$ are vectors, or first-rank tensors. The pyroelectric coefficient is defined by

$$\mathbf{p} = \left(\frac{\partial \mathbf{P}_s}{\partial \theta}\right)_{X,E}, \tag{7.2}$$

where $\mathbf{P}_s$ is spontaneous polarization. The constraints are constant elastic stress X due to inherent piezoelectric properties and electric field E. When the two surfaces of a pyroelectric element are connected to form a closed circuit, the charge on the surface flows through the circuit when the element is heated or cooled. The generated current i_p can be calculated from

$$i_p = A\mathbf{p}\frac{\partial T}{\partial t}. \tag{7.3}$$

The pyroelectric material can be illustrated as a thermal transducer because it converts thermal energy into electrical energy.

7.2.1 Ferroelectric effect

Ferroelectricity is the ability of a material to have a spontaneous polarization $\mathbf{P}_s$ (without the application of an electric field) that can be reversed by the application of an electric field.[7] The relation between an applied electric field and the corresponding polarization, or electric displacement, is nonlinear and displays hysteresis.[8] Figure 7.1 shows the lower half of the hysteresis loop occurring when the electric field E increases, while the upper half occurs when E decreases. This figure is repeated from Chapter 1 for its relevance here. The electric displacement at zero to the applied electric field is the spontaneous polarization $\mathbf{P}_s$. The electric field necessary to achieve zero polarization is the coercive field E_c. Electric displacement also has a saturation level D_{sat}. The strongest electric field that a material can possibly withstand before breakdown is the breakdown electric field E_b. At applied E_b, material loses its insulating ability and begins to conduct. When an electric field applied to a ferroelectric material is isothermally cycled, joule heating dissipates the electrical input provided to the system. The energy dissipated per unit volume of the ferroelectric material $\forall$ equals the area enclosed by the D-E diagram of the hysteresis loop:

$$\frac{W}{\forall} = \oint dDE. \tag{7.4}$$

The $\mathbf{P}_s$-E cycle can be used in energy harvesting.

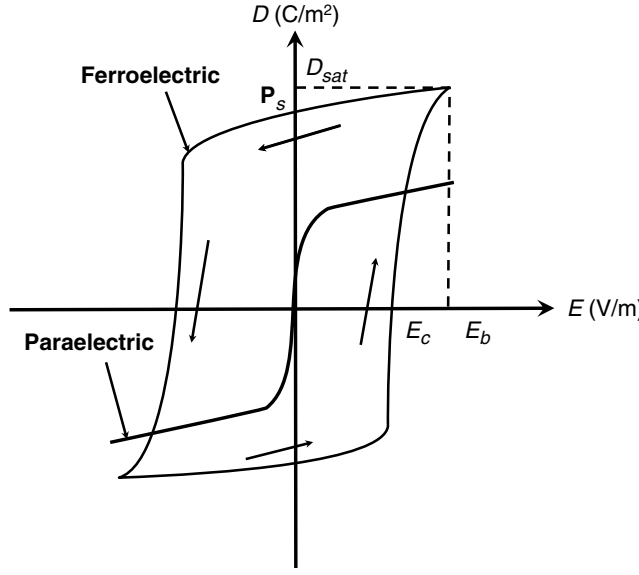

Figure 7.1 Typical electric displacement D versus electric field E cycle for ferroelectric and paraelectric materials (adapted from Ref. 8 with permission).

7.2.2 Paraelectric effect

Paraelectricity is the ability of a material with no spontaneous polarization to become polarized under an applied electric field. Paraelectric behavior is caused by the distortion of individual ions and the polarization of molecules. The domains, or area, of uniform polarization in paraelectric materials as compared to those of ferroelectric materials are unordered with a weak internal electric field. Figure 7.1 demonstrates the relationship between the electric displacement D and electric field E of an ideal paraelectric material. It can be observed that there is no spontaneous polarization in Fig. 7.1. However, electric displacement is generated when an electric field is applied. In reality, a paraelectric material often exhibits a small spontaneous polarization and a hysteresis loop. Finally, note that the paraelectric D-E curve is nonlinear because electric permittivity ε is also a function of the electric field.

7.2.3 Phase transitions

A material can transition from ferroelectric to paraelectric phase under certain conditions. Figure 7.2 displays electric displacement versus an electric field curve for a dielectric material that transitions from ferro- to paraelectric phase at three different temperatures T_1, T_2, and T_3, such that $T_1 < T_2 < T_3$. At the initial temperature T_1, the material is ferroelectric with both positive and negative spontaneous polarization $+\mathbf{P}_s$ and $\mathbf{P}_s$.[8] As the material is heated from T_1 to T_2,

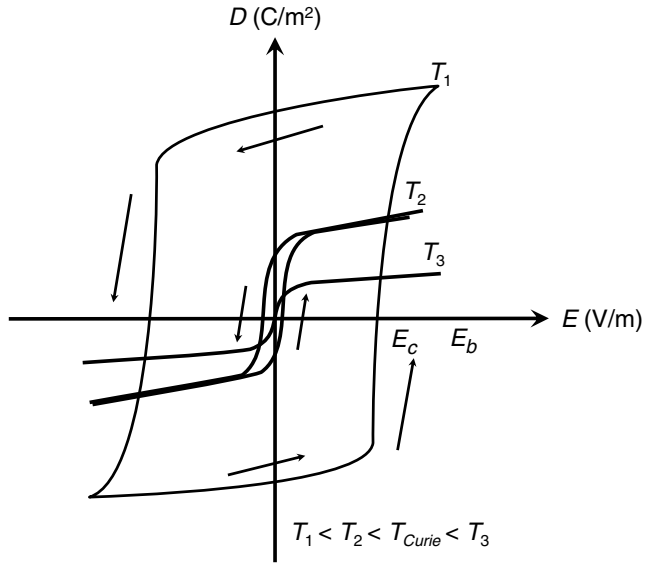

Figure 7.2 Electric displacement versus electric field cycle for a dielectric material that has transitions from ferro- to paraelectric phase at temperatures below and above the Curie temperature, $T_{C,\uparrow}(T_1 < T_2 < T_{C,\uparrow} < T_3)$ (adapted from Ref. 8 with permission).

the spontaneous polarization decreases, allowing charges to be transferred out for energy harvesting purposes. The spontaneous polarization vanishes when the material is heated to T_3, transitioning the crystal from ferroelectric to paraelectric.[9] The temperature when the phase of the dielectric material transitions from ferro- to paraelectric is called the Curie temperature, or phase transition temperature, denoted by $T_{C,\uparrow}$. The hysteresis becomes narrower as the material approaches $T_{C,\uparrow}$ until it becomes a line through the origin. In addition, the slope of the *D*-*E* curve decreases as temperature increases.

Pyroelectric materials also undergo a phase transition when they are cooled from T_3 to T_2 at a temperature other than $T_{C,\uparrow}$. This temperature is denoted by $T_{C,\downarrow}$ and can be lower by as much as 50 °C.[10] The temperature difference between these two phase transitions is denoted as ΔT_C. Pyroelectric energy converters make use of these phase transitions to generate current.

7.2.4 Pyroelectric performance

In general, the following properties are important when assessing the performance of pyroelectric materials, depending on their applications:[11]

1. A large pyroelectric coefficient p is desired so that the generated current according to Eq. (7.3) will be higher.
2. The larger the saturation electric displacement D_{sat}/P_s of a pyroelectric material, the larger the amount of charge can be stored on the material's surface and, hence, the higher the current that can be generated from the pyroelectric material.
3. Large breakdown voltage E_b is desired so that a larger electric field can be applied before the material breaks down.
4. The energy converters take advantage of the phase transition difference ΔT_C. In such applications a small ΔT_C is desired.
5. A short discharge period t_d is desirable in applications where the time required to discharge the surface charges is critical and preferably short.
6. Dielectric material should ideally insulate and not conduct current, yet, because its large resistance is not infinite, a small leakage current occurs. To achieve the best pyroelectric performance, that leakage current should be as low as possible.

7.3 Thermodynamic Cycles for Pyroelectric Energy Conversion

This section reviews energy harvesting from temperature variations using ferroelectric/pyroelectric materials' phase-transition characteristics as a microelectric generator based on thermodynamics-based cycles. This is also known as thermodielectric power generation. More harvested energy is obtained than with direct pyroelectric energy harvesting, but at the cost of a cumbersome apparatus. The thermodynamic power generator has several

advantages over a traditional thermoelectric system. A high source temperature is not required, allowing for use in both high- and low-temperature regimes, which eliminates the need for expensive materials. The ability of many thermodielectric materials to remain stable at high temperatures (up to 1200 °C or more) enables energy harvesting with higher thermodynamic energy efficiency and power density. Additionally, their low operating temperature and absence of moving parts make them reliabile and resilient, and, thus, attractive for portable applications. However, their major disadvantage is their unsteady operation in that the thermo-dielectric systems are subjected to both the thermal and electrical cycles.[2]

Some of the methods for and attempts at pyroelectric energy conversion based on thermodynamic cycles are discussed in the following sections.[2,12] The mechanism and process of a PEG is similar to a heat engine. A device that is operated in a thermodynamic cycle, absorbing thermal energy from a source, rejecting a part of it to a sink, and presenting the difference between energy absorbed and energy rejected as work to the environment, is called a heat engine. Thus, for better understanding, heat and work fundamentals, including thermodynamic cycles, are also described below.

7.3.1 Heat and work fundamentals[13]

Heat and work are the two ways to change the state of a system. *Heat* provides a way to change the energy of a system by virtue of only a temperature difference. Any other means of changing the energy of a system are called *work*. The first law of thermodynamics quantifies these changes. For every system, there exists a property called energy E. The system energy can be considered as a sum of internal energy, kinetic energy, potential energy, and chemical energy. The zeroth law of thermodynamics defined the useful property, temperature. The first law of thermodynamics defines the useful property, energy. The two new terms are the internal energy and the chemical energy. For most situations in this chapter, the chemical energy will be neglected. The internal energy U will be used in a P-V-type system. Internal energy arises from the random, or disorganized, motion of molecules in the system through the addition of heat T in specific volume V. Since this molecular motion is primarily a function of temperature, the internal energy is sometimes called "thermal energy." The internal energy U is a function of the state of the system. Thus, $U = U(P, T)$ or $U = U(P, V)$ or $U(V, T)$.

The first law of thermodynamics states that total energy, including heat energy, is always conserved. *The change in energy of a system equals the difference between the heat added to the system and the work done by the system* [units are joules (J)]:

$$\Delta E = Q \quad W, \tag{7.5}$$

where E is the energy of the system, Q is the heat input to the system, and W is the work done by the system.

For a cyclic process, heat and work transfers are numerically equal: $U_{final} = U_{initial}$; therefore,

$$\Delta U = 0 \quad \text{and} \quad Q = W \quad or \quad \oint dQ = \oint \delta W, \tag{7.6}$$

where the concept of energy is not sufficient, and a new property must appear. This property can be developed and the second law introduced in much the same way as the zeroth and first laws were presented. For every thermodynamic system in equilibrium, there exists an extensive scalar property called the entropy S, such that in an infinitesimal reversible change of state of the system,

$$dS = dQ/T, \tag{7.7}$$

where T is the absolute temperature, and Q is the amount of heat received by the system. The entropy of a thermally insulated system cannot decrease and is constant if, and only if, all of the processes are reversible. The idea of a completely reversible process is central. A process is called completely reversible if, after the process has occurred, both the system and its surroundings can be wholly restored by any means to their respective initial states.

The combined first- and second-law expressions can be obtained for reversible processes $dW = PdV$, $dQ = TdS$ in terms of enthalpy as

$$dH = TdS + VdP. \tag{7.8}$$

All heat engines can be represented, generally, as a transfer of heat from a high-temperature reservoir to a device that does work on the surroundings, followed by a rejection of heat from that device to a low-temperature reservoir (see Fig. 7.3).

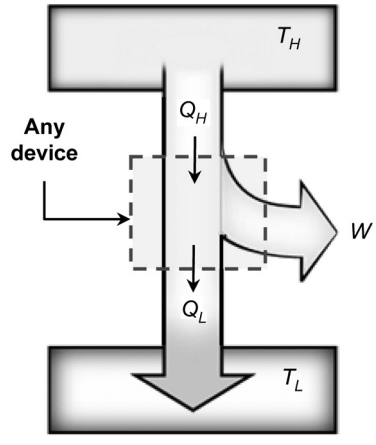

Figure 7.3 A generalized heat engine (adapted from Ref. 13 with permission).

A Carnot cycle, as shown in Fig. 7.4, has four processes. There are two adiabatic reversible legs and two isothermal reversible legs. Let us construct a Carnot cycle with many different systems, with the concepts using a familiar working fluid, the ideal gas. The system can be regarded as a chamber enclosed by a piston and filled with ideal gas.

The four processes in the Carnot cycle are:

1. At temperature T_2, the system is at state a. It is brought in contact with a heat reservoir, which is a liquid or solid mass of large enough extent such that its temperature does not change appreciably when some amount of heat is transferred to the system. In other words, the heat reservoir is a constant temperature source (or receiver) of heat. The system then undergoes an isothermal expansion from a to b, with heat absorbed Q_2.
2. At state b, the system is thermally insulated (removed from contact with the heat reservoir) and then allowed to expand to state c. During this expansion, the temperature decreases to T_1. The heat exchanged during this part of the cycle gives $Q_{bc} = 0$.
3. At state c the system is brought in contact with a heat reservoir at temperature T_1. It is then compressed to state d, rejecting heat Q_1 in the process.
4. Finally, the system is compressed adiabatically back to the initial state a. The heat exchange is $Q_{da} = 0$.

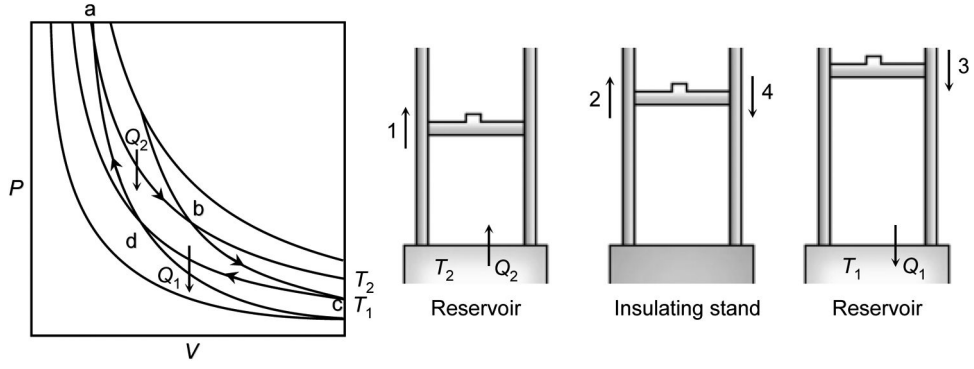

Figure 7.4 Carnot cycle: different stages in the thermodynamic cycle for a system composed of an ideal gas (adapted from Ref. 13 with permission).

The thermal efficiency of the cycle is given by

$$\eta = 1 \quad \frac{Q_R}{Q_A} = 1 + \frac{Q_1}{Q_2} \tag{7.9}$$

In this equation, a sign convention is implied. The quantities Q_A, Q_R, as defined, are the magnitudes of the heat absorbed and rejected, respectively. The quantities Q_1, Q_2, on the other hand, are defined with reference to heat received by the system. In this example, the former is negative, and the latter is

positive. The heat absorbed and rejected by the system takes place during isothermal processes:

$$Q = W_{ab} = NRT_2[\ln(V_b/V_a)], \tag{7.10}$$

$$Q_1 = W_{cd} = NRT_2[\ln(V_d/V_c)] = \quad [\ln(V_c/V_d)], \tag{7.11}$$

where Q_1 is negative. The efficiency can now be written, in terms of the volumes at the different states, as

$$\eta = 1 + \frac{T_1[\ln(V_d/V_c)]}{T_2[\ln(V_b/V_a)]}. \tag{7.12}$$

The paths from states b to c and from states a to d are both adiabatic and reversible. For a reversible adiabatic process, we know that $PV^{\gamma} = \text{a constant}$. Using the ideal gas equation of state, we have

$$\left(\frac{V_d}{V_c}\right)^{\gamma\ \ 1} = \frac{(T_2/T_1)}{(T_2/T_1)}\left(\frac{V_a}{V_b}\right)^{\gamma\ \ 1}. \tag{7.13}$$

Comparing the expression for thermal efficiency shows two consequences. First, the heats received and rejected are related to the temperatures of the isothermal parts of the cycle by

$$\frac{Q_1}{T_1} + \frac{Q_2}{T_2} = 0. \tag{7.14}$$

Second, the efficiency of a Carnot cycle is given concisely by

$$\eta = 1 \quad \frac{T_1}{T_2}. \tag{7.15}$$

The efficiency can be 100% only if the temperature at which the heat is rejected is zero.

7.3.2 Pyroelectric energy harvesting efficiency

To compare the efficiencies and parameters of thermodynamic cycles, one should first consider classical cycles via well-known governing equations of pyroelectric materials.[12] It is worth mentioning that the pyroelectric coefficient is in general a vector, but for practical reasons is treated as a scalar. Furthermore, vectors are assumed to be collinear and normal to the sample surface as is the case in all of the practical applications described in this book for electric displacement **D**, electric field **E**, and polarization **P**. Thus, only their magnitudes are presented (in italics) and one can write

$$dD = \varepsilon_{33}^{\theta} dE + pd\theta, \tag{7.16}$$

$$d\Gamma = pdE + c\frac{d\theta}{\theta}, \tag{7.17}$$

where D is electric displacement, E is electric field, θ is temperature, and Γ is entropy.

The assumed constants of the coefficient are

$$\varepsilon_{33}^{\theta} = \frac{dD}{dE}\Big|_{\theta}, \quad p = \frac{dD}{d\theta} = \frac{d\Gamma}{dE}, \quad c = \frac{dU}{d\theta}\Big|_{E}, \tag{7.18}$$

and also

$$d\Gamma = \frac{dQ}{\theta} \quad , \quad \eta = \frac{|\delta W_{cycle}|}{|Q_h|}, \tag{7.19}$$

where Q_h and W_{cycle} are the heat taken from a hot reservoir and a cycle network, respectively.

7.3.3 Carnot cycle for polarization–electric field (PE) cycles

The Carnot cycle is defined as two adiabatic and two isothermal curves on the polarization–electric field (PE) cycles, as depicted in Fig. 7.5.

The Carnot cycle is considered to be the optimum energy harvesting cycle, whose efficiency is

$$\eta_{Carnot} = 1 \quad \frac{\theta_c}{\theta_h}, \tag{7.20}$$

where θ_c and θ_h are the cold and hot temperatures, respectively. In the first adiabatic increase of the electric field $d\Gamma = 0$ [path 1-2 in Fig. 7.5 and from Eq. (7.18)],

$$\frac{d\theta}{\theta} = \quad \frac{p}{c} dE, \tag{7.21}$$

$$\ln\left(\frac{\theta_h}{\theta_c}\right) = \frac{p}{c} E_M, \tag{7.22}$$

where E_M is the maximum amplitude of the applied electric field. This equation shows the relation of electric field amplitude with temperature ratio. In the isothermal decrease of the electric field $d\theta = 0$ (path 2-3),

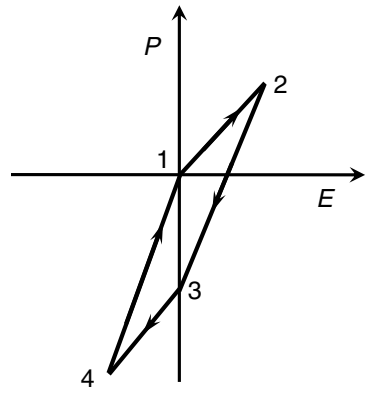

Figure 7.5 Polarization-electric field (PE) thermodynamic Carnot cycle.

$$d\Gamma = \frac{dQ_h}{\theta_h} = pdE, \tag{7.23}$$

$$Q_h = \quad p\theta_h E_M. \tag{7.24}$$

The two following steps are similar and are not detailed here (path 4-1 is similar to 2-3, and path 3-4 is similar to 1-2). The resulting energy conversion ratio is given by

$$W_e = (\theta_h \quad \theta_c)\delta\Gamma = \quad pE_M \frac{\theta_h \quad \theta_c}{\theta_h}. \tag{7.25}$$

It is worthwhile to note that from Eq. (7.25), in this cycle the energy conversion ratio does not depend on materials properties, instead it depends on temperature variations.

7.3.4 Ericsson cycle for the PE cycle

The Ericsson cycle is defined as two constant electric fields and two isothermal process curves on the PE cycle as depicted in Fig. 7.6. The Ericsson cycle starts by applying electric field E_1 at cold temperature θ_c. Polarizations subsequently increase to the P_2 value (path 1-2).

The temperature is then increased to hot temperature θ_h at a constant electric field (path 2-3). The polarization of the material decreases to P_3. Then, with the decrease of the applied electric field from E_{max} to 0, the polarization decreases to P_4 (path 3-4). The temperature is then finally decreased to its initial value, completing the cycle (path 4-1).

Electrical and thermal energies can be determined for each segment of the cycle. Consequently, we can write

$$W_{cycle} = \quad (\theta_h \quad \theta_c) \int_0^{EM} pdE. \tag{7.26}$$

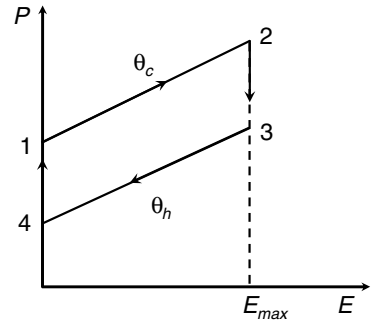

Fig. 7.6 PE thermodynamic Ericsson cycle.

The energy taken from the hot temperature reservoir is

$$Q_h = c(\theta_h \quad \theta_c) + \int_0^{EM} p\theta_h dE. \tag{7.27}$$

Then the energy conversion ratio can be expressed as

$$\eta = \frac{|W_{cycle}}{Q_h} = \frac{\int_0^{EM} pdE}{c + \frac{\theta_h}{\theta_h \quad \theta_c} \int_0^{EM} pdE} \tag{7.28}$$

and defined as the ratio of the net electric work to the energy taken from the hot temperature reservoir. Whereas, compared to the Carnot cycle efficiency, one can write

$$\frac{\eta}{\eta_{Carnot}} = \frac{\int_0^{EM} pdE}{c(\theta_h \quad \theta_c) + \int_0^{EM} p\theta_h dE}. \tag{7.29}$$

The ratio of efficiencies decreases with increase of temperature variation.

7.3.5 Lenoir cycle for the PE cycle

The Lenoir cycle is an idealized thermodynamic cycle often used to model a pulse-jet engine. For the ferroelectric material, the Lenoir cycle is defined as a constant electric polarization, a constant electric field, and a constant entropy curve on the PE cycle, as depicted in Fig. 7.7.

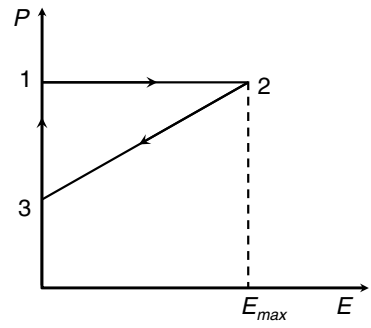

Figure 7.7 PE thermodynamic Lenoir cycle.

The first path is the increase of electric field $dD = 0$ (path 1-2); from Eq. (7.16), one can write

$$\varepsilon dE = \quad pd\theta, \tag{7.30}$$

$$dQ_{12} = p\theta dE + cd\theta, \tag{7.31}$$

where dQ_{12} is the thermal heat input. In the iseotropic path $d\Gamma = 0$ (path 2-3) from Eq. (7.17), one can write

$$\frac{d\theta}{\theta} = \quad \frac{p}{c} dE, \tag{7.32}$$

$$W_e = \int EdD. \tag{7.33}$$

The electrical work can be harvested in this step [Eq. (7.33)]. In the constant electric field $dE = 0$ (path 3-1) from Eqs. (7.16) and (7.17):

$$dD = pd\theta, \;\; d\Gamma = c\frac{d\theta}{\theta}, \tag{7.34}$$

$$Q_{31} \quad c(\theta_3 \quad \theta_1), \tag{7.35}$$

where Q_{31} is the outgoing heat from the material.

7.3.6 Pyroelectric energy conversion based on the Clingman cycle

In the early 1960s, Clingman and others attempted pyroelectric energy conversion via what is known as the Clingman cycle.[14,15] The cycle, illustrated in Fig. 7.8, is performed as follows:

1. Initially, the pyroelectric sample is at a temperature $T \sim T_{C,\downarrow}$, and the electric displacement and applied electric field are both equal to zero at point 1.
2. Next, the applied electric field is isothermally increased from zero to E_1, and the electric displacement also increases from zero to D_1 at point 2.
3. In the next step, the pyroelectric sample is heated at constant electric displacement D_1 from $T = T_{C,\downarrow}$ to $T > T_{C,\uparrow}$ resulting in an increase of electric field from E_1 to E_2 at point 3.
4. Then, the sample is isothermally discharged at temperature $T = T_{C,\uparrow}$, and the electric displacement and applied electric field both return to zero at point 4.
5. In the final step, the sample is cooled to its initial temperature $T = T_{C,\downarrow}$ to close the cycle at point 5.

The efficiency of this cycle was theoretically calculated to be well below 1% because the energy required to increase the temperature was much larger than the energy that can be converted to electrical energy from the cycle. The results discouraged further research efforts in pyroelectric conversion until the

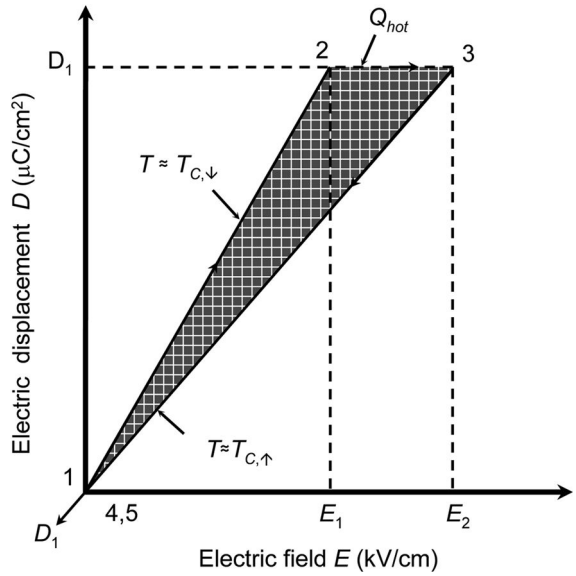

Figure 7.8 Pyroelectric energy conversion cycle used by Clingman and Moore. Adapted with permission from W. H. Clingman and R. G. Moore, "Application of ferroelectricity to energy conversion process," *J. App. Phys.* **32**, 675–68 (1961). Copyright 1961, AIP Publishing LLC.

early 1980s, when R. B. Olsen attempted to convert energy using a newly proposed electrical-thermal cycle.[16]

7.3.7 Pyroelectric energy conversion based on the Olsen cycle

The Olsen pyroelectric energy converter is essentially an electric form of a heat engine.[16] In order to repeatedly extract electrical energy from the pyroelectric medium, it is necessary to cycle the temperature as well as the electrical condition of the pyroelectric. Figure 7.9 displays the *D-E* diagram for PZST at temperatures above $T_{C,\uparrow}$, below $T_{C,}\downarrow$, and between both. The cycle in Fig. 7.9 consists of two isotherms and two constant overlapping electric field lines. In the cycle, the shaded area bounded by 1-2-3-4 is the Olsen energy conversion cycle.

Energy density N_D is represented by the shaded area of the cycle and is expressed in J/L. The total converted energy can be calculated by

$$W_E = N_D \forall_{PE} = \oint E_{PE} dD_{PE} \forall_{PE}, \tag{7.36}$$

where, $\forall_{PE}$ is the volume of the pyroelectric element.

The Olsen cycle is performed as follows:

1. First, the pyroelectric element is charged by isothermally increasing the applied voltage from V_L to V_H at temperature T_L (process 1-2).
2. Then, the pyroelectric element is discharged by increasing the temperature to T_H above $T_{C,\uparrow}$ at constant electric field (process 2-3).

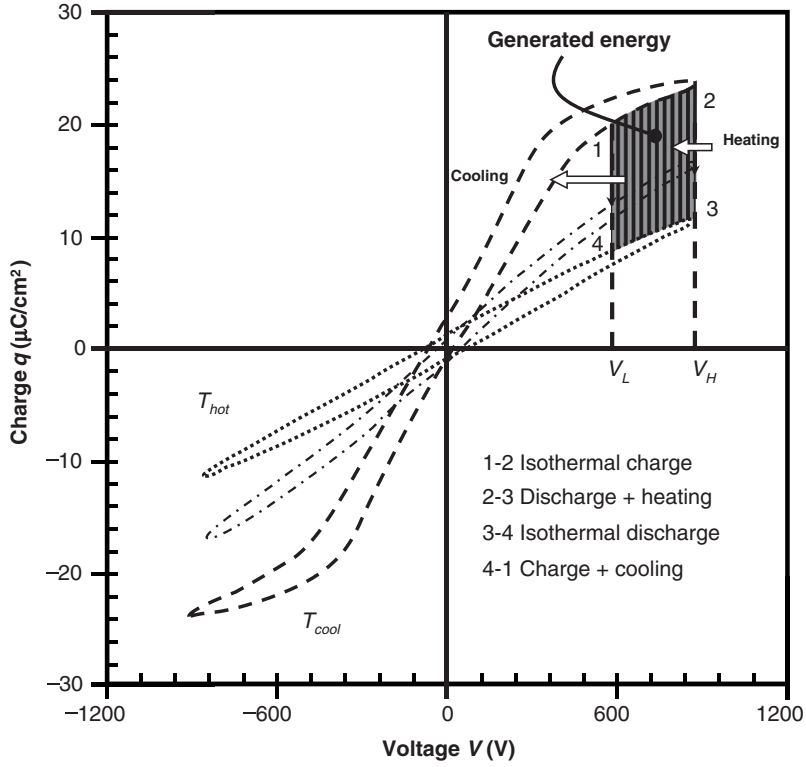

Figure 7.9 Electric Ericsson cycle superimposed on a charge-to-voltage hysteresis curve of a ferroelectric material, showing energy harvested from employing such a cycle. Adapted from Ref. 16 with permission AIP Publishing LLC.

3. Next, further discharge is achieved by decreasing the voltage isothermally from V_H to V_L (process 3-4).
4. Finally, the pyroelectric element is recharged to its spontaneous polarization at constant electric field with applied voltage V_L by cooling it below $T_{C,\downarrow}$ (process 4-1).

It is not required to heat and cool beyond the Curie temperatures, but doing so generates more electric current conversion from heat. The heat supplied to increase the temperature above $T_{C,\uparrow}$ is entirely converted into electrical energy during the phase transition from ferro- to paraelectric at this temperature.

Efficiency of the conversion cycle is calculated by comparing the electrical energy generated to the thermal energy or heat supplied to the PE. The thermodynamic efficiency of the system is denoted by η and is calculated by Eq. (7.37), where Q_{in} is the total heat transferred to the material during one

cycle (in watts), and W_E is the total electrical energy generated during that cycle (in watts) with time period τ.

$$\eta = \frac{\dot{W}_E}{\dot{Q}_{in}} \tag{7.37}$$

$$W_E = \frac{\dot{W}_E}{\tau} \tag{7.38}$$

Heat losses to the surroundings as well as leakage current have been accounted for in measured $\dot{Q}_{in}$ and $\dot{W}_E$.

7.4 Pyroelectric Energy Conversion and Harvesting: Recent Progress

In the past, researchers attempted to investigate the process of energy harvesting using pyroelectric material without exploring innovative ways to increase the efficiency of energy conversion.[11,15,17 19] In more recent years, researchers have tried to improve energy conversion efficiency by improving the physical properties of the materials and/or by using more energy-efficient techniques in which energy conversion behavior is highly dependent on the time derivative of temperature.[20 24]

7.4.1 Pyroelectric energy harvesting based on the direct pyroelectric effect

This section presents the capabilities of pyroelectric materials in harvesting energy when subjected to cyclic or linear temperature variations. Pyroelectric material is considered to exhibit no losses with purely linear properties. Assuming limited heat exchange on the outer surface of the pyroelectric element,

$$D = \varepsilon E + p\theta, \tag{7.39}$$

and

$$S = pE + c\theta/\theta, \tag{7.40}$$

where D is electric induction, E is electric field, θ is temperature, and S is entropy. The pyroelectric constants are dielectric permittivity ε, pyroelectric coefficient p, and heat capacity c.[20] Dotted variables denote time derivatives.

Based on Newton diffusion, the equations coupling external variables to the pyroelectric element are

$$Q = \frac{h}{e}(\theta \quad \theta_{ext}), \tag{7.41}$$

$$E = \rho D, \tag{7.42}$$

where Q is the exchange heat per unit volume, θ_{ext} is the external temperature, h is the surface heat exchange coefficient, e is the sample thickness, and ρ is

resistivity connected to the pyroelectric element. Sehald et al. considered the electrical loading of the pyroelectric element as purely resistive, where power was generated by stimulating an electric field and an electric induction that exhibited a $\pi/2$ phase shift to give output power per unit volume.[25] Using parameters $p = 746\ \mu Cm^{-2}K^{-1}$, $\varepsilon = 2100\varepsilon_0$, $c = 2.5 \times 10^6\ Jm^{-3}K^{-1}$, and a temperature amplitude of 20 °C peak-to-peak at 0.01 Hz for 0.75 $Pb(Mg_{1/3}Nb_{2/3})O_3$-0.25$PbTiO_3$ ceramic, with a heat exchange of 10 $Wm^{-2}K^{-1}$ by forced convection of air, an output power of 13.4 μWcm^{-3} was obtained. Similar studies predicted output power for an external temperature variation of 20 °C peak-to-peak at 0.01 Hz and $h = 10\ Wm^{-2}K^{-1}$ with a thickness of 100 μm that provided the following results on different materials: (1) output power of 100–169 μWcm^{-3} for a single crystal of 111PMN-0.25PT (p = 1300–1790 $\mu Cm^{-3}K^{-1}$, ε = 961–1100), (2) output power of 12.9 μWcm^{-3} for a ceramic PZT (p = 533 $\mu Cm^{-2}K^{-1}$, ε = 1116), (3) output power of 13.4 μWcm^{-3} for PMN-0.25PT ceramic ($p = 746\ \mu Cm^{-3}K^{-1}$, $\varepsilon = 2100$), and (4) output power of 6.12 μWcm^{-3} for polymer PVDF ($p = 33\ \mu Cm^{-2}K^{-1}$, $\varepsilon = 9$).[25,28]

When investigating the performance of pyroelectric PVDF (with 10-cm^2 and 0.1-mm thickness) under a room temperature variation of 0.3 °C, Mohammadi and Khodayari obtained a harvested power of 4.33 μW.[29] They also proved that the harvested energy is proportional to the electroded surface area.

Xie et al. modeled results for harvesting energy using the pyroelectric effect with PZT-5A (commercial name), PMN-PT, and PVDF and compared the measured results with the simulated values.[30] The results were within 4% for PMN-PT, 8% for PVDF, and 9% for PZT-5A. Peak power densities were experimentally determined to be 0.33, 0.20, and 0.12 $\mu W/cm^2$, respectively.

Dalola et al. investigated thick films of PZT, characterized as thermal energy harvesters, in order to supply a low power to an autonomous system that can work in a low-duty-cycle switched mode for measurement and transmission operations.[31] The charge extracted from the energy converter was stored in a capacitor using full-wave and Schenkel doubler circuits with a sinusoidal temperature rate of 1.8 °C/s peak. The maximum value of the current generated by the samples was 140 nA.

Zhang et al. proposed a solar microenergy harvester using the pyroelectric effect and low wind flow.[32] The basic concept was validated by laboratory experiments in which the average power density with the PZT as pyroelectric material was 4.2 μWcm^{-3} with the time variation of temperature reaching 0.53 °C/s, with radiation of 1000 W/m^2, and the controlled speed of airflow at 2 m/s.

Hsiao et al. proposed the concept of etching a PZT sample to form cavities in an effort to improve the temperature variation rate of a thicker PZT film, and thereby enhance the energy conversion efficiency.[33]

To generate thermal transients, Ravindran et al. proposed a novel microthermomechanic-pyroelectric energy generator (μTMPG) that converts

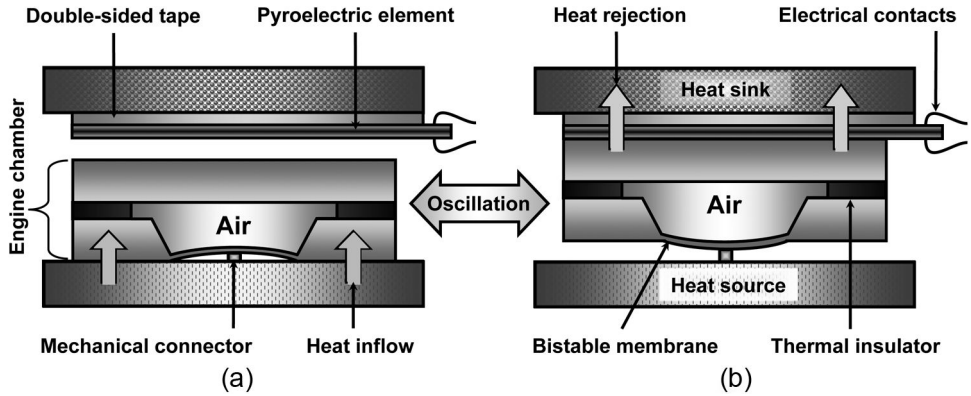

Figure 7.10 A simplified thermomechanical-pyroelectric energy generator in (a) a PEG in cooling state and (b) a PEG in heating state. Adapted from Ref. 34 with permission from AIP Publishing LLC.

a stationary spatial thermal gradient into the desired transient temperature profile across a PEG.[34] In this device, a thermal heat shuttle is moved between the hot and cold sides of a thermomechanical heat engine, thereby transferring heat onto a PEG in a periodic-pulse time pattern (Fig. 7.10). Consequently, the PEG is continuously stimulated by thermal transients and generates charge packets via the pyroelectric effect.

Ravindran et al. used an active element Vibrit 1100 (from Johnson Matthey Piezoproducts) with a pyroelectric coefficient 409.1 $\mu C/m^2K$ and dielectric constant of 3462.2. The harvesters generated 3.03 μW of electric power from a spatial temperature difference of 79.5 K, thus demonstrating the technical feasibility of their concept.

Cuadras et al. investigated pyroelectric cells based on screen-printed PZT films and commercial PVDF films as thermal energy harvesting sources.[35] Electric currents on the order of 10^{-7}A and charges on the order of 10^{-5}C were achieved for temperature fluctuations of 300–360 K in a time period of the order of 100 s.

Yang et al. designed and fabricated ZnO nanowire arrays based on a pyroelectric energy nanogenerator for harvesting thermoelectric energy.[36] The pyroelectric current was 1.5 nC/cm^2K, and voltage coefficients were $\sim$1.2 and $\sim 2.5–4.0 \times 10^4$ V/mK for nanowires with an average diameter of 200 nm. The energy characteristic coefficient obtained was $\sim$0.05–0.08 Vm^2/W.

Recently, Scott R. Hunter's group at Oak Ridge National Laboratory designed a novel pyroelectric energy harvester that uses a resonantly driven pyroelectric capacitive bimorph-cantilever structure.[37] It has the potential for energy conversion efficiencies several times those of any previously demonstrated pyroelectric or thermoelectric thermal energy harvesters. A

side view of the bimorph cantilever structure showing the cantilevered capacitor thin-film layers is illustrated in Fig. 7.11.[37]

Batra et al. characterized a pyroelectric lithium tantalate (LT) element for electrical parameters as a function of temperature.[38] They modeled and simulated energy harvesting capacity with temperature variations. The results showed that harvested energy can be compatible with an autonomous sensor module operating in a low-duty-cycle switched-supply mode. Using measured data, they attempted to predict the voltage and power generation through known analytical methods used by Xie et al.[39] They also examined three important parameters that affect power generation. The details of their full investigation are presented in this section. An equivalent circuit diagram of the pyroelectric device utlized as the model to analytically simulate and predict voltage and power generatation is shown in Fig. 7.12.[39]

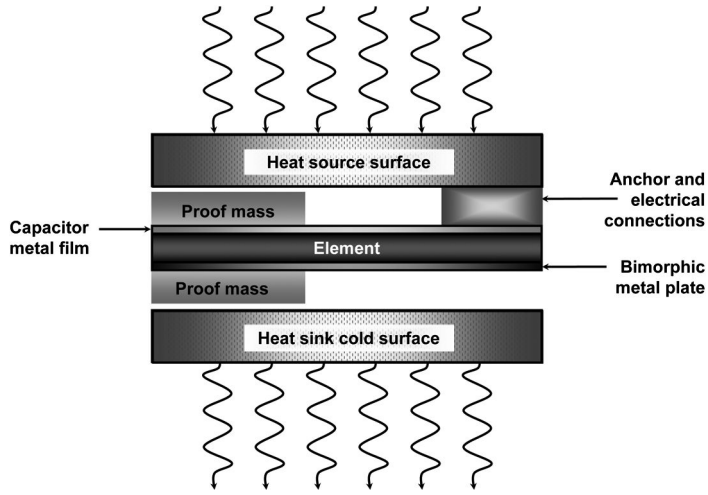

Figure 7.11 Conceptual view of a pyroelectric thermal energy scavenging device (adapted with permission from Ref. 37).

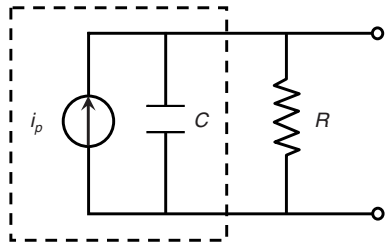

Figure 7.12 Pyroelctric circuit diagram where i_p is the generated current, C is the capacitance of the pyroelectric chip, and R is the external resistance.

Figure 7.13 shows the dependence of measured capacitance C on the temperature of the LT element. Figure 7.14 shows the dependence of the pyroelectric coefficient p on the temperature of the LT element. The capacitor-based transducer was fabricated by coating silver electrodes on a Z-cut LT sample. These parameters increase with the increase of temperature, as is expected for pyroelectrics.

The pyroelectric current generator is modeled as a current source with a capacitance and resistor in parallel with a current source (Fig. 7.10). The current is generated within an element through change in temperature. The

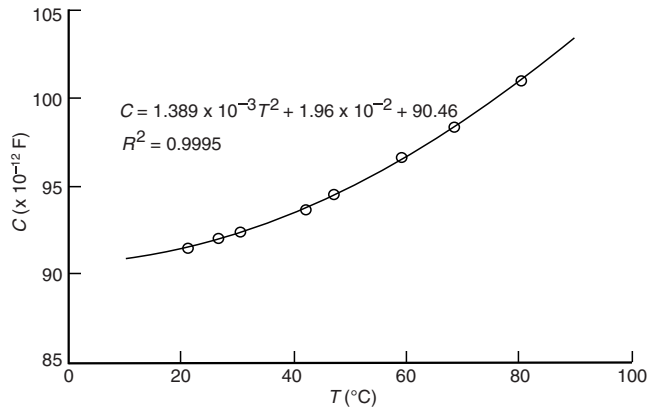

Figure 7.13 Measured capacitance C versus temperature of the LT-based device (adapted with permission from Ref. 38).

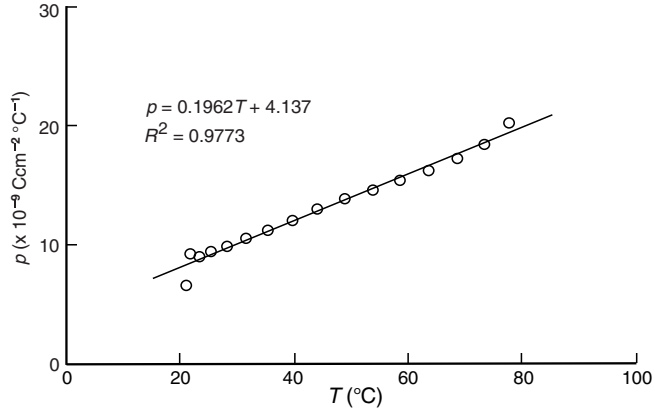

Figure 7.14 Measured pyroelectric coefficient p versus temperature of the LT-based device (adapted with permission from Ref. 38).

circuit in Fig. 7.12 can be modeled with the following first-order differential equation:

$$C(T)\frac{dV}{dt}+\frac{V}{R}=i_p=p(T)A\frac{dT}{dt}, \tag{7.43}$$

where $C(T)$ is capacitance as a function of temperature, R is resistance, V is voltage, i_p is pyroelectric current, A is the cross-sectional area of the sample, dT/dt is temperature gradient, and $p(T)$ is the pyroelectric coefficient as a function of temperature. This equation is then numerically solved with a given temperature profile using the Runge–Kutta fourth-order numerical integration technique, as follows:

$$V_{i+1}=V_i+\frac{1}{6}(k_1+2k_2+2k_3+k_4)h, \tag{7.44}$$

and

$$k_1=f(t_i,V_i),\quad k_2=f\left(t_i+\frac{1}{2}h,V_i+\frac{1}{2}k_1h\right),\quad k_3=f\left(t_i+\frac{1}{2}h,V_i+\frac{1}{2}k_2h\right),\quad k_4=f(t_i+h,V_i+k_3h), \tag{7.45}$$

where

$$f(t,V)=\frac{A}{C(T)}p(T)\frac{dT}{dt}\quad\frac{V}{RC(T)}, \tag{7.46}$$

and $h=\Delta t$ is the step size. The capacitance (shown in Fig. 7.13) and the pyroelectric coefficient as a function of temperature (shown in Fig. 7.14) were obtained from the experiment. For the purpose of simulation, temperature is chosen as a linear function of time. The temperature is calculated at various time instances, and the corresponding values of p and C are obtained from Figs. 7.13 and 7.14, respectively. Equation 7.36 is then solved using Eq 7.44. Figure 7.15 shows the simulation results of the voltage and power generated as a function of time.

Utilizing the proposed model and analysis, it is possible to optimize the rate of heating as well as circuit resistance to obtain maximum power generation. To show the effect of the heating rate on the generated voltage, results from an investigation in which heating rates and circuit resistances were varied with time are depicted in Fig. 7.16. Enhancing the voltage generated in pyroelectric energy harvesters by increasing the pyroelectric coefficients is still a considerable challenge. However, the unique techniques proposed here can be further pursued to enhance IR-detector performance for energy harvesting.[40 43] It has been demonstrated that IR-detector responsivity can be greatly increased through incorporation of the following unique techniques: (1) response can be increased more than one hundredfold by adopting multilayer structures/bimorphs of pyroelectrics,[40] (2) the effective pyroelectric coefficient can be increased by nearly two orders of magnitude

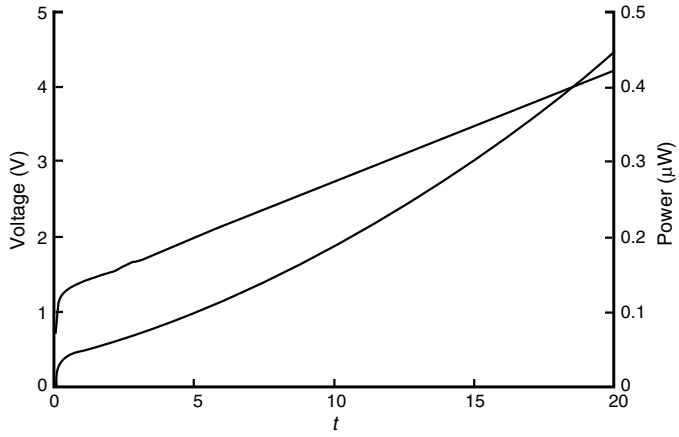

Figure 7.15 Predicted (simulated) voltage and power generated versus time by the LT-based device during heating at 5 °C/s (adapted with permission from Ref. 38).

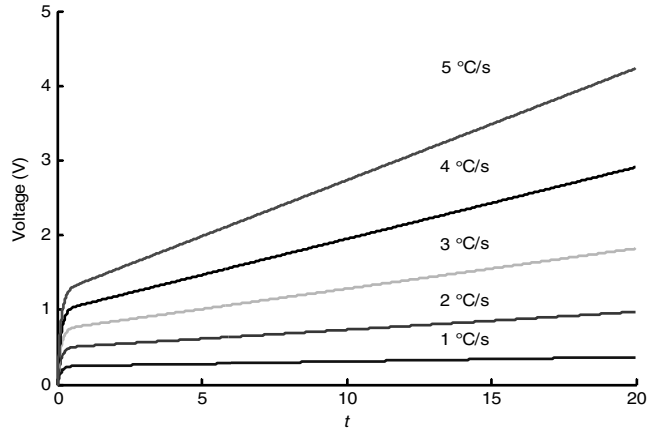

Figure 7.16 Predicted (simulated) voltages generated as a function of time at different heating rates of the LT-based device (adapted with permission from Ref. 38).

over those observed from conventional pyroelectric thin-film devices by fabricating compositionally graded structures,[41] (3) performance can be increased fourfold through the fabrication of porous films of PZT, and (4) by embedding silver nanoparticles in pyroelectric composites; [P(VDF-TrFE): $LiTaO_3$] has shown a considerable increase in the pyroelectric coefficient.[42,43]

Batra et al. concluded that the power extracted from a pyroelectric element is typically low but can guarantee a continuous operation for low-power autonomous sensors.[38] It has also been proposed that piezoelectrically converted energy can be accumulated in a storage capacitor using proper power management techniques, and then transferred to the load during short time intervals.[44]

Table 7.1 Properties of investigated smart materials: pyroelectric coefficient (p, nC/cm^{2}K), dielectric constant (ε', real part).

#	Material	Sample form	Pyroelectric coefficient p	Dielectric constant (ε') d
1	Doped lead lanthanum zirconate titanate (DPLZT)	Bulk ceramic	41	768
2	Lead lanthanum zirconate titanate (PLZT)	Bulk ceramic	45	700
3	PZT multilayer (PZTML)	Thin films	34	845
4	Triglycine selenate	Bulk single crystals	420	420
5	Lead lanthanum zirconate titanate (PLZT 1): 8/40/60	Bulk ceramic	120	429
6	Lithium tantalate (LT)	Bulk single	$f(T)$	$f(T)$
7	PVDF lithium tantalite composite embedded with silver nanoparticles	Thick film	$f(T)$	$f(T)$
8	Modified lead metaniobate	Bulk ceramic	$f(T)$	$f(T)$
9	Modified lead titanate	Bulk ceramic	$f(T)$	$f(T)$
10	Cement nanocarbon fiber composite (Ce NFC): 0.63% noncarbon fibers	Bulk ceramic	$f(T)$	$f(T)$

Recently, Batra et al. numerically simulated the energy harvesting capacity of laboratory-fabricated and commercially available pyroelectric elements/transducers by capturing the thermal energy of pavements.[45] Single- and polycrystalline elements characterized for applicable performance parameters were triglycine selenate, lithium tantalate, modified lead zirconate titanate, modified lead titanate, modified lead metaniobate, pyroelectric polymer nanocomposites (such as Portland cement), nanocarbon fibers, polymer-lithium tantalate embedded with silver nanoparticles, and others. The energy harvesting capacity of these samples was investigated through modeling and numerical simulation using the available pavement's temperature profile data over an extended period of time. The results indicate that electrical energy harvesting via pyroelectricity is a feasible technique for powering autonomous low-duty electric devices. Based on the analysis of a single electric-energy-harvesting unit, Batra et al. proposed that the triglycine selenate pyroelements will perform better than others in regard to the amount of voltage and energy densities extracted with respect to time. The modeling and analysis process and results are presented below in detail.

Pyroelectric materials and their attributes are presented in Table 7.1. The appropriate electric circuit for ultimately designing a single-module "microelectric harvester" for modeling and numerical simulation of energy harvesting from pavements via pyroelectricity is illustrated in Fig. 7.17.

A variety of materials were selected from three categories:

1. Single crystalline: triglycine selenite (TGSe), lithium tantalate (LT);
2. Polycrystalline: lead metaniobate (PN), doped lead lanthanum zirconate titanate (DPLZT), lead lanthanum zirconate titanate (PLZT), modified

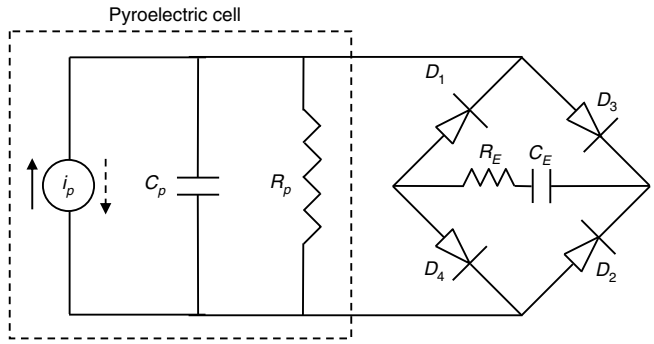

Figure 7.17 Pyroelectric cell current generator with a full-wave-bridge rectifier circuit for charge storage in C_E using diodes D_1-D_2 and D_3-D_4.

lead metaniobate (PN), lead lanthanum zirconate titanate (8/40/60, PLZT-1), and modified lead titanate (MPT);

3. Polymer pyroelectric composites: Portland cement nanocarbon fibers and silver nanoparticles embedded in P(VDF-TrFE):LT(PVT:LT-Ag).

Figures 7.18–7.21 demonstrate the dependence of dielectric constant ε' and pyroelectric coefficient p on temperature in all of the materials listed in Table 7.1. With each material, ε' and p increase with an increase in temperature—as is expected in pyroelectrics. Modified lead niobate shows the highest ε', whereas PVT:LT-Ag shows the lowest. The highest pyroelectric coefficient is obtained from PVT:LT-Ag composite. In cement composites, p also increases with the increase in carbon nanofiber content. Figure 7.20 shows the effect of temperature on ε' for the cement composite containing different percentages of carbon nanofiber content. The observed increase in the dielectric constant for

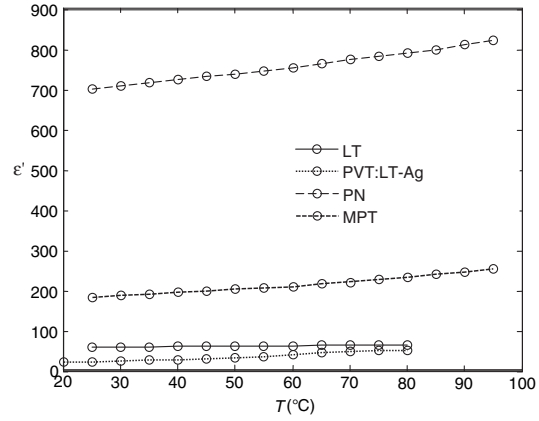

Figure 7.18 The effect of temperature on the dielectric constant ε' of selected pyroelectric materials.

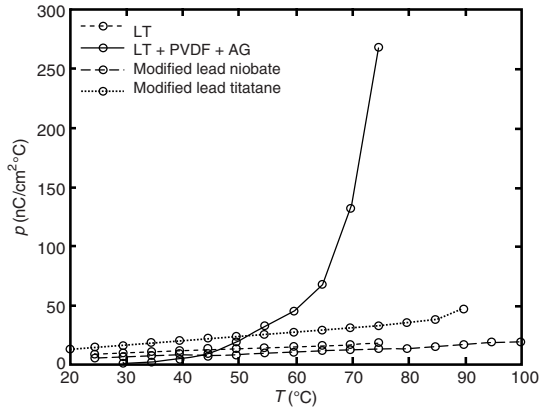

Figure 7.19 Changes in the pyroelectric coefficient p when varying the temperatures of selected materials.

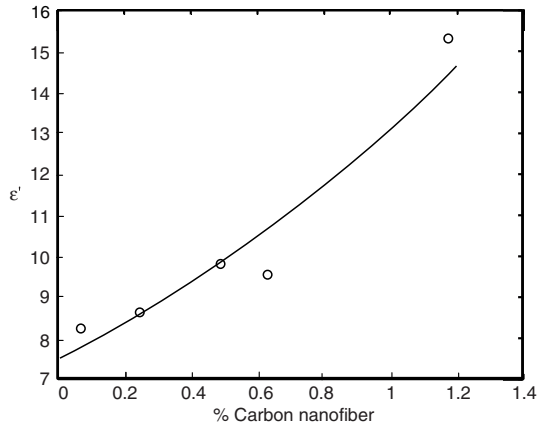

Figure 7.20 Changes in the dielectric constant ε' of different Ce-NFC composites with varying percentages of nanocarbon fiber content at 1 kHz and 40 °C.

the cement composite can be attributed to the increase in the mobility of ions as temperature increases, whereas in the case of other materials, the increase of ε' is due to the increase in dipole moments in the material.

The PEG is modeled as a current source with a capacitor and a resistor in parallel with the pyroelectric element.[43] The current is generated within the cell from the change in temperature. Figure 7.17 shows the circuit used to model pyroelectric sensors for energy conversion and charge storage. Equation 7.47 indicates that the pyroelectric current is directly proportional to the rate of temperature change as listed below:

$$dQ = di_p dt = pA\frac{dT}{dt} = pAdT. \tag{7.47}$$

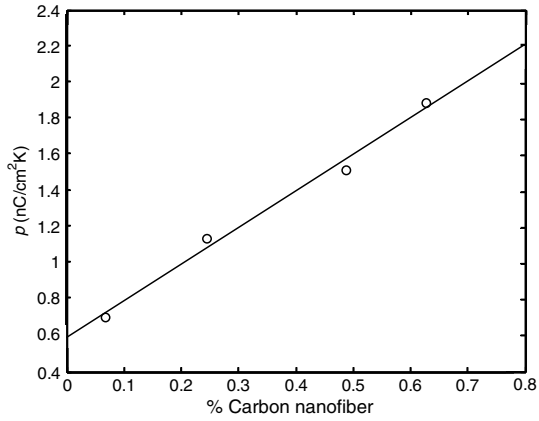

Figure 7.21 Changes in the pyroelectric coefficient p of different Ce-NFC composites with varying percentages of nanocarbon fiber content at 1 kHz and 40 °C.

However, one problem with this behavior is that the current flows in the opposite direction when the rate changes from positive to negative or vice-versa. In other words, changing the temperature by heating or cooling will produce charge accumulation in different directions. However, to charge an external capacitor, it is essential that the capacitor be continuously charged.

To mitigate this problem, a full-wave-bridge diode-rectifier circuit can be used, as shown in Fig. 7.17. The pyroelectric source is connected to an external capacitor C_E and an external resistor R_E. There are two pairs of diodes. One pair is used for each direction of charge flow. Diodes D_1-D_2 are used when the charges flow in one direction, and diodes D_3-D_4 are used when the charges flow in the opposite direction. When only the forward-biased diodes work, the other two pairs block current flow under the reverse-biased condition. In both cases, the external capacitor C_E is charged via charge flows in one direction, causing the voltage to increase across the external storage capacitor.

The charge flow in the two-capacitor system can be modeled as follows: when the new charge is accumulated, it is distributed in both capacitors, and the charge balance equation can be written as[46]

$$\Delta Q_n = Q_{E,n} \quad Q_{E,n\ 1} + Q_{P,n} \pm Q_{P,n\ 1} \tag{7.48}$$

$$\begin{aligned} Q_{P,n} &= V_n C_P, \\ Q_{P,n\ 1} &= V_{n\ 1} C_P, \\ Q_{E,n} &= V_n C_E, \text{and} \\ Q_{E,n\ 1} &= V_{n\ 1} C_E, \end{aligned} \tag{7.49}$$

where C_P is pyroelectric cell capacitance, C_E is external charging capacitance, V_n is voltage at temperature data point n, $V_{n\ 1}$ is voltage at temperature data point $n-1$, Q_P is charge accumulated in the pyroelectric cell, Q_E is external

capacitance, and ΔQ_n is the additional charge generated at the n^{th} data point (from heating or cooling). The $\pm$ sign in front of the fourth rightside term in Eq. (7.48) indicates that the current generated in the pyroelectric cell can be in the opposite direction if the sign of the temperature rate change shifts from the $(n-1)^{\text{th}}$ data point to the n^{th} data point. Substitution of Eq. (7.48) into Eq. (7.49) results in the following recurrence equation, from which the voltage across the external capacitance can be calculated at a given temperature data point:

$$V_n = \frac{\Delta Q}{C_P + C_E} + \left(\frac{C_E + C_P}{C_E + C_P}\right) V_{n\ 1} = \frac{pA\Delta T}{C_P + C_E} + \left(\frac{C_E + C_P}{C_E + C_P}\right) V_{n\ 1} \quad (7.50)$$

Once the voltage is determined, the energy stored at the n^{th} data point can be calculated from the following equation:

$$E_n = 0.5 C_E V_n^2. \quad (7.51)$$

Equations 7.50 and 7.51 have been used to simulate the voltage and energy, respectively, produced from a measured temperature profile of actual pavement temperature. Figure 7.22 shows the temperature profile between May and October at a weather station location in Huntsville, Alabama. The temperature profile was obtained from the Environmental and Climatic Database in the "Mechanistic Empirical Pavement Design Guide" (MEPDG).[47]

When storing energy from temperature change/fluctuations, the values of C_P and C_E should be optimized to achieve the highest energy storage. Furthermore, the external resistor R_E and the external capacitor C_E can be adjusted to obtain fast charging. The parameters of the materials used for the simulation are presented in Table 7.1. The simulated voltage and energy stored for the materials listed in Table 7.1 are shown in Figs. 7.23 and 7.24, respectively. The circuit is simulated assuming a 1.0-cm^2 area of the

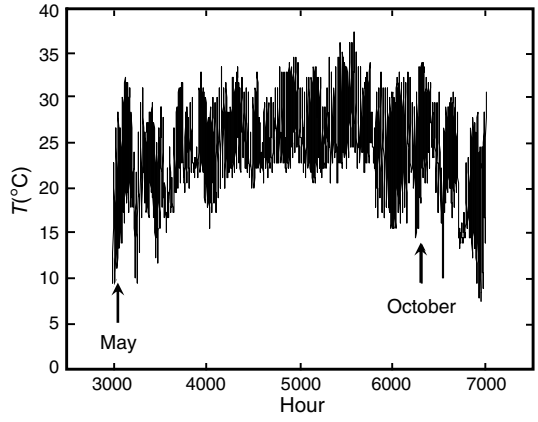

Figure 7.22 Temperature profile (May–October) at station 03856 in Huntsville, Alabama (USA).[47]

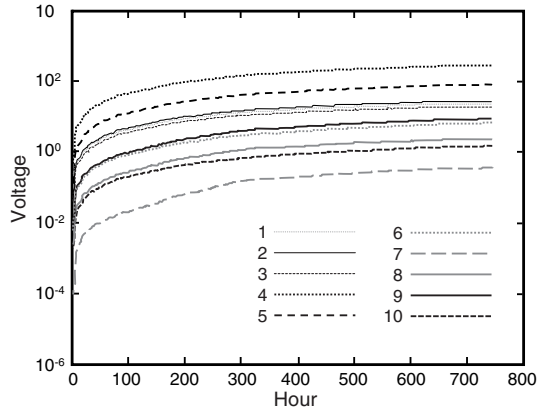

Figure 7.23 Voltage generated via storing charges in a capacitor caused by a typical variation of temperature during May (per Fig. 7.22); legend: 1-DPZT, 2-PLZT, 3-PZTML 4-TGSe, 5-PLZT-1, 6- LT, 7-PVT:LT-Ag, 8-PN, 9-MPT, 10-Ce-NFC.

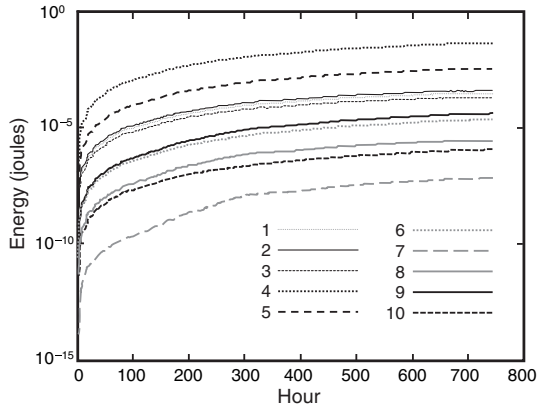

Figure 7.24 Electric energy generated via storing charges in a capacitor caused by a typical variation of temperature during May (per Fig. 7.22); legend: 1-DPZT, 2-PLZT, 3-PZTML 4-TGSe, 5-PLZT-1, 6-LT, 7-PVT:LT-Ag, 8-PN, 9-MPT, 10-Ce-NFC.

pyroelectric cell with 0.1-cm thickness. The external storage capacitor is assumed to be 1.0 μF. For materials whose pyroelectric coefficient and dielectric constant are functions of temperature, the actual functional relationship has been used. For other materials, constant values of p and ε' have been used. Figure 7.23 shows the accumulated voltage for 800 h during the month of May starting from zero voltage. Figure 7.24 shows the associated accumulated energy. The highest maximum voltage accumulated during the month of May is approximately 278 V from a triglycine selenate sample, and the corresponding electric energy is approximately 0.04 J. Furthermore, it is worth mentioning that this maximum voltage can be

controlled by choosing a suitable value for external storage capacitor C_E. Finally, researchers at the U.S. National Cooperative Highway Research Program concluded that the materials' parameters have successfully been used to perform numerical simulation with *actual* pavement temperature data obtained from the climatic database of MEPDG.[47] Among the pyroelectrics selected for simulation, triglycine selenate (TGSe) is an attractive candidate for energy harvesting from pavements due to its high pyroelectric coefficient near ambient temperatures. Its real application will determine if the predicted performance can be realized or not. To fabricate and embed an "energy harvesting module" based on TGSe materials, technology must be developed.

Guyomar et al. studied the feasibility of heat-energy harvesting using the pyroelectric effect in a PVDF microgenerator for a given thermal cycle.[20,48] In order to improve the effectiveness of the conversion of energy from heat to electricity, they applied and experimentally tested the synchronized switch harvesting on inductor (SSHI) technique. The SSHI technique consists of nonlinearly processing the pyroelectric voltage using an electrical switching device connected to the pyroelectric elements. For several amplitude variations of temperature (0.5–8.0 K), the conversion efficiency was found to be about 0.02% of the Carnot thermodynamic cycle with a standard interface (diode bridge type). Under the same heating conditions, the SSHI technique increased the converted energy by a factor of about 2.5 times the standard interface, at which the efficiency became practically 0.05% of the Carnot thermodynamic cycle. With the improved interfacing technique, the electrical power produced with a temperature amplitude of 7 K was more than 0.3 mW for an energy harvesting device composed of 8 g of active material (PVDF). The main power limitation was found to be caused by the temperature frequency and low speed of heat transfer.

7.4.2 Pyroelectric energy harvesting based on thermodynamic cycles

Pyroelectric energy conversion offers a novel and direct way to convert waste thermal energy into electricity by alternatively heating and cooling a pyroelectric material resulting in electricity generation via thermodynamic cycles. In this regard, early theoretical studies predicted low efficiencies, while experimental studies have shown better results.[14,49 59] Recent works by various researchers based on the thermodynamic cycles listed in the previous section, including design of prototypes fabricated for energy harvesting, are reviewed in the following paragraphs.

Mohammadi and Khodayari and others numerically investigated lead magnesium niobate-lead titanate [PMN-25PT-75%PMN-25%PT)] single crystal for its pyroelectric energy harvesting capacity utilizing the Lenoir and Ericsson thermodynamic cycles.[58,60 62] The pyroelectric coefficient, heat capacity, and dielectric permittivity of PMN-25PT were 1790 $\mu C/m^2K$, 2.5 $J/m^3 \cdot K$, and 961, respectively.[61] The authors found that harvested

energy increases nonlinearly in regards to electric field. The values of harvested energy, efficiency η, and efficiency related to the Carnot cycle $\eta/\eta_{Carnot}\%$ for the Lenoir cycle are 17 mJ/cm^3, 0.07, and 0.7, respectively, and for the Ericsson cycle 35.5 mJ/cm^3, 0.15, and 4.6, respectively, at 2 kV/mm electric field. It was found that harvested energy decreased with the increase of initial temperature with the Ericsson cycle, whereas it remained independent of the initial temperature in the Lenoir cycle. Thus, the authors concluded that the advantage of the Lenoir cycle is that it can be used in various temperature conditions.

Khodayari et al. investigated the energy harvesting capacity with temperature variations in a $Pb(Zn_{1/3}Nb_{2/3})_{0.955}Ti_{0.045}O_3$ single crystal using the Ericsson thermodynamic cycle.[62] The efficiency of this cycle compared to the Carnot cycle is 100 times higher than direct pyroelectric energy harvesting, and it can be as high as 5.5% for a 10 °C temperature variation and 2 kV/mm electric field. The amount of harvested energy for a 60 °C temperature variation and 2 kV/mm electric field was 242.7 mJ $\cdot$ cm ^{3}. The influence of ferroelectric phase transitions on the energy harvesting performance was illustrated with experimental results. As demonstrated by the authors, energy harvesting based on a ferroelectric–ferroelectric (FE-FE) transition strongly depends on the applied electric field and the temperature conditions due to the volatility of this transition.

The efficiency of the Ericsson cycle using the FE-FE transition was found to be higher than techniques that used linear properties of pyroelectric materials, such as the SSHI technique.[35] The efficiency of the Ericcson cycle compared to the Carnot cycle was 100 times that of the SSHI technique with a PVDF film. For a temperature variation of 10 °C, the value of harvested power based on an FE-FE transition using the Ericsson cycle was 3 times higher than the harvested power of the thermoelectric device.

The research of Sebald et al. dealt with energy harvesting from temperature variations.[62] It was shown that direct pyroelectric energy harvesting is not effective, whereas Ericsson-based cycles give energy 100 times higher. The principle and experimental validations of the Ericsson cycle were shown with the example of $0.90Pb(Mg_{1/3}Nb_{2/3})O_3$–$0.10PbTiO_3$ ceramic. Harvested energy reached 186 mJ $\cdot$ cm ^{3} for a 50 °C temperature variation and electric field cycle of 3.5 kV mm ^{1}. A correlation between the electrocaloric effect and pyroelectric energy harvesting was also shown. Harvested electric energy with Ericsson cycles was simply expressed as electrocaloric heat multiplied by the Carnot efficiency. Several examples were given, using materials with the highest known electrocaloric effect. This leads to energies of hundreds of mJcm ^{3} for a limited 10 °C temperature variation. Compared to Carnot's efficiency, this is much higher than the best thermoelectric materials based on the Seebeck effect. The authors demonstrated large energy harvesting possibilities, but practical implantation needs to be developed in order to confirm the viability of such interesting results.

Zhu et al. studied the effect of the electric field frequency on energy harvesting in $Pb(Zn_{1/3}Nb_{2/3})_{0.955}Ti_{0.045}O_3$ single crystals with an Ericsson cycle.[63] At the lowest frequency of 0.01 Hz (which corresponds to the slope for the application of the electric field), the maximum harvested energy was 86 mJcm ^{3}.

In the framework of microelectric generators, Sebald et al. presented the key points for energy harvesting from temperature using ferroelectric materials.[64] It is known that energy harvesting from thermoelectric devices requires temperature spatial gradients, whereas ferroelectric materials require temporal fluctuation of temperature, thus leading to different application targets. Ferroelectric materials can harvest the available thermal energy with nondependency on the material's properties (limited by Carnot conversion efficiency), whereas thermoelectric material efficiency is limited by each material's properties (ZT, figure of merit). However, the necessary electric fields for Carnot cycles are far beyond the breakdown limit of bulk ferroelectric materials. Thin films might be an excellent solution for achieving ultrahigh electric fields and outstanding efficiency. The authors presented advantages and drawbacks of different thermodynamic cycles. Using the Carnot cycle, the harvested energy would be independent of the material's properties. However, using more realistic cycles, the energy conversion effectiveness remains dependent on the material's properties. Authors proposed a particular coupling factor called the energy harvesting figure of merit, defined to quantify and check the effectiveness of pyroelectric energy harvesting—similar to an electromechanical coupling factor as $k^2 = p^2\theta_o/(\varepsilon_{33}^{\theta}\ C_E)$, where p, θ_o, $\varepsilon_{33}^{\theta}$, and C_E are the pyroelectric coefficient, maximum working temperature, dielectric permittivity, and specific heat, respectively. This figure of merit provides the effectiveness of all of the techniques of energy harvesting (except the Carnot cycle). Authors showed that very high efficiency could be reached by using $<111>0.75Pb(Mg_{1/3}Nb_{2/3})$-$0.25PbTiO_3$ single crystals and synchronized switch harvesting on an inductor (almost 50% of Carnot efficiency).[35] Finally, practical implementation of key points of pyroelectric energy harvesting are presented showing that the different thermodynamic cycles are feasible and potentially effective, even compared to thermoelectric devices.

Based on the concept of a coupling factor, called an energy harvesting figure of merit, Chang and Huang showed enhancement in the pyroelectric coefficient in 2-2 connectivity laminate composites.[64,65] The authors found that in a lead zirconate titanate and stainless steel laminate composite, an 88% pyroelectric coefficient enhancement is shown to increase the maximum power density, efficiency, and electrothermal coupling factor by 254%. The authors also showed that other material pairings exhibit great promise in this energy harvesting application, owing to a large pyroelectric coefficient enhancement accompanied by a reduction in total thermal mass.

Nguyen et al. investigated the design and construction of a PEG and its ability to directly convert waste heat into electricity via the Olsen cycle, as

depicted in Fig. 7.9.[66] Their device consisted of a cylindrical Teflon® chamber with a vertically oscillating piston driving a working fluid back and forth between a heat source and a cold heat exchanger. The Olsen cycle was performed on copolymer 60/40 [P(VDF-TrFE)] thin films sandwiched between metallic electrodes with 50-cSt silicone oil as the working fluid. The effects of channel width, frequency, and stroke length on temperature swing, heat input, and energy and power densities were also investigated. Reducing the channel width and increasing the stroke length had the largest effect on the performance of the designed device. A maximum energy density of 130 J/l was achieved at 0.061-Hz frequency with temperature oscillating between 69.3 °C and 87.6 °C. Furthermore, a maximum power density of 10.7 W/l was obtained at 0.12 Hz between 70.5 °C and 85.3 °C. In both cases, the low and high electric fields in the Olsen cycle were 202 kV/cm and 739 kV/cm, respectively. To the best of the authors' knowledge, this is the largest energy density achieved by any pyroelectric energy converter using P(VDF-TrFE) that matched the performances reported in the literature for more expensive lead zirconate stannate titanate (PZST) ceramic films operated at higher temperatures (30 J/l).[9] The authors proposed that such a device could be used for waste heat recovery from internal combustion engines and various other electronic devices.

For the first time, Lee et al. reported a procedure to implement the Olsen cycle by alternatively placing a pyroelectric material in thermal contact with a cold and a hot source.[67] [P(VDF-TrFE)] copolymer thin films with 60/40 VDF/TrFE mole fraction were used. A maximum energy density of 155 J/L per cycle was achieved at 0.066 Hz between 25 °C and 110 °C, and electric fields were cycled between 200 kV/cm and 350 kV/cm. Heating and cooling of the film was achieved by conductive heat transfer using a stamping technique. It was proposed that the procedure could be implemented in a compact automated device.

Kandilian et al. reported on direct thermal-to-electrical energy conversion by performing the Olsen cycle on pyroelectric materials with following energy density:[68]

$$N_D = (E_H \quad E_L)\left\{\frac{\varepsilon_0}{2}[\varepsilon_r(T_{cold}) \quad \varepsilon_r(T_{hot})](E_H \quad E_L) + [P_S(T_{cold}) \quad P_S(T_{hot}) + \frac{d_{33}x_{33}}{s_{33}}]\right\}, \quad (7.52)$$

where $x_3 = \alpha_3(T_{hot} \quad T_{cold})$, d_{33}, and s_{33} are strain, elastic compliance, and piezoelectric coefficient, respectively.

The energy harvesting capability of commercially available (001)-oriented $68PbMg_{1/3}Nb_{2/3}O_3$-$32PbTiO_3$ (68PMN-32PT) single-crystal capacitors was measured experimentally. An energy density of 100 mJcm ^{3}/cycle, corresponding to 4.92 mWcm ^{3}, was obtained by successively dipping the material in oil baths at temperatures $T_{cold} = 80$ °C and $T_{hot} = 170$ °C, and cycling the electric field between 2 and 9 kV cm ^{1}. Similarly, an energy density of

55 mJcm ^{3}/cycle was obtained between 80 °C and 140 °C. An estimated 40% of this energy resulted from the strain polarization due to the rhombohedral-to-tetragonal phase transition. The strain from this transition disappeared when the maximum operating temperature exceeded the Curie temperature by about 150 °C. The optimal low electric field E_L used in the Olsen cycle was found by the authors to be around 2 kVcm ^{1}, thereby maximizing energy harvested. In addition, the material suffered from (1) dielectric breakdown for electric fields larger than 9 kVcm ^{1} and (2) cracking from thermal stress for operating temperature differences in excess of 90 °C. A physical model predicting the total amount of energy harvested was also derived (with few limitations such as simulation of hysteresis behavior), accounting for thermal expansion as well as temperature-dependent dielectric constant and spontaneous polarization. The model predictions fell within 20% of the experimental results in the temperature range between 80 °C and 170 °C and electric fields ranging from 2 to 9 kVcm ^{1}.

McKinley et al. recently reported on the direct thermal-to-electrical energy conversion by performing the Olsen (or Ericsson) cycle on [001]-poled $0.945PbZn_{1/3}Nb_{2/3}O_3$-$0.055PbTiO_3$ (PZN-5.5PT) single crystals.[69] The cold operating temperature T_{cold} was fixed at 100 °C. The hot temperature T_{hot} was varied from 125–190 °C. The electric fields E_L and E_H ranged from 0–0.2 MVm ^{1} and from 0.5–1.5 MVm ^{1}, respectively. The overall cycle (see Fig. 7.25) varied from 0.021 to 0.15 Hz by changing the duration of the isoelectric field heating and cooling processes 2-3 and 4-1, whereas the time rate of change of the

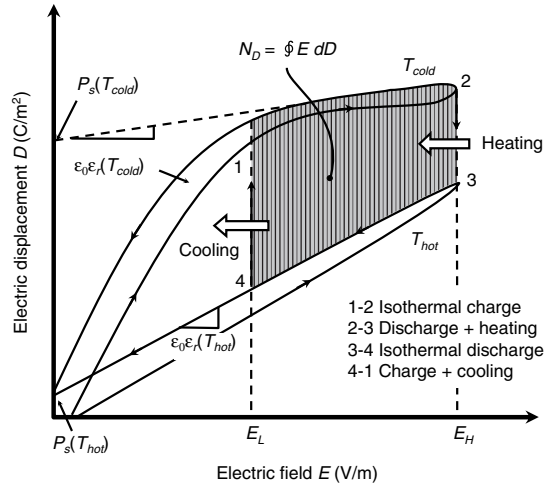

Figure 7.25 Electric displacement as a function of electric field for a typical pyroelectric material at temperature T_{hot} and T_{cold} along with the Olsen cycle. Adapted from Ref. 69 with permission from Elsevier.

electric field during isothermal processes 1-2 and 3-4 remained the same at 0.4 MVm ^{1}s ^{1}.

The authors found that as the Olsen cycle frequency increased, the energy density decreased, while the power density increased up to 0.1 Hz when the frequency cycle reached a peak. The maximum energy density obtained was 150 J/l/cycle for temperatures between 100–190 °C and electric field between 0.0 and 1.2 MV m ^{1} at a frequency of 0.034 Hz. The maximum power density reached 11.7 W/l at 0.1 Hz for temperatures between 100 and 190 °C and electric fields between 0.2 and 1.5 MVm ^{1}. Finally, Kandilian et al. showed an agreement between the experimental results and the predictions by a recently developed temperature-dependent property model validated with PMN-32PT using the Olsen cycle under quasi-equilibrium conditions.[68]

Lee et al. reported findings on the electrical energy generated by lanthanum-doped lead zirconate titanate (8/65/35 PLZT) subjected to the Olsen cycle.[70] The material was alternately dipped in cold and hot 100-cSt-silicone oil baths under specified electric fields. A maximum energy density of 888 J l ^{1}/cycle was obtained with a 290-μm thick 8/65/35 PLZT sample for temperatures between 25 and 160 °C and electric fields cycled between 0.2 and 7.5 MVm ^{1}. To the best of the authors' knowledge, this is the largest experimentally measured pyroelectric energy density with multiple cycles that corresponds to a power density of 15.8 W l ^{1}.

Vanderpool et al. numerically simulated a model for a prototypical pyroelectric converter by solving the 2D mass, momentum, and energy equations using finite element methods.[71] The pumping and electrical power generated were estimated from the computed pressure, temperature, and velocity. The results show that the energy efficiency increases as the density and specific heat of the working fluid and the pyroelectric material decrease. Moreover, the power density increases as the density and specific heat of the working fluid increase and those of the pyroelectric material decrease. Vanderpool et al. proposed that one could reasonably achieve an energy efficiency of 40% of the Carnot efficiency and a power density of 24 W/l of pyroelectric material such as PSZT.

Recently, Moreno et al. validated the numerical model simulating a prototype pyroelectric converter in detail, proposing that their model could be used to design and operate the next generation of PEGs based on oscillatory convective heat transfer to maximize the device performance in an affordable, time-efficient manner.[71 73]

7.5 Conclusions

The efficient conversion of waste thermal energy into electrical energy is of great importance due to the huge sources of low-grade thermal energy available in almost all societies on Earth. Based on the research discussed in

this chapter, energy harvesters utilizing both the linear and nonlinear properties of pyroelectric materials can play a significant role. Though commercial pyroelectric/ferroelectric energy harvesters are not yet available, fully functional pyroelectric energy generators are foreseeable in the near future.

References

1. S. Priya, "Advances in energy harvesting using low profile piezoelectric transducers," *J. Electroceram*. **19**, 165–182 (2007).
2. A. Khodayari, S. Mohammadi, and D. Guyomar, *Pyroelectric Energy Harvesting*, VDM Verlag Dr. Müller, Saarbrucken, Germany, pp. 1–15 (2011).
3. S. Beeby and N. White, *Energy Harvesting for Autonomous Systems*, Artech House, Norwood, Massachusetts, pp. 91–103 (2010).
4. Pavegen Systems, "Pavegen systems home page,"accessed July 29, 2010, http://www.pavegensystems.com.
5. A. K. Batra, M. D. Aggarwal, P. Guggilla, M. E. Edwards, P. G. Penn, and J. R. Currie, Jr., "Pyroelectric materials for uncooled IR detectors: processing, properties and applications," *NASA Technical Memorandum* **NASA/TM-2010-6373**, 1–71 (2010).
6. A. J. Simon and R. D. Belles, "Estimated State-Level Energy Flows in 2008," U.S. Energy Flow, Lawrence Livermore National Laboratory, September 16, 2009, https:/publicaffairs.llnl.gov/news/energy/energy.html#2009.
7. Y. Xu, *Ferroelectric Materials and Their Applications*, North-Holland, Amsterdam, pp. 29–35 (1991).
8. D. Vanderpool, "Numerical and Experimental Study of a Pyroelectric Energy Converter for Harvesting Waste Heat," M.S. Thesis, Mechanical Engineering, University of California, Los Angeles, pp. 16–30 (2008).
9. T. Yamada, T. Ueda, and T. Kitamaya, "Ferroelectric to paraelectric phase transition of vinylidene fluoride-trifluoethylene copolymer," *J. App. Phys.* **53**, 948–952 (1981).
10. F. J. Belta Calleja and A. Gonzalez Arche, et al., "Structure and properties of ferroelectric copolymer pf poly(vinylidine fluoride)," *Advances in Polymer Science* **108**, pp. 1–48 (1993).
11. M. Salwa, "Modeling and Development of a MEMS Device for Pyroelectric Energy Scavenging," Ph.D. Dissertation, University of Tennessee, pp. 26–40 (2011).
12. S. Mohammadi and A. Khodari, "Pyroelectric energy harvesting: with thermodynamic-based cycles," *Smart Mat. Res.* **2012**, 160956, 1–5 (2012).

13. Z. Spakovszky, *16.050 Thermal Energy, Fall 2002*. (Massachusetts Institute of Technology: MIT OpenCourseWare), http://ocw.mit.edu (Accessed July 09, 2013). License: Creative Commons BY-NC-SA.
14. W. H. Clingman and R. G. Moore, "Application of ferroelectricity to energy conversion process," *J. App. Phys.* **32**, 675–681 (1961).
15. E. Fatuzzo, H. Kiess, and R. Nitsche, "Theoretical efficiency of pyroelectric power converters," *J. App. Phys.* **37**, 510–516 (1966).
16. R. B. Olsen, D. A. Bruno, J. M. Briscoe, and E. W. Jacobs, "Pyroelectric conversion cycles," *J. App. Phys.* **58**, 4709–4716 (1985).
17. J. Gonzalo, "Ferroelectric materials as energy converters," *Ferroelectrics* **11**, 423–427 (1976).
18. J. D. Childress, "Application of a ferroelectric material in an energy conversion device," *J. App. Phys.* **33**, 1793–1798 (1962).
19. R. C. Buchanan and J. Huang, "Pyroelectric and sensor properties of ferroelectric thin film for energy conversion," *J. Europ. Ceram. Soc.* **19**, 1476–1471 (1999).
20. D. Guyomar, G. Sebald, E. Lefeuvre, and A. Khodayari, "Toward heat energy harvesting using pyroelectric material," *J. Intell. Mat. Syst. and Struct.* **20**, 265–271 (2009).
21. D. Guyomar, G. Sebald, S. Pruvost, M. Lallart, A. Khodayari, and C. Richard, "Energy harvesting from ambient vibrations and heat," *J. Intell. Mat. Syst. and Struct.* **20**, 609–624 (2009).
22. G. Sebald, et al., "On thermoelectric and pyroelectric energy harvesting," *Smart Mater. Struct.* **18**, 5006 (2009).
23. G. Sebald, D. Guyomar, and A. Agbossou, "Pyroelectric energy conversion: optimization principles," *IEEE Transactions on Ultrasonics, Ferroelectrics and Frequency Control* **55**, 538–551 (2008).
24. G. Sebald, D. Guyomar, and A. Agbossou, "On thermoelectric and pyroelectric energy harvesting," *Smart Mater. Struct*. **18**, 125006-1–125006-6 (2009).
25. G. Sebald, L. Sevetrat, D. Guyomar, L. Lebrun, B. Guiffard, and S. Pruvost, "Electrocaloric and pyroelectric properties of $0.75Pb(Mg_{1/3}Nb_{2/3})O_3$-$0.25PbTiO_3$ single crystals," *J. Appl. Phys.* **100**, 124112-1–124112-6 (2006).
26. W. Y. Ng, B. Ploss, H. L. W. Chan, F. G. Shin, and C. L. Choy, "Pyroelectric properties of PZT/P(VDF-TeFE) 0-3 composites," *ISAF 2000: Proc. IEEE Int. Symp. on Applications of Ferroelectrics*, 767–270 (2000).
27. D. Guyomar, G. Sebald, L. Sevetrat, and L. Lebrun, "Ferroelectric electrocaloric conversion in $0.75(PbMg_{1/3}Nb_{2/3}O_3)$-$0.25(PbTiO_3)$ ceramics," *J. Phys. D: Appl. Physics* **39**(20), 4491–4496 (2006).

28. S. B. Lang and S. Muensit, "Review of some lesser-known applications of piezoelectric and pyroelectric polymers," *Appl. Physics A* **25**, 125–134 (2006).
29. S. Mohammadi and A. Khodayari, "Free energy harvesting from ambient temperature variations," *Int. J. Mech. Mater. Engn. (IJMME)* **6**, 167–170 (2011).
30. J. Xie, X. P. Mane, C. W. Green, K. M. Mossi, and K. K. Leang, "Performance of thin piezoelectric materials for pyroelectric energy harvesting," *J. Intell. Mater. Syst. Struct.* **21**, 243–249 (2010).
31. S. Dalola, V. Ferrari, and D. Marioli, "Pyroelectric effect in PZT thick films for thermal energy harvesting for low-power sensors," *Procedia Engineering* **5**, 585–688 (2010).
32. Q. Zhang, A. Agbossou, Z. Feng, and M. Cosnier, "Solar micro-energy harvesting with pyroelectric effect and wind flow," *Sensors and Actuators A* **168**, 335–342 (2011).
33. C. Hsiao, J. Ciou, A. Siao, and C. Lee, "Temperature field analysis for PZT pyroelectric cells for thermal energy harvesting," *Sensors* **11**, 10458–10473 (2011).
34. S. K. T. Ravindran, T. Huesgen, M. Kroener, and P. Wolas, "A self-sustaining micro thermomechanic-pyroelectric generator," *Appl. Phys. Lett.* **99**, 104102-1–104102-3 (2011).
35. A. Cuadras, M. Gasulla, and V. Ferrari, "Thermal energy harvesting through pyroelectricity," *Sensors and Actuators A: Physical* **158**, 132–139 (2010).
36. Y. Yang, et al., "Pyroelectric nanogenerators for harvesting thermoelectric energy," *Nano Lett.* **12**(6), 2833–2838 (2012).
37. S. R. Hunter, N. V. Lavrik, T. Bannuru, S. Mostafa, S. Rajic, and P. G. Datskos, "Development of MEMS based pyroelectric thermal energy harvesters," *Proc. SPIE* **8035**, 80350V-1–80350V-12 (2011) [doi: 10.1117/12.882125].
38. A. Batra, S. Bhattacharjee, A. Chilvery, and J. Stephens, "Energy harvesting via pyroelectric transducer," *Sensors & Transducers J.* **138**(3), 114–121 (2012) http://www.sensorsportal.com/HTML/DIGEST/P 953.htm.
39. J. Xie, X. P. Mane, C. W. Green, K. M. Mossi, and K. Leang, "Performance of piezoelectric materials for pyroelectric energy harvesting," *J. Intell. Mat. Systs. Struc.* **0**, 1–7 (2009).
40. S. B. Lang and M. Alexe, "Optimization and experimental verification of pyroelectric bimorph radiation detector," *IEEE Appl. Ferroelectrics* **8**, 195–198 (1998).

41. S. Zhong, S. P. Alpay, and Z. G. Ban, "Effective pyroelectric response of compositionally graded ferroelectric materials," *Appl. Phys. Lett.* **86**, 092903-1–092903-2 (2005).

42. A. K. Batra, J. Corda, P. Guggilla, M. D. Aggarwal, and M. E. Edwards, "Electrical properties of silver nanoparticles reinforced $LiTaO_3$:P(VDF-TrFE) composite films," *Proc. SPIE* **7419**, 741904 (2009) [doi: 10.1117/12.824384].

43. M. D. Aggarwal, A. K. Batra, P. Guggilla, M. E. Edwards, B. G. Penn, and J. R. Currie, Jr., "Pyroelectric materials for uncooled IRdetectors: processing, properties,and applications," NASA **NASA/TM,216373**, 1–81 (2010).

44. J. Xie, X. P. Mane, C. W. Green, K. M. Mossi, and K. Leang, "Energy harvesting by pyroelectric effect using PZT," *Proc. of ASME* **10**, 1–5 (2008).

45. A. K. Batra, S. Bhattacharjee, A. K. Chilvery, M. D. Aggarwal, M. E. Edwards, and A. Bhalla, "Simulation of energy harvesting from roads via pyroelectricity," *J. Photonics for Energy* **1**, 014001-1–014001-12 (2011).

46. A. Cuadras, M. Gasulla, and V. Ferrari, "Thermal energy harvesting through pyroelectricity," *Sensors and Actuators A* **158**, 132–139 (2010).

47. "Guide for Mechanistic Empirical Design of New and Rehabilitated Pavement Structures: Final Report," National Cooperative Highway Research Program (NCHRP), *NCHRP Project No. 1-37A*, Transportation Research Board, National Research Council, Washington DC (2004).

48. D. Guyomar, G. Sebald, A. Lefeurvre, and C. Richard, "Toward energy harvesting using active materials and conversion by nonlinear processing," *IEEE Trans. Ultrasonic, Ferroelectrics and Frequency Control* **53**, 584–595 (2005).

49. R. B. Olsen, D. A. Bruno, and J. M. Briscoe, "Cascaded pyroelectric energy converter," *Ferroelectrics* **59**, 205–219 (1984).

50. R. B. Olsen, D. A. Bruno, and J. M. Briscoe, "Pyroelectric conversion cycles," *J. App. Phys.* **58**, 4709–4716 (1985).

51. R. B. Olsen, D. A. Bruno, J. M. Briscoe, and W. F. Butler, "A pyroelectric energy converter which employs regeneration," *Ferroelectrics* **38**, 975–978 (1981).

52. R. B. Olsen, "Ferroelectric conversion of heat to electrical energy—a demonstration," *J. Energy* **6**, 91–95 (1982).

53. R. B. Olsen and D. D. Brown, "High-efficiency direct conversion of heat to electrical energy—related pyroelectric measurements," *Ferroelectrics* **40**, 17–27 (1982).

54. R. B. Olsen, D. A. Bruno, and J. M. Briscoe, "Pyroelectric conversion cycle of vinylidene fluoride-trifluoroethylene copolymer," *J. App. Phys.* **57**, 5036–5042 (1985).
55. A. van der Ziel, "Solar power generation with the pyroelectric effect," *J. App. Phys.* **45**, 4128–4132 (1974).
56. M. Ikura, "Conversion of low-grade heat to electricity using pyroelectric copolymer," *Ferroelectrics* **267**, 403–408 (2002).
57. L. Kouchachvili and M. Ikura, "High performance pyroelectric converter," *Proc. of the Sixth IASTED International Conference European Power and Energy Systems*, 366–371 (2006).
58. A. Khodayari, S. Pruvost, G. Sebald, D. Guyomar, and S. Mohammadi, "Nonlinear pyroelectric energy harvesting from relaxor single crystals," *IEEE Transactions on Ultrasonics, Ferroelectrics, and Frequency Control* **56**, 693–700 (2009).
59. R. B. Olsen and J. M. Briscoe, "Regenerative pyroelectric heat engine," *16th Intersociety Energy Conversion Engineering Conference* **3**, 2081–2085 (1981).
60. S. Mohammadi and A. Khodayari, "Pyroelectric energy harvesting with thermodynamic-based cycles," *Smart Mat. Res.* **2012**, 160956 (2012).
61. G. Sebald, L. Seveyrat, D. Guyomar, L. Lebrun, B. Guiffard, and S. Pruvost, "Electrocaloric and pyroelectric properties of $0.75(Mg_{1/3}Nb_{2/3})O_3$-$0.25PbTiO_3$ single crystals," *J. App. Phys.* **100**, 124112 (2006).
62. G. Sebald, S. Pruvost, and D. Guyomar, "Energy harvesting based on Ericsson pyroelectric cycles in a relaxor ferroelectric ceramic," *Smart Mater. Struct.* **17**, 1–12 (2008).
63. H. Zhu, S. Pruvost, D. Guyomar, and A. Khodayari, "Thermal energy harvesting from $Pb(Zn_{1/3}Nb_{2/3})_{0.955}Ti_{0.045}O_3$ single crystals phase transitions," *J. App. Phys.* **106**, 124192-1–124192-7 (2009).
64. G. Sebald, E. Lefeuvre, and D. Guyomar, "Pyroelectric energy conversion: optimization," *IEEE Trans. Ultrasonics, Ferroelectrics, and Frequency Control* **55**, 538–551 (2008).
65. H. H. S. Chang and Z. Huang, "Laminate composites with enhanced pyroelectric effects for energy harvesting," *Smart Mater. Struct.* **19**, 065018 (2010).
66. H. Nguyen, A. Navid, and L. Pilon, "Pyroelectric energy converter using co-polymer P(VDF-TrFE) and Olsen cycle for waste heat energy harvesting," *Applied Thermal Engineering* **30**, 2127–2137 (2010).
67. F. Y. Lee, A. Navid, and L. Pilon, "Pyroelectric waste heat energy harvesting using heat conduction," *Applied Thermal Engineering* **37**, 30–37 (2012).

68. R. Kandilian, A. Navid, and L. Pilon, "The pyroelectric energy harvesting capabilities of PMN–PT near the morphotropic phase boundary," *Smart Mater. Struct.* **20**, 1–10 (2011).

69. I. M. McKinley, R. Kandilian, and L. Pilon, "Waste heat energy harvesting using the Olsen cycle on $0.945Pb(Zn_{1/3}Nb_{2/3})O_3$-$0.055PbTiO_3$ single crystals," *Smart Mater. Struct.* **21**, 1–10 (2012).

70. F. Y. Lee, S. Goljahi, I. M. McKinley, C. S. Lynch, and L. Pilon, "Pyroelectric waste heat energy harvesting using relaxor ferroelectric 8/65/35 PLZT and the Olsen cycle," *Smart Mater. Struct*. **21**,1–12 (2012).

71. D. Vanderpool, J. H. Yoon, and L. Pilon, "Simulations of a prototypical device using pyroelectric materials for harvesting waste heat," *International J. Heat and Mass Transfer* **51**, 5052–5062 (2008).

72. R. C. Moreno, B. A. James, A. Navid, and L. Pilon, "Pyroelectric energy converter for harvesting waste heat: simulation versus experiments," *Int. J. Heat Mass Transfer* **55**, 4301–4311 (2012).

73. A. Navid, D. Vanderpool, A. Bah, and L. Pilon, "Towards optimization of a pyroelectric energy converter for harvesting waste heat," *Int. J. Heat Mass Tranfer,* **53**, 4060–4070 (2010).

Appendix
Major Pyroelectric Manufacturing Companies

Major manufacturing companies for pyroelectric-IR detectors, imaging devices, and related products are listed in the table below for easy reference. The list is not comprehensive and is subject to change.

Company	Website	Location
DIAS Infrared GmbH	www.dias infrared.com	USA
Eltec Instruments, Inc.	www.eltecinstruments.com	USA
Excelitas Technologies	www.excelitas.com	USA
Gentec EO USA, Inc.	www.gentec eo.com	USA
InfraTec GmbH	www.InfraTec.de	Germany
KUBE Electronics AG	www.kube.ch	Switzerland
Murata Manufacturing Co., Ltd.	www.murata.com	Japan
Ophir Spiricon, LLC	www.ophiropt.com	USA
Silverlight Ltd.	www.silverlight.ch	Switzerland

Index

0-3 connectivity composites, 60
3D pattern of recessed holes in the sensitive element, 113
3D ZnO film, 113

A
aerosol deposition rapid process, 113
aluminum nitride (AlN) films, 91

B
$Ba_{0.8}Sr_{0.2}TiO_3$ thin films, 83
barium strontium titanate, 81
$Bi_{1.5}Zn_{1.0}Nb_{1.5}O_7$, 111
bimorph radiation detectors, 105
bimorphs, 105
BZN-buffered BTS thin films, 112

C
carbon multiwall nanotubes, 32
Carnot cycle, 144
ceramic, 50
Clingman cycle, 147
comb-like electrode, 113
commercial PVDF films, 152
compact 14.1-MeV neutron source, 128
compositionally graded ferroelectric devices, 107
compositionally graded structure, 108
cool-X, 129
crystal growth, 47
crystal systems, 2
crystallographic groups, 3
Curie–Weiss relation, 14
current responsivity, 26
CVD process, 52
Czochralski technique, 48

D
detection of simulants for chemical nerve agents, 131
detectivity, 27
deuteration of TGS, 67
dielectric materials, 1
domain-engineered pyroelectric radiometer, 116
domain-engineered TFLT pyroelectric detector, 40

E
electric displacement, 6
electrostrictive effect, 7
energy dissipated per unit volume of the ferroelectric material, 15
energy harvesting, 135
Ericsson cycle, 145

F
fabrication of ceramics, 51
fabrication of PZT films, 51
ferroelectric domain, 14
ferroelectric material, 2
ferroelectricity, 137

field ionization in pyroelectric-crystal D–D-fusion experiments, 129
figures of merit
high detectivity of PCT films, 109
modified TGS crystals, 67
pyroelectric element on a heat sink, 30
flux density, 6
fully covered electrode, 117

G
GaN, 92
GaN resonator IR detector, 39
graded ferroelectric devices, 107
group-III nitride oxides, 91

H
harvested electric energy with Ericsson cycles, 164
harvesting energy using PZT-5A, 151
high-pressure casting, 60
hybrid focal-plane array, 35
hysteresis loop, 14

I
interdigital electrodes, 116
IR camera, 36
IR detectors, 39, 41
IR radiation sensors, 21, 22

J
Johnson noise, 28

K
key ferroelectric/pyroelectric materials, 3

L
laser ablation deposition, 52
lead magnesium niobate-lead titanate, 163
lead titanate, 69
lead-free ceramics, 93
lead-free pyroelectric ceramics, 93
Lenoir and Ericsson thermodynamic cycle, 163
Lenoir cycle, 146
lithium niobate, 78
lithium tantalate, 78
lithium tantalate chip, 37

M
metal-black coatings, 31
metalorganic CVD, 53
microelectric generator, 139
MOD method, 55
modeled and simulated energy harvesting capacity, 153
modified TGS crystals, 67
monolithically integrated FPA of a pyroelectric PLZT, 35
multilayer thin films, 106

N
nanoporosity, 112
neutron generation via D–D fusion, 125
neutron production, 127
$(NH_2CH_2COOH)_3{\cdot}H_2SO_4$, 65
noise sources
in detector element, 26
of the pyroelectric element, 28
novel uncooled IR detector, 38

O
Olsen pyroelectric energy converter, 148
organic pyroelectrics, 86

P
paraelectricity, 16
partially covered electrode (PCE), 117
PCT films, 109
phenomenological approach, 7

physics of current generation, 11
piezoelectric coefficients, 8
piezoelectric effect, 7
piezoelectric voltage coefficient, 9
piezoelectricity, 2
plasma-enhanced CVD, 53
PMN-PT, 85
poling, 15
polycrystalline macrodomains, 114
polyvinylidene fluoride, 86
primary pyroelectric effect, 9
pyroelectric accelerators, 122
pyroelectric capacitive bimorph-cantilever structure, 152
pyroelectric coefficient
  in 2-2 connectivity laminate composites, 165
  of compositionally graded PZT film, 109
pyroelectric current, 13
pyroelectric detector
  high-performance, 41
  noise, 26
  operation, 22
  simplest arrangement, 24
  single element, 30, 32
pyroelectric effect, 9
pyroelectric energy generator, 151
pyroelectric fusion, 125
pyroelectric material performance, 139
pyroelectric materials, 9
pyroelectric phenomenon, 1
pyroelectric radiometer, 116
pyroelectric trap detector, 37
pyroelectricity, 2
pyroelectric–polymer composites, 87
PZT films, 51
PZT-based ferroelectric-oxide, 72

Q
quarter-wavelength absorbers, 31

S
screen printing, 59
screen-printed PZT films, 152
secondary pyroelectric effect, 9
signal-to-noise ratio, 27
silicon substrate, 34
smart materials, 3
sol-gel processing, 54
solvent casting, 60
specific detectivity, 27
spider-web-type absorber, 32
sputtering methods, 51
strontium barium niobate, 84
symmetry elements, 2

T
tertiary pyroelectric effect, 11
thermal energy harvesting sources, 152
thermal energy of pavements, 157
thermal noise voltage, 28
thermistor bolometer, 118
thermodynamics-based cycles, 139
thin metal, 31
triglycine sulfate (TGS), 65

V
VDF/TrFE copolymer, 87
voltage responsivity, 26

X
x-ray and electron sources, 129
x-ray fluorescence analysis, 131
x-ray generator, 129
x-ray irradiated/field-treated TGS, 67

Z
zinc oxide, 92
ZnO pyroelectric device, 113

Ashok Batra holds a Master's of Technology and Ph.D. from the Indian Institute of Technology, Delhi. With more than 20 years of experience in the diverse areas of solid state physics/materials and their applications, he is currently Associate Professor of Physics at Alabama A&M University. His research experience and interests encompass ferroelectric, pyroelectric, and piezoelectric materials and their applications; design, fabrication and characterization of pyroelectric, piezoelectric, photothermal and photovoltaic devices; nonlinear optical organic crystals, organic semiconductors, crystal growth from solution and melt, microgravity materials research, nanocomposites, and chemical sensors. Dr. Batra is currently engaged in research related to the development of ambient energy harvesting nanoparticle-based chemical sensors, and organic photovoltaic solar cells. He has been both a principal and co-investigator for various research grant awards from the U. S. Army/SMDC, NSF, DHS, and NASA, including a NASA grant related to the International Microgravity Laboratory-1 experiment flown aboard the Space Shuttle Discovery. Recipient of a *NASA Group Achievement* award and the Alabama A&M University School of Arts and Sciences *Researcher of the Year* award, he has published more than 120 publications including book chapters, proceedings and review articles, and NASA TMs. Dr. Batra is a member of SPIE, MRS, AES, and AAS.

Mohan Aggarwal is chair and professor at the Department of Physics, Chemistry, and Mathematics in the College of Engineering, Technology, and Physical Sciences at Alabama A&M University. He earned his Ph.D. in Physics in 1974 from the Saha Institute of Nuclear Physics, Calcutta University, and did his postdoctoral work at Pennsylvania State University in solid state devices, going on to join the NASA Spacelab-3 Space Flight Experiment as a researcher on the growth of IR crystals in microgravity at Alabama A&M University. Dr. Aggarwal has extensive experience in bulk crystal growth and the characterization of a variety of organic and inorganic nonlinear optical crystals, such as divinyl anisole, Schiff-base compounds, bismuth silicon oxide, barium titanate, piezoelectric materials (e.g., PMN-PT), and scintillator materials (e.g., lanthanum bromide) using melt growth techniques. He has authored and coauthored more than 207 publications and is a member of many academic societies including the American Physical Society, American Vacuum Society, and SPIE.

Pyroelectric Materials

Infrared Detectors, Particle Accelerators, and Energy Harvesters

A. K. Batra · M. D. Aggarwal

This monograph contains comprehensive information on pyroelectric materials and their preparation, properties, and applications, such as uncooled wideband infrared detectors, particle generators, and ambient energy harvesters. The complete lifecycle of a pyroelectric material is presented here for readers—from the theory of operation, to structure, processing, and applications—providing a cohesive overview of essential concepts, including the theoretical background and current developments in the field of pyroelectric devices. The book describes the preparation, structure, properties, and figures of merit for practical pyroelectric materials such as triglycine sulfate, lead zirconate titanate, lithium tantalate, lithium niobate, barium strontium titanate, lead magnesium niobate-lead titanate, polyvinylidene fluoride, zinc oxide, and others, including the merits and demerits of their use in devices.

ISBN 978-0-8194-9331-6
9 780819 493316 90000

SPIE

P.O. Box 10
Bellingham, WA 98227-0010

ISBN: 9780819493316
SPIE Vol. No.: PM231

Pyroelectric Materials: Infrared Detectors, Particle Accelerators, and Energy Harvesters
BATRA · AGGARWAL

SPIE PRESS